Cortical microvessels and the tripartite synapse in chronic pain studied with synchrotron radiation

Veronica del Grosso

To cite this version:

Veronica del Grosso. Cortical microvessels and the tripartite synapse in chronic pain studied with synchrotron radiation. Human health and pathology. Université Grenoble Alpes, 2017. English. NNT : 2017GREAS034 . tel-01719388

HAL Id: tel-01719388
https://theses.hal.science/tel-01719388

Submitted on 28 Feb 2018

Communauté
UNIVERSITÉ Grenoble Alpes

THÈSE

Pour obtenir le grade de

DOCTEUR DE LA COMMUNAUTE UNIVERSITE GRENOBLE ALPES

Spécialité : **BIS - Biotechnologie, instrumentation, signal et imagerie pour la biologie, la médecine et l'environnement**

Arrêté ministériel : 25 mai 2016

Présentée par

Veronica Del Grosso

Thèse dirigée par **Alberto BRAVIN (EDISCE), habilitation ponctuelle en 2014** et codirigée par **Gabriele E.M. Biella**

préparée au sein du **European Synchrotron Radiation Facility** dans **l'École Doctorale Ingénierie pour la santé la Cognition et l'Environnement**

"Cortical microvessels and the tripartite synapse in chronic pain studied with synchrotron radiation"

Thèse soutenue publiquement le **30/10/2017**
devant le jury composé de :

Monsieur Antoine Depaulis (Président)
Directeur de recherche, Grenoble Institut Des Neurosciences
Monsieur Alessandro Olivo (Rapporteur)
Professeur, University College of London
Monsieur Rasmus Petersen (Rapporteur)
Senior Lecturer and Principal Investigator, University of Manchester
Madame Paola Coan (Examinateur)
Professeur associé, Ludwig Maximilians Universität
Monsieur Alberto Bravin (Directeur de thèse)
Directeur de Recherche, European Synchrotron Radiation Facility
Monsieur Gabriele E.M. Biella (Co-directeur de thèse)
Chargé de Recherche, National Research Council of Italy
Monsieur Sam Bayat (Invité)
Professeur, Centre Hospitalier Universitaire de Grenoble

To my Grandmother…

Résumé

La douleur chronique (DC) est un trouble sensoriel complexe caractérisé par des changements structurels, c'est-à-dire par des réarrangements anatomiques sévères du cortex somatosensoriel et des changements fonctionnels, à savoir des anomalies dans la connectivité fonctionnelle du réseau et la transmission de l'information au niveau du circuit thalamo-cortical. Structurellement, dans chaque module cortical, une unité morpho-fonctionnelle peut être reconnue, appelée unité neuro-gliale-vasculaire, où les cellules gliales représentent les structures de pontage permettant le transfert de métabolites et d'oxygène aux neurones. La dépendance fonctionnelle entre les éléments neuronaux et vasculaires, explorée en grande partie par microscopies confocale 3D et bi photonique a élargi le concept de l'espace synaptique en une forme plus complexe, appelé «synapse tripartite», où malgré la présence de neurones pré et post-synaptiques, un composant glial est ajouté face au contexte microvasculaire. Il semble donc correct d'analyser les effets microscopiques corticaux de l'image macroscopique. Des études récentes de notre groupe ont traité de l'origine et l'évolution de la DC dans des modèles expérimentaux de rat DC (Seltzer) grâce à des analyses microstructurales et fonctionnelles axées sur le substrat neuronal corticale et les propriétés micromorphologiques et vasculodynamiques du sang. La microarchitecture du réseau vasculaire cortical a été révélée via la microtomographie par rayonnement X synchrotron aux lignes ID17 et ID16A (ESRF, Grenoble) ainsi qu'à la ligne TOMCAT (SLS, Villigen). S'en est suivi une analyse morphométrique du réseau vasculaire 3D par squelettisation et transformation du graphe spatial. Ensuite, une étude comparative "Neuropathique vs Contrôle", basée sur les propriétés du réseau vasculaire (nombre de vaisseaux, points de branche, segments de squelette et diamètre du vaisseau) a montré des changements évidents dans les compartiments microvasculaires corticaux: une augmentation généralisée des micro-vaisseaux et des capillaires sanguins dans les régions étudiées (cortex somatosensoriel SS1) caractérisent tous les rats DC. Parallèlement, une réduction du diamètre moyen des vaisseaux des rats DC prouve que les capillaires et les microvaisseaux ont une affinité prédominante pour ces événements angiogénétiques. L'évolution des néogènes est très présente dès la première étape de la neuropathie (2 semaines), puis diminue mais persiste durant la dernière étape considérée (6 mois). En outre, un flux sanguin maximal accru a été trouvé dans l'état de DC, indiquant que les réseaux vasculaires DC sont compatibles avec un flux enrichi soutenu par l'angiogenèse. Ces résultats provenant de la micro et nanotomographie ont été confirmés via microscopie en immunofluorescence: les échantillons DC ont montré la positivité à trois marqueurs de néogénèse vasculaire (VEGFR1, VEGFR2 et VWF). En parallèle, pour analyser fonctionnellement la genèse et l'évolution des circuits thalamo-corticaux dans les conditions de DC, l'activité neurale a été enregistrée par une matrice de 32 microélectrodes implantée dans le cerveau, recevant simultanément des signaux du noyau thalamique VPL et du cortex SS1. Tous les rats DC montrent des troubles de connectivité révélés aussi par l'évolution de la topologie du réseau de «Modules et Hubs» à une organisation «aléatoire» où les connexions fonctionnelles intra et intercommunautaires diminuent. Ces résultats confirment comment la dynamique neuronale est liée à l'activité vasculaire: les événements néo-génétiques des microvaisseaux corticaux dans la DC sont fortement corrélés aux anomalies fonctionnelles de la dynamique des réseaux neuronaux. L'implication microvasculaire dans la DC ouvre une nouvelle façon de l'interpréter, non seulement reconnue comme pathologie sensorielle, mais aussi comme une maladie neurologique où les réseaux de connectivité neuronale et vasculaire sont largement impliqués dans le système.

Mots clés: douleur chronique, microvaisseaux corticales, synapse tripartite, cortex somatosensoriel

Abstract

Chronic pain (CP) is a complex sensory disorder characterized by structural changes, i.e. severe anatomical rearrangements of somatosensory cortex, and functional changes, i.e. anomalies in network functional connectivity and in information transmission at the level of thalamo-cortical circuit. From the structural point of view, within each cortical module, a morpho-functional unit can be recognized, also called neuro-glial-vascular unit, where the glial cells represent the bridging structures allowing for the transfer of metabolites and oxygen to neurons. Namely, the functional dependency between neuronal and vascular elements, largely explored by 3D confocal microscopy and two photon microscopy, has expanded the concept of synaptic space to a more complex form, indicated as "synapse tripartite", where besides the presence of the pre- and post- synaptic neurons, a glial component is added facing on the microvascular context. Due to this dependency it appears, thus, correct to analyse the cortical microscopical effects of the macroscopical picture. Novel studies by our group have recently investigated CP origin and evolution in experimental CP rat models (Seltzer) through microstructural and functional analyses focused both on the cortical neuronal substrate and the blood micromorphological and vasculodynamic properties. The 3D microarchitecture of cortical vascular network has been revealed by means of synchrotron X-ray micro Computed Tomography (CT) at the ID17 and ID16A beamlines (ESRF, Grenoble) and the TOMCAT beamline (SLS, Villigen). A subsequent morphometric analysis of the 3D vascular network has been implemented by means of skeletonization and spatial graph transformation. Then, a comparative study "Neuropathic vs Control", based on the estimated vascular network properties (number of vessels, branch points, skeleton segments and vessel diameter), showed evident changes in cortical microvascular compartments: a widespread increase of blood microvessels and capillaries in the investigated regions (the somatosensory [SS1] cortical area) has been found in all CP rats. In parallel, a reduced mean value of vessel diameter in all CP rats prove that capillaries and small microvessels are predominantly interested by these angiogenetic events. By investigating the time evolution of the neogenesis, it appears strongly present since the first stage of the neuropathy (2 weeks), fading away, but still present, during the last time stage considered (6 months). In addition, an increased maximum blood flow, sustained by the vascular network, has been found in CP condition, indicating that CP vascular networks are compatible with an enriched blood flow sustained by the promoted novel angiogenesis. These results from micro- and nano-tomography have been further confirmed also by immunofluorescence microscopy analysis: CP samples have shown the positivity to three markers of vascular neo-genesis (VEGFR1, VEGFR2 and VWF). In parallel, to functionally analyse the genesis and the evolution of the thalamo-cortical circuits in CP conditions, the neural activity has been recorded by means of 32-microelectrode matrices implanted in the brain, simultaneously receiving signals from the VPL thalamic nucleus and the SS1 cortex. All the CP groups show connectivity disorders exhibited also by the evolution of the network topology from "Modules and Hubs" to a "random" network organisation where the intra-community and inter-community functional connections decrease. These results clearly confirm how the neuronal dynamics is strictly linked to the vascular activity: the cortical microvessel neo-genetic events in CP are strongly correlated to the functional anomalies in neuronal network dynamic. The microvascular involvement in CP opens a new way of interpretation of CP disease, not only recognized as sensory pathology, but also as a neurological disease where neuronal and vascular connectivity networks are extensively involved in the whole system.

Key words: chronic pain, cortical microvessels, tripartite synapse, somatosensory cortex

Contents

Chapter 1: Biological Background

Chapter 2: Materials and methods

Chapter 3: Results

Chapter 4: Discussion

List of abbreviations

aCSF =artificial Cerebrospinal Fluid

AD=Alzheimer’s disease

AlAS=Anterolateral Ascending System

ALS=Amyotrophic Lateral Sclerosis

AP=Anterior-Posterior

BM=Bending Magnets

BOLD=Blood Oxygenation Level-Dependent

BSA=Bovine Serum Albumine

CBF=Cerebral Blood Flow

CCD=Charged Coupled device

CD31=Cluster of Differentiation 31

Ch=Chattering

CMOS=Complementary Metal Oxide Semiconductor

CNR=Consiglio Nazionale delle Ricerche

CNS=Central Nervous System

CP=Chronic Pain

CT=Computed Tomography

DAPI=4’,6-Diamidino-2-Phenylindole

DCMM=Double Crystal Multilayer Monochromator

DW-MRI=Diffusion Weighted Magnetic Resonance Imaging

EEG=Electroencephalography

EMSC=ESRF-made Multislit Collimator

ESRF=European Synchrotron Radiation Facility

fMRI=Functional Magnetic Resonance Imaging

FPB =Filtered Back Projection Algorithm

FReLoN= Fast REadout LOw Noise

FS=Fast Spiking

GAM=Goat Anti-Mouse

GE=Global Effect

GUI=Graphical User Interface System

HIER=Heat-Induced Epitope Retrieval

IASP=International Association for the Study of Pain

IB=Intrinsically Bursting

IBFM=Institute of Molecular Bioimaging and Physiology

IC=Ionization Chamber

ID=Insertion Device

IP=Intra Peritoneal

KB=Kirkpatrick-Baez

LED=Light-Emitting Diode

LFPs=Local Field Potentials

LTS=Low Threshold Spiking

MB=Microbeams

ML=Multi-layer

MNT=Mechanical Nociceptive Threshold

MRT=Microbeam Radiation Therapy

NCS=Normalized Compression Similarity

NE=Neuronal Ensembles

NGV=Neuro-glial-vascular

NIRS=Near InfraRed Spectroscopy

NLCG=Non-Linear Conjugate Gradient

NSAID=Non Steroidal Anti-inflammatory Disease

NVC=Neurovascular Coupling

PAG=Peri-Acqueductal Gray

PBPCI=Propagation Based Phase Contrast Imaging

PBS=Polyphosphate Buffered Solution

PCB=Printed Circuit Board

PCI=Phase Contrast Imaging

PET=Positron Emission Tomography

PSL=Partial Sciatic Ligature

PyHST=Python High Speed Tomography

RS=Regular Spiking

RVM=Rostroventromedial

SB=Spectral Brightness

SCI=Sciatic Constriction Injury

SE=Staged Effect

SLS=Swiss Light Source

SN=Single Neuron

SPC=Super-Paramagnetic Clustering

SSRT=Stereotactic Synchrotron Radiation Therapy

SS1=Somatosensory

TC=Thalamo-Cortical

TIE=Transport of Intensity Equation

VB=Ventrobasal

VEGFR1=Vascular Endothelial Growth Factor 1

VEGFR2=Vascular Endothelial Growth Factor 2

VL=Ventrolateral

VPL=Ventral posterior lateral

VPM= Ventral posterior medial

VWF= Von Willebrand Factor

XOP=X-ray Optics software

Introduction Générale

D’après la définition de l'Association internationale pour l'étude de la douleur (IASP) (Merskey 1994), la douleur chronique (DC) représente le motif perceptuel commun accompagnant de nombreux états pathologiques qui présentent des troubles sensoriels atroces des troubles sensoriels atroces bien distincts dans leurs caractéristiques d'origine, fréquence, amplitude et temporal (Weiner 2001). En raison de sa complexité, les substrats neuronaux et extraneuronaux enchevêtrés générant de la DC, du stade moléculaire jusqu'à la perception, sont, au mieux, mal compris, malgré les récents progrès conceptuels importants (Tracey et al. 2007). En outre, alors que des douleurs aiguës évoquées par de brefs avertissements nocifs ont été minutieusement étudiées par les neuroscientifiques, et leurs mécanismes de transmission sensorielle sont généralement bien compris, la DC, caractérisée par une douleur sévère associée à une blessure ou à une pathologie discernable, est un mystère (Melzack 2001). La contrepartie neurale reflétant cet état perceptuel complexe est complémentairement composite et souvent non linéairement liée aux signes perceptifs. Par exemple, la douleur spontanée expérimentale, ou allodynie, et l'hyperalgésie sont apparemment reflétées, dans la moelle épinière neuronale, par hyperactivité spontanée ou hyperréactivité à des stimuli liés (Hao, Kupers et Xu 2004 ; Sotgiu, Biella et Riva 1994 ; CA Porro et al. 1998). Parallèlement, de fortes corrélations entre les schémas spatiaux de l'activité cérébrale altérée et le comportement lié à la douleur dans le modèle de la douleur chronique chez le rat ont également été démontrées (A. Zippo et al. 2011). De manière comparable, chez les humains, la cohérence de la magnitude de l'activation avec l'intensité estimée de la douleur a été rapportée dans les études d'imagerie et d'électrophysiologie (Endo et al. 2008 ; Porro 2003 ; Green et al. 2009). En revanche, de nombreux enregistrements neuronaux et des données d'imagerie ont souvent montré des mosaïques mutuellement incohérentes d'activation et d'inactivation de la zone cérébrale (Bushnell et al. 1999 ; Iadarola et al. 1995). Tous ces problèmes inspirent vivement l'évaluation de l'activité par défaut et la connectivité de la douleur chronique (Tracey 2005). Les modèles de représentation de la douleur répartie dans le cerveau, comme l'hypothèse de Neuromatrix (Melzack 1999), une théorie d'intégration plus récente (Apkarian, Baliki et Geha 2009), interprètent diversement la DC comme résultat d'activités régionales intégratives actives également dans les états de repos impliquant la voie neuronale établie entre le thalamus et le cortex (circuit thalamo-cortical), ainsi qu’entre le cortex et le système limbique. Au niveau anatomique, les études de fMRI sur le cortex somatosensoriel des patients avec la DC ont révélé une densité de matière grise réduite et des réarrangements macroscopiques de l'architecture corticale (Apkarian et al. 2004). Tous ces troubles anatomiques et fonctionnels caractérisant l'état de la DC ont généralement été décrits comme des "états de plasticité inadaptés" de régions sensorielles spécifiques du cerveau. Ces milieux bien structurés, cependant, ne donnent aucune indication sur la façon dont les substrats du cerveau neuronal se comportent dans la DC. Étant donné que l'activité de l'unité n'est pas représentative de la complexité perceptuelle de la douleur, il est discutable qu'une caractéristique, une sorte de signature neurale, soit dans le neurone unique, soit dans les activités du réseau, puisse comporter des marqueurs de la DC spontanée.

Dans des études antérieures réalisées par le scientifique du laboratoire CNR (A. Zippo et al. 2011; A. Zippo et al. 2016) utilisant des enregistrements électrophysiologiques massifs simultanés du thalamus et du cortex somatosensoriel, il est apparu que la DC a affecté la connectivité neuronale au sein du réseau thalamo-cortical somatosensoriel, réduisant ses capacités de traitement de l'information, et entrainant untransfert d'information affaibli et une dégradation globale du réseau topologique. Dans l'ensemble, ces conditions concourent à générer des configurations de réseau récursives et stéréotypées, qui semblent apparaître comme des contreparties anatomo-fonctionnelles de la perception continue de la douleur, une image pouvant être récupérée de tous les modèles DC examinés. Dans le but de fournir une rénovation de la connectivité thalamo-corticale et de relancer l'équilibre de l'alternance d'intégration/ségrégation sans intervention chimique ou modulations électriques, une expérience a été réalisée par le groupe CNR à la ligne d'identification ID17 (ESRF, Grenoble). Des microfaisseaux collimatés ont été utilisés (dans des rats vivants anesthésiés avec et sans modèles DC) afin d'obtenir un cortex sensoriel modulé artificiellement capable d'exprimer différents comportements neurodynamiques, enrichissant ainsi le contenu d'information du réseau thalamo-cortical. En détail, les microbeams parallèles (sept microbeams de rayons X de 100 µm de large, espacés de 400 µm et déposant une dose maximale 360 Grays) ont créé 8 modules putatifs dans les rats DC qui, plus tard, ont montré que i) la connectivité fonctionnelle était rétablie de manière comparable pour contrôler les animaux; ii) les paramètres comportementaux tels que le temps de réponse aux stimulations périphériques nociceptives et non-nociceptives ont été rétablis au niveau normal (aucun changement fonctionnel/électrophysiologique ou comportemental n'était évident chez les animaux témoins). La dynamique réduite du cortex a été enrichie en multipliant les modules somatosensoriels indépendants qui ont augmenté le transfert d'informations et l'adaptabilité des circuits thalamo-corticaux.

But de la thèse

En dehors de la voie ouverte par ces études précédentes, le but de ce travail est l'exploration plus approfondie du comportement du contexte gliale et vasculaire qui régule la dynamique neuronale. Cette étude traite, en particulier, la relation délicate anatomique et fonctionnelle entre la synapse tripartite et les micro-vaisseaux sanguins dans des conditions normales et en cas de la douleur chronique. Les synapses neuronaux entremêlés et les architectures glio-vasculaires (Woolsey et al. 1996) représentent un module électrochimique et métabolique de base, également unité neuro-gliale-vasculaire (NGV), au niveau cortical dans le cerveau. En fait, l'activité électrique synaptique, enregistrée sous le nom de Local Field Potentials (LFPs), dépend de la dynamique optimale du compartiment vasculaire vasculaire, où les cellules gliales sont les structures de pontage permettant le transfert des métabolites et de l'oxygène des microvaisseaux

aux neurones. Des recherches récentes effectuées par le groupe CNR ont démontré la dépendance des Spikes à partir des LFPs, une empreinte synaptique dans les activités neuronales, ce qui pourrait éventuellement étendre la dépendance de l'activité de pointe à la dynamique des microvaisseaux (Storchi et al. 2012). Les activités synaptiques transmettent les messages neuronaux non seulement d'un neurone à l'autre, mais aussi des astrocytes à proximité qui sont à leurs tours confrontés aux membranes microvasculaires. Les messages passant des neurones aux vaisseaux, en régulant leurs diamètres, sont surtout conduits par l’intermédiation des astrocytes. Cet enchainement complexe de caractéristiques fonctionnelles est basé sur une architecture composite neurale et glio-vasculaire. Des techniques d’imagerie par lumière visible ont fourni des données soutenant la tendance que le noyau des neurones est plus éloigné des vaisseaux que ce à quoi on pourrait s’attendre avec une répartition spatiale aléatoire. Cela montre qu’au sein de chaque couche corticale la densité de somata neuronal et la répartition de micro-vaisseaux ont un ratio spécifique, qui détermine une architecture spatiale unique et montre une dépendance fonctionnelle mutuelle entre les vaisseaux et les neurones. **Avec ce travail, je voudrais analyser les troubles micro/nano architecturaux dans les espaces corticaux potentiellement reliés aux importants réarrangements anatomiques** impliquant l’architecture macroscopique.

Ce travail a été mené selon deux analyses parallèles :

- **Analyse microstructurale** : des expériences de micro et nano tomographie par rayonnement synchrotron réalisées au sein de deux synchrotrons (l’ESRF de Grenoble et le SLS de Villigen), ont été menées pour évaluer la micro-architecture des anomalies potentielles imbriquées dans la texture corticale microscopique recevant les matrices de la fonction neuro-gliale des vaisseaux. Une analyse morphologique concentrée sur la caractérisation du réseau vasculaire a permis l’identification des changements vasculaires dans des conditions de douleurs chroniques.
- **Analyse neurodynamique :** les enregistrements électrophysiologiques chroniques *in vivo* faits aux laboratoires CNR de Milan (Italie), ont prédit les origines et les changements de temps de la connectivité fonctionnelle du cerveau et de la transmission d’information. Les sessions préliminaires d’enregistrement destinées à évaluer l’activité des micro-vaisseaux du sang et des capillaires combinées avec les dynamiques des réseaux neuronaux ont été menées par la technique NIRS (Near Infrared Spectroscopy probe) (Giardini et al. 2016).

A cause de la dépendance microstructurale entre les vaisseaux et les neurones, la réorganisation du substrat neural devrait impliquer de profonds réarrangements micro vasculaires avec un effet rétrograde potentiel. Une appréciation submicroscopique de cette reconstruction devrait mettre en lumière une potentielle nouvelle approche des anomalies de la DC de fond et de nouvelles approches thérapeutiques.

Techniques expérimentales

L'analyse morpho-fonctionnelle de la DC précédemment mentionnée a été menée en utilisant trois méthodes et techniques expérimentales différentes:

- **Imagerie via microtomographie et nanotomographie par rayonnement X synchrotron** comme outil pour l'analyse 3D (dans une optique non destructive) de la microstructure interne des échantillons corticaux somatosensoriels des rats normaux et rat avec la DC. En particulier, la technique d'imagerie à contraste de phase (Snigirev et al., 1995; Cloetens et al., 1996), a été adoptée car elle est largement reconnue comme un des meilleurs outils d'imagerie pour des échantillons biologiques avec peu de variations de densité de masse et de coefficient d'absorption à haute résolution.
- **L'immunofluorescence et l'immunohistochimie** sont utilisées comme analyses complémentaires pour valider les résultats obtenus grâce à l'imagerie à rayons X concernant les changements morphologiques dans les micro-vaisseaux corticaux.
- **Les enregistrements *in vivo* électrophysiologiques chroniques** faits avec une technologie de multi-électrodes implantables sans-fil, sont utilisés pour évaluer l'origine et l'évolution de la douleur chronique. Grace à la technique d'implants de microélectrodes chroniques, il a été possible d'enregistrer simultanément les activités de l'ensemble neuronal dans différentes régions du cerveau (circuit thalamo-corticale) sur le même animal implanté.

Structure de la thèse

La thèse est composée de trois principaux chapitres qui sont présentés brièvement ci-dessous.

Chapitre 1: Une introduction biologique à l'anatomie du système nerveux central (CNS) et aux composants principaux est présentée avec une attention soutenue sur la synapse tripartite et l'anatomie des micro-vaisseaux sanguins et leur rôle fonctionnel mutuel. Le système somato-sensoriel est donc décrit : l'organisation anatomique et fonctionnelle du cortex et du thalamus somato-sensoriels et leur voie de communication sont présentées pour bien comprendre la physiologie de la perception de la douleur, présentée plus tard. La fin du chapitre est dédiée à l'analyse complexe de la maladie de la DC : les interprétations montrées ici et les limites de la recherche actuelle stimulent une nouvelle approche de l'étude de la DC retenue dans ce travail.

Chapitre 2: Les matériaux et les méthodes utilisés pour réaliser l'activité scientifique ont été rapportés dans ce chapitre : la tomographie par rayonnement synchrotron calculée par ordinateur pour la micro et nano imagerie d'échantillons corticales somatosensoriel des rats, la microscopie de l'immunofluorescence et les enregistrements électro-physiologiques chroniques *in vivo*. Pour chaque technique les principes majeurs, l’instrumentation et les procédures expérimentales développées ont été rapportés précisément. A la fin, un premier aperçu sur la technique NIRS pour l’évaluation des changements hémodynamiques de l’activité micro-vasculaire du cortex des rats est fourni.

Chapitre 3: Les données collectées durant les trois sessions expérimentales principales sont résumées dans ce chapitre. Les résultats de l’étude comparative ‘Neuropathique contre Contrôle’ des rats portant sur les changements morphologiques du réseau micro-vasculaire du cortex sont illustrés en détail. La microscopie de l’immunofluorescence visant à confirmer les dernières découvertes sur les micro-vaisseaux des rats est montrée. Finalement, les résultats des enregistrements électro-physiologiques chroniques sont présentés au moyen de la Théorie des Graphes.

Chapitre 4: Cette dernière partie est dédiée à la discussion générale sur les découvertes importantes suite à cette étude du scénario complexe de la DC.

Conclusion et perspectives futures.

General introduction

Along its definition in the International Association for the Study of Pain (IASP) files (Merskey 1994) chronic pain (CP) represents the common perceptual motif accompanying many pathological conditions that exhibit excruciating sensory disorders yet in distinctive modal, magnitude, origin or temporal features (Weiner 2001). Because of its complexity, the entangled neural and extra neural substrates generating CP, from the molecular up to the perceptual stage, are, at best, poorly understood, notwithstanding recent important conceptual advancements (Tracey et al. 2007). Furthermore, while acute pains evoked by brief noxious inputs have been meticulously investigated by neuroscientists, and their sensory transmission mechanisms are generally well understood, CP, characterized by severe pain associated with little or no discernible injury or pathology, remains a mystery (Melzack 2001). The neural counterpart reflecting this complex perceptual state is complementarily composite and often not linearly related to the perceptual signs. For instance, experimental spontaneous pain or allodynia and hyperalgesia are seemingly mirrored, in the neuronal spinal cord, by spontaneous hyperactivity or hyper responsiveness to related stimuli (Hao, Kupers, and Xu 2004; Sotgiu, Biella, and Riva 1994; C. A. Porro et al. 1998). Concurrently, strong correlations between spatial patterns of altered brain activity and pain related behaviour in rat chronic pain model have also been shown (A. Zippo et al. 2011). Comparably, in humans, coherence of activation magnitude with the estimated intensity of pain has been reported in imaging and electrophysiological studies (Endo et al. 2008; Porro 2003; Green et al. 2009). **In contrast, many neuronal recordings and imaging data often showed mutually inconsistent mosaics of brain area activation and inactivation** (Bushnell et al. 1999; Iadarola et al. 1995). All these problems vividly inspire the appraisal of default activity and connectivity in chronic pain (Tracey 2005). Models of distributed pain representation in the brain, like the Neuromatrix Hypothesis (Melzack 1999), a more recent integration theory (Apkarian, Baliki, and Geha 2009), diversely interpret CP as the result of integrative regional activities active also in resting states involving the neuronal pathway established between thalamus and cortex (thalamo cortical circuit) as well as between the cortex and the limbic system. At the anatomical level, fMRI studies on the somatosensory cortex of CP patients revealed reduced grey matter density and macroscopic rearrangements of the cortical architecture (Apkarian et al. 2004). All these anatomical and functional disorders characterizing CP condition have been generally described as "maladaptive plasticity conditions" of specific brain sensory regions. **These yet well framed backgrounds, however, give no hints on the way the neuronal brain substrates behave in CP.** Because it is not the unit activity to be representative of the perceptual complexity of pain, it is however arguable that some feature, a kind of neural signature, either in the single neuron or in the network activities may embody markers of spontaneous CP.

In previous studies performed by the scientist of the CNR laboratory (A. Zippo et al. 2011; A. Zippo et al. 2016) using simultaneous massive electrophysiological recordings from the thalamus and the somatosensory cortex, it emerged that CP affected the neuronal connectivity within the somatosensory thalamo-cortical network reducing its capabilities of information processing along with a weakened information transfer and overall topological network degradation. As a whole, these conditions concur to generate recursive and stereotyped network configurations, which seemingly appear as anatomo-functional counterparts of the continuous percept of pain, a picture recoverable from all the examined CP models. With the aim of providing a renovation of the thalamo-cortical connectivity and reigniting integration/segregation alternation balance with no chemical intervention or electrical modulations an experiment has been carried out by CNR group at the ID17 beamline (ESRF, Grenoble). It consisted in the delivery of collimated **Microbeams** (in living anesthetized rats with and without CP models) in order to achieve an artificially modulated sensory cortex able to express different neurodynamic behaviours thus enriching the information content of the thalamo-cortical network. In detail, **the parallel microbeams** (seven X-ray microbeams 100 µm wide, spaced of 400 µm and depositing a peak dose of 360 Greys) created 8 putative modules in the CP rats which later on **showed that i) the functional connectivity was re-established comparably to control animals; ii) the behavioural parameters such as the time of response to peripheral nociceptive and non-nociceptive stimuli were restored** to the normal level (no functional/electrophysiological or behavioural changes were evident in control animals). The reduced dynamics of the cortex has been enriched by multiplying the independent somatosensory modules that increased the information transfer and the adaptability of the thalamo-cortical circuitry.

Aim of the Thesis work

Along the pathway opened by these previous studies, the aim of the present work is the deeper exploration of the **behaviour of the glial and vascular contexts that regulate the neuronal dynamics**. In particular, it deals with the study of the delicate anatomical and functional relation among the **tripartite synapse** and the **blood microvessels in normal and CP conditions**. The intermingled neural synapses and the surrounding glio-vascular architectures (Woolsey et al. 1996) represent a basic electrochemical and metabolic module, also called neuro-glial-vascular (NGV)-*unit*, at the cortical level in the brain. In fact, the synaptic electrical activity, recorded as Local Field Potentials (LFPs), depends from optimal glial-vascular compartment dynamics, where **glial cells are the bridging structures allowing for the transfer of metabolites and oxygen from microvessels to neurons**. Recent research made by the CNR group has further evidenced the dependency of Spikes from LFPs, a synaptic fingerprint in the neural activities thus potentially extending the spiking activity dependence on the microvessel dynamics (Storchi et al. 2012). The synaptic activities transmit the neuronal messages not only from one neuron to another, but also to the nearby astrocytes that in turn are faced over the microvessel membranes. Messages from neurons to vessels, regulating their diameters are mainly driven by astrocytes' intermediation. This complex thread of functional features is based on composite neural and glio-vascular architectures. Visible light imaging techniques have provided data supporting the tendency for neuronal nuclei to lie further away from vessels than it would be expected from a random spatial distribution. This indicates that within each cortical layer the density of neuronal somata and the distribution of microvessels have specific ratio, determining unique spatial architecture and indicating a mutual functional dependency between vessels and neurons.

By this work, I wish to investigate the micro/nano architectural disorders in cortical spaces potentially related to the heavy anatomical rearrangements involving the macroscopic architecture. The work has been carried out along two parallel analyses:

- **Microstructural analysis**: through X-ray micro-nanoCT Imaging experiments performed into two different Synchrotron facilities (the ESRF, Grenoble, and the SLS, Villigen) to evaluate the micro-architectural anomalies potentially nested in the cortical microscopic texture hosting the neuron-glia-vessel matrices. A morphological analysis focused on the characterization of vascular network allowed for the identification of vascular changes in CP conditions.
- **Neurodynamic analysis**: through *in vivo* chronic electrophysiological recordings performed at the CNR laboratories (Milan, Italy) to predict the origin and time changes in brain functional connectivity and in information transmission. Preliminary recording sessions intended to evaluate the activity of blood microvessels and capillaries strictly intertwined with the dynamics of the neuronal networks have been carried out by Near Infrared Spectroscopy probe (NIRS) (Giardini et al. 2016).

Due to the microstructural dependency between vessels and neurons, the reorganization of the neural substrate should involve deep microvascular rearrangements with potential backward effects. A submicroscopic appraisal of this remodeling should throw a light on a potential new approach on CP core anomalies and on potential new therapeutic approaches.

Experimental techniques

The previously mentioned morpho-functional analysis of CP induced changes has been carried out by using three different experimental methods and techniques:

- **Synchrotron X-ray Micro and Nano Computed Tomography (CT) Imaging** as tool for 3D analysing, in a non-destructive way, the inner microstructure of somatosensory cortical samples of both normal and CP rats. In particular, the Phase Contrast Imaging technique (Snigirev et al. 1995; Cloetens et al. 1996), has been adopted, since it is largely recognized as one of the best imaging tool for imaging biological samples with small variations of mass density and absorption coefficient at very high resolution.

- **Immunofluorescence and immunohistochemistry** as complementary analyses for validating the results obtained through X-ray microCT Imaging related to the morphological changes in cortical microvasculature.
- ***In vivo* chronic electrophysiological recordings** with implantable wireless multi-electrode array technology, to evaluate the origin and the evolution of CP. Thanks to chronic implantable microelectrodes array it has been possible to simultaneously record the neuronal ensemble activities from multiple brain regions (TC circuit) in time on the same implanted animal.

Structure of the thesis

The present thesis is structured in four main chapters here briefly presented.

Chapter 1. A biological introduction to the anatomy of the CNS and its main components is provided with major attention on the tripartite synapse and the blood microvessels anatomy and mutual functional role. The somatosensory system is then described: the anatomical and functional organization of the somatosensory thalamus and cortex and their communication pathway are presented to well understand the physiology of pain perception, later introduced. The end of the chapter is dedicated to the complex analysis of CP disease: the present understandings and the limits of the current research stimulated a novel approach for the study of CP adopted in this work.

Chapter 2. The huge experimental activity has been analytically reported in this chapter entirely dedicated to the description of all the materials and methods involved in the CP morpho-functional study: Synchrotron X-ray Computed Tomography for micro- and nano-imaging of rat somatosensory cortical samples, immunofluorescence microscopy and *in vivo* chronic electrophysiological recordings. For each technique the main principles, the instrumentation and the experimental procedures developed have been accurately reported. At the end, a brief insight on NIRS technique for the evaluation of haemodynamic changes in rat cortical microvascular activity is provided.

Chapter 3. All the large amount of data collected from the three main experimental sessions are reported in this chapter. Results from the comparative study “Neuropathic vs Control” rats focused on morphological changes of cortical microvascular network are extensively illustrated. Then, the immunofluorescence microscopy aiming at confirming previous findings in rat microvasculature are shown. Finally, the results coming from chronic electrophysiological recordings are presented by means of Graph Theory.

Chapter 4. This last part is dedicated to the general discussion risen from the important findings emerged through this study in the complex scenario of CP disease.

Conclusions and future perspectives.

References

Apkarian A.V., Baliki M.N. and Geha P.Y. 2009. "Towards a Theory of Chronic Pain." *Progress in Neurobiology* 87 (2): 81–97. doi:10.1016/j.pneurobio.2008.09.018.

Apkarian A.V., Sosa Y., Sonty S., Levy R.M., Harden R.N., Parrish T.B. and Gitelman D.R.. 2004. "Chronic Back Pain Is Associated with Decreased Prefrontal and Thalamic Gray Matter Density." *The Journal of Neuroscience*. doi:10.1523/JNEUROSCI.2541-04.2004.

Bushnell M.C., Duncan G.H., Hofbauer R.K., Ha B., Chen J.I. and Carrier B.. 1999. "Pain Perception: Is There a Role for Primary Somatosensory Cortex?" *Proceedings of the National Academy of Science*. doi: 10.1073/pnas.96.14.7705

Cloetens P., Barrett R., Baruchel J., Guigay J. and Schlenker M. 1996. "Phase Objects in Synchrotron Radiation Hard X-Ray Imaging." *Journal of Physics. D: Applied. Physics.* doi.org/10.1088/0022-3727/29/1/023

Endo T., Spenger C., Hao J., Tominaga T., Wiesenfeld-Hallin Z., Olson L. and Xu X. 2008. "Functional MRI of the Brain Detects Neuropathic Pain in Experimental Spinal Cord Injury." *Pain*. doi:10.1016/j.pain.2007.12.017.

Giardini M.E., Zippo A.G., Valente M., Krstajic N. and Biella G.E.M. 2016. "Electrophysiological and Anatomical Correlates of Spinal Cord Optical Coherence Tomography." *PLoS ONE* 11 (4). doi:10.1371/journal.pone.0152539.

Green A. L., Wang S., Stein J.F., Pereira E., Kringelbach M.L., Liu X., Brittain J.S. and Aziz T.Z. 2009. "Neural Signatures in Patients with Neuropathic Pain." *Neurology*. doi:10.1212/01.wnl.0000342122.25498.8b.

Hao J. X., Kupers R.C. and Xu X. 2004. "Response Characteristics of Spinal Cord Dorsal Horn Neurons in Chronic Allodynic Rats after Spinal Cord Injury." *Journal of Neurophysiology*. doi:10.1152/jn.00121.2004.

Iadarola M., Max M., Berman K., Byas-Smith M., Coghill R., Gracely R. and Bennett G. 1995. "Unilateral Decrease in Thalamic Activity Observed with Positron Emission Tomography in Patients with Chronic Neuropathic Pain." *Pain*. doi:10.1016/0304-3959(95)00015-K.

Melzack R. 2001. "Pain and the Neuromatrix in the Brain." *Journal of Dental Education* 65 (12): 1378–82.

Melzack R.. 1999. "From the Gate to the Neuromatrix." *Pain*. doi:10.1016/S0304-3959(99)00145-1.

Merskey H. 1986. "Classification of Chronic Pain. Descriptions of Chronic Pain Syndromes as Definitions of Pain." *Pain, Suppl 3, 226.*

Porro C., Cettolo V., Francescato M. and Baraldi P. 1998. "Temporal and Intensity Coding of Pain in Human Cortex." *Journal of Neurophysiology*. doi:101152/jn1998.80.6.3312.

Porro C. 2003. "Functional Imaging and Pain: Behavior, Perception, and Modulation." *The Neuroscientist : A Review Journal Bringing Neurobiology, Neurology and Psychiatry*. doi:10.1177/1073858403253660.

Snigirev A., Snigireva I., Kohn V., Kuznetsov S. and Schelokov I. 1995. "On the Possibilities of X-Ray Phase Contrast Microimaging by Coherent High-Energy Synchrotron Radiation." *Review of Scientific Instruments*. doi:10.1063/1.1146073.

Sotgiu M.L., Biella G.E.M. and Riva L. 1994. "A Study of Early Ongoing Activity in Dorsal Horn Units Following Sciatic Nerve Constriction." *Neuroreport*.

Storchi R., Zippo A.G., Caramenti G.C., Valente M. and Biella G.E.M. 2012. "Predicting Spike Occurrence and Neuronal Responsiveness from LFPs in Primary Somatosensory Cortex." *PLoS ONE* 7 (5). doi:10.1371/journal.pone.0035850.

Tracey I. 2005. "Functional connectivity and Pain: Howeffectivelyconnected Is Your Brain?." *PAIN* 116 (3). http://journals.lww.com/pain/Fulltext/2005/08000/Functionalconnectivity_and_pain_.1.aspx.

Tracey I. and Mantyh P. 2007. "The Cerebral Signature for Pain Perception and Its Modulation." *Neuron*. doi:10.1016/j.neuron.2007.07.012.

Weiner R.S. 2001. "*Pain Management: A Practical Guide for Clinicians, Sixth Edition*." *American Academy of Pain Management, CRC Press.*

Woolsey T., Rovainen C., Cox S., Henegar M., Liang G., Liu D., Moskalenko Y., Sui J. and Wei L. 1996. "Neuronal Units Linked to Microvascular Modules in Cerebral Cortex: Response Elements for Imaging the Brain." *Cerebral Cortex* 6 (5): 647–60. http://dx.doi.org/10.1093/cercor/6.5.647.

Zippo A.G., Storchi R., Valente M., Caramenti G.C. and Biella G.E.M. 2011. "Neural Substrates of Chronic Pain in the Thalamocortical Circuit." *Nature Precedings*. http://precedings.nature.com/documents/6548/version/1.

Zippo A.G., Valente M., Caramenti G.C. and Biella G.E.M. 2016. “The Thalamo-Cortical Complex Network Correlates of Chronic Pain.” *Scientific Reports (6)*. 34763. http://dx.doi.org/10.1038/srep34763.

Chapter 1: Biological Background

Summary

The first part of the chapter is dedicated to the description of the Central Nervous System (CNS) anatomy and its main components with major attention on the tripartite synapse and the blood microvessel compartments and their mutual functional role. The somatosensory system is then introduced: the anatomical and functional organization of the somatosensory thalamus and cortex and their communication pathway are presented to well understand the physiology of pain perception, later described. At the end of the chapter, the Chronic Pain (CP) disease is depicted: the present understandings and the limits of the current research stimulated a novel approach for the study of CP adopted in this work.

Résumé

La première partie du chapitre est dédiée à la description de l'anatomie du système nerveux central (SNC) et de ses composantes principales avec une attention particulière portée aux compartiments de la tripartite synapse et des microvaisseaux sanguins et leur rôle fonctionnel mutuel. Le système somatosensoriel est ensuite exposé: l'organisation anatomique et fonctionnelle du thalamus et du cortex somatosensoriels et leur voie de communication sont présentées pour bien comprendre la physiologie de la perception de la douleur, décrite plus tard. À la fin du chapitre, la maladie de la douleur chronique (DC) est présentée: les compréhensions et les limites de la recherche actuelles ont stimulé une approche novatrice pour l'étude de la DC adoptée dans ce travail.

Contents

1 Biological background

1.1 Elements of neuronal anatomy

The CNS consists of the brain and the spinal cord. Two are the major groups of cells in the nervous system: neurons and glia. These are broad categories, within which are many types of cells that differ in structure, chemistry, and function. Despite the number of studies relating the quantification of neuronal and glial cells in the brain, involving a large variety of techniques, their exact estimation is still an open issue in neuroscience. The debate, opened by Franz Nissl in 1898 (Nissl 1898) with its comparative studies on brain composition, was then carried out by Reinhard Friede, who established, in 1954, the number of glial cells per neuron as a parameter of investigation (Friede 1954). He called this parameter the glial index (the ratio between the number of glial cells, G, and the number of neurons, N, in the tissue), but it became most often referred to in the literature as the glia/neuron ratio, a term proposed by Bass in 1971 (Bass, Hess, Pope, & Thalheimer, 1971). Recent studies, carried out by Suzana Herculano-Houzel have found that the glia/neuron ratio varies with the brain size and therefore it varies across the different brain structures of mammalian species in a non-uniform way (Herculano-Houzel, 2011). In addition, they showed also how the glia/neuron ratio uniformly varies not with brain size, but with neuronal density. According to her quantitative analysis on the whole brain, a total average of 86.1 ±8.1 billion neurons and 84.6 ±8.1 billion non neuronal cells in the whole human brain has been found, yielding a maximal glia/neuron ratio of 0.99. What we can derive from such large amount of studies is that considering the glial relative number in relation to the number of neurons is becoming of functional importance, due to the growing recognition of their role of glial cells (Herculano-Houzel, 2014) (Paragraph 1.2).

A typical neuron consists of several parts: the soma, the axon, the synaptic terminals and the dendrites (Figure 1.1). The dendrites are tree-like structures that represent the main receptive area of the neuron. The soma is the central unit that contains the cellular nucleus and computes the signals transmitted by dendrites. The major diameter can be as large as 10 to 60 µm. The axon is constituted like a filament extending from the exit area of the soma, called hillock, and can be meters long. The axon may be completely nude or covered by one or more layers of myelin sheaths, composed by wrapped myelin cells around the axons. Myelinisation dramatically increases the signal conduction up to 120 m/s. The extension of the myelin sheath is not a continuative coverage at every definite distance it is interrupted (about 1 µm gaps), leaving the axonal surface in contact with the extracellular environment (node of Ranvier). These interruptions are strategic being signal amplifiers of electrical signals subject to natural fading along the myelinated axonal branch. The synapse is a highly complex structure where the signal transmission between neurons takes place. As a rule, a neuronal axon can establish a number of synapses with the receiving structures of another neuron.

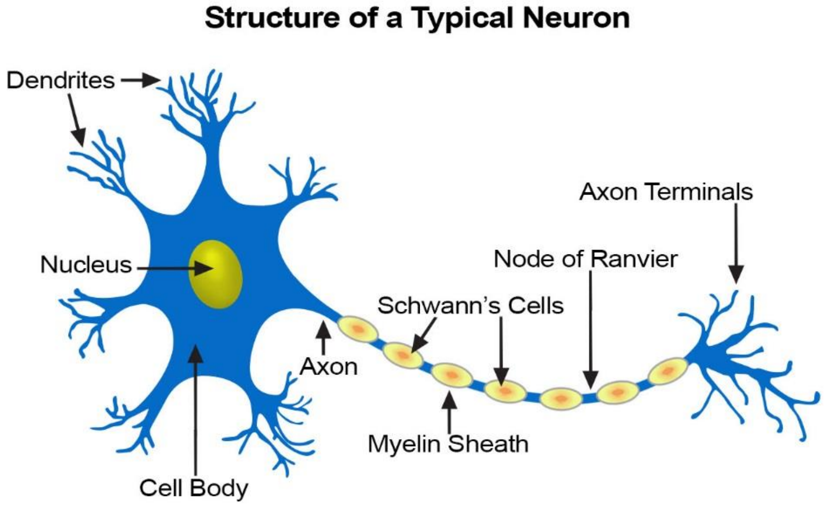

Figure 1.1. Schematic representation of a typical neuron, mainly consisting of three parts: a cell body (soma), one or more dendrites, and an axon. (Image taken from www.visionlearning.com)

Specifically, the transmission can be established by the branching axon terminals on the dendrites, on the soma or on the axon. The respective synapses are thus called axo-dendritic, axo-axonic and axo-somatic. The axon terminals that constitute synapses present bag-shaped enlargements that contain vesicular bodies filled of neurotransmitters. In these regions (called presynaptic terminals), the vesicle membranes coalesce, by a complex mechanism, with the axon terminal membrane, delivering the substance contained in vesicle. These substances, generally aminoacids, aminoacid-based compounds or peptides, are called neurotransmitters. On the postsynaptic membrane there is a lot of complex structures called receptors (Figure 1.2), mainly constituted by proteins, that can receive the molecules delivered by the presynaptic vesicles. The space between the presynaptic and postsynaptic membrane is called synaptic cleft (about 20 nm). The response of a transmitter by a receptor triggers several fast electrochemical changings that induce the generation of spike signals similar to the presynaptic spike. The ensemble of presynaptic membrane, synaptic cleft, postsynaptic membrane is called synapse. There exists a large variety of neurotransmitters (and of other substances called neuromodulators) as well as of postsynaptic receptors. This extraordinary multiplicity of transmitters, modulators, receptors allows incredibly flexible signal transmission (Bear, M; Connors, B; Paradiso, 2014).

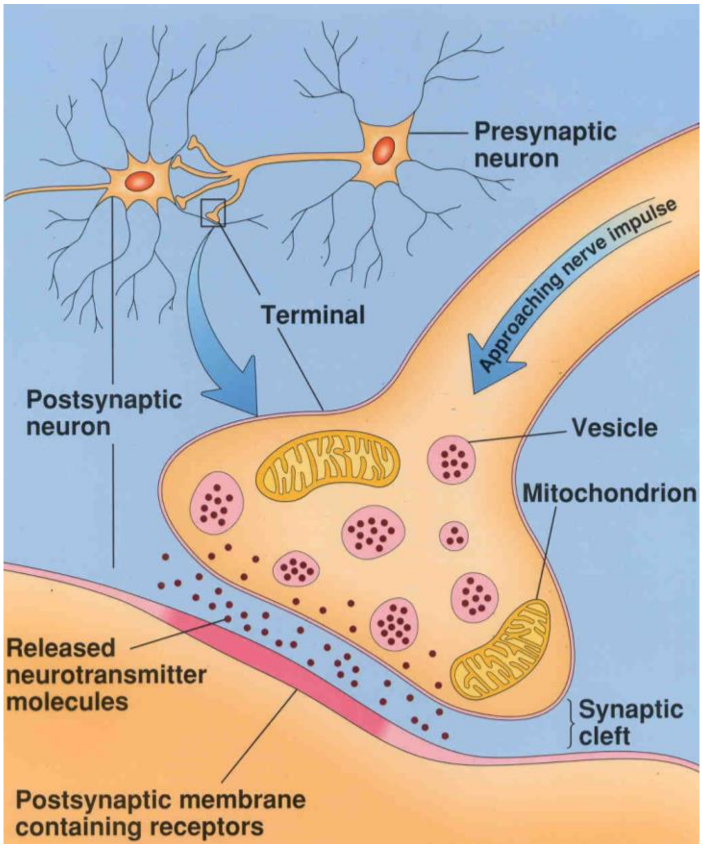

Figure 1.2. Representation of a synapse. The nerve impulse does not cross the tiny gap between cells (synaptic cleft) as an electrical event, but the communication is established chemically by the release of chemicals called neurotransmitters. (Image adopted from Wadsworth Inc., 1992).

1.2 Glial Cells

In the last years, several brain functional studies have underlined the importance of glial cells for brain proper development and function. In particular, they play an active role in blood flow regulation, they provide much-needed energy to neurons, and supply the building blocks of neurotransmitters, which fuel synapse function (Bolton & Eroglu, 2009; Eroglu, Barres, & Stevens, 2008). There are three types of glial cells in the mature central nervous system: astrocytes, oligodendrocytes, and microglial cells (Figure 1.3). The astrocytes elaborate local processes that give these cells a starlike appearance (hence the prefix “astro”). They fill most of the spaces between neurons. Their process extensions define domain extremities and they end up wrapping the central synapses producing a synaptic structure called “tripartite synapse” (Araque, Parpura, Sanzgiri, & Haydon, 1999; Oberheim, Wang, Goldman, & Nedergaard, 2006) (Paragraph 1.3). Astrocyte processes also envelop parenchymal brain arterioles and capillaries in unique spatial domains, extending terminal structures known as endfeet that are directly in contact with the vascular basal lamina (Oberheim et al., 2006; Simard, Arcuino, Takano, Liu, & Nedergaard, 2003). For this unique bidirectional position, they play an essential role in regulating the chemical content of the extracellular space and maintaining an appropriate chemical environment for neuronal signalling. In addition, they participate actively to blood flow regulation since their endfeet express surface proteins, such as glucose transporters, for uptake of energy substrates from the endothelium (Kacem, Lacombe, Seylaz, & Bonvento, 1998) and are capable of releasing transmitters that influence local blood flow (Metea & Newman, 2006; Mulligan & MacVicar, 2004; Simard et al., 2003; Zonta et al., 2003).

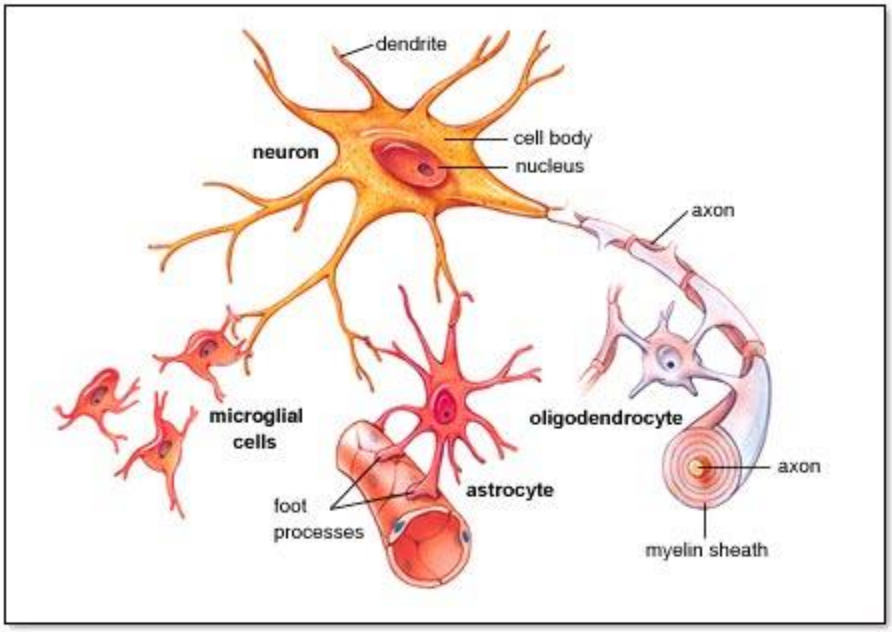

Figure 1.3. A representation of the three types of glial cells: astrocytes, oligodendrocytes and microglial cells (Image taken from rsdadvisory.com).

1.3 The tripartite synapse

Tripartite synapse refers to the functional integration and physical proximity of the presynaptic membrane, postsynaptic membrane, and their intimate association with surrounding glia as well as the combined contributions of these three synaptic components to the production of activity at the chemical synapse (Araque et al., 1999) (Figure 1.4). The term was first introduced in the late 1990s to account for a growing body of evidence that glia are not merely passive neuronal support cells but, instead, play an active role in the integration of synaptic information through bidirectional communication with the neuronal components of the synapse as mediated by neurotransmitters and gliotransmitters (Gertrudis Perea et al., 2009).

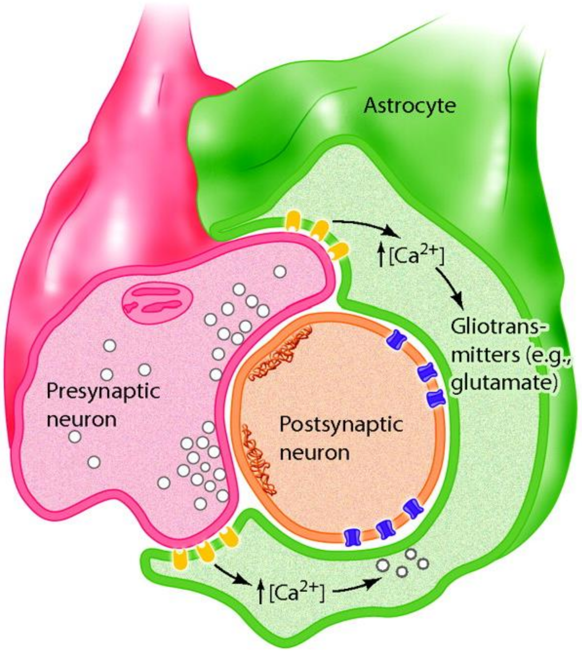

Figure 1.4. Illustration of the tripartite synapse: not only the presynaptic and postsynaptic neurons contribute to the activity of the synapse, but also the glial component is present. (Image adopted from Fellin and Haydon 2005).

The role of astrocytes in the integration and processing of synaptic integration can be evidenced if we think about their functional and structural properties. First of all, they are excitable cells: they can produce transient changes in their intracellular calcium concentrations through the release of calcium stores from the endoplasmic reticulum (Gertrudis Perea & Araque, 2005). Then, they can communicate bidirectionally with neurons. In fact, through changes in their calcium concentration excitability, they are able to detect neurotransmitters and other signals released from neurons at the synapse (Gertrudis Perea 2005) and can release their own neurotransmitters or gliotransmitters (Volterra) that are, in turn, capable of modifying the electrophysiological excitability of neurons (Newman, 2003). In the end, they integrate and modulate information from their synaptic inputs by varying their final calcium concentration, as a response to different types of neurotransmitter stimulations.

1.4 Neurovascular coupling

The human brain comprises only 2% of the body's mass, but it consumes 20% of the energy that is produced when the body is in a resting state. This high consumption of energy is crucial for the normal functioning of the brain (Attwell et al., 2010). Recent studies have demonstrated that most of this energy is used on synapses (Harris & Attwell, 2012). The term neurovascular coupling (NVC) has been adopted to express the temporal and spatial coupling between increased neuronal activity and cerebral blood flow (CBF). It is a highly regulated phenomenon that ensures adequate supply of oxygen and glucose to the neurons at work during a given task. The magnitude and spatial location of blood flow changes are tightly linked to changes in neural activity through a complex sequence of coordinated events involving neurons, glia, and vascular cells. Synaptic activity and activation of neurons increase energy consumption by local neurons and astrocytes. This additional energy demand is mainly driven by activities of ion pumping (Attwell & Laughlin, 2001) and by various associated metabolic processes (Iadecola & Nedergaard, 2007). This energy is produced locally from glucose and oxygen supplied by blood through local small vessels. In response to transient neural activity nearby vessels dilate, substantially increasing CBF. The exact physiological function served by this large increase of flow remains still unclear.

In recent years, it has been suggested that glial cells contribute to neurovascular coupling in the brain (Filosa, 2004; Harder, Alkayed, Lange, Gebremedhin, & Roman, 1998; Koehler, 2006; Mulligan & MacVicar, 2004; Paulson & Newman, 1987; Zonta et al., 2003). Glial cells are well suited to mediate this response because of their close contacts with both neurons and blood vessels (Anderson & Nedergaard, 2003; Harder et al., 1998). In addition, glia generate increases in intracellular Ca^{2+} in response to neuronal activity (Newman, 2005; Schipke & Kettenmann, 2004) and can produce vasoactive agents after such calcium increases.

Many vascular-based functional brain imaging techniques, such as fMRI, rely on this coupling to infer changes in neural activity. Measured in functional magnetic resonance imaging (fMRI), the blood oxygenation level-dependent (BOLD) contrast has become widely used to map brain activation in animals and humans in response to multiple types of neural stimulations (Ogawa, Shulman, Glynn, Yamane, & Navon, 1978). At the voxel level, the BOLD signal is related to changes of blood volume and deoxyhemoglobin concentration at a typical spatial resolution of 1 or 2 mm and temporal resolution of about 1 s (Buxton, 2013). Optical techniques, such as near-infrared spectroscopy (NIRS), can also measure blood oxygenation variations associated with transient neural activity. Conversely to fMRI, optical techniques have worse spatial resolution and are unable to explore deep brain structures but have a high temporal resolution that can reach 1 ms (Strangman, Boas, & Sutton, 2002). In the materials and methods section (Paragraph 2.4.6) the NIRS principle to measure hemodynamic changes during somatosensory cortical activation will be described.

1.5 Introduction to the somatosensory system

After the brief introduction dedicated on the principal anatomical elements of brain anatomy, an overview on the structural and functional properties of the somatosensory system is here provided. In fact, the sensory information processed by the somatosensory systems travels along different anatomical pathways depending on the information carried. In the next paragraphs the anatomy of the somatosensory system will be explored, describing all the anatomical features of its components. Then, the principal anatomo-functional pathways involved in pain sensation will be presented, in order to fully understand the origin and modulation of pain sensation.

1.5.1 The somatosensory system

The somatosensory system processes the sensory inputs to the body and namely it displays estimating properties for proprioception, touch, temperature, nociception and so on. The somatosensory system is constituted by receptors placed in the periphery of the body (the cutaneous district, tendons and muscles, viscera, the special senses), the peripheral sensory neurons and by the central neurons delivering the signals up to the thalamus and to cortices. The sensory information is, by these means, conveyed to the cortex. In the CNS, two brain regions play a crucial role in the sensory information processing: the primary somatosensory cortex located in the postcentral gyrus of the parietal lobe (SS1), and the ventrobasal nuclear complex (VB) of the thalamus. The cerebral cortex (the outermost part of the brain and the largest part by volume) contains an estimated 15-33 billion neurons, each of which is connected to thousands of other neurons. In total, around 100 billion neurons and 1,000 billion glial cells make up the human brain.

1.5.2 The Somato-Sensory Thalamus

The thalami are two paired symmetrical organs and represent the major part of diencephalon. They are made up of grey matter that is partitioned by a “Y” shaped white matter structure known as the internal medullary lamina. As a result of the location of the internal medullary lamina, each thalamus is divided into roughly three main parts: the anterior, medial and lateral thalamus. The anterior part lies between the short limbs of the internal medullary lamina, while the medial and lateral parts lie on the respective side of the main stem of the “Y”. The left thalamus communicates with the right thalamus by way of the interthalamic adhesion. Each of the two thalami is divided in many subsets, histologically distinguishable, called nuclei (Figure 1.5). The nuclear nomenclature respects, in general, the internal thalamus topography: there are the anterior, medial, intralaminar, posterior nuclei, etc. The major role of thalamus is to gate and otherwise modulate the flow of information to cortex. In particular, important nuclei of VB complex are responsible for the processing of the somatosensory information: the Ventral posterolateral (VPL) nucleus and the Ventral lateral (VL) nucleus and the Ventral posteromedial (VPM). They are called *relay nuclei* since they receive very well defined inputs and project this signal to functionally distinct areas of the cerebral cortex. In particular, the VL nucleus receives inputs from the basal ganglia and the cerebellum and send output to the primary motor cortex and the premotor cortex. It forms the motor functional division in the thalamic nuclei devoted to the regulation and coordination of the movement. The VPL nucleus receives information from the neospinothalamic tract and the medial lemniscus of the posterior column-medial lemniscus pathway. It then projects this sensory information to Brodmann's Areas 3, 1 and 2 in the postcentral gyrus that make up the primary somatosensory cortex of the brain. In the end, the VPM receives inputs from face and oral cavity conveyed through the anterior (ventral) trigeminothalamic tract and the posterior (dorsal) trigeminothalamic tract. It finally projects these signals to the post central gyrus. The VPM also receives taste afferent information from the solitary tract and projects to the cortical gustatory area.

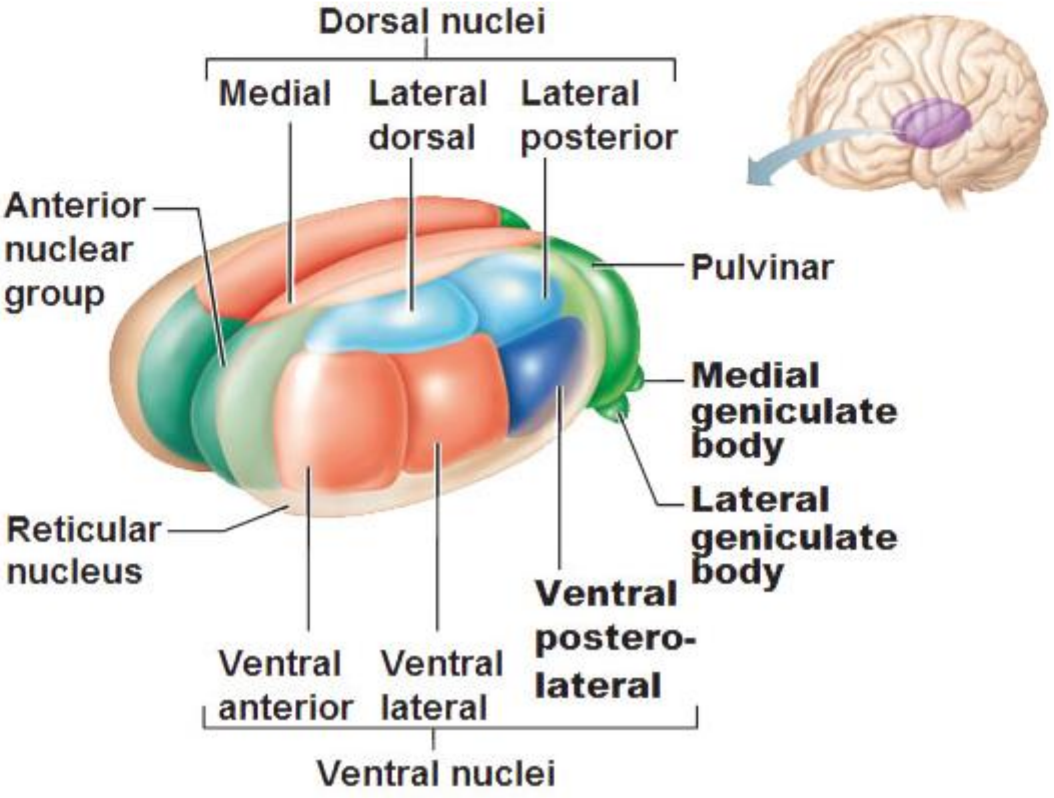

Figure 1.5. Main thalamic nuclei in human brain. (Image taken from corpshumain.ca)

All the nuclei of the somatosensory thalamus and many nuclei of intralaminar and medial thalamus are populated by neurons connected to the cortex: the thalamocortical (TC) neurons (else thalamic relay neurons) and local inhibitory neurons. These last are present only in the superior mammals. Another crucial nuclear complex involved in the function of thalamocortical loop is the reticularthalamic (RT) nucleus. While the relay thalamic neurons are excitatory neurons (on the reticular thalamic neurons and on the cortical neurons), the reticular thalamic neurons display strong inhibitions onto the thalamic relay neurons.

1.5.2.1 Other somatosensory thalamic nuclei

Elegant studies have shown that in rodents, the somatosensory information processing involves not only the VPL and VPM thalamic nuclei, but also the PoM (postero medial complex) nucleus (Diamond, Armstrong-James, & Ebner, 1992; Petersen, 2007). This nucleus is highly developed in rodents and it seems to receive projections from the whisker barrel cortex, that is involved with fine discrimination or tactile light processes (Figure 1.6). In particular, it has been found that layer VI of rat somatosensory cortex sends inputs not only to the VPM, like in humans, but its lower portion sends inputs also to the PoM. Furthermore, corticothalamic axons originating in layer V project exclusively to PoM. The existence of these two distinct thalamo-cortical pathways has been supported by the differential functional and structural properties characterizing their cells: different spatial distribution, intrinsic membrane properties and excitability, nature of their response (excitatory, inhibitory or dual) to corticothalamic stimulation.

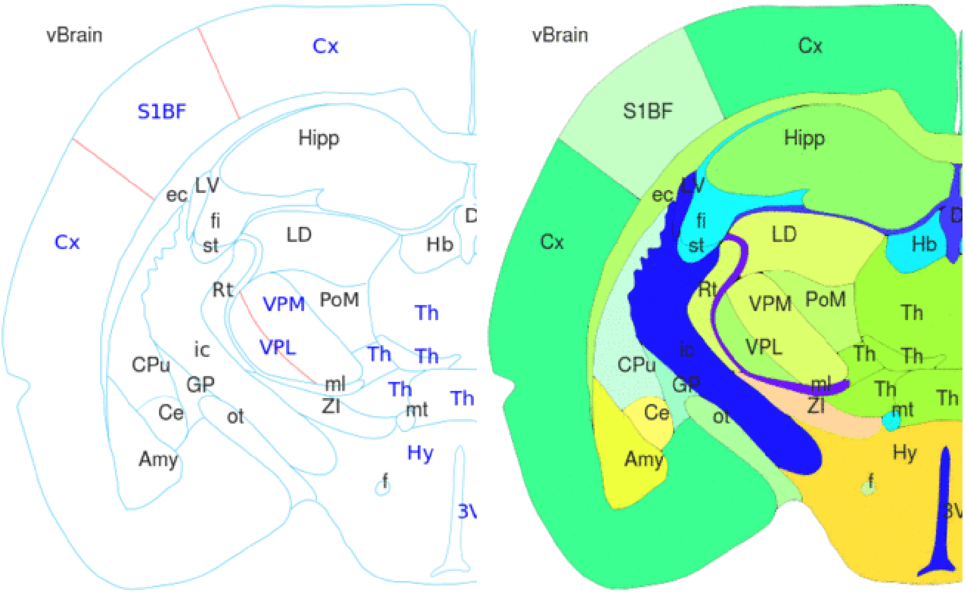

Figure 1.6. Coronal section of rat brain showing other thalamic substructures. Amy: amygdala; Ce: central amygdaloid nucleus; CPu: caudate putamen; Cx: cerebral cortex; ec: external capsule; f: fornix; fi: fimbria of the hippocampus; GP: globus pallidus; Hb: habenula; Hipp: hippocampal formation; ic: internal capsule; LD: laterodorsal thalamic nucleus; LV: lateral ventricle; ml: medial lemniscus; mt: mammillothalamic tract; ot: optical tract; PoM: posteromedial thalamic nucleus; Rt: reticular thalamic nucleus; S1BF: primary somatosensory cortex, barrel field; st: stria terminalis; ZI: zona incerta. (Image taken from www.3dbar.com)

It has been proposed that the layer VI inputs play a more modulatory role, whereas the layer V inputs serve as the primary “driver” of PoM cells characteristics (Feig & Harting, 1998; Reichova, 2004; Sherman &

Guillery, 2006). In humans, nociceptive neurons have been recorded in VP, VPM nuclei (Ohara, Lenz, & Norgren, 2003).

These two nuclei appear less important in clinical studies and may be equalized to fine discrimination thalamic nuclei in humans such as VPL and VPM. PoM has not clear role in CP and that cells studied in monkey PoM nucleus could have some role in acute nociceptive responses (Friedman, Murray, O’Neill, & Mishkin, 1986). The PoM nucleus projects to the retro- insular cortex in monkeys (Burton & Jones, 1976). In this view the PoM nucleus can have some role in CP that is still to be elucidated.

1.5.3 The Somato-Sensory Cortex

In humans, the Somatosensory (SS1) cortex is a prominent structure of the neocortex located in the postcentral gyrus of the parietal lobe, corresponding to Brodmann's areas 3a, 3b, 1 and 2 (Figure 1.7). The cerebral cortex is the most superficial layer of the brain and makes up the largest portion of the brain’s gray matter.

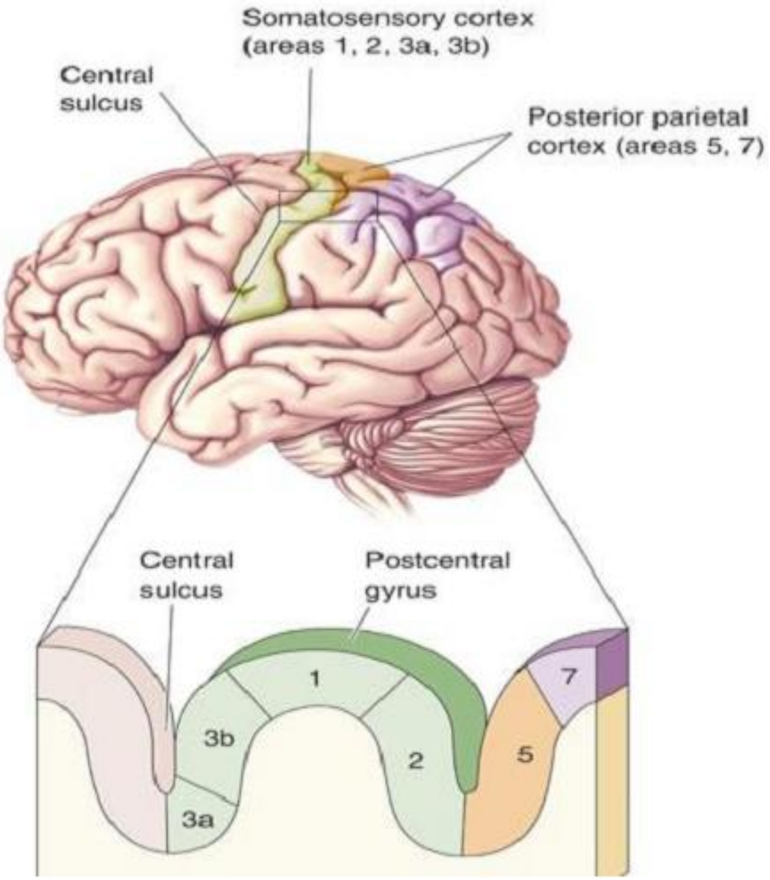

Figure 1.7. Cortical areas of human brain and location of somatosensory cortex (Image taken from Bear et al., 2006)

In the experimental animals, such as rats, the cortex is not folded but smooth. Mammals with an unfolded cortex are denominated as lissencephalic whereas those with cortical folds are described as gyrencephaic. Gyrencephaly represents a geometric escamotage to increase the brain surface within the skull fixed space and the consequent functional dynamic properties. Despite these differences, many functional aspects of cortical dynamics can be studied in lissencephalic animals extending the observed features to gyrencephalic ones. The rat SS1 is found on the dorsolateral aspect of the cerebral cortex stereotactically recoverable at points -1.2 mm antero-posterior, 2.6 mm medial-lateral from Bregma (a repere point for all the neurosurgical interventions where the medial sagittal and the coronal sutures of the skull meet). Different authors subdivide the primary somatosensory area of rodents into six subareas that include: the whisker, the nose, the mouth, the upper limb, the trunk and the lower limb sensory areas. The cerebral cortex meanly presents a layered structure with six different layers, numbered from the pia surface to deep (Figure 1.8).

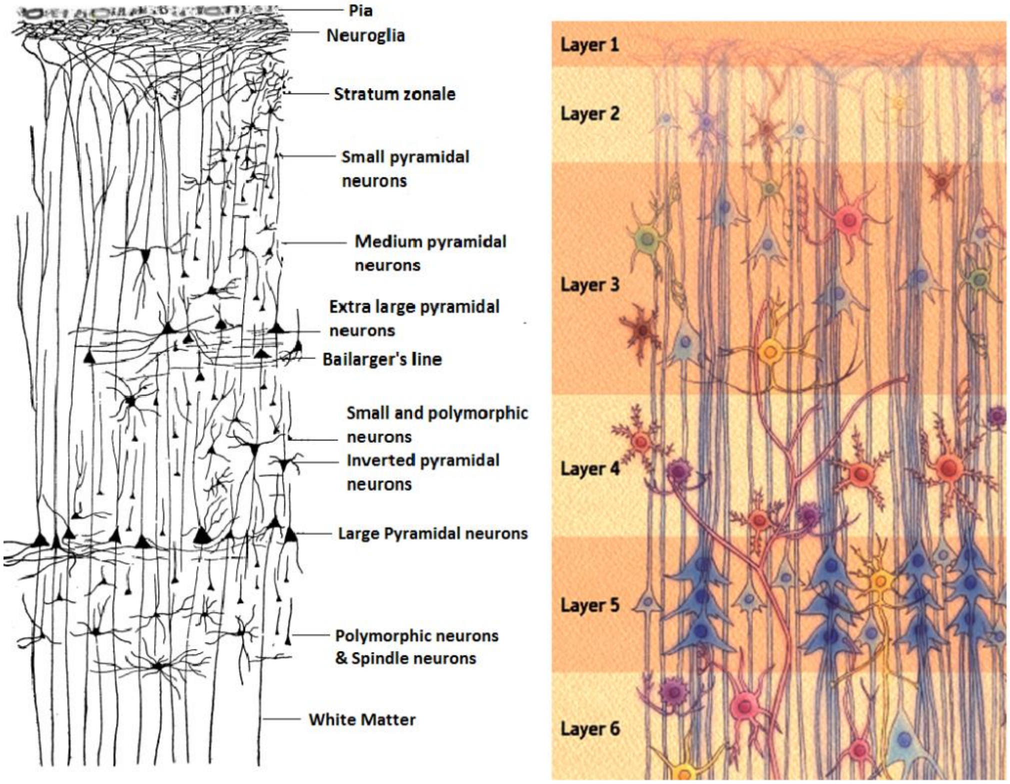

Figure 1.8. Histological structure of cerebral cortex: six layers can be distinguished on the basis of morphology and structure. (Image taken from quora.com)

Layer I is the molecular layer, which contains very few neurons; layer II the external granular layer; layer III the external pyramidal layer; layer IV the internal granular layer; layer V the internal pyramidal layer;

layer VI the multiform, or fusiform layer. Each cortical layer contains different neuronal shapes, sizes and density as well as different organizations of nerve fibres.

Each of the six layers endorses different functions and three main groups can be distinguished from functional point of view. The *supragranular* layers consist of layers I to III. They are the primary origin and termination of intracortical connections, which are either associational (i.e., with other areas of the same hemisphere), or commissural (i.e., connections to the opposite hemisphere, primarily through the corpus callosum). The supragranular portion of the cortex is highly developed in humans and permits communication between one portion of the cortex and other regions. The *internal granular layer*, layer IV, receives thalamocortical connections, especially from the specific thalamic nuclei. This is most prominent in the primary sensory cortices. The *infragranular* layers, layers V and VI, primarily connect the cerebral cortex with subcortical regions. These layers are most developed in motor cortical areas. The motor areas have extremely small or non-existent granular layers and are often called *"agranular cortex"*. Layer V gives rise to all of the principal cortical efferent projections to basal ganglia, brain stem and spinal cord. Layer VI, the multiform or fusiform layer, projects primarily to the thalamus.

A somatotopic functional map of the SS1 has been reconstructed though intensive electrophysiological studies both on human (Penfield & Boldrey, 1937) and monkey brain (Woolsey, Erickson, & Gilson, 1979). It has known as cortical “*homunculus”*, meaning “little man” from the Latin, and it visually portrays the anatomical divisions of the primary motor cortex and the primary somatosensory cortex (Figure 1.9). It represents how our body is perceived within the brain and how the neurons are distributed in these areas in order to create this perception. The size of a body area is not proportional to its representation in the cortical homunculus, but it results proportional to the innervation density in the body. Certain areas such as the hands, lips and face occupy disproportionately large areas of the cortex, due to the importance of fine motor skills and the extensive innervation of these areas.

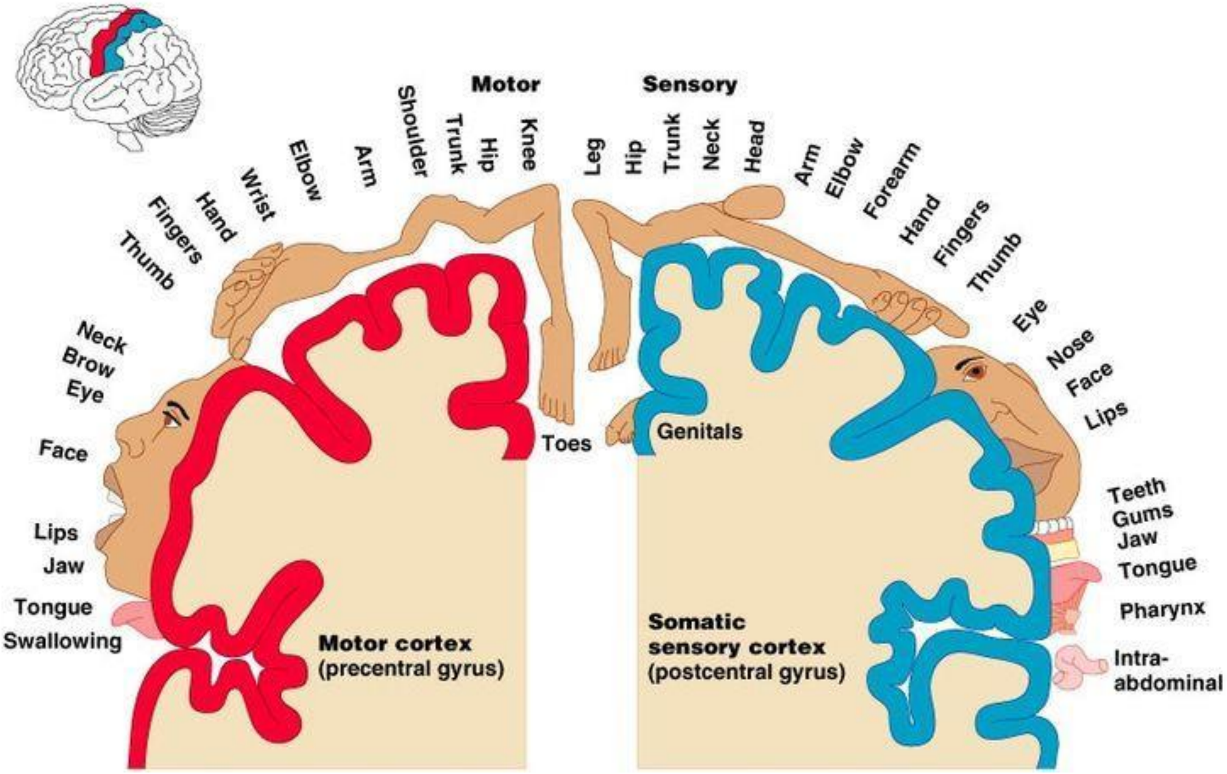

Figure 1.9. Representation of the cortical "homunculus" for motor and sensory areas. The amount of cortex devoted to any given body region is proportional to how richly that region is innervated. A large part of the cortex is devoted to represent face and hands. (Image taken from Pearson Education Inc., 2004)

As in humans, also in rats, SS1 houses the entire representation of the body, the "rattunculus" (in analogy to the "homunculus"), that is, the representation of the body areas within the SS1 proportionally to the innervation density in the body. In the rat brain, for example, an inordinate amount of the somatic sensory cortex is devoted to represent the large facial whiskers that provide a key component of the somatic sensory input for rats and mice.

1.5.4 Cortical modularity

Observations over the last 40 years have revealed that there is an iterated substructure within the somatic sensory (and many other) cortical maps. This substructure takes the form of units called *modules*, each involving hundreds or thousands of nerve cells in repeating patterns vertically distributed. These vertically units have been first noticed in the 1920s by the Spanish neuroanatomist Rafael Lorente de Nó, on his studies in the rat and later confirmed by Mountcastle's studies on cat primary somatosensory cortex (Mountcastle, 1956). He firstly hypothesized the existence of an 'elementary unit of organization in the somatic cortex made up of a vertical group of cells extending through all the cellular layers', termed 'column'. Then, by deeper investigations he discovered that each individual column, about 500 µm wide, are constituted by narrow chain of neurons extending vertically across the cellular layers II-VI, perpendicular to the pial surface. They were termed ‘mini-columns’ and they are considered the basic modular unit of cortex. They contain some 80–100 neurons and span 40–50 μm in transverse diameter (Figure 1.10). Neurons in minicolumns share some functional properties, such as somatotopy, the representation within the cortex of each body part, and modality, the specific responsiveness to definite or adequate stimuli. Cortical columns are also distinguished from each other by their patterns of circuitry. The majority of intracortical circuits are local, connecting neurons within the same columns, with only a minority of connections being between columns. Even if the identification of the column has shed a light on the organization of cortical neurons and their functional connectivity, the meaning of these iterated patterns for brain function remain largely unknown.

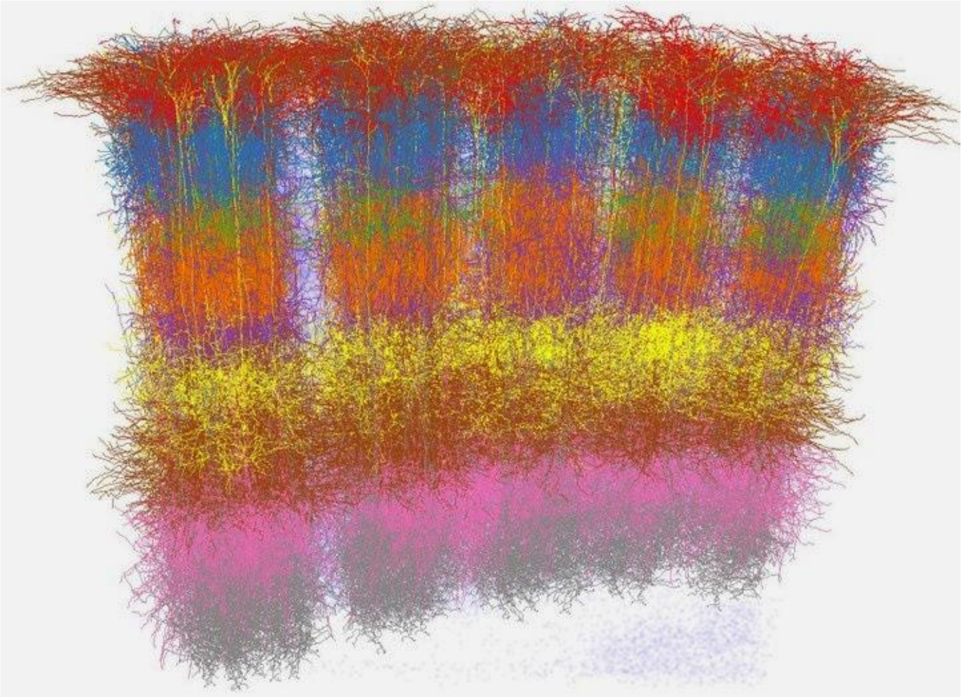

Figure 1.10. Illustration of columnar organisation of cortex: cell-type-specific 3D reconstruction of five neighbouring barrel columns in rat vibrissal cortex. (Image taken from Meyer et al. 2013).

1.5.5 Cortical neurons

Cortical neurons represent a heterogeneous population most variegated for structural and functional features. Due to the peculiar overall scheme impinging on the thalamocortical circuit and the importance of this network on CP, I will focus predominantly on those cells directly involved in this loop. Specifically, the fourth layer neurons, called granule cells for their granular-like appearing in histological observations and the fifth and sixth layers neurons, housing the so called pyramidal cells. They are characterized by a large soma of diameter of 20 to 50 μm and their apical dendrite extends all the way to layer I of the cortex and several basal dendrites projecting laterally. A long axon that arises from the base of the pyramidal cell leaves the cortex, making connections with other brain regions, particularly with the Thalamus, by extending through the white matter deep to the cortex. Granule cells, in contrast, are typically small multipolar neurons, with a soma diameter of 10 μm. They have been found in a wide assortment of shapes, with a short axon that does not leave the neocortex, anyway it is involved in short connections within the cortex itself.

1.5.6 The Thalamo-Cortical circuit

As previously mentioned (Paragraph 1.5.2), TC neurons are the principal responsible for the connection between cortex and thalamus. Taking into consideration these connections and the diverse neurons in both structures, it is possible to divide the thalamo-cortico-thalamic (TCT) loop dynamics in three main mechanisms (Figure 1.11):

1. The first system represents the feedback mentioned so far: the thalamo-cortical (TC) cells that receive input from sensory spinal cord pathways transmit the signals onto both the granular cortical layer and the reticular thalamus. The former produces an excitatory effect on granular layer. Simultaneously it can be observed an excitement of RT neurons that rapidly induce a negative feedback, i.e. an inhibition on the TC cells themselves.

2. In the meantime, the granular layer neurons induce an excitement of pyramidal neurons of below layers. These pyramidal neurons excite both the TC neurons of point 1 and the RT neurons. This system represents the second excitatory loop of the whole TCT.

3. Because from the fifth pyramidal layer there is another excitatory pathway toward the RT neurons, these last are reactivated and produce a second inhibitory input on the TC cells. This last system is both excitatory and inhibitory.

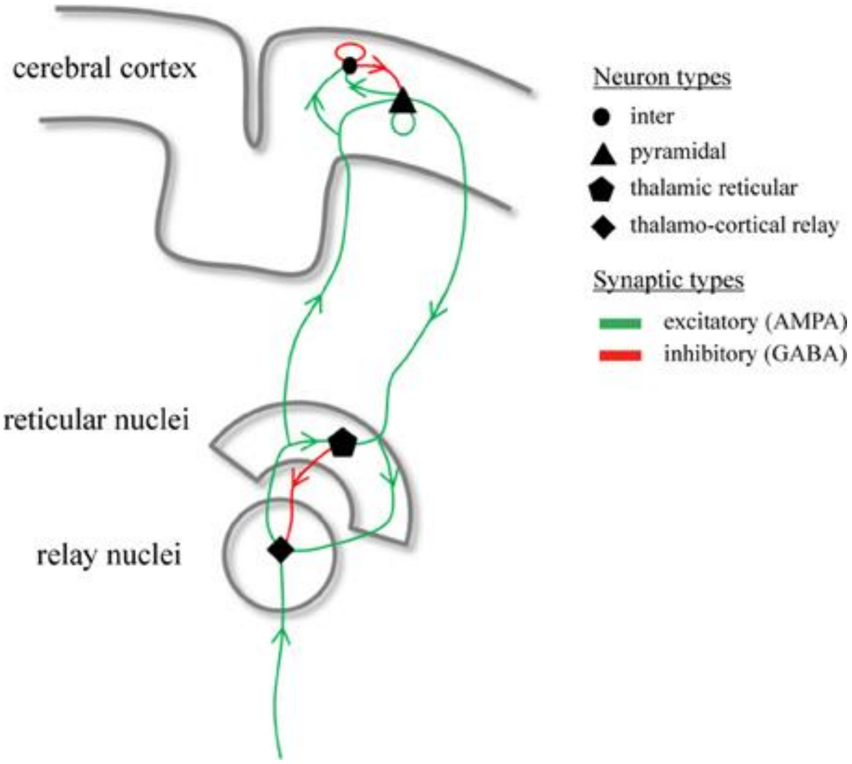

Figure 1.11. Schematic representation of the TC circuit: four types of cells which are connected through excitatory (green) and inhibitory (red) synaptic projections. (Image taken from Hindriks et al, 2013).

The slight temporal differences among the three mechanisms provide a reached variety of discharging mode with complex rhythms and oscillations (Hull & Scanziani, 2007). Anyway, the TCT system is more complex than it looks. In fact, somatosensory information from the VPL and VPM nuclei is subjected to, at least, four types of processing including those mentioned above: local synaptic processing within the nucleus itself of ascending sensory pathways; modulation by brainstem inputs, such as noradrenergic and serotoninergic systems; inhibitory feedbacks from the reticular nucleus; excitatory feedback from the neocortex. Thus, the thalamus is subject to a variety of inputs, not only sensory, that modulate the recurrent activity of TCT pathways.

1.6 Introduction to pain

Pain is defined by the International Association for the Study of Pain (IASP) as "an unpleasant sensory and emotional experience associated with actual or potential tissue damage, or described in terms of such damage". In this definition the double nature of pain disease is revealed: pain has not only a sensory component, triggered by the stimulation of specific receptors distributed in the body, but also an emotional component, which makes the reactions to pain extremely subjective and influenced by individual factors. In fact, many people report pain in the absence of tissue damage or any likely pathophysiological cause;

usually this happens for psychological reasons. There is often no way to distinguish experience due to tissue damage if we take the subjective report. If they regard their experience as pain, and if they report it in the same ways as pain caused by tissue damage, it should be accepted as pain. Thence, pain is not the direct expression of a sensory event but rather the product of elaborate processing by the brain of a variety of neural signals. Pain is always a neuropsychological state, affected by psychological factors such as past experiences, beliefs about pain, fear or anxiety.

1.6.1 Critical differences between acute and chronic pain

From a biological point of view, pain represents a defence system, when encodes an alarm signal due to a tissue injury, allowing the central nervous system for receiving information about potentially damaging stimuli to the body. In these conditions, pain (said acute or physiological pain) plays a protective role, and it's used to change certain behavioural responses, ensuring the subject to avoid harmful stimuli. Anyway, pain becomes pathological/chronic when it turns to be self-maintained, and appears to lose its alerting function. In such situation, pain can cause very serious behavioural, metabolic and functional disorders. Thus, acute pain in these terms plays an important adaptive role, essential for both the survival and reproduction. In contrast, Chronic Pain (CP) seems to have no evolutionary role and this make its comprehension highly obscure, without any biological meaning.

1.6.2 Pain perception: physiology

Since pain is a submodality of somatic sensations, giving a global and comprehensive description of it is a complex task. In addition, talking about CP, it should be emphasized that it often becomes a cerebral elaboration sustained by non-sensory events making oneself a central representation regardless of the peripheral inputs. In this complex picture, some general anatomo-functional features are distinguishable in pain sensation and they can be considered as the initial input that may trigger CP. The general scheme behind the pain sensation is the following: nociceptive sensory inputs from various noxious and non-noxious stimuli are received by specific peripheral receptors that act as transducers and then transmitted by nerve action potentials along specific nerve pathways toward the central nervous system (CNS). Nociceptive stimuli activate a chain of neurons starting with the peripheral first-order (1°) afferent (Figure 1.12). The 1° afferents have their cell bodies located in the peripheral dorsal roots or trigeminal ganglia. They have a peripheral axon-like process that forms somatosensory receptors and a central process that makes synapses with second-order (2°) afferent neuron in the spinal cord or brain stem nuclei. The sensory information is then further processed as it progresses, via the ascending sensory systems (pathways), to the cerebral cortex or to the cerebellum. Sensory information is also relayed to other parts of the CNS where it may function to elicit a reflex response, or may be integrated into pattern-generating circuitry.

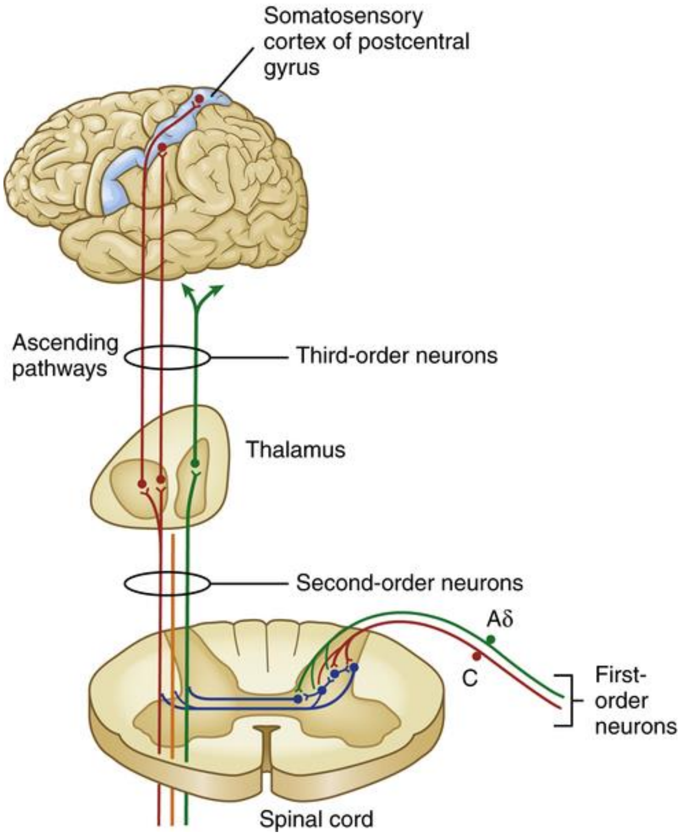

Figure 1.12. Illustration of nociception pathways. Aδ and C fibres comprise the primary, first-order sensory afferents coming into the gate at the dorsal horn of the spinal cord. Second-order neurons cross the cord ("decussate") and ascend to the thalamus. Third-order afferents project to higher brain centers of the limbic system, the frontal cortex, and the primary sensory cortex. (Image taken from McCance and Huether 2013).

In the following subsections all the elements involved in pain sensory process will be briefly described from structural and functional point of view.

1.6.2.1 Nociceptors

Nociceptors are the specialised sensory receptors responsible for the detection of noxious (unpleasant) stimuli, transforming the stimuli into electrical signals, which are then conducted to the central nervous system. They are the free nerve endings of primary afferent Aδ and C fibres. Distributed throughout the body (skin, viscera, muscles, joints, meninges) they can be stimulated by mechanical, thermal or chemical stimuli (Figure 1.13). They can be further classified into three groups:

- Mechanosensitive nociceptors (of Aδ fibres), which are sensitive to intense mechanical stimulation (such as pinching with pliers) or injury to tissues.
- Temperature-sensitive (thermosensitive) nociceptors (of Aδ fibres), which are sensitive to intense heat and cold.

- Polymodal nociceptors (of C fibres), which are sensitive to noxious stimuli that are mechanical, thermal, or chemical in nature. Although most nociceptors are sensitive to one particular type of painful stimulus, some may respond to two or more types.

Inflammatory mediators (e.g. bradykinin, serotonin, prostaglandins, cytokines, and H^+) are released from damaged tissue and can stimulate nociceptors directly. They can also act to reduce the activation threshold of nociceptors so that the stimulation required to cause activation is less. This process is called primary sensitisation. The release of these substances sensitizes the nociceptors (C fibres) and reduces their threshold. This effect is referred to as peripheral sensitization (in contrast to central sensitization that occurs in the dorsal horn). Within 15-30 seconds after injury, an area of several centimetres around the injured site shows reddening (caused by vasodilation) called a flare. This response (inflammation) becomes maximal after 5-10 minutes, and this region shows a lowered pain threshold (i.e., hyperalgesia).

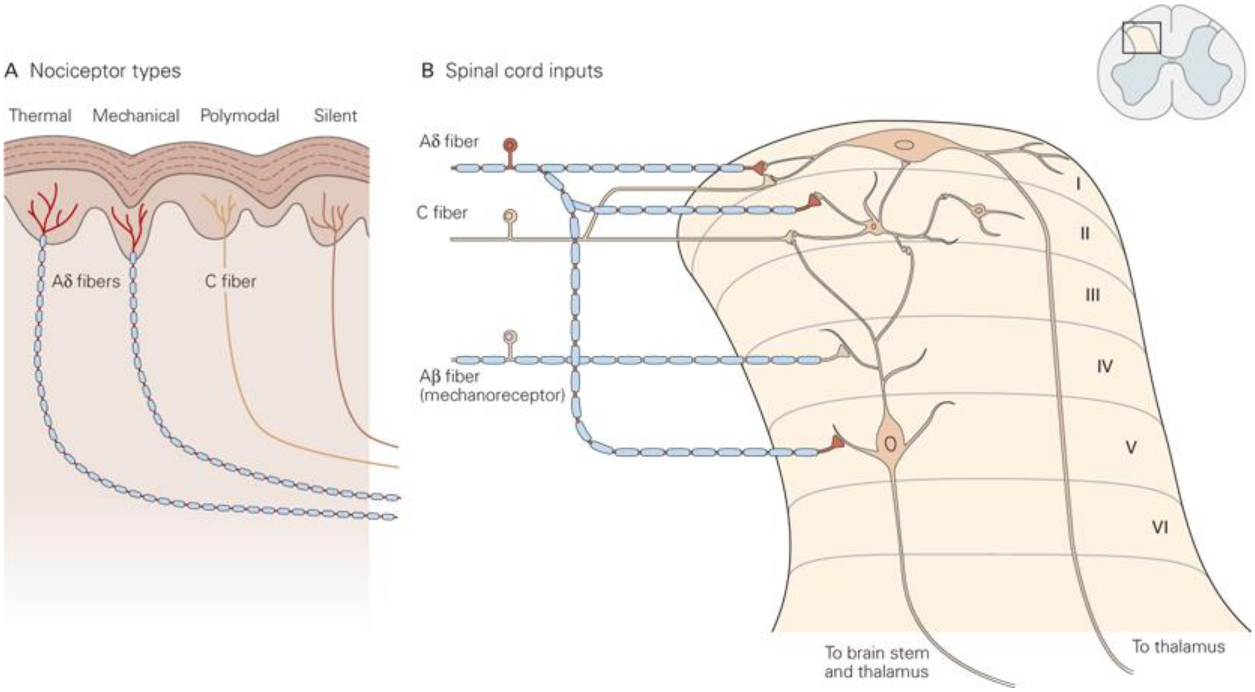

Figure 1.13. Principal nociceptors located in the skin **(A)** and their receptive field in the spinal cord **(B)**. The dorsal horn is histologically divided into laminae (from I to VI) where the specific sensory input is received from neurons. (Image taken from Kandel et al. 2013).

1.6.2.2 Primary afferent fibres

In addition to the Aδ and C fibres that carry noxious sensory information, there are primary afferent Aβ fibres that carry non-noxious stimuli. Each of these fibre types possesses different characteristics that allow the transmission of particular types of sensory information.

- Aβ fibres are highly myelinated and of large diameter, therefore allowing rapid signal conduction. They have a low activation threshold and usually respond to light touch and transmit non noxious stimuli.

- Aδ fibres are lightly myelinated and smaller diameter, and hence conduct more slowly than Aβ fibres. They respond to mechanical and thermal stimuli. They carry rapid, sharp pain and are responsible for the initial reflex response to acute pain.

- C fibres are unmyelinated and are also the smallest type of primary afferent fibre. Hence they demonstrate the slowest conduction. C fibres are polymodal, responding to chemical, mechanical and thermal stimuli. C fibre activation leads to slow, burning pain.

1.6.2.3 Secondary afferent neurons

Aδ and C fibres synapse with secondary afferent neurons in the dorsal horn of the spinal cord. The dorsal horn can be divided histologically into six layers called Rexed laminae. Aδ and C fibres transmit information to nociceptive specific neurons in Rexed lamina I and II, in addition to projections to other laminae. Primary afferent terminals release a number of excitatory neurotransmitters including glutamate and substance P. Complex interactions occur in the dorsal horn between afferent neurons, interneurons and descending modulatory pathways.

1.6.2.4 Ascending tracts in the spinal cord

There are three major ascending pathways that contribute to the central processing of nociceptive information, these are: neospinothalamic, paleospinothalamic and archispinothalamic tracts, all belonging to anterolateral ascending system (AlAS). Neospinothalamic tract constitutes the direct pathway of the AlAS and it has a crucial role in the transmission of nociceptive information. In this route, second order afferent neuron axons, after crossing the midline of the spinal cord mainly at their segment of origin, ascend in the anterolateral white matter before terminating in the thalamic nuclei, where they make synapses with the third-order neurons. Paleospinothalamic tract is involved in the indirect pathway of the AlAS and conveys inputs mainly to the ascending reticular formation, which in turn projects to diverse thalamic nuclei and to different cortex areas. Lastly, the archispinothalamic tract, phylogenically the oldest, is a multisynaptic diffuse tract. In fact, the second-order neurons belonging to this route may send their information to the periacqueductal gray area (PAG), hypothalamus, some areas of the thalamus and limbic system nuclei. These fibres mediate visceral, emotional and autonomic reactions to pain. The combination of these three contingents in a complex and not completely clear manner, can contribute to set supraspinal anomalies that could be the basis of CP condition (Figure 1.14).

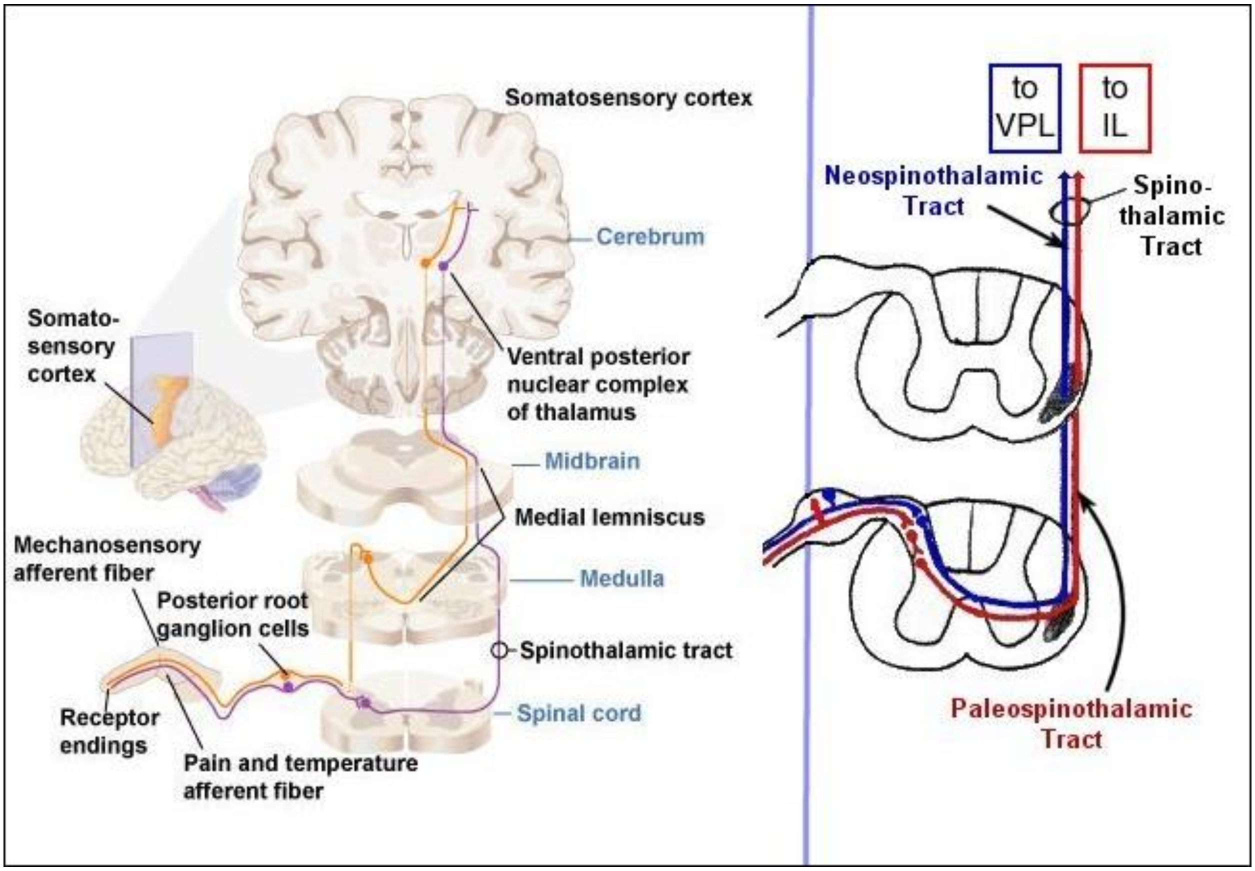

Figure 1.14. Principal pain ascending pathways: neospinothalamic, paleospinothalamic and spinorecticular tracts. (Image adopted from Neuroanatomy online).

All the mechanisms caused by peripheral sensitization, could generate an enhanced central sensitization in post-synaptic dorsal horn neurons, i.e. an increased responsiveness of nociceptive neurons in the CNS to their normal or subthreshold afferent input. In fact, under anomalous peripheral conditions C fibres may be induced to fire repetitively and the response of dorsal horn neurons increases progressively (F Cervero, 1995). This mechanism of gradual enhancement in the excitability of dorsal horn neurons has been termed "wind up".

1.6.2.5 Third order neurons

Cell bodies of the third order neurons of the nociception-relaying pathway are mainly housed in the VPL and VPM thalamic nuclei (Paragraph 1.5.2). They receive the major inputs from second-order neuron fibres, belonging mostly to the AlAS, which make excitatory synapses with them. Then, third-order neurons send their axons, called thalamocortical radiation, up to the specific neocortex areas, where the stimuli are further integrated.

1.6.2.6 Pain descending pathways

The descending pain pathways close a large loop, acting as a connecting link among inputs and outputs, so that, allow the modulation of nociceptive incoming inputs already in the first phases of their processing. Complex networks of pain descending pathways impinge on neurons housed in the brainstem nuclei and in the dorsal horn of spinal cord, with the purpose of modulating pain inputs from the periphery. Indeed, numerous investigations in the last years have established that activation of midbrain and specific medullary sites can exert bidirectional control over nociception (Figure 1.15). For instance, the periaqueductal gray (PAG) receives inputs from higher brain centres as well as ascending nociceptive inputs from the spinal dorsal horns. This structure is capable of activating an endogenous pain inhibitory system. Farther, many nuclei in the rostroventromedial medulla (RVM) receive inputs mainly from the PAG. Then, RVM can or facilitate or inhibit nociceptive inputs acting as a final relay in the control of descending pain system. Therefore, these structures provide a mechanism through which cortical and subcortical sites can influence the nociception by way of endorphines, serotonin, noradrenaline and other transmitters.

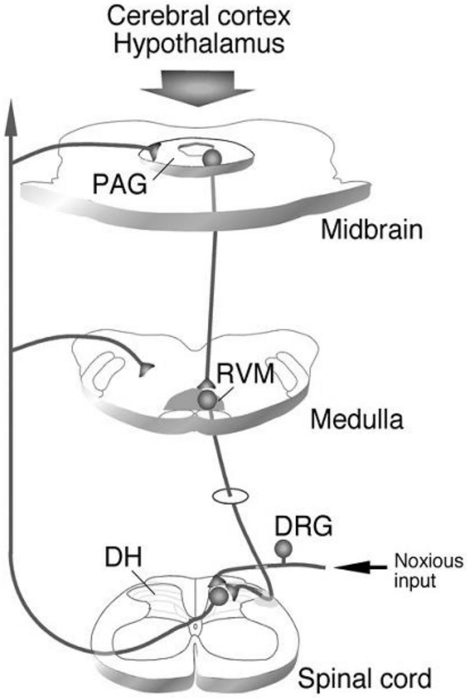

Figure 1.15. Pain modulation through descending pathways linking the periaqueductal gray (PAG), rostroventromedial medulla (RVM) and the spinal cord. (Image adopted from Guo et al. 2006).

The importance of these pathways is given by the growing evidence supporting the concept that chronic pain may also be associated with a dysregulation in descending pain pathway modulation (Ossipov, Morimura, & Porreca, 2014). A disruption in the balance of descending modulatory circuits could promote and maintain CP conditions.

This anatomo-functional introduction provided a selective presentation that overlook in a programmatic way some elements and dynamics, and it is driven by the need to focus only on those aspects that concern directly with CP and what we are going to investigate in this context.

1.7 Chronic Pain: present understandings

Chronic pain is a common problem that presents a major challenge to health-care providers because of its complex natural history, unclear aetiology, and poor response to therapy. Whether pain originates in the central or peripheral nervous system, it frequently becomes centralized through maladaptive responses within the central nervous system that can profoundly alter brain systems and thereby behaviour (e.g. depression) (Borsook, 2012). From the extensive studies on CP, we can observe that CP induces significant changes in function, anatomy and chemistry, which occur following pathophysiological alterations in pain pathways. These changes take place in areas of the brain involved in sensory, emotional and modulatory systems and are ‘brain-wide’ (e.g. including regions not normally associated with pain such as the cerebellum) (Moulton, Schmahmann, Becerra, & Borsook, 2010). They represent the direct consequence of pain or secondary to comorbid changes such as depression or anxiety (Elman, Zubieta, & Borsook, 2011).

Turning back to the sensory anomalies, a number of experimental, clinical and anatomo-pathological studies have shown that both anatomical and functional markers are recurrently recovered in CP at the level of the Central Nervous System. In particular, functional magnetic resonance imaging (fMRI) studies revealed that CP state is often accompanied by metabolic dysfunctions and local macrostructural signs such as cortical thickness reductions or cortical laminar misalignments (May, 2008). At lower, cell-level scales, CP related functional disorders have been described, in the past, mostly as gangliar, spinal or central neuronal dynamic irregularities (Biella, 1997; Biella & Sotgiu, 1995; Fernando Cervero & Laird, 1996; Liu & Sandkühler, 1998; Sandkühler & Liu, 1998; Sotgiu, Biella, & Riva, 1995). These mainly, but not exclusively, included spontaneous hyper- or hypoactivities, hyperresponsiveness to non-noxious and noxious stimuli, anomalous spiking patterns, often accompanied by variable signs of local neuronal degeneration of the sensory projection fields. The signs appeared complementary and ascribed to perceptual conditions such as spontaneous pain, allodynia and hyperalgesia.

In this scenario, it would be necessary to carry out a new consideration of CP, studying it in a different manner, starting from the "pure" and simplest questions, in order to try to give a necessary frame of reference of CP.

1.7.1 Limits of the current researches

As a proof of the arduous effort of elaborating a novel CP theory, there are many observations on developed therapies that confirm the complexity of the actual framework. The existing therapies for CP are transient and often lead to widespread side effects. Just to think on morphine and all the different types of opiates therapies, or on nonsteroidal anti-inflammatory (NSAID), cortisone and antidepressant. It is evident that none of these is used to set a real treatment of the whole pathology. This is due to the fact that, till now, the majority of researcher have investigated CP on the basis of complex issues: they focused both on the modalities to overcome pain, synthesizing new drugs which often offer pharmacological effects similar to pre-existing ones, and on cerebral physiopathology studies by using all sorts of advanced imaging techniques as positron emission tomography (PET) or fMRI. All these techniques have allowed to identify unknown molecular mechanisms and many "stopgap" therapies. Nevertheless, the management of CP remains almost unsolvable and a theoretical description from the tenet is still missing. In fact, the true internal networks that are spontaneously activated in CP have been identified mostly by clinical imaging, especially by fMRI or diffusion-weighted MRI (DW-MRI) the former being a functional measure, the latter focusing on the structural data. Although the advantages brought in by fMRI, this technique reveals a limitation: it represents data from indirect measures of cerebral activation, since it reflects the relative hemodynamic responses to potential neural activations. In addition, this imaging technique is affected by relative low temporal resolution (~1-2 seconds for whole brain images) where these delays in monitoring the cerebral activity, from a neural point of view, may be still too slow in comparison with proper electrophysiological techniques displaying sub-millisecond resolutions. Indeed, the electrophysiological techniques, such as electroencephalography (EEG), although ensuring a suitable temporal resolution (in range of milliseconds), they lack of spatial resolution (in range of 2-3 cm), in comparison with fMRI. In this scenario, it would be needful to set a multi-scale approach, in order to probe the brain at different levels to have an accurate appraisal of the networks involving CP.

1.7.2 Pilot experiments before my thesis

In previous studies performed by the Italian CNR laboratory of Neurophysiology and Neurophysiopathology of Sensory Disorders and Chronic Pain led by G. E. M. Biella (A. Zippo et al. 2011; A. Zippo et al. 2016) using simultaneous massive electrophysiological recordings from the thalamus and the somatosensory cortex, it appeared that chronic pain affects: (i) the capacities of groups of neurons to effectively communicate between them and (ii) to integrate the different tasks simultaneously running in the thalamo-cortical brain network. In particular, in a regime of ongoing activity of the thalamo-cortical network, different animal models of CP homogeneously exhibit neural functional signs well distinguishable from those in control animals. Remarkably, the three CP models chosen for the studies (Inflammatory, Seltzer and the Bennet-Xie, namely) shared comparable connectivity disorders where the somatosensory thalamo-cortical network exhibits reduced capabilities of information processing along with weakened information transfer and overall topological network degradation.

The dynamic stereotypy of the sensory cortex in the different CP conditions is strictly related to the neurophysiological anomalies as above described. An approach to reinstate plastic dynamics and an integration/segregation alternation balance in thalamo-cortical circuit has been proposed by CNR group and carried out at the ID17 beamline (ESRF, Grenoble). It consisted in the delivery of collimated X-ray Microbeams (MB) (in living anesthetized rats with and without CP models) in order to achieve an artificially modulated sensory cortex able to express different neurodynamic behaviours thus enriching the information content of the thalamo-cortical network. In detail, the seven parallel MB, 100 µm wide, spaced of 400 µm and depositing a peak dose of 360 Gray, (Figure 1.16) created 8 putative modules in the CP rats which later on showed that: i) the thalamo-cortical functional connectivity was re-established comparably to control animals and ii) the behavioural parameters such as the time of response to peripheral nociceptive and non-nociceptive stimuli were restored to the normal level (no functional/electrophysiological, or behavioural changes were evident in control animals). The reduced dynamics of the cortex has been enriched by multiplying the independent somatosensory modules that increased the information transfer and the adaptability of the thalamo-cortical circuitry.

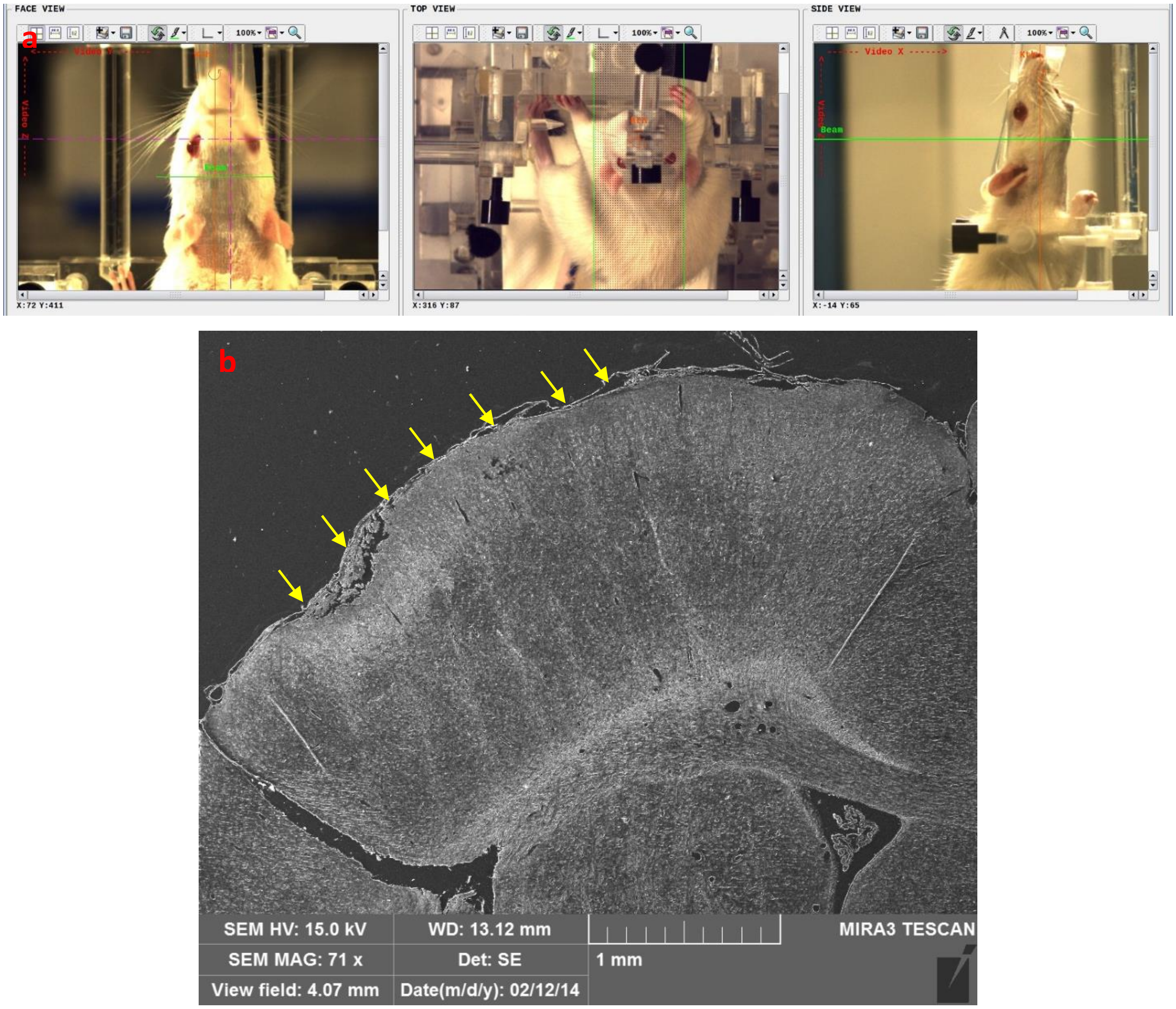

Figure 1.16. X-ray MB delivery over the somatosensory cortex of experimental rat **(a)**. The 7 MB are clearly visible through the histological section analysed by a Scanning Electron Microscope **(b)**.

1.8 Aim of the present study

Along the pathway opened by the previous studies, performed by CNR scientists, and with the aim of providing a more detailed picture of CP, a multi-approach analysis has been here proposed, not focused only on neuronal networks characterization but also on a micro-structural characterization of the glial and vascular contexts that regulate the neuronal dynamics. In particular, the delicate anatomical and functional relation among neurons, glial cells and vessels will be investigated in normal and CP conditions.

It is conceivable that due to the heavy rearrangements of the macroscopic architecture in chronic pain, consequent micro/nano architectural disorders could be highlighted in those structures. This complex thread of functional features is based on composite neural and glio-vascular architectures. Studies on the rat sensory cortex have elucidated that each micro-column is largely supplied from penetrating arterioles (Nishimura et al., 2006). The possibility to visualize with an increasing spatial resolution the cortical cyto-architecture has made possible to describe the spatial distribution of cells and vessels. For instance, photonic techniques imaging have provided data supporting the tendency for neuronal nuclei to lie further away from vessels than would be expected from a random spatial distribution. This indicates that, within each cortical layer, the density of neuronal somata and the distribution of microvessels have specific ratios, determining unique spatial architecture and indicating a mutual functional dependency between vessels and neurons. The functional relationship between neurons and the brain microvasculature is now better known, and techniques like oxygen-level dependent functional magnetic resonance (fMR) and intrinsic optical imaging are largely based on this dependency, estimating changes in neuronal activity from alterations in local concentration of blood oxygenation. Namely, the functional dependency of neurons from blood vessels has expanded the concept of synaptic space to a more complex form, indicated as “tripartite synapse” where besides the presence of the pre- and post- synaptic neurons, a glial component is added facing on the microvascular context. The electrophysiological analyses directly relate the Local Field Potentials (LFPs) that is the activity of synapses to the activity of the microvessels regulated by the glial cells (Logothetis, Pauls, Augath, Trinath, & Oeltermann, 2001). Recent research from CNR lab has further evidenced the dependency of spikes from LFPs, thus potentially extending the spiking activity on the microvessel dynamics (Storchi, Zippo, Caramenti, Valente, & Biella, 2012). Some work on CP evidenced architectural reorganization of the cortical texture (Apkarian, Hashmi, & Baliki, 2011; Flor et al., 1995). Due to the microstructural dependency between vessels and neurons, the reorganization of the neural substrate should involve deep microvascular rearrangements with potential backward effects. A submicroscopic appraisal of this remodelling should throw a light on a potential new approach on CP core anomalies and on potential new therapeutic approaches.

By this work, we wish to investigate both the micro/nano architectural disorders in cortical spaces potentially related to these heavy rearrangements involving the macroscopic architecture and the network dynamic anomalies emerging and stabilizing in CP**.** Therefore, a dual analysis has been performed including:

-Neurodynamic analysis through electrophysiological recordings to predict the origin of changes in brain functional connectivity and in information transmission. These recordings will be paired to microBOLD measurements by Near Infrared Spectroscopy probe to preliminary probe the activity of blood microvessel and capillaries strictly intertwined with the dynamics of the neuronal networks.

-Microstructural analysis through micro- and nano-CT imaging experiments to evaluate the micro- and nano-architectural anomalies potentially nested in the cortical microscopic texture hosting the neuron-glia-vessel matrices.

Due to the microstructural dependency between vessels and neurons, the reorganization of the neural substrate should involve deep microvascular rearrangements with potential backward effects. A submicroscopic appraisal of this remodeling should throw a light on a potential new approach on CP core anomalies and on potential new therapeutic treatments.

References

Anderson C.M. and Nedergaard M. 2003. “Astrocyte-mediated control of cerebral microcirculation.” *Trends in Neurosciences*. https://doi.org/10.1016/S0166-2236(03)00141-3.

Apkarian A.V., Hashmi J.A. and Baliki M.N. 2011. “Pain and the brain: specificity and plasticity of the brain in clinical chronic pain.” *Pain*, *152*(3 Suppl), S49.

Araque A., Parpura V., Sanzgiri R.P. and Haydon P.G. 1999. “Tripartite synapses: glia, the unacknowledged partner.” *Trends in Neurosciences*, *22*(5), 208–215. https://doi.org/10.1016/S0166-2236(98)01349-6.

Attwell D., Buchan A. M., Charpak S., Lauritzen M., MacVicar B. A. and Newman E. A. 2010. “Glial and neuronal control of brain blood flow.” *Nature*, *468*(7321), 232–243. https://doi.org/10.1038/nature09613.

Attwell D. and Laughlin S.B. 2001. “An Energy Budget for Signaling in the Grey Matter of the Brain.” *Journal of Cerebral Blood Flow & Metabolism*, *21*(10), 1133–1145. https://doi.org/10.1097/00004647-200110000-00001.

Bass N.H., Hess H.H., Pope A. and Thalheimer C. 1971. “Quantitative cytoarchitectonic distribution of neurons, glia, and DNA in rat cerebral cortex.” *Journal of Comparative Neurology*. https://doi.org/10.1002/cne.901430405.

Bear M., Connors B. and Paradiso M. 2014. *“NEUROSCIENCE Exploring the Brain.” Lippincott Williams & Wilkins*. https://doi.org/10.1007/s13398-014-0173-7.2.

Biella G.E.M. 1997. “Interaction between neurons in different laminae of the dorsal horn of the spinal cord. A correlation study in normal and neuropathic rats.” *European Journal of Neuroscience*. https://doi.org/10.1111/j.1460-9568.1997.tb01452.x.

Biella G.E.M. and Sotgiu M.L. 1995. “Evidence that inhibitory mechanisms mask inappropriate somatotopic connections in the spinal cord of normal rat.” *Journal of Neurophysiology*.

Bolton M.M. and Eroglu C. 2009. “Look who is weaving the neural web: glial control of synapse formation.” *Current Opinion in Neurobiology*, *19*(5), 491–497. https://doi.org/10.1016/j.conb.2009.09.007.

Borsook D. 2012. “Neurological diseases and pain.” *Brain*, *135*(2), 320–344. https://doi.org/10.1093/brain/awr271.

Burton H. and Jones E. G. 1976. "The posterior thalamic region and its cortical projection in new world and old world monkeys." *The Journal of Comparative Neurology*, *168*(2), 249–301. https://doi.org/10.1002/cne.901680204.

Buxton R. B. 2013. "The physics of functional magnetic resonance imaging (fMRI)." *Reports on Progress in Physics*, *76*(9), 96601.

Cervero F. 1995. "Visceral pain: mechanisms of peripheral and central sensitization." *Annals of Medicine*. https://doi.org/10.3109/07853899509031965.

Cervero F. and Laird J. M. A. 1996. *"From acute to chronic pain: mechanisms and hypotheses."* (pp. 3–15). https://doi.org/10.1016/S0079-6123(08)62561-3.

Diamond M.E., Armstrong-James M. and Ebner F. F. 1992. "Somatic sensory responses in the rostral sector of the posterior group (POm) and in the ventral posterior medial nucleus (VPM) of the rat thalamus." *The Journal of Comparative Neurology*, *318*(4), 462–476. https://doi.org/10.1002/cne.903180410.

Elman I., Zubieta J.-K. and Borsook D. 2011. "The Missing "P" in Psychiatric Training: Why is it Important to Teach Pain to Psychiatrists?" *Archives of General Psychiatry*, *68*(1), 12–20. https://doi.org/10.1001/archgenpsychiatry.2010.174.

Eroglu C., Barres B.A. and Stevens B. 2008. "Glia as active participants in the development and function of synapses." *Structural And Functional Organization Of The Synapse*. https://doi.org/10.1007/978-0-387-77232-5_23.

Feig S. and Harting J. K. 1998. "Corticocortical communication via the thalamus: Ultrastructural studies of corticothalamic projections from area 17 to the lateral posterior nucleus of the cat and inferior pulvinar nucleus of the owl monkey." *Journal of Comparative Neurology*. https://doi.org/10.1002/(SICI)1096-9861(19980808)395:3<281::AID-CNE2>3.0.CO;2-Z.

Fellin T. and Haydon P. G. 2005. "Do astrocytes contribute to excitation underlying seizures? " *Trends in Molecular Medicine*, *11*(12), 530–533. https://doi.org/10.1016/j.molmed.2005.10.007.

Filosa J.A. 2004. "Calcium Dynamics in Cortical Astrocytes and Arterioles During Neurovascular Coupling." *Circulation Research*. https://doi.org/10.1161/01.RES.0000148636.60732.2e.

Flor H., Elbert T., Knecht S., Wienbruch C., Pantev C., Birbaumers, N. et al. 1995. "Phantom-limb pain as a perceptual correlate of cortical reorganization following arm amputation." *Nature*, *375*(6531), 482–484.

Friedman D.P., Murray E.A., O'Neill J.B. and Mishkin M. 1986. "Cortical connections of the somatosensory fields of the lateral sulcus of macaques: Evidence for a corticolimbic pathway for touch." *The Journal of Comparative Neurology*, *252*(3), 323–347. https://doi.org/10.1002/cne.902520304.

Guo W., Robbins M.T., Wei F., Zou S., Dubner R. and Ren K. 2006. "Supraspinal Brain-Derived Neurotrophic Factor Signaling: A Novel Mechanism for Descending Pain Facilitation." *The Journal of Neuroscience*, *26*(1), 126 LP-137. http://www.jneurosci.org/content/26/1/126.

Harder D. R., Alkayed N. J., Lange A.R., Gebremedhin D. and Roman R. J. 1998. "Functional hyperemia in the brain: hypothesis for astrocyte-derived vasodilator metabolites." *Stroke; a Journal of Cerebral Circulation*. https://doi.org/10.1161/01.STR.29.1.229.

Harris J.J. and Attwell D. 2012. "The Energetics of CNS White Matter." *The Journal of Neuroscience*, *32*(1), 356 LP-371. http://www.jneurosci.org/content/32/1/356.

Herculano-Houzel S. 2011. "Not all brains are made the same: New views on brain scaling in evolution." *Brain, Behavior and Evolution*. https://doi.org/10.1159/000327318.

Herculano-Houzel S. 2014. "The glia/neuron ratio: How it varies uniformly across brain structures and species and what that means for brain physiology and evolution." *Glia*, *62*(9), 1377–1391. https://doi.org/10.1002/glia.22683.

Hull C. and Scanziani M. 2007. "It's about time for thalamocortical circuits." *Nature Neuroscience*. https://doi.org/10.1038/nn0407-400.

Iadecola C. and Nedergaard M. 2007. "Glial regulation of the cerebral microvasculature." *Nature Neuroscience*, *10*(11), 1369–1376. https://doi.org/10.1038/nn2003.

Kacem K., Lacombe P., Seylaz J. and Bonvento G. 1998. "Structural organization of the perivascular astrocyte endfeet and their relationship with the endothelial glucose transporter: A confocal microscopy study." *Glia*, *23*(1), 1–10. https://doi.org/10.1002/(SICI)1098-1136(199805)23:1<1::AID-GLIA1>3.0.CO;2-B.

Kandel E.R., Schwartz J.H., Jessell T. M., Siegelbaum S. A. and Hudspeth A. J. 2013. "*Principles of Neural Science*" *Fifth Edition*. *McGraw Hill*. https://doi.org/10.1007/s13398-014-0173-7.2.

Koehler R.C. 2006. "Role of astrocytes in cerebrovascular regulation." *Journal of Applied Physiology*. https://doi.org/10.1152/japplphysiol.00938.2005.

Liu X.G. and Sandkühler J. 1998. "Activation of spinal N-methyl-D-aspartate or neurokinin receptors induces long-term potentiation of spinal C-fibre-evoked potentials." *Neuroscience*. https://doi.org/10.1016/S0306-4522(98)00107-9.

Logothetis N.K., Pauls J., Augath M., Trinath T. and Oeltermann A. 2001. "Neurophysiological investigation of the basis of the fMRI signal." *Nature*. https://doi.org/10.1038/35084005.

May A. 2008. "Chronic pain may change the structure of the brain." *Pain, 137*(1), 7–15. https://doi.org/10.1016/j.pain.2008.02.034.

McCance K.L. and Huether S.E. 2013. "Pathophysiology - the biologic basis for disease in adults and children." *Journal of Chemical Information and Modeling*. https://doi.org/10.1017/CBO9781107415324.004.

Metea M.R. and Newman E.A. 2006. "Glial Cells Dilate and Constrict Blood Vessels: A Mechanism of Neurovascular Coupling." *The Journal of Neuroscience, 26*(11), 2862 LP-2870. http://www.jneurosci.org/content/26/11/2862.

Meyer H.S., Egger R., Guest J. M., Foerster R., Reissl S. and Oberlaender M. 2013. "Cellular organization of cortical barrel columns is whisker-specific." *Proceedings of the National Academy of Sciences of the United States of America*, *110*(47), 19113–8. https://doi.org/10.1073/pnas.1312691110.

Moulton E.A., Schmahmann J.D., Becerra L. and Borsook D. 2010. "The Cerebellum and Pain: Passive Integrator or Active Participator?" *Brain Research Reviews*, *65*(1), 14–27. https://doi.org/10.1016/j.brainresrev.2010.05.005.

Mountcastle V. 1957. "Modality and topographic properties of single neurons of cat's somatic sensory cortex." *Journal of Neurophysiology 20(4),* 408-34. https://doi.org/10.1152/jn.1957.20.4.408.

Mulligan S.J. and MacVicar B.A. 2004. "Calcium transients in astrocyte endfeet cause cerebrovascular constrictions." *Nature, 431*(7005), 195–199. http://dx.doi.org/10.1038/nature02827.

Newman E.A. 2005. "Calcium Increases in Retinal Glial Cells Evoked by Light-Induced Neuronal Activity." *Journal of Neuroscience*. https://doi.org/10.1523/JNEUROSCI.1354-05.2005.

Nishimura N., Schaffer C. B., Friedman B., Tsai P. S., Lyden P. D. and Kleinfeld D. 2006. "Targeted insult to subsurface cortical blood vessels using ultrashort laser pulses: three models of stroke." *Nature Methods, 3*(2), 99–108. http://dx.doi.org/10.1038/nmeth844.

Oberheim N.A., Wang X., Goldman S. and Nedergaard M. 2006. "Astrocytic complexity distinguishes the human brain. ” *Trends in Neurosciences*, *29*(10), 547–553. https://doi.org/10.1016/j.tins.2006.08.004.

Ogawa S., Shulman R.G., Glynn P., Yamane T. and Navon G. 1978. “On the measurement of pH in Escherichia coli by 31P nuclear magnetic resonance. ” *Biochim Biophys Acta*. https://doi.org/0005-2728(78)90130-5.

Ohara S., Lenz F.A. and Norgren R. 2003. “Medial lateral extent of thermal and pain sensations evoked by microstimulation in somatic sensory nuclei of human thalamus.” *Journal of Neurophysiology*, *90*(4), 2367–77. https://doi.org/10.1152/jn.00450.2003.

Ossipov M.H., Morimura K. and Porreca F. 2014. “Descending pain modulation and chronification of pain.” *Current Opinion in Supportive and Palliative Care*. https://doi.org/10.1097/SPC.0000000000000055.

Paulson O.B. and Newman E.A. 1987. “Does the Release of Potassium from Astrocyte Endfeet Regulate Cerebral Blood Flow?” *Science (New York, N.Y.)*, *237*(4817), 896–898. http://www.ncbi.nlm.nih.gov/pmc/articles/PMC2505270/

Penfield W. and Boldrey E. 1937. “Somatic motor and sensory representation in the cerebral cortex of man as studied by electrical stimulation. ” *Brain*. https://doi.org/10.1093/brain/60.4.389.

Perea G. 2005. “Properties of Synaptically Evoked Astrocyte Calcium Signal Reveal Synaptic Information Processing by Astrocytes.” *Journal of Neuroscience*. https://doi.org/10.1523/JNEUROSCI.3965-04.2005.

Perea G. and Araque A. 2005. “Glial calcium signaling and neuron-glia communication.” *Cell Calcium*. https://doi.org/10.1016/j.ceca.2005.06.015.

Perea G., Navarrete M. and Araque A. 2009. “Tripartite synapses: astrocytes process and control synaptic information.” *Trends in Neurosciences*. https://doi.org/10.1016/j.tins.2009.05.001.

Petersen C.C.H. 2007. “The Functional Organization of the Barrel Cortex.” *Neuron*, *56*(2), 339–355. https://doi.org/10.1016/j.neuron.2007.09.017.

Reichova I. 2004. “Somatosensory Corticothalamic Projections: Distinguishing Drivers From Modulators.” *Journal of Neurophysiology*. https://doi.org/10.1152/jn.00322.2004.

Sandkühler J. and Liu X. 1998. “Induction of long-term potentiation at spinal synapses by noxious stimulation or nerve injury.” *European Journal of Neuroscience*. https://doi.org/10.1046/j.1460-9568.1998.00278.x.

Schipke C.G. and Kettenmann H. 2004. “Astrocyte responses to neuronal activity.” *GLIA*. https://doi.org/10.1002/glia.20029.

Sherman S. M. and Guillery, R.W. 2006. “*Exploring the Thalamus and Its Role in Cortical Function*.” *San DiegoAcademic Press*. https://doi.org/10.1007/0-387-22733-4_12.

Simard M., Arcuino G., Takano T., Liu Q.S. and Nedergaard M. 2003. “Signaling at the Gliovascular Interface.” *The Journal of Neuroscience*, *23*(27), 9254 LP-9262. http://www.jneurosci.org/content/23/27/9254.

Sotgiu M. L., Biella G.E.M. and Riva L. 1995. “Poststimulus afterdischarges of spinal WDR and NS units in rats with chronic nerve constriction.” *Neuroreport*. https://doi.org/10.1097/00001756-199505090-00018.

Storchi R., Zippo A.G., Caramenti G.C., Valente M. and Biella G.E.M. 2012. “Predicting spike occurrence and neuronal responsiveness from LFPs in primary somatosensory cortex.” *PLoS ONE*, *7*(5). https://doi.org/10.1371/journal.pone.0035850.

Strangman G., Boas D.A. and Sutton J. P. 2002. “Non-invasive neuroimaging using near-infrared light.” *Biological Psychiatry*, *52*(7), 679–693. https://doi.org/10.1016/S0006-3223(02)01550-0.

Woolsey C.N., Erickson T.C. and Gilson W.E. 1979. “Localization in somatic sensory and motor areas of human cerebral cortex as determined by direct recording of evoked potentials and electrical stimulation.” *Journal of Neurosurgery*, *51*(4), 476–506. https://doi.org/10.3171/jns.1979.51.4.0476.

Zippo A.G., Valente M., Caramenti G. C. and Biella G. E. M. 2016. “The thalamo-cortical complex network correlates of chronic pain.” *Scientific Reports 6*, 34763. http://dx.doi.org/10.1038/srep34763.

Zippo A.G., Storchi R., Valente M., Caramenti G.C. and Biella G.E.M. 2011. “Neural Substrates of Chronic Pain in the Thalamocortical Circuit.” *Nature Precedings*. http://precedings.nature.com/documents/6548/version/1.

Zonta M., Angulo M.C., Gobbo S., Rosengarten B., Hossmann K.-A., Pozzan T. and Carmignoto G. 2003. “Neuron-to-astrocyte signaling is central to the dynamic control of brain microcirculation.” *Nature Neuroscience*, *6*(1), 43–50. http://dx.doi.org/10.1038/nn980

Chapter 2: Materials and Methods

Summary

The CP morpho-functional study is here reported by analytically describing all the materials and methods involved in the three main experimental activities: Synchrotron X-ray Computed Tomography Imaging of rat somatosensory cortical samples for analyzing the microstructure of vascular network; immunofluorescence microscopy analysis as comparing tool; in vivo electrophysiological recordings to investigate the neuronal dynamics. For each technique the main principles, the instrumentation and the experimental procedures developed are accurately reported. At the end, a brief insight on Near InfraRed Spectroscopy technique for the evaluation of haemodynamic changes in rat cortical microvascular activity is provided.

Résumé

L'étude morpho-fonctionnelle de la douleur chronique est présentée ici en décrivant analytiquement tous les matériaux et méthodes impliqués dans les trois activités expérimentales principales: la micro-tomographie par rayonnement X synchrotron des échantillons corticaux somatosensoriels de rat pour l'analyse de la microstructure du réseau vasculaire; l'analyse de microscopie d'immunofluorescence comme outil de comparaison; les enregistrements électrophysiologiques in vivo pour étudier la dynamique neuronale. Pour chaque technique, les principes directeurs, l'instrumentation et les procédures expérimentales développées sont décrits avec précision. À la fin, un bref aperçu de la technique de la spectroscopie Near InfraRed pour l'évaluation des changements hémodynamiques dans l'activité microvasculaire corticale du rat est fourni.

Contents

2 Materials and methods

The experimental workflow foreseen for the structural and functional evaluation of Chronic Pain effects on the somatosensory cortical microarchitecture required the implementation, development and refinement of several different experimental methods and materials.

Three main techniques have been adopted in this work:

- **Synchrotron X-ray Computed Tomography** to evaluate the micro-vessels anomalies potentially nested in the cortical microscopic texture.
- **Immunofluorescence and immunohistochemistry** as complementary analyses for validating the results obtained by X-ray morphological micro Imaging.
- ***In vivo* electrophysiology coupled to NIRS** to evaluate potential changes in both neuronal and hemodynamic activity in CP conditions respect to controls.

In the next sections, a throughout description of all the experimental techniques is provided.

2.1 Synchrotron X-ray Computed Tomography

2.1.1 Synchrotron X-ray sources

A tomographic setup consists mainly in an X-ray source, a rotational sample stage and an X-ray detector. The latter is usually a photon flux measurement device where a scintillator detector intercepts the incident X-ray photons and converts them into visible light. The light is then collected and converted into an electrical signal by photodiodes. Over the years, a new research field emerged in high-resolution X-ray tomography, called micro-CT. This method has been developed since the eighties using laboratory-scale X-ray source (Elliott and Dover 1982, 1985; Sato et al. 1981), gamma-ray sources (Gilboy 1984) and synchrotron radiation (Bonse et al. 1986; Grodzins 1983). The high brilliant flux of synchrotron radiation results in a clear superiority in terms of achievable spatial resolution and signal-to-noise ratio (Baruchel et al. 2006), but the number of synchrotron facilities is limited due to their high cost. (Figure 2.1)

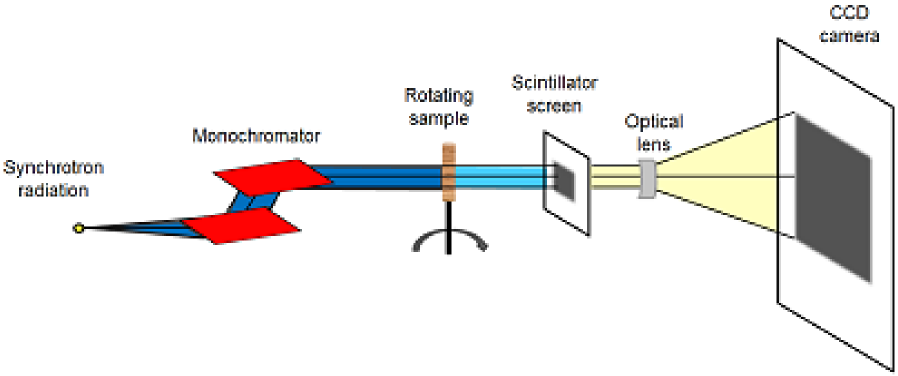

Figure 2.1. Typical synchrotron based micro-CT Imaging setup. (Image from Cnudde and Boone 2013).

Synchrotron radiation is generated when electric or magnetic fields force electrons or other charged particles, moving at relativistic speeds, to follow curved trajectories. Synchrotron radiation emitted by electrons in particle accelerators is extremely intense and extends over a broad energy range from the infrared until the hard X-ray region of the electromagnetic spectrum. Electrons are generated by heating a cathode (typically made of tungsten) and pulled out by a strong electric field; they are then channelled toward a linear accelerator (LINAC). When their energy reaches several millions of electron volts (MeV), they are transferred to a Booster Ring that gives them a boost in energy to reach the Giga electronvolts (GeV); at that point, they are injected into the final circular accelerator or Storage Ring. It consists of an evacuated tube where the electrons are forced to follow closed paths under the action of the so called bending magnets. Once injected into the storage ring, a quasi-stationary regime is achieved: the electrons, forced to change trajectory by the bending magnets, loose the energy emitted as synchrotron radiation. This part of lost energy is fully regained in passing through the RF cavities. In more detail, storage rings consist of an array of magnets for focussing and bending the beam connected by straight linear sections. In one or more of these linear sections, RF cavities are installed in order to accelerate the particles that have lost part of their energy by emitting radiation in one of the magnets. A general scheme of a synchrotron source is illustrated in Figure 2.2. During one full turn, the electrons are deflected from their path by 64 bending magnets each inducing beam deviation of 5.625°. Dipole magnets (bending magnets) are located in the curved sections to bend the electrons trajectory in order to maintain them in a closed orbit and/or produce SR with a continuous spectrum.

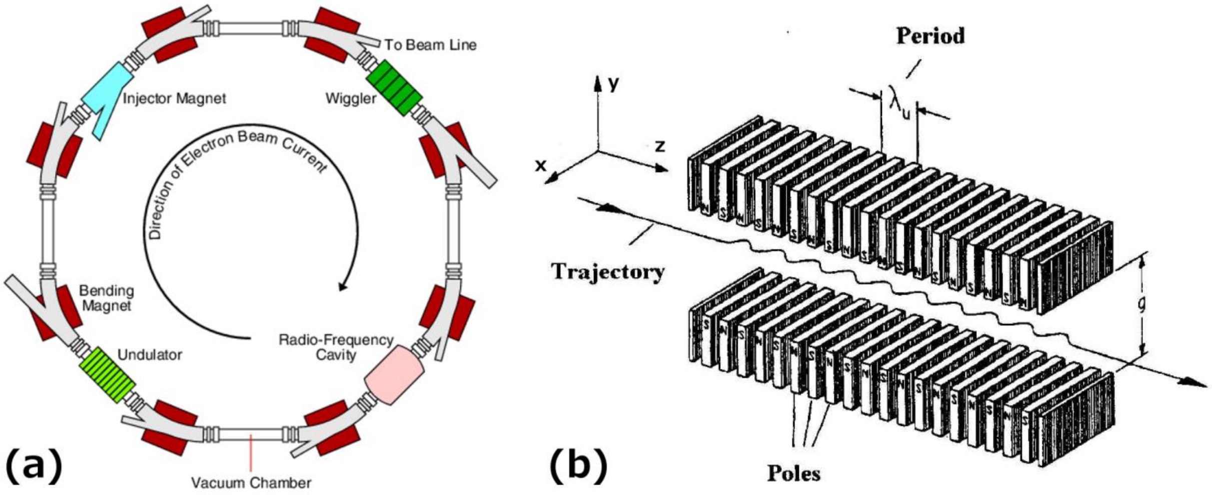

Figure 2.2 (a) Schematic representation of the electron ring in a synchrotron (Image from pd.chem.ucl.ac.uk); **(b)** representation of a wiggler (Image from www.project.slac.standford.edu).

In a bending magnet the orbits of the electrons are circular and the radiation is emitted tangentially. This is collected, for experiments, through a horizontal slit (S) of width w, at a distance, D, from the electron orbit; this corresponds to an angular aperture, $\Delta\theta = w/D >> \psi$ (see below).

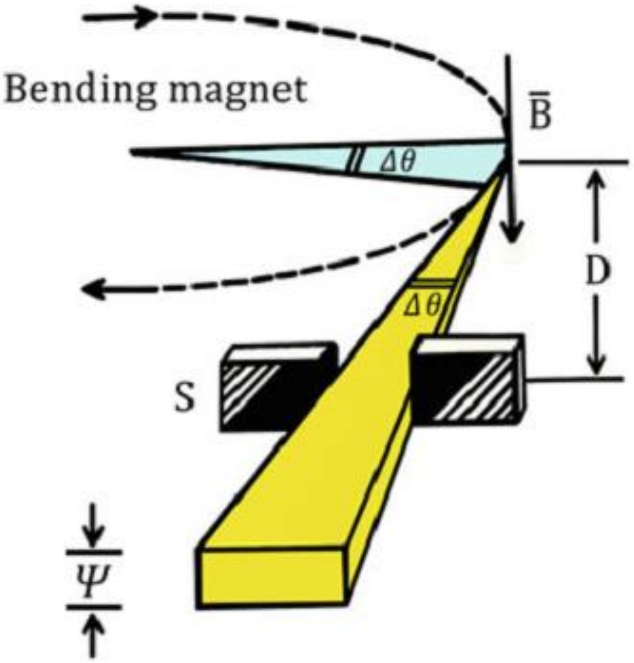

Figure 2.3. Synchrotron radiation emitted by a relativistic electron travelling along a curved trajectory. The magnetic field is perpendicular to the electron orbit plane, ψ is the natural opening angle in the vertical plane while $\Delta\theta$ is horizontal angular distribution, much wider than ψ. (Image from Mobilio, Boscherini, and Meneghini 2015).

It means that all the radiation, emitted along an orbital arc $\Delta\theta$, is collected and summed incoherently. The natural narrow collimation ψ is preserved only in the vertical direction, the direction perpendicular to the plane of the orbit, as also shown in Figure 2.3.

The electrons, at a quasi-stationary speed, cyclically undergo the effects of other magnetic fields produced by wigglers, undulators and sequences of dipole magnets of alternating polarities (Figure 2.2). In these magnetic combs, the electrons are forced to oscillate around a straight-line trajectory. Therefore, they emit energy as *radiation cone* and then superimpose. To better understand this phenomenon a short explanation is given (Figure 2.4).

For a classical electron moving at a speed v, much lower than the speed of light c, ($v << c$), the emitted pattern is similar to the one of an oscillating dipole with its maximum of intensity in the direction perpendicular to the acceleration and not depending on the electron speed.

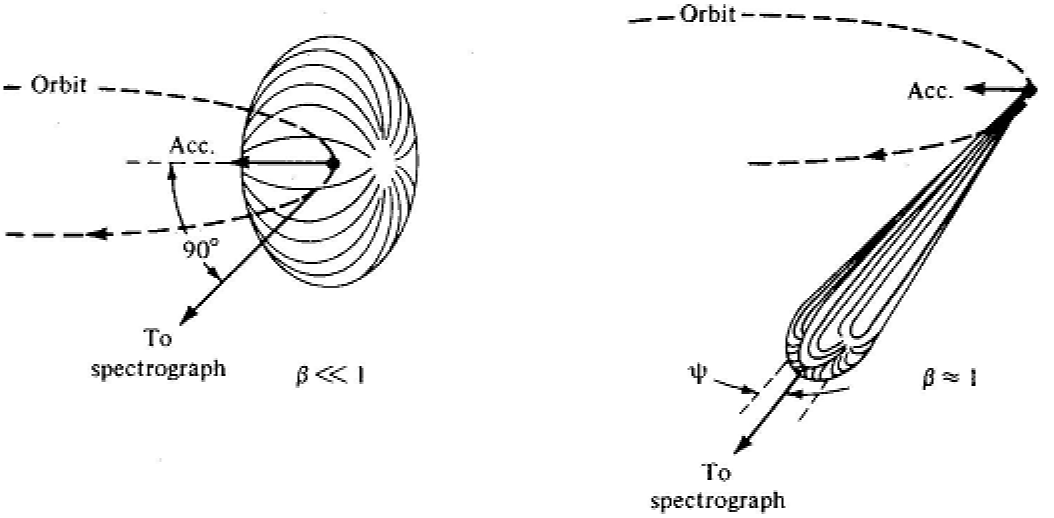

Figure 2.4. The dipole pattern achieved for slow particles (left) ($\beta = v/c << 1$) is distorted into a narrow cone when $\beta \approx 1$(right). (Figure taken from Mobilio and Balerna 2003).

When the speed of the electrons increases to relativistic values ($v \approx c$ and $\beta \approx 1$) the radiation pattern is compressed into a narrow cone in the direction of motion, maintaining an emission tangential to the particle orbit with an emission angle, called vertical half-opening angle, ψ, given by: $\psi \approx mc^2/E \approx \gamma^{-1}$. These phenomena originate the different spectral emission distribution. In the case of a storage ring of energy E = 1 GeV and with an electron rest mass mc^2 = 0.511 MeV, it follows that $\psi \approx 0.5$ mrad. This means that synchrotron radiation is highly collimated, providing, in this way, highest fluxes on very small areas also at distances of tenths of metres from the storage ring.

There has been a long debate in literature on the use of the terms *"brilliance"* and "*brightness"* addressed to the measure of the number of photons emitted per second per bandwidth per unit solid angle and unit area of the source (Mills et al. 2005). From the conclusion of D.M. Mills et Al in "Report of the Working Group on Synchrotron Radiation Nomenclature - Brightness, Spectral brightness or Brilliance?", the term *"spectral brightness"* (SB) will be used in this thesis to define the quantity described before.

2.1.1.1 The European Synchrotron Radiation Facility (ESRF)

The ESRF is a third-generation synchrotron able to produce high-SB X-rays, called "hard" X-rays, which have wavelengths of 0.10 to 0.01 nm or energy in the range 10 to 120 keV. The SB is the most important advantage of synchrotron radiation. Then, a synchrotron source, like the ESRF, has a SB that is more than a billion times higher than a laboratory source. It is defined as:

$$\mathrm{SB} = \frac{\mathrm{Photons}}{\mathrm{second} \cdot \mathrm{mrad}^2 \cdot (\mathrm{mm}^2 \mathrm{source\ area}) \cdot (0.1\%\ \mathrm{bandwidth})} \tag{2.1}$$

ESRF is one of three most powerful synchrotrons in the world with the Advanced Photon Source in the United States and the Spring 8 in Japan. ESRF was founded in 1988 in Grenoble (France) and, nowadays, the ESRF is the result of an international consortium of 21 countries focussing their efforts in the development of cutting-edge science with photons.

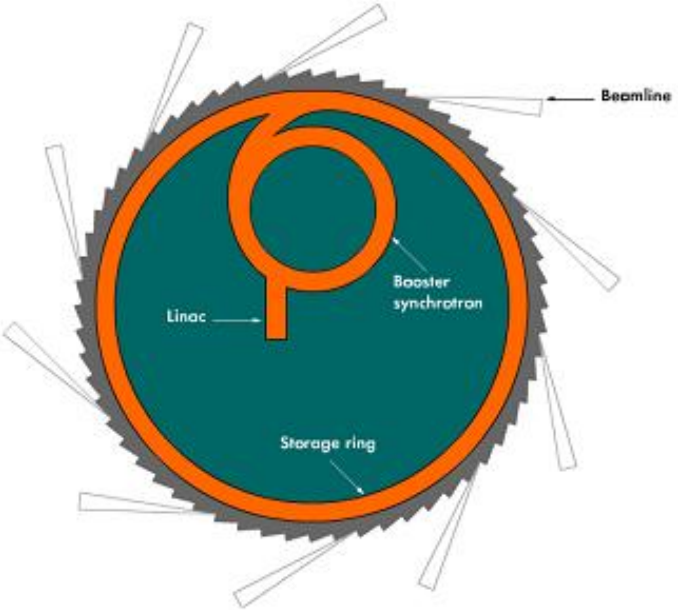

Figure 2.5. Scheme of the ESRF. Electrons are injected and accelerated in the Linac, re-accelerated in the booster, to circulate at a constant speed in the storage ring. (Source: www.esrf.eu.).

At the ESRF (Figure 2.5), the synchrotron radiation X-ray beam is produced by a LINAC that accelerates electrons up to 200 MeV; a booster with a circumference of 300 m and a repetition rate of 10 Hz; and a 6.04 GeV electron storage ring (844.4 m of perimeter). The beam is guided by 64 bending magnets and focused by 320 quadrupoles and 224 sextupoles (www.esrf.eu). The 42 beamlines available at the ESRF are used for a wide variety of scientific topics as mentioned at the beginning of this paragraph. In particular, ID17 is one of the few synchrotron beamlines in the world dedicated to biomedical research.

The radiation emitted by the bending magnets (BM) or by the insertion device (ID) is transferred to the experimental stations inside in-vacuum beamlines. Each beamline is specialized in a particular research area, and hosts three kind of hutches:

- optical hutch(es), closest to the ring, where all the optical instruments necessary to model the beam according to the requirements of different experiments are located (monochromators, slits, attenuators);

- experimental hutch(es), comprising different types of detectors for measuring and recording the information generated by the radiation-matter interaction;

- control room(s), used by scientists to control the experiment remotely and acquire data.

2.1.1.2 The ID17 beamline at the ESRF

At the ESRF, ID17 beamline is dedicated to bio-medical applications. In particular, preclinical and clinical studies in radiation therapy and X-ray imaging are carried out. Several techniques are applied at this beamline: for example, Phase contrast imaging, bronchography, brain perfusion studies, preclinical Microbeam Radiation Therapy (MRT) and Stereotactic Synchrotron Radiation Therapy (SSRT).

ID17 is one of the three long ESRF beamlines. It is divided into three sections: the first includes one optical and one experimental hutch and is located within the large ESRF experimental hall, at a distance ranging from 25 to 50 m from the source hutches. The beam is then transported to the satellite building (third section) in a ~100 m long in-vacuum tube (second section). In the satellite building are located the second optics hutch and the second experimental hutch, where only monochromatic beam is allowed. The aim of such high distance from the source is to achieve a sufficiently large beam for imaging purposes and to obtain a high degree of spatial coherence (Van cittert 1934). The beam in the second experimental hutch can reach ∼250x10 mm^2 (horizontal x vertical) thanks to the beam divergence and the long distance from the source. However, the horizontal size of the beam is reduced in practice due to optical constrains (*i.e.* monochromators and other optics). As a result, a beam of about 150x10 mm^2 is available in the second experimental hutch. The insertion device installed for X-ray radiation emission is a multi-pole wiggler magnet (*w150*) with an adjustable gap (21 poles, period of 15 cm and maximum magnetic field of 1.6 T at the minimum allowed gap-24.8 mm). This corresponds to a maximum critical energy of 38.1 keV (unfiltered radiation). A second wiggler (*w125*) characterized by 22 poles, with 12.5 cm of period and a maximum magnetic field of 1.8 T at a gap of 11 mm is installed with the purpose to increase the photon flux when needed. All the optical components were designed and manufactured to reduce and avoid, when possible, the spurious signals, loss of coherence on the X-ray path and/or to maintain the beam inhomogeneity at the sample position.

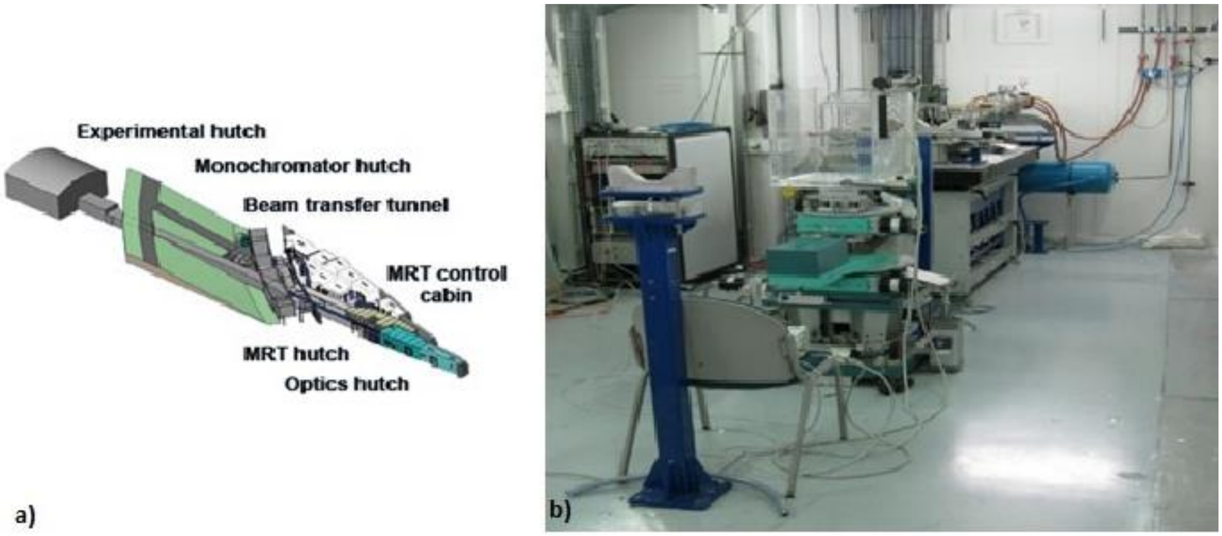

Figure 2.6. **(a)** The internal section of the ID17 beamline. **(b)** A picture of the MRT hutch with the sample positioning system (image from www.esrf.eu and from Romanelli et al. 2011).

As shown in the scheme (Figure 2.6), the beamline starts at the front-end, which is the interface between the beamline and the storage ring. The front-end contains a shutter, used to enable or disable the beam's passage through the beamline, and various other elements, such as safety devices for vacuum and radioprotection. The beam exiting the wiggler travels inside a long stainless steel pipe under vacuum. Along the beamline, several valves and Be windows (300–500 μm-thick) isolate each one the different vacuum sections. Along the way, different detectors such as diodes or ionization chambers (IC) are used to monitor the beam.

The MRT hutch. Here the white beam is directed towards in the first experimental hutch, which is located after the first optical hutch, where all optical elements directly hit by the white beam, are water cooled to dissipate the heat load induced by the radiation. In its path, the beam encounters several beam modifiers. The low energy part of the spectrum (< 30 keV), which is not used by the scientific programmes, is eliminated progressively through a series of filters: 0.5 mm beryllium (Be), 0.5 mm carbon (C), 1.25 mm aluminium (Al), and 1 mm copper (Cu).

The resulting spectrum ranges approximately from 50 to 350 keV, with a maximum at 83 keV. As shown in Figure 2.7, primary slits allow a first spatial selection of the beam after filtration. These primary slits are in vacuum and located before the filters, and consist of four independent, remotely controlled blades: a couple for defining the beam height, and a second one for determining the overall horizontal beam width. The 'fast shutter' and the photon absorber are key elements since they are responsible for stopping the radiation in within 30 ms, after the irradiation process has been completed. The fast shutter consists of two

15-mm-thick tungsten carbide blades coupled to two actuator magnets. During the closing time of the 'fast shutter', the beam is absorbed by the photon absorber (cooled 40-mm-thick Cu block), which has a longer reaction time (about 1 s). More information on this system can be found in the work by Renier et al. (Renier et al. 2002). Therefore, the SR beam passes through a system composed by slits (vertical and horizontal) that defined the total width of the synchrotron beam used downstream.

First experimental hutch. In the experimental hutch horizontal tungsten slits limit the beam width to 38 mm and three adjustable positions offer a choice of different beam heights (50, 100, and 500 µm). Vertical tungsten slits, mounted on a translation stage and positioned just upstream the collimator, are aligned with the center of the beam to allow horizontal scanning of the individual microbeams with 1 µm steps. The beam passes from ultrahigh vacuum into air through a beryllium window, which separates the vacuum beamline from the external atmosphere; beryllium has the advantage of being very transparent to X-rays for energies above 10 keV. After the window, the beam goes through an ionization chamber (IC) before impinging on the multislit collimator, internally called EMSC (ESRF-made multislit collimator) to distinguish it from the previous, less advanced versions. The collimator allows for the synchrotron radiation fractioning into microbeams. The used spectrum contains photons in the interval from 30 up to 600 keV with a mean energy of 107 keV.

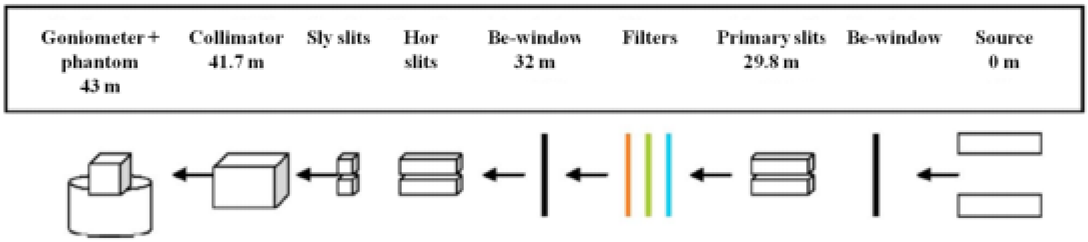

Figure 2.7. Sketch of the MRT experimental setup with the distance of the elements from the X-ray source. (Extracted from Bräuer-Krisch et al. 2009).

The EMSC is assembled with two identical ~8 mm thick blocks made of tungsten carbide (86.8%, in weight) and Cu (12.0%) movable one in front of the other to select the desired microbeam width; each block is composed by 125, three mm high, and 100 µm wide equidistant slits to fractionate the oncoming seamless X-ray beam, regularly repeated with a uniform pitch of 400 µm centre-to-centre (c-t-c) (Figure 2.7) (Bräuer-Krisch et al. 2009). Before irradiation, and with the animal sample already sitting on the 3-axis Kappa-type high precision positioning system goniometer (Huber, Germany), the target is identified by acquiring low dose radiographs following an imaging protocol (Serduc et al. 2008) . In this phase, the collimator is temporarily removed. Images are acquired by vertically scanning the goniometer step by step and simultaneously acquiring the X-ray images with a FReLoN camera (A. Bravin et al. 2003). Thanks to a graphical user interface system (GUI) the target area of the treatment can be identified according with the skull structures.

Second optic hutch. A second set of slits, absorbers, beam monitors and monochromators is installed then in the second optics hutch. Three systems of monochromators are present:

1) The multilayer monochromator (ML) and the Bragg-Bragg monochromator. The ML monochromator originally included two sets of 2 mirrors. The first set (20 Å d-spacing) still operates at energies ranging from 20 to 60 keV, delivering a beam of broader bandpass than the Laue-Laue CT monochromator, but with a reduced (~1 mm) beam height. The second set of mirrors (40 Å d-spacing) has been replaced in 2015 by a Si(111) Bragg-Bragg monochromator system allowing to select energies in the range 30-80 keV. This change has been made to provide the beamline with flat crystals giving a minimally distorted plane wave to be used in phase contrast imaging applications requiring a highly homogeneous background.
2) The Computed Tomography monochromator. It uses two cylindrically bent Si crystals in the Laue geometry, determining a 40 mm offset between the white and the monochromatic beams. It operates in the energy range 25 to ~200 keV.
3) The single Laue monochromator. It delivers two beams at energies ranging from 17 to100 keV and is used for dual energy imaging. A single Si(111) crystal is bent to focus vertically the beam on the target. A tungsten beam splitter may be used to block the central part of the beam and hence create two monochromatic beams at energies slightly different and typically separated by ~300 eV. These two beams can be made crossing at the sample position and then recorded either by the 2-line germanium detector, or by a scintillator plus visible light optics connected with a detector (FReLoN camera or PCO.Edge).

The monochromators are immediately followed by an optics bench supporting a Plexiglas attenuator set to adjust the radiation intensity, tungsten slits in air to clean up the beam before entering the second experimental hutch, and X-ray beam monitors to tune the monochromator. The hutch contains also a fast shutter for allowing rapid image expositions.

Second experimental hutch. At the end of the beamline is located the second experimental hutch, which contains different experimental setups. Experiments on cells, tissues, live samples are performed, as well as the SSRT clinical trials. A second control room is located close to this hutch. In the following session (Paragraph 2.5.1), the experimental set-up implemented for the first microCT Imaging test is described.

The main imaging experimental setups present are the Analyzer Based Imaging, the 2 stages for micro-tomographic imaging and the recently commissioned high-resolution imaging setup (using optics from 8 to 3.1 µm).

With the aim of investigating the morphology of cortical vascular network through X-ray Phase Contrast Imaging technique, first tests have been carried out at ID17 in order to optimize the experimental settings, sample preparation procedures and data treatment tools for the present microstructural study of CP disease.

2.1.1.3 The ID16A beamline at the ESRF

ID16A is a long beamline of ESRF with the end station situated at 184 m from the source for coherent imaging. As illustrated in Figure 2.8, two beamlines are sharing the satellite building: ID16B, dedicated to nano-analysis and ID16A, focused on nano-imaging. ID16A provides a high-brightness beam focused down to nanometre size, allowing quantitative 3D characterization of the morphology and the elemental composition of specimens in their native state by combining coherent imaging techniques and X-ray fluorescence microscopy. The beamline covers different application fields such as biomedicine, materials science, nanotechnology, environmental science and planetary science. Offering two discrete energies, 17 keV and 33.6 keV with beam focused down to 20 – 30 nm, the instrument is optimized for high stability, high resolution measurements. The geometrical magnification of the divergent beam gives access to pixel sizes in the range 10 nm to 130 nm, with fields of view up to 260 µm. Five detectors are available: two six elements silicon drift diode fluorescence detectors, two FreLoN cameras for high-resolution imaging and a MAXIPIX detector for far-field ptychography.

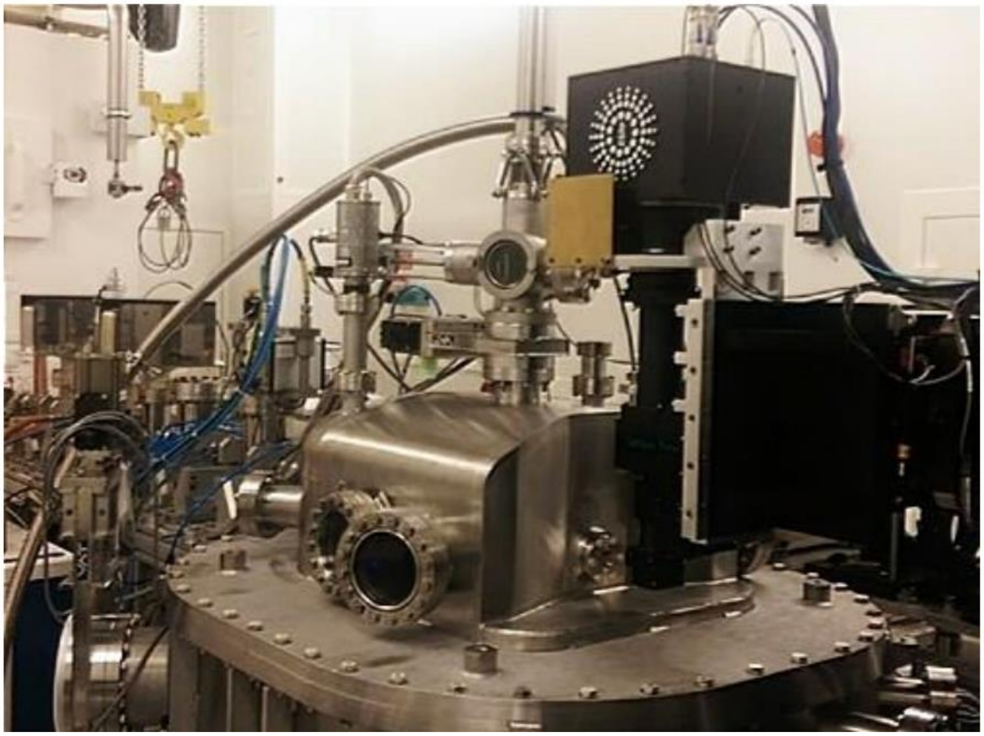

Figure 2.8. ID16A end station (image from Langer, 2015).

2.1.1.4 The TOMCAT beamline at the Swiss Light Source

In one of the experimental session, tomographic datasets were acquired at the TOMCAT beamline at the Swiss Light Source (SLS) of PSI, Villigen, Switzerland.

The TOMCAT receives photons from a 2.9 T superbending magnet with a critical energy of 11.6 keV, which provides a photon flux between 8 and 45 keV (Figure 2.9). A double crystal multilayer monochromator (DCMM) is used to select X-rays with defined X-ray photon energy. At the TOMCAT, this energy ranges between 12 and 20 keV. The small source size (Σ x=53 μm, Σ y=16 μm), coupled with optical components, delivers a transversally highly coherent beam (Marone et al. 2010). The TOMCAT X-ray detector consists of a Ce-doped Y3Al5O12 single crystal scintillator able to convert the X-rays into visible light. This light then passes through an optical microscope, reflected in a mirror is finally projected on a 2048 × 2048 pixels CCD camera with a 14 bit dynamic range. The specific microscope configuration is optimized for each experiment. Additional information can be found on the paper of F. Marone et al, “X-ray Tomographic Microscopy at TOMCAT” (2008) (Marone et al. 2008).

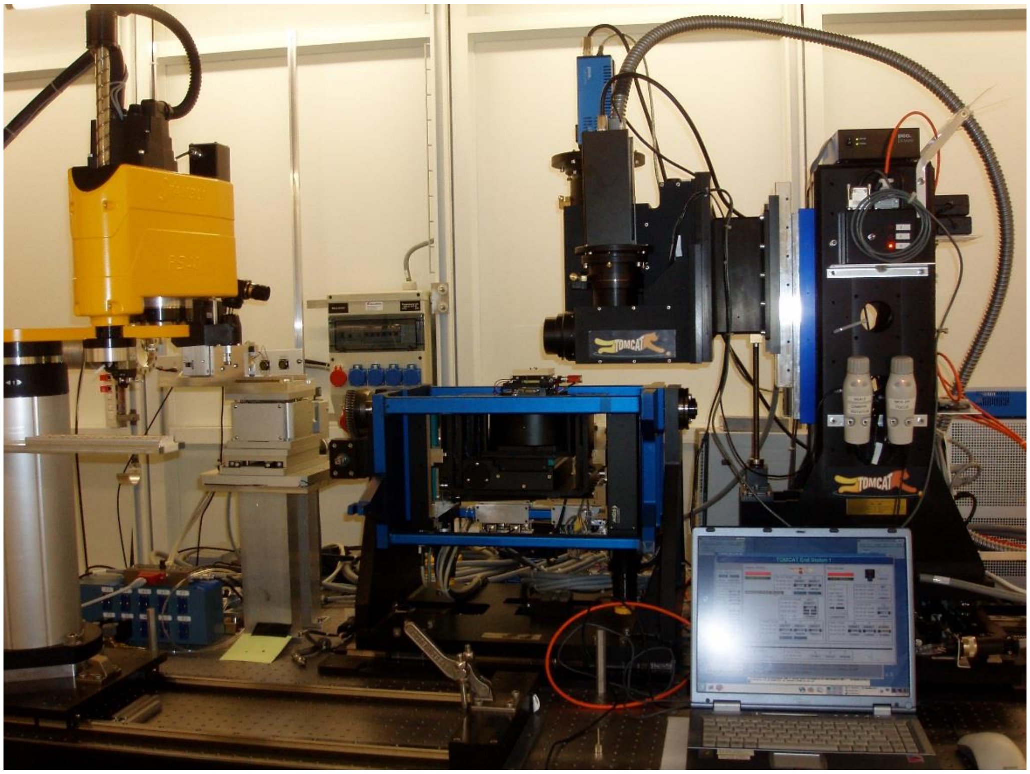

Figure 2.9. The TOMCAT beamline hutch (Image from www.psi.ch).

2.2 Techniques: Computed Tomography

2.2.1 Principles of X-ray CT

X-ray computed tomography (CT), is a non-destructive technique to visualize three-dimensionally the inner structure of objects by combining the information of several projections acquired at different angles. The origin of the word "tomography" is from the Greek word "tomos" meaning "slice" or "section" and "graphein" meaning "to draw". A CT imaging system produces cross-sectional images or "slices" of the analysed objects. X-rays with a wavelength longer than 1 Å (energies smaller than 12.4 keV) are typically indicated as soft X-rays, while X-rays with a wavelength shorter than 1 Å are known as hard X-rays. Soft X-rays cannot penetrate as deeply into materials as hard X-rays do, thus they are less suitable for investigating thick samples. X-ray tomography applications range from life sciences to materials science, including environmental and earth sciences.

Tomographic imaging consists in directing X-rays to object from multiple orientations and measuring the intensity of the emerging X-rays along a series of linear paths. The number of X-rays entering the sample is decreased going through the sample, due to photon-matter interactions, mainly in the form of scattering and photoelectric absorption; this behaviour is represented by the Beer's Law, which describes the macroscopic attenuations of the X-ray beam through a homogeneous material (Cnudde and Boone 2013; Beer 1852). In case of a monochromatic X-ray beam, the law states that:

$$\mathrm{I} = \mathrm{I}_0 \exp(-\mu \mathrm{x}) \tag{2.2}$$

with I_0 the beam intensity measured in the absence of the object, μ the linear attenuation coefficient for the material being illuminated and x the thickness of sample along the X-ray path. Considering a heterogeneous material made of a finite, discrete number of components, the Beer's law becomes:

$$\mathrm{I} = \mathrm{I}_0 \exp[\sum_{\mathrm{i}} (-\mu_{\mathrm{i}} \mathrm{x}_{\mathrm{i}})] \tag{2.3}$$

where the sum is performed over the total number of components.

However, the attenuation coefficient is a function of the incoming X-ray energy (E), which in general is polychromatic. Thus, the equation can be rewritten as an integral over the range of the X-ray spectrum:

$$\mathrm{I} = \int \mathrm{I}_0 (\mathrm{E}) \exp [\sum_{\mathrm{i}} (-\mu_{\mathrm{i}} \mathrm{x}_{\mathrm{i}})] \, \mathrm{dE} \tag{2.4}$$

The main physical processes responsible for the macroscopic attenuation of an X-ray beam through a material within the typical hard-X-ray energy range used in CT imaging are the photoelectric absorption, the Compton scattering and elastic (Rayleigh) scattering. The photoelectric effect occurs when the incoming X-ray energy is transferred to an inner electron causing its ejection. At higher photon energies, Compton and Rayleigh scattering take place. The elastic scattering over the electron shell makes the photons deviate without energy loss. In Compton scattering instead the incident photon is deflected from its original path by an interaction with a quasi-free electron of the traversed material. The photon partially loses its energy, which is transferred to the scattered electron made then free, and thus its wavelength increases. In X-ray tomographic imaging of soft tissues, such as brain tissue, the typically used energy range is between 10 and 35 keV.

2.2.2 X-ray coherence

Coherence represents a key property for phase contrast imaging. Two types of coherence can be distinguished: (Figure 2.10)

-*temporal coherence* ξ_{T}, also known as longitudinal coherence length:

$$\xi_{\mathrm{T}} = \lambda \frac{\mathrm{E}}{\Delta \mathrm{E}} \tag{2.5}$$

where $\frac{\Delta E}{E}$ denotes the energy bandwidth and λ the wavelength. The temporal coherence ξ_T is thus related to the monochromaticity of the beam: the more monochromatic the beam is, the more temporally coherent the beam it is. At the ESRF, the energy band pass $\frac{\Delta E}{E}$ ranges between 10^{-4} and 10^{-2}, so the temporal coherence length corresponding to the energy used for imaging of biological samples (around 30 keV) varies between 1 and 10^2 µm.

-*Spatial coherence* ξ_S, also known as transverse coherence length:

$$\xi_S = \lambda \frac{\alpha}{\Delta\alpha} \tag{2.6}$$

where $\frac{\Delta\alpha}{\alpha}$ denotes the angular acceptance and λ the wavelength. The spatial coherence ξ_S depends on the angle from which the source is viewed by the sample; therefore it depends on the source size and the distance from the source. The smaller the spot is, and/or the farthest from a source the sample is placed, the more spatially coherent is the beam. As an example, for a small spot size (a few micrometres) and long beamlines (100 m to 200 m), the spatial coherence length is about 100 µm.

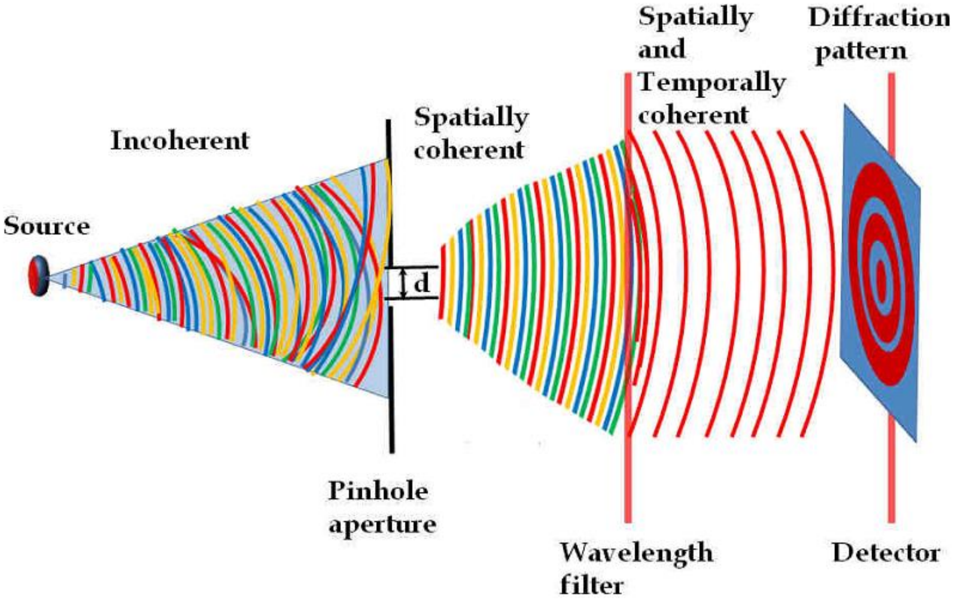

Figure 2.10. Illustration of temporal and spatial coherence. (Image taken from Davidoiu et al. 2013).

Most phase contrast imaging modalities require a temporally coherent (i.e. monochromatic) and spatially coherent (i.e. quasi parallel) X-ray beam, with a high flux (Peyrin et al. 1997), to benefit from the high sensitivity offered by the phase-shift. The SR delivered by the ESRF fulfils these requirements.

2.2.3 The physical bases of Phase Contrast Imaging (PCI)

Unlike conventional absorption-based imaging, which is only sensitive to the attenuation of the incoming X-ray beam, PCI also relies on the phase shift of X-rays occurring when they pass through a medium. This modality offers a better sensitivity than conventional radiology, since for hard X rays (10-100 keV) and low-Z materials (such as soft tissues), refraction is at least two or three orders of magnitude higher than absorption at typical imaging energies (Momose et al. 1996).

When X-rays pass through an object, because of the refraction, not only their amplitude but also their phase is altered. The propagation of X-rays through the matter is generally described with reference to the complex refractive index n, which can be expressed as (Jackson 1975):

$$n = 1\text{-}\delta + i\beta \tag{2.7}$$

where δ represents the refractive index decrement, which is related to the phase shifts of the electromagnetic wave in the matter and, therefore, its deviation from the incident direction due to the scattering with electrons of the medium (Azároff 1968). β is the absorption term which is linked to the absorption of X-rays into the matter, mainly due to the photoelectric effect for low X-ray energies (< 20 keV for oxygen, lower energies in case of lighter elements) and also Compton scattering in the other cases.

Under the influence of the electromagnetic field of the incident radiation, the polarization of the medium, for hard X-rays and far from the absorption edges, is well described by the free-electrons model where the electric susceptibility χ is proportional to the electron density ρ_E. The terms δ and β are related to the real and imaginary part of χ, respectively, by the following expressions (Zachariasen 1945):

$$\delta = \text{-}\frac{1}{2}\chi_{0r} \tag{2.8}$$

$$\beta = \frac{1}{2}\chi_{0i} \tag{2.9}$$

Such relations can be otherwise written as (Jackson 1975):

$$\delta = \frac{r_e \lambda^2 \rho_e}{2\pi} \tag{2.10}$$

$$\beta = \frac{r_e \lambda^3 \rho_e}{4\pi^2 c} \sum_j \frac{f_j \gamma_j}{Z} \tag{2.11}$$

where r_e represents the electron radius, λ the X-rays wavelength, f_j is the number of electrons per atom with damping constant γ_j, and Z is the atomic number that gives the total number of electrons per atom; the sum is over all the j electrons of the atom.

The quantity ρ_e is linked to the macroscopic mass density of the medium ρ by the relation $\rho_e = Z/V = Z\rho N_A/A$ where V is the volume of reference, N_A the Avogadro's number and A the atomic weight.

The refractive index, mainly influenced by Thomson scattering, can be also expressed as:

$$\delta = \frac{r_e \lambda^2}{2\pi V} \sum_j (Z + f'_j) \tag{2.12}$$

with f'_j the real part of the wavelength-dependent dispersion correction of the atomic scattering factor.

Similarly, the absorption index β can be also written in terms of the imaginary part of the wavelength-dependent dispersion correction, f''_j, as:

$$\beta = \frac{r_e \lambda^2}{2\pi V} \sum_j f''_j \tag{2.13}$$

For energies far from the absorption edges, f'_j is approximately zero, whereas f''_j dominated by the absorption process, behaves with the energy as E^{-m}, with $m \in [3,4]$.

β is related to the linear absorption coefficient μ, through the relation (Raven, Snigirev, and Snigireva 1996):

$$\mu = \frac{2\pi\beta}{\lambda} \tag{2.14}$$

The quantities δ and β are functions of the spatial coordinates (x, y, z) because of local changes in the matter. In the energy range normally used in radiology the δ term is much larger than β and differs at least by three orders of magnitude from β. This large difference between δ and β is the reason for the advantages of PCI with respect to absorption-based radiology; the phase contribution being an additional and important source of contrast when the absorption counterpart is very weak or undetectable. The energy dependence of the two terms δ and β, for energies far from the absorption edges and for low Z materials, is approximately given by $\delta \sim E^{-2}$ and $\beta \sim E^{-4}$.

Since the X-ray phase φ is related to δ by $\varphi = -2\pi\delta t/\lambda$, where t is the thickness traversed by X-rays, the energy dependence of the phase and of the linear attenuation coefficient may be expressed as $\varphi \sim E^{-1}$ and $\mu \sim E^{-3}$. Therefore, the sensitivity ratio between absorption and phase-contrast imaging is given by the ratio of β to δ. The calculated sensitivity ratios (δ/β) to atomic number for various X-ray energies are plotted in Figure 2.11. The results show that the ratio of light elements, such as hydrogen, oxygen, nitrogen, and carbon, runs to about 1000 times.

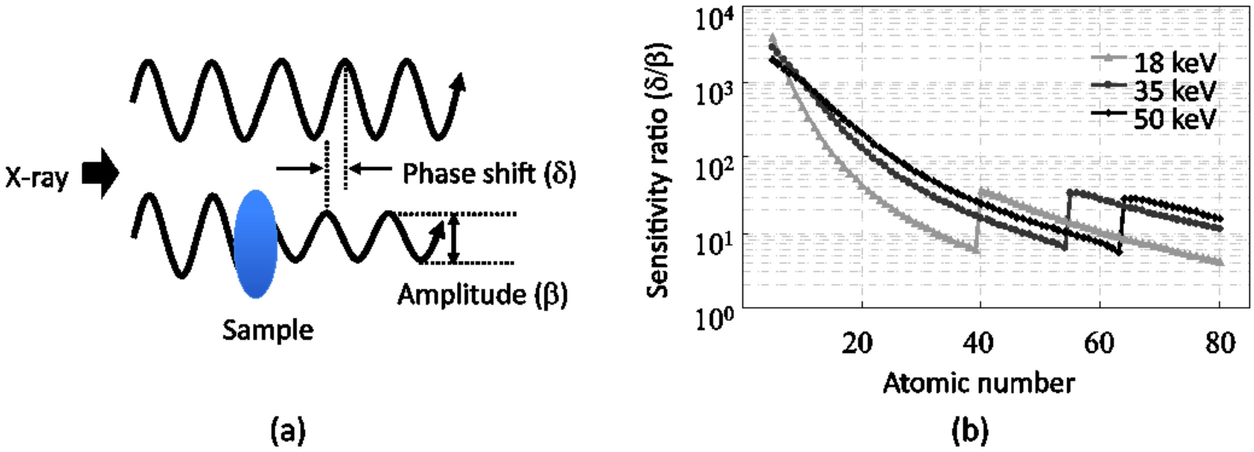

Figure 2.11 (a) Interaction between X-ray and sample. When X-ray passes through sample, its amplitude is decreased and phase is shifted. **(b)** Sensitivity ratios between phase- and absorption-contrast imaging. Ratios increase to about 1000 for light elements. (Figure adopted from Yoneyama et al 2011).

Thus, the sensitivity of phase-contrast X-ray imaging for light elements is about 1000 times higher than that of absorption-contrast X-ray imaging in principle.

2.2.4 The Propagation-Based Phase Contrast Imaging (PBPCI) technique

Since the emergence of phase contrast, several techniques have been developed, like the propagation-based (free-space propagation) imaging, the analyser-based imaging, the interferometric-based techniques (i.e. crystal and grating interferometry) and the non-interferometric (e.g. the edge-illumination) imaging methods (Alberto Bravin, Coan, and Suortti 2013). They enable to measure the phase shift of the wave front, induced by the sample, or a signal related to the phase-shift (e.g. its gradient or Laplacian). The propagation-based mode technique has been adopted in this kind of analysis since its simple set-up, where no optical elements along the beam are necessary, the direct full flux delivered by the insertion device can be exploited, and the limitations in spatial resolution are only related to the detector characteristics.

The propagation-based imaging (PBI) is experimentally the simplest way to visualize the phase-contrast (Figure 2.12). It consists in letting a spatially coherent beam propagate after passing through a sample. If the detector is close to the sample "at contact plane", an absorption image of the object is recorded. Phase contrast signal can be obtained by moving the detector downstream.

When a coherent wave-front traverse the sample and the distorted wave-front propagates sufficiently far, an interference occur between the part of the wave that has traversed the sample (and that is therefore phase shifted) and the part which passes outside it; this combination of waves with different phases give rise to an interference signal and to a characteristic pattern (*Fresnel fringes*) that is then recorded by a detector placed at a convenient distance (Snigirev et al. 1995; Peter Cloetens et al. 1996). Thanks to the Fresnel diffraction, the phase shifts are therefore transformed in detectable intensity variations (Born and Wolf 1994).

This technique can be easily extended to tomographic imaging, by acquiring projections at several angular positions of the object, using a high-resolution detector (Fast REadout LOw Noise [FReLoN] camera (Labiche et al. 2007) to image the interference fringes at a sufficient distance from the sample. The recorded measurements are directly related to the Laplacian of the phase, ∇^2, in the near-field regime approximation, as shown below.

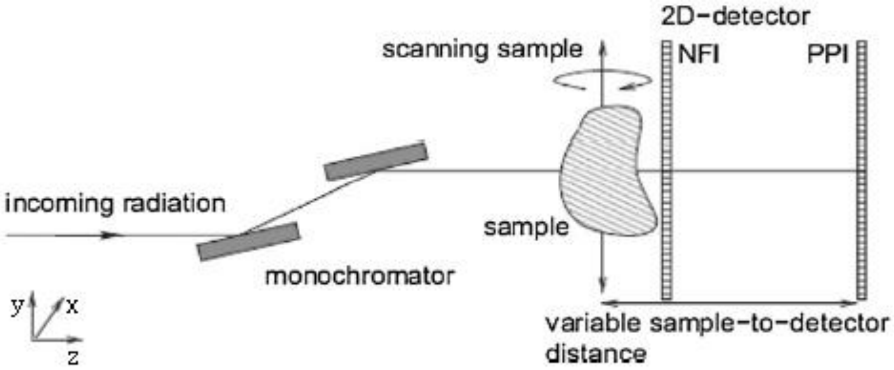

Figure 2.12. The experimental set-up of the propagation-based imaging technique. A, transversally coherent X-ray fan beam traverses the sample, and is recorded by a 2D detector positioned at a certain distance (Near Field Imaging, NFI). Changing the propagation distance (Phase Propagation Imaging, PPI), generates different signals on the detector, allowing investigating different spatial frequencies. The choice of the distance is related to the kind of study of interest. (Image from Keyriläinen, Fernández, and Suortti 2002).

At each angle θ, the interaction between the object and the X-ray wave can be described as a transmittance function T_θ, involving the projections of the attenuation and the phase shift at the angle θ, respectively B_θ

and φ_θ. The Transport of Intensity Equation (TIE) (Teague 1982) was implemented to describe both the intensity and the phase of a monochromatic beam propagating along an axis z, recorded by the detector.

This technique has been refined by Cloetens et al (Cloetens et al. 1999) to a multiple distances acquisition. This particular method is called holotomography, and consists in acquiring projections for a complete rotation of the sample, at different sample to detector distances. Since this method will be applied for nanoCT imaging, it will be described in details in the following section.

The classical phase contrast image reconstruction process consists in performing phase retrieval at each projection angle, followed by tomographic reconstruction. The existing phase retrieval algorithms of propagation-based phase contrast imaging will be reported in the following paragraphs.

2.2.5 Image formation and reconstruction

A slice of an object can be reconstructed from the acquired radiographs if the number of projections is sufficiently large, i.e. if the projections constitute a complete basis of images (Herman 2009). This process is called image reconstruction.

If $f(x, y)$ represents the density of a two-dimensional object to be measured and I_0 the applied X-ray intensity, the intensity coming out and attenuated by the object along the line L can be written following the Beer's law:

$$I_{out} = I_0 e^{-\int_L f(x,y)dl} \qquad (2.15)$$

By taking the logarithm of the relative attenuation, the line integral value of the object function becomes:

$$\int_L f(x, y)\, dl = -\ln \frac{I_{out}}{I_0} \qquad (2.16)$$

Hence, X-ray measurements may be considered as line-integration values after the simple manipulation in equation (2.15). Primary measurements in the form of line-integrals are the basis for all CT reconstruction techniques. We can define the line integral as:

$$P_\theta(t) = \int_{(\theta,t)line} f(x, y) ds \qquad (2.17)$$

Using a delta function, this can be rewritten as:

$$P_\theta(t) = \int_{-\infty}^{+\infty} \int_{-\infty}^{+\infty} f(x, y)\delta(x \cos\theta + y \sin\theta - t) dx\, dy \qquad (2.18)$$

The function $P_\theta(t)$ is known as the *Radon transform* of the function $f(x, y)$.

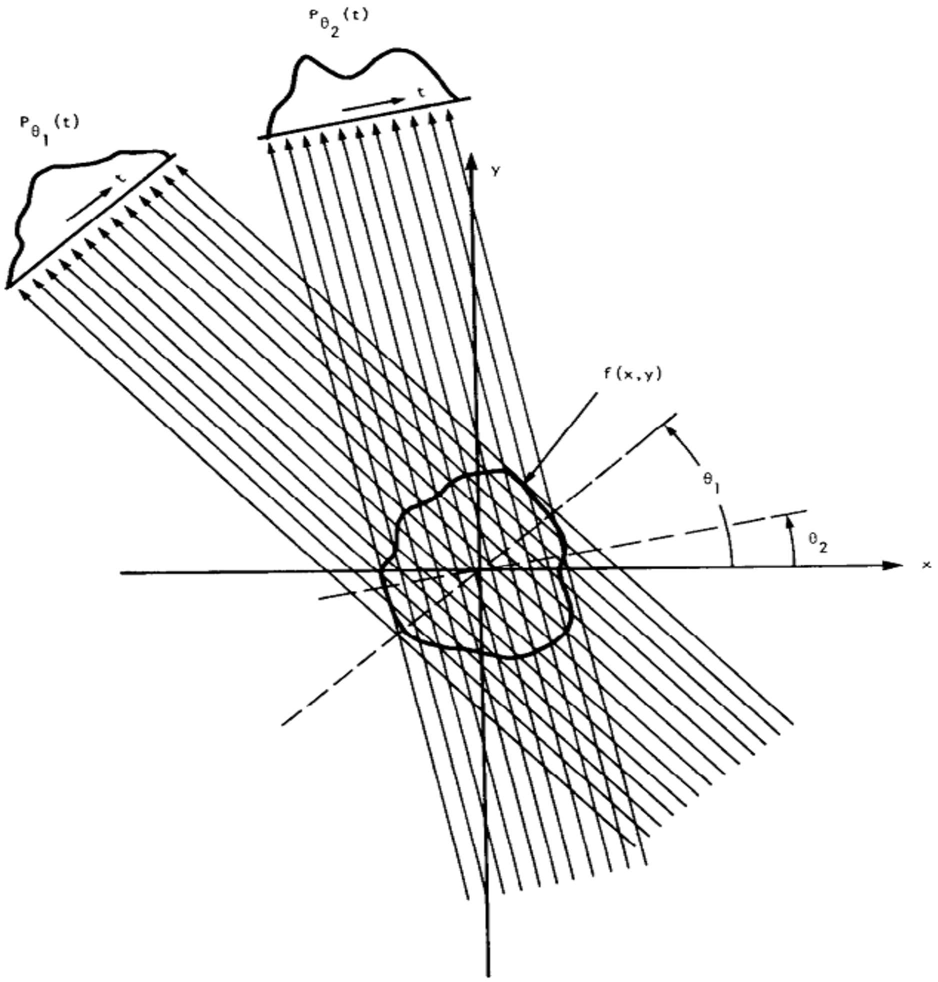

Figure 2.13. Parallel projections collected as a set of parallel rays for different angles. (Image from Kak and Slaney 1988).

A projection is the combination of a set of line integrals. The simplest projection is a collection of parallel ray integrals as is given by $P_\theta(t)$ for a constant θ. This is known as a parallel projection and is shown in Figure 2.13. It could be measured by moving an X-ray source and detector along parallel lines on opposite sides of an object.

2.2.6 The Fourier slice theorem

The Fourier Slice Theorem is the basis of all CT reconstruction techniques. It is also known as the *central-slice theorem* or *central-section theorem* or *projection-slice theorem*: by denoting with $p_\theta(t)$ the Radon transform of $f(x, z)$, then the 1D Fourier transform of $p_\theta(t)$, indicated by $P_\theta(\nu)$, is equal to the slice at angle θ through the 2D Fourier transform of $f(x, z)$.

$$P_\theta(\nu) = \int_{-\infty}^{\infty} p_\theta(t) e^{-i2\pi\nu r} dt \tag{2.19}$$

Denoting with $F(u, v)$ the 2D Fourier transform of $f(x, z)$, *i.e.*,

$$F(u, v) = \int_{-\infty}^{\infty} \int_{-\infty}^{\infty} f(x, z) e^{-i2\pi(ux+vz)} dxdz \tag{2.20}$$

The Fourier-slice theorem can then be expressed mathematically as:

$$P_\theta(v) = F(v \cos\theta, u \sin\theta) \tag{2.21}$$

that is equivalent to Figure 2.13. It is possible to notice that with the Fourier-slice theorem the Radon transform describes completely any (Fourier transformable) object $f(x, z)$, because there is a correspondence one to one between the Radon transform and the 2D Fourier transform $F(u, v)$; from $F(u, v)$ the object $f(x, z)$ can be recovered by applying the inverse 2D Fourier transform.

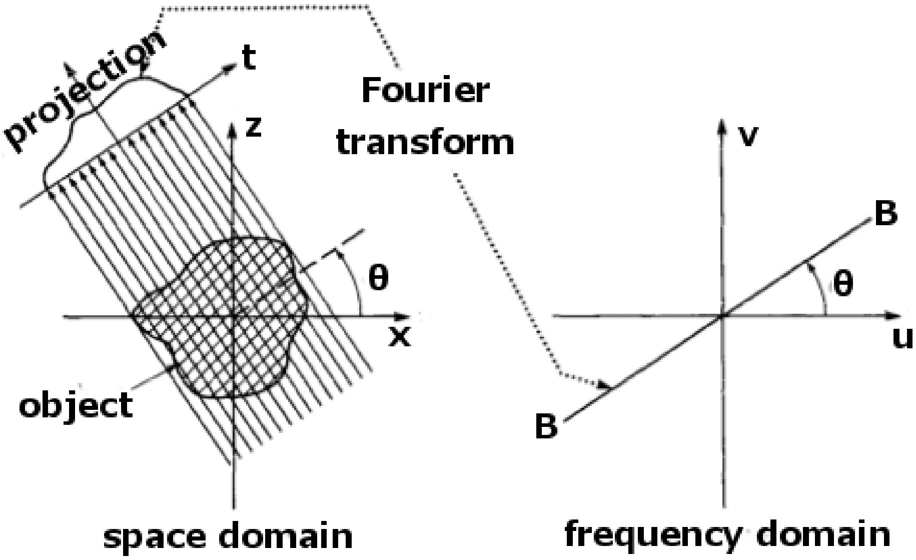

Figure 2.14. Fourier-slices theorem: the Fourier transform of $p_\theta(t)$ gives the values of $F(u, v)$ along the line BB. (Image from Kak and Slaney 1988).

The derivation of the Fourier Slice Theorem can be placed on a more solid foundation by considering the (t, s) coordinate system to be a rotated version of the original (x, y) system as expressed by:

$$\begin{bmatrix} t \\ s \end{bmatrix} = \begin{bmatrix} \cos\theta & \sin\theta \\ -\sin\theta & \cos\theta \end{bmatrix} \begin{bmatrix} x \\ y \end{bmatrix} \tag{2.22}$$

In the (t, s) coordinate system a projection along lines of constant t is written:

$$P_{\theta}(t) = \int_{-\infty}^{+\infty} f(t, s)ds \tag{2.23}$$

and if we consider its Fourier transform:

$$S_{\theta}(w) = \int_{-\infty}^{+\infty} P_{\theta}(t)e^{-j2\pi wt}dt \tag{2.24}$$

Substituting the definition of a projection into the above equation we find:

$$S_{\theta}(w) = \int_{-\infty}^{+\infty} [\ f(t, s)ds\ ]\ e^{-j2\pi wt}dt \tag{2.25}$$

The right-hand side of this equation now represents the two-dimensional Fourier transform at a spatial frequency of $(u = w \cos\theta, v = w \sin\theta)$ or:

$$S_{\theta}(w) = F(w, \theta) = F(w \cos\theta, w \sin\theta) \tag{2.26}$$

This equation indicates that by taking the projections of an object function at angles $\theta_1, \theta_2\ \ldots, \theta_k$ and by Fourier transforming each of these, we can determine the values of $F(u, v)$ on a radial line as shown in the previous Figure 2.14. Knowing $F(u, v)$, the object function $f(x, y)$ can be recovered by using the inverse Fourier transform:

$$f(x, y) = \int_{-\infty}^{\infty} \int_{-\infty}^{\infty} F(u, v)e^{-i2\pi(ux+vz)}dudv \tag{2.27}$$

2.2.7 Filtered back projection algorithm (FPB)

By the Fourier slice theorem, we have seen that the object projection gives the values of the object's two-dimensional Fourier transform along a single line. If the values of the Fourier transform of this projection are inserted into their proper place in the object's two-dimensional Fourier domain, then a simple reconstruction can be formed by assuming the other projections to be zero and finding the two- dimensional inverse Fourier transform. Therefore, the reconstruction so formed is equivalent to the original object's Fourier transform multiplied by the simple filter shown in Figure 2.15 (b). What we really want from a simple reconstruction procedure is the sum of projections of the object filtered by pie-shaped wedges as shown in Figure 2.15 (b). As the name implies, there are two steps to the filtered backprojection algorithm: the filtering part, which can be visualized as a simple weighting of each projection in the frequency domain, and the backprojection part, which is equivalent to finding the elemental reconstructions corresponding to each wedge filter mentioned above.

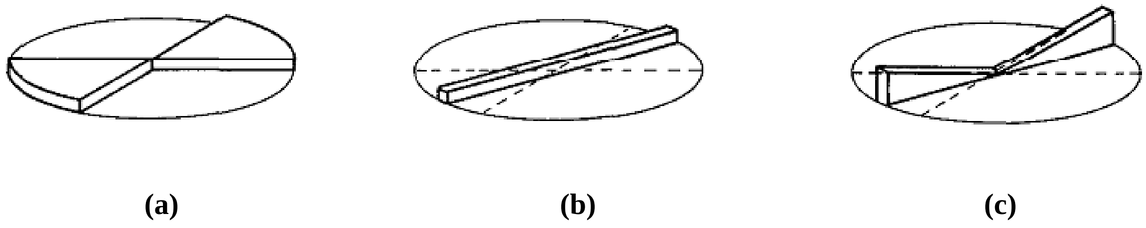

Figure 2.15. Frequency domain data available from one projection. **(a)** is the ideal situation. A reconstruction could be formed by simply summing the reconstruction from each angle until the entire frequency domain is filled. What is actually measured is shown in **(b)**. The filtered backprojection algorithm takes the data in **(b)** and applies a weighting in the frequency domain so that the data in **(c)** are an approximation of those in **(a)**. (Image from Kak and Slaney 1988).

By recalling the formula for the inverse Fourier transform, the object function, $f(x, y)$, can be expressed as:

$$f(x,y) = \int_{-\infty}^{+\infty}\int_{-\infty}^{+\infty} F(u,v)e^{j2\pi(ux+vy)}\,du\,dv \tag{2.28}$$

By exchanging the rectangular coordinate system in the frequency domain, (u, v), for a polar coordinate system, (w, θ), by making the substitutions: $u = w\cos\theta$ and $v = w\sin\theta$, the differentials become $dudv = w\,dwd\theta$. So the inverse Fourier transform can be written as:

$$f(x,y) = \int_{0}^{2\pi}\int_{0}^{+\infty} F(w,\theta)e^{j2\pi w(x\cos\theta+y\sin\theta)}\,w\,dw\,d\theta \tag{2.29}$$

This integral can be split into two by considering 0 from 0^{o} to 180^{o} and then from 180^{o} to 360^{o} and then by using the property:

$$F(w, \theta + 180°) = F(-w, \theta) \tag{2.30}$$

the above expression for $f(x, y)$ may be written as:

$$f(x,y) = \int_{0}^{\pi}\left[\int_{-\infty}^{+\infty} F(w,\theta)|w|e^{j2\pi wt}\,dw\right]d\theta \tag{2.31}$$

If we substitute the Fourier transform of the projection at angle θ, $S_\theta(w)$ for the two-dimensional Fourier transform $F(w, \theta)$ we get:

$$f(x,y) = \int_0^{\pi} \left[\int_{-\infty}^{+\infty} S_\theta(w)|w|e^{j2\pi wt}\,dw \right] d\theta \tag{2.32}$$

This integral in (2.28) may be expressed as:

$$f(x,y) = \int_0^{\pi} Q_\theta(x\cos\theta + y\sin\theta)d\theta \tag{2.33}$$

where:

$$Q_\theta(t) = \int_{-\infty}^{+\infty} S_\theta(w)\ |w|e^{j2\pi wt}dw \tag{2.34}$$

This estimate of $f(x,y)$, given the projection data transform $S_\theta(w)$, has a simple form. Equation (2.34) represents a filtering operation, where the frequency response of the filter is given by $|w|$; therefore $Q_\theta(w)$ is called a “ filtered projection”. The resulting projections for different angles θ are then added to form the estimate of $f(x,y)$.

The book of Kak & Slaney, 1988, gives the entire mathematical demonstration of the FBP method.

At the ESRF, the tomographic reconstruction is based on FBP (Salomé et al. 1999). The software currently used, called PyHST (Python High Speed Tomography), has been developed by A. Hammersley and later optimized by A. Mirone (Mirone et al. 2014).

2.2.8 The Paganin algorithm for phase retrieval

The intensity recorded by the detector is equal to the squared modulus of this wavefield, and entangles phase and attenuation information. Retrieving the phase information from recorded data is thus a nonlinear inverse problem. Over the last three decades, many phase retrieval methods have been developed for all the phase contrast modalities.

The algorithm adopted for the micro-tomographic volume reconstruction is the one proposed by Paganin et Al in the early 2000’s for simultaneous extraction of phase and amplitude signals from a single image (Paganin et al. 2002). The major assumptions adopted by the Paganin algorithm used in the current study are two, e.g. the sample has a slowly varying refractive index (Wu, Liu, and Yan 2005) and its distance from the detector fulfils the near-field conditions (Gureyev et al., 2008). The more these assumptions are far from the ideal mathematical case, the less the phase reconstruction is quantitative. The Figure 2.16 below illustrates the general scheme of propagation phase contrast Imaging.

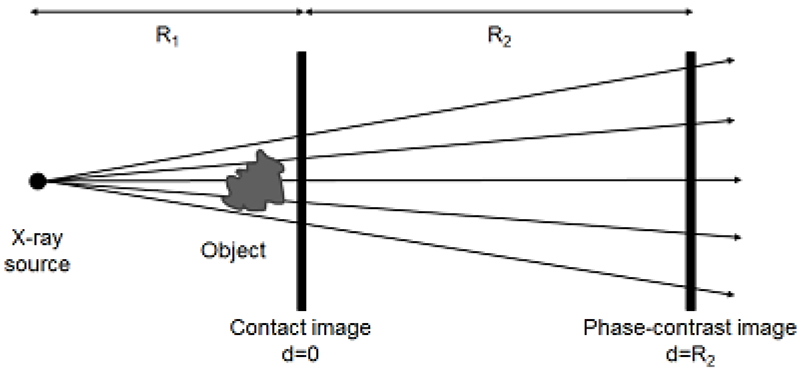

Figure 2.16. Scheme for propagation phase contrast imaging using a point source. (Image from Paganin et al. 2002).

The method relies on the Transport of Intensity Equation (TIE) model and explicitly uses the relationship between phase and absorption with the ratio δ_n/β for the considered homogeneous material.

This phase retrieval method is largely employed both at the ESRF and at TOMCAT because of its simple implementation. The theoretical values of the physical parameters of the material (δ_n and β) are calculated using the Xray Optics software XOP (Del Río and Dejus 2004), given its composition. The ratio δ_n/β can also be optimized by visual observation or using other computer vision tools (Rositi et al. 2014).

2.2.9 Phase contrast nano-tomography

X-ray phase contrast nano-tomography emerged only during last few years as a new Imaging tool providing a non-destructive 3D imaging of samples with a very high sensitivity and sub-micrometric resolution (Langer et al. 2012). In this case, conversely to the micro-tomography technique, a multiple distance propagation-based Imaging approach is adopted with a divergent beam configuration. Beam divergence and different sample-to-detector distances induce different magnification factors of the projections recorded by the detector (Figure 2.17).

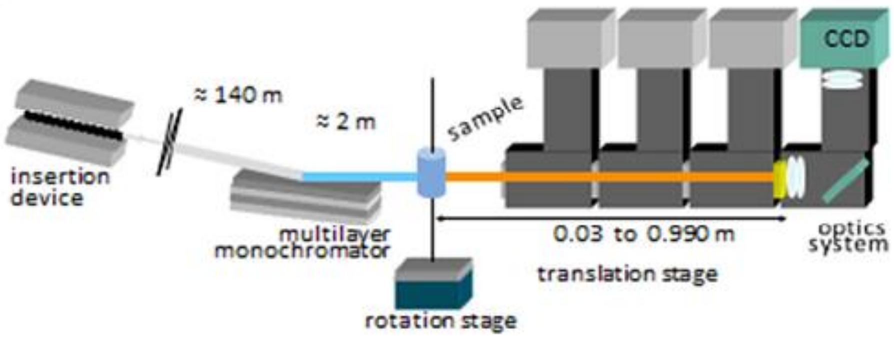

Figure 2.17. Set-up for multiple propagation distances acquisition (holotomography). (Image from Langer, Cloetens, and Peyrin 2010).

In practice, the projections are rescaled to the highest magnification factor that gives the smallest pixel size. Phase retrieval is finally performed according to a two-step process: a linear least-squares method to roughly assess the phase, and a non-linear conjugate gradient (NLCG) method to refine it.

The set-up of phase nano-CT is depicted in Figure 2.18. Kirkpatrick-Baez (KB) mirrors, curved reflective optics, focus the incoming parallel X-ray beam (X) horizontally and vertically onto a focal spot (F). D_1 is the distance between the focal spot and the sample (S), and D_2 is the propagation distance, i.e. the distance between the sample and the detector.

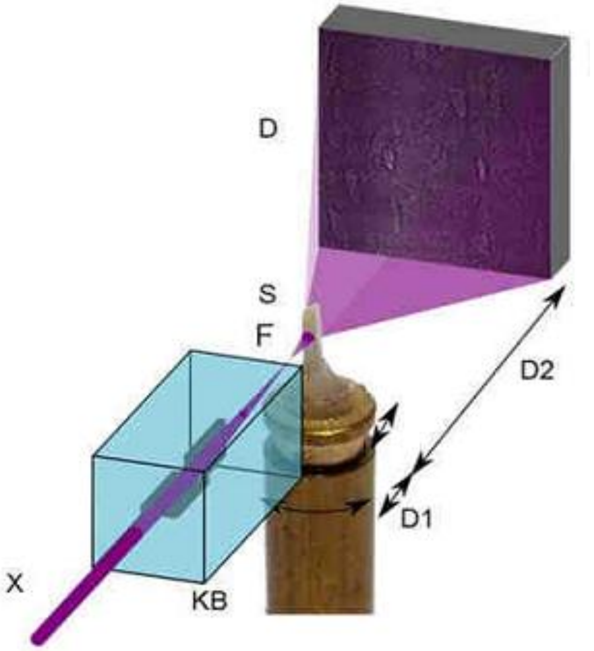

Figure 2.18. Set-up of phase nanoCT. The incoming parallel X-ray beam (X) is focused onto a focal spot (F) using specific optical elements (Kirkpatrick-Baez, KB, mirrors). D_1 is the distance between the spot and the sample (S), and D_2 is the propagation distance from the detector (D).

Since the beam is spatially divergent, recording an image at sample-to-detector distance D_2 also induces, apart from phase contrast, magnification of the projections. The Thales' theorem can be used for expressing the magnification M:

$$M = \frac{D_1 + D_2}{D_1} \tag{2.35}$$

Projections with different magnifications are obtained by modifying the propagation distance. In practice, the detector and the focus point are fixed, i.e. $D_1 + D_2$ is kept constant. This means that the sample is moving along a translation stage to get images with different magnifications. It is noteworthy that in this case of divergent beam, the wave front is spherical; the spherical wave Fresnel diffraction phenomenon can be seen as a plane wave illumination problem at the defocusing distance D (Guigay 1977), defined by:

$$\frac{1}{\mathrm{D}} = \frac{1}{\mathrm{D}_1} + \frac{1}{\mathrm{D}_2} \tag{2.36}$$

which is equivalent to:

$$\mathrm{D} = \frac{\mathrm{D}_1 \mathrm{D}_2}{\mathrm{D}_1 + \mathrm{D}_2} = \frac{\mathrm{D}_2}{\mathrm{M}} \tag{2.37}$$

This means that the defocusing distance D is an equivalent of the propagation distance that takes into account the magnification.

Holotomographic acquisition results in a large amount of data: usually several thousands of projections, multiplied by 3 or 4 propagation distances. Classically, the workflow of the reconstruction of a single phase volume is the following:

- **Dark- and flat-fielding**. Each acquired projection is first corrected, using the flat-field and the dark-field signals. The correction process is the same as for the microCT Imaging (Paragraph 2.5.1).

- **Registration step**. Prior to the acquisition, the translation stage with the detector is aligned with the beam, so that the sample remains in the same position of the image at each propagation distance. Nevertheless, residual shifts (a few pixels) can remain between the projections at different propagation distances, due to set-up vibrations or sample stage motor drift. To alleviate this misalignment, a registration of projections is required. This is performed at selected angles (usually every 100 projections or less), using a correlation-based method (maximization of the correlation coefficient), to determine the shifts between each distance, every 100 projections. For in-between projections, shift values are interpolated. As a result, the values of residual shifts between a propagation plane and the other propagation planes are given.

- **Selection of the reference plane**. The most stable propagation plane is deemed as the reference plane. It is determined by visual inspection of the registered projection. Then, every single projection is shifted with the calculated value, leading to the final registration of the whole dataset.

- **Choice of regularization parameter**. Phase retrieval is first performed at one projection angle, for several regularization parameters. Then, it’s possible to choose the optimal regularization value, before launching phase retrieval on every projection.

- **Phase retrieval**. The phase retrieval is parallelized with respect to the projection angle, which reduces computation time, depending on the number of projections to process, the size of the images, the number of distances used, and the availability of computing resources.

- **Tomographic reconstruction**. Once all the phase projections are collected, it's possible to launch the tomographic reconstruction. This step has also been parallelized, and could take up to a few hours.

2.2.10 Phase retrieval for multi distances approach

Phase retrieval is performed in two stages. A first initial guess of the phase is determined using a classical linear least-squares method. This first estimate corresponds to the linear part of the retrieved phase, but is not sufficient to provide good image quality at such high resolution. Consequently, the non-linear term is determined recursively, using a non-linear conjugate gradient algorithm. It improves the recovery of the high frequencies of the phase, and thus its resolution.

2.3 The microstructural imaging study of the rat somatosensory cortex at ID17, TOMCAT and ID16A

The studies of the microvessel and of the rat brain somatosensory cortex morphology have been performed at three different beamlines: ID17 and ID16A at the ESRF and TOMCAT beamline at the SLS. In particular:

-ID17: the first imaging tests has been carried out on samples extracted from the somatosensory cortex in order to primarily optimize the parameters for image acquisition, to verify the optimal sample preparation and for determining the needed spatial resolution for this study. Thanks to its microCT Imaging setup, by using the Propagation Based Phase Contrast Imaging, we succeeded in analysing the cortical macro-vasculature down to 3.5 µm.

-TOMCAT: the 3D visualization of the whole cortical microvasculature has been carried out here thanks to the high resolution microCT Imaging setup available. Also in this case the PBPC Imaging technique has been applied. The combination of the very high spatial resolution (0.625 µm) with a special sample preparation set up at ID17, allowed us to reveal in 3D the microarchitecture of the investigated somatosensory cortical regions.

- ID16A: The nanoCT Imaging setup available enables to reach nano-resolution and to see the inner structures within the cortical spaces. The PBPC Imaging with a multi-distances approach has been applied (*holotomography*). Due to the new environmental conditions (measures have been carried out under-vacuum), a new sample preparation was necessary in this case. With a nano spatial resolution (pixel size of

100 nm) it has been possible to visualize not only the vascular, but also the glial and neuronal components without the injection of any contrast agent in the animal vasculature.

In the next section the three different experimental sessions will be described.

2.4 Biological techniques

After describing all the methods and materials involved in X-ray CT Imaging, an overview of the biological materials and methods employed in this work is now presented. In particular, I was actively involved in the following experimental activities carried out at the CNR labs:

- CP Model on experimental rats.
- Sample preparation for the three X-ray Imaging sessions.
- Immunofluorescence and immunohistochemistry on the X-ray scanned samples.
- In vivo electrophysiological recordings paired with NIRS measurements of microBOLD signal.

2.4.1 Animal ethics

All the animals (70) albino Sprague-Dawley male rats 225-250g) have been used in accordance to the Italian, French and European Laws on animal treatment in Scientific Research (Italian Bioethical Committee, Law Decree on the Treatment of Animals in Research, 27 Jan 1992, No. 116, guideline n. 86/609/EEC European Community). The research in Italy was approved by the Ministry of Health and classified as “Biella 3/2011 and further as “Biella 1/2014” into the files of the Ethical Committee of the University of Milan, Italy. The experiments at the ESRF were approved by the Ethical committee #113, under the file 14_ethax16; the experiments at the ID16A beamlines (European Synchrotron Radiation Facility, ESRF, Grenoble, France) and at TOMCAT did not necessitate any ethical authorization because were performed post-mortem.

2.4.2 Creation of CP Models

Different types of animal models have been established to meet the diverse aetiology and consequently the diverse manifestations of the neuropathy that include peripheral nerve injury and Sciatic Constriction Injury (SCI)-induced peripheral and central pain models of neuropathy (Jaggi, Jain, and Singh 2011). Seltzer et al. developed a model consisting in the partial ligature of the sciatic nerve (PSL) (Seltzer, Dubner, and Shir 1990). This model has been adopted for the present morphological and functional study of Chronic Pain.

In order to establish this model on our animals, every rat was deeply anesthetized by intraperitoneal injection of a barbiturate drug (Pentobarbital, [Nembutal®], 50mg/kg). Prior to surgery all the materials for the nerve constriction and the surgical sutures were prepared. After a deep level of anaesthesia was reached (checking by applying a strong pressure over the tail tip or the posterior paw finger with no retraction response), the surface of the right posterior thigh was shaved and the skin soaked with antiseptic solutions. Then, the animal was placed over a surgical bed and a surgical incision orthogonal to the major axis of the posterior paw was practiced. The surgical wound was then slightly enlarged in order to reach a good visibility of the underlying muscle field. All the muscle plans were separated in two contingents until the sciatic nerve was clearly appearing on the bottom of the surgical field. Then, under surgical microscope control, the nerve was de-sheathed from the neighbouring structures (muscle capsules). After exposing the nerve through suture forceps, a suture needle with surgical silk tie was inserted in the full body of the nerve, obtaining a separation of the nerve fibre into two parts. Then, the silk tie was knotted with a strangling manoeuvre around one of the two parts, leaving intact the other one. Subsequently, all the displaced muscle plans were realigned and the wound was finally sutured. An antibiotic topical therapy was then applied (Streptomicin powder, Streptosil with Neomycin 99.5%+0.5%). At the end of the surgical session, the animals, still deeply anaesthetized, were placed in a warmed environment for a smooth wake up.

After the model instantiation, the animals were divided into six groups (3 controls + 3 treated for each time stage, i.e. at 15 days, 2 months (60dd) and six months (180dd) from surgery), in order to study the evolution of the neuropathy in time. All of them were maintained in a temperature-controlled room with a 12-h light/dark cycle and free access to food and water.

2.4.3 Sample preparation

The X-ray morphological study of rat somatosensory cortex has been carried out in three different experimental sessions by using both micro and nanoCT Imaging. The experiments have been performed at three different facilities, each one having a specific protocol for the sample preparation. This part represents a very crucial stage for a successful image acquisition and analysis. The sample preparation consisted of two main steps: the animal's perfusion, during which different kinds of solutions were injected through the circulatory system, to uniformly fix and eventually stain specific structures in brain tissue and, finally, the somatosensory cortical region extraction from the perfused rat brain.

2.4.3.1 Rat's perfusion

-For the first imaging tests, performed at ID17, samples, coming from control rats, have been prepared by perfusing the rat in order to clean brain vasculature from all blood sediments and, therefore, make them clearly visible to X-ray imaging analysis.

The whole operation was carried out under a hood. After being anaesthetized, the rat was placed into a plastic box in a supine position. All the surgery operations were carried out within this box because it was provided with a discharge tube (all the fluids from the perfusion, blood and injected chemicals were conveniently collected in opportune plastic containers to be sent to a specialized waste disposal company). After identifying the sternal xyphoid process, located in the midline at the lower border of the thorax, the skin over the xyphoid process was lifted up and a Y-shaped surgical cut was then operated proceeding cranially with a bifurcated cut contouring the lateral margins of the xyphoid bone. The ribs on both sides of the thoracic cage were cut until the clavicles. The sternal plastron was plied over the snout and maintained in place by a forceps applied at the xyphoid process. This operation allowed for an easy inspection of the thoracic cavity.

Subsequently, a large diameter needle (11 Gauge), connected to a small-diameter tube carrying the perfusion fluids pushed through a peristaltic pump, was inserted into the left ventricle of the heart. After gently blocking the beating heart by a pair of smoothed forceps, keeping stable the heart, the needle was inserted. The other end of the tube was immersed in the flask of degassed heparinized saline. Activating the pump, the solution was pushed through the needle into the circulatory system of the rat and the runoff of the perfusing liquids was allowed by cutting the wall of the right atrium. All the blood was progressively pushed off by the saline solution that was continuously circulated into the circulatory system for some half an hour to clean thoroughly all the vessels. After this stage, the peristaltic pump was turned off in order to substitute the heparinized saline with a solution of 10% formalin. The flask containing the formalin solution was equipped with a cap to avoid the external discharge of toxic fumes. The activation of the pump allowed the formalin to flow into the circulatory system in order to fix all the tissues and organs of the animal. The internal circulation of aqueous solutions (saline and formalin) was confirmed by the change of the colour of limbs and organs (first of all the liver): they lose their original red or reddish colour becoming progressively pale. After a total quantity of 250 ml was injected, the pump was turned off, the needle was extracted from the ventricle and the rat was placed on a guillotine to be decapitated. The head of the rat was hold under the light in order to see the insertion point of the spinal cord to the Atlas (C1). From here two internal cuts, on left and right sides, were carried out proceeding transversally along the occipital and temporal lobes up to the frontal one, over the hears. Then, the superior temporal and occipital bones were removed from the brain by applying them a light pressure upwards. The bregma (the meeting point between the coronal and the sagittal sutures) clearly visible on brain was marked with a small point of staining to have a reference point for the localization of the somatosensory cortex. In the end, a scalpel was inserted between the frontal bones and the brain surface and gently put in until the sphenoid process was reached. In this position, the scalpel was used as a lever to easily free the brain from cartilaginous structures and immersed into a Falcon tube containing 2% Paraformaldehyde solution.

-For TOMCAT microCT imaging experiments, samples were prepared by perfusing the animals, with the same procedure previously described, with two additional steps, required for a better visualization of cortical microvasculature through a contrast agent. For this purpose, a special marking system, based on an ink was injected to mark the vasculature. The setup of this protocol was refined after several optimization tests including imaging sessions. After formalin injection (250 ml), a cycle of 10 minutes of air was left circulating in order to free the vessels from most of circulated fluid residuals. The tube of the pump was then put into the Indian Ink flask and it was left circulating in the circulatory system. After some minutes, it was possible to see another change in the colour of the rat organs: they started to become progressively dark with an evidence of the superficial vessel and microvessel thread by the black ink. After a total quantity of 150 ml was injected, the pump was turned off, the needle was extracted from the ventricle and the rat was placed on the guillotine to be decapitated. The brain extraction was carried out by following the same procedure reported before. When the tissue reached a god level of fixation, (after 48 hours) it was possible to collect the portions of interest from the entire piece.

-The nanoCT imaging experimental session differed from the microCT mainly on the set-up. The passage to a very high resolution set-up imposed limitations on both the sample size and shape, due respectively to the available reduced field of view and to the environmental conditions (high vacuum). In this case, with the aim of preserving the original tissue contrast and structure, no perfusion was performed. The rat brain was extracted after the animal sacrifice according to the procedure described before.

2.4.3.2 The somatosensory cortex sample extraction

-For the first imaging tests samples have been embedded in paraffin in order to obtain parallelepiped blocks. These samples were collected by prepared by incising the brain with a scalpel to obtain a small parallelepiped (3 x 3 mm^2) centred respectively on the bregma at − 1.5 mm anterior-posterior (AP) as suggested by Paxinos Atlas. At this point, the sample underwent to alcohol dehydration process to displace the water inside the tissue. At first, it was left 18 hours in ethanol (EtOH) 70% by applying a gentle agitation. Then, changing the bath each hour, it was passed through EtOH 80%, 95% and two times in EtOH 100%. After the dehydratation procedure, the sample was put in a clearing agent (Xylene) for 1 hour to displace the ethanol and then 1 hour in Xylene-paraffin (1:1) at 56°C. At the end, the tissue was entirely soaked in liquid heated paraffin (60°C) and let to spontaneous cooling. When the paraffin was completely cooled and hardened (30 minutes at 4 °C), the sample was ready. A picture of the extracted brain and of the collected sample is shown in Figure 2.19.

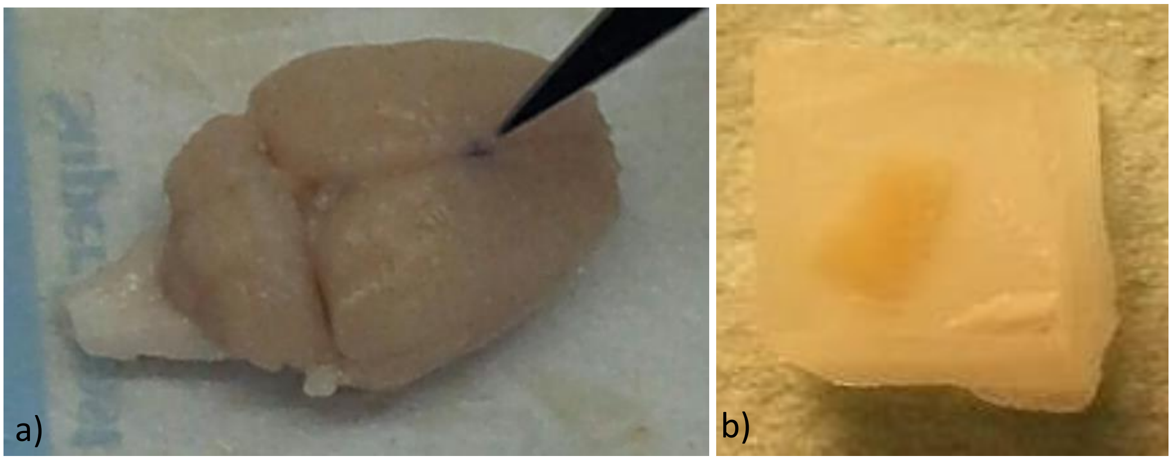

Figure 2.19. Rat brain sample for microCT Imaging tests: **a)** brain extracted after perfusion, **b)** sample of somatosensory cortex embedded in paraffin.

-For the TOMCAT imaging experiments, the samples of somatosensory cortex were collected by using a punching technique applied with a Teflon tube (2.1 mm in diameter and 12 mm in height). The tube was positioned in correspondence of the somatosensory region and delicately pushed into the brain turning it back and forth through the brain tissue, until the basis of the brain was reached. The obtained carrot was immersed in polyphosphate buffered solution (PBS) and maintained in constant hydration conditions until the microCT analysis. The extracted sample within the Teflon tube is represented in Figure 2.20.

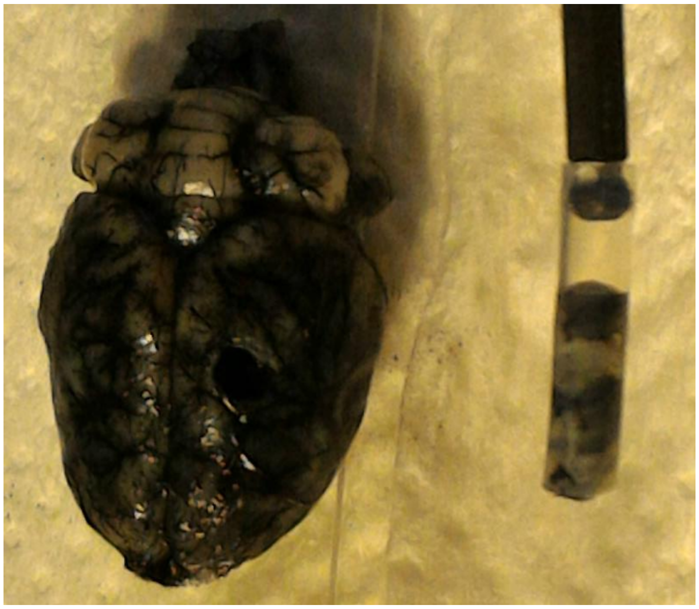

Figure 2.20. Rat brain sample perfused with contrast agent (Indian Ink) for microCT Imaging: the Teflon tube used for the sample extraction is shown on the right.

-For the nanoCT Imaging experiment, the samples extracted from the somatosensory cortex were collected by delicately pushing into the brain a small syringe needle (diameter = 10 Gauge). Subsequently, after being washed in PBS, the tissue sample was dehydrated through a series of graded ethanol baths to displace the water inside the tissue (same steps illustrated before). The paraffin layer in excess was removed with the help of a blade, in order to not to exceed the thickness limit of 500 µm, imposed by the sample holder dimensions available at ID16A. A picture of the very thin sample obtained is shown in Figure 2.21.

Figure 2.21. Sample of the somatosensory cortex for nanoCT imaging: the tissue was extracted without perfusing the rat and was then embedded in paraffin (thickness 500 mm).

2.4.4 Immunofluorescence analysis

Immunofluorescence is a common laboratory technique used for determining, by light microscopy, cell distribution and morphology on tissue sections, cultured lines or individual cells.

This technique uses fluorescent dyes that bind to specific antibodies made by the immune system when it is under attack by a particular antigen. The newly made antibody attaches to the antigen, and therefore allows visualization of the distribution of the target molecule through the sample. The specific region an antibody recognizes on an antigen is called an *epitope* (Mandrell, Griffiss, and Macher 1988). There are two classes of immunofluorescence techniques (Figure 2.22):

- **Primary (or direct)**: it uses a single antibody that is chemically linked to a fluorophore. The antibody recognizes the target molecule and binds to it, and the carried fluorophore can be detected by microscopy. This technique has several advantages over the secondary (or indirect) protocol because of the direct conjugation of the antibody to the fluorophore. This reduces the number of steps in the staining procedure, therefore making the process faster; additionally, it can reduce the background signal by avoiding some issues related to antibody cross-reactivity or non-specificity. However, since the number of fluorescent molecules that can be bound to the primary antibody is limited, direct immunofluorescence is less sensitive than indirect immunofluorescence.
- **Secondary (or indirect)**: the unlabeled first (primary) antibody specifically binds the target molecule, and the secondary antibody, which carries the fluorophore, recognises the primary antibody and binds to it. Multiple secondary antibodies can bind a single primary antibody. This provides signal amplification by increasing the number of fluorophore molecules per antigen. This protocol is more complex and time consuming than the primary (or direct) protocol, but it allows more flexibility because a variety of different secondary antibodies and detection techniques can be used for a given primary antibody.

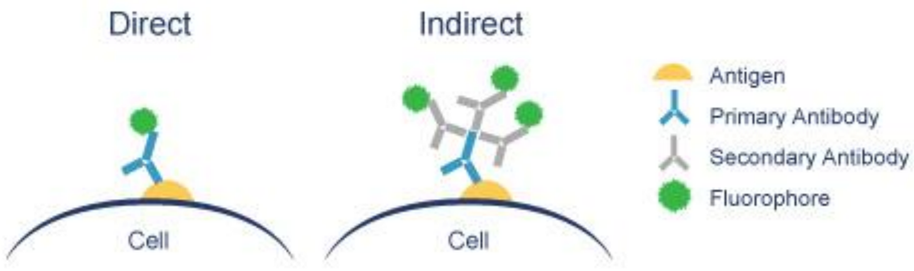

Figure 2.22. Mechanisms of direct and indirect immunofluorescence methods (Image taken from www.abcam.com)

Immunofluorescence can be used in combination with other, non-antibody methods of fluorescent staining, for example, the use of DAPI to label DNA.

In the present study, immunofluorescence techniques have been used to validate the outcome from the samples analysed by microCT imaging. In detail, the purpose was to assess the angiogenetic events in CP rat samples with respect to the control ones, emerged from the microstructural study of vascular network. For this purpose, four different primary antibodies have been adopted as markers of vascular angiogenesis:

- **CD31** (or cluster of differentiation 31). It is a protein found in endothelial cells, platelets, macrophages and Kupffer cells, granulocytes, lymphocytes. It has been used to demonstrate the presence of endothelial cells in the tissue.

- **VEGFR1** and **VEGFR2**. They are receptors for vascular endothelial growth factor (VEGF) (Holmes et al. 2007; Stuttfeld and Ballmer-Hofer 2009), that is an important signalling protein involved in both vasculogenesis (formation of circulatory system) and angiogenesis (the growth of blood vessels from pre-existing vasculature).

- **VWF** (or Von Willebrand factor). It is a blood glycoprotein involved in haemostasis. Recent studies suggested its involvement in the formation of blood vessels themselves (Randi and Laffan 2017).

The detailed immunohistochemical protocol will be described in Paragraph 2.5.4.

2.4.5 Electrophysiological techniques

Electrophysiology is the study of the electrical properties of biological cells and tissues. In neuroscience, it includes measurements of the electrical activity of neurons, and particularly the action potential activity. It represents the preferred method for analysing brain activity due to the ability to capture a wide range of neural phenomena, from the spiking activity of the single neurons, to the slower network oscillation of small populations (Llinas 1988; Contreras 2004; Assad et al. 2014).

2.4.5.1 The action potential

Information is carried out within and between neurons by electrical and chemical signals. These electrical signals-receptor potentials, synaptic potentials, and action potentials, are all produced by temporary changes in the current flow into and out of the cell that drive the electrical potential across the cell membrane away from its resting value. The cell membranes as well as all cellular membranes, present typically a lipid bilayers. Each layer is a flat sheet that forms a continuous barrier around the cell, few nanometer thick and impermeable to most water-soluble polar molecules. Cluster of proteins are embedded in the membrane establishing a functional connection from the inside to the outside of the cell. They are called *voltage gated ion channels* for their peculiar role: they can vary their conformation with membrane potential changes allowing for their opening and closing (gate) thanks to complex mechanism. In this way they regulate the passage of substances (mainly neurotransmitters and ions) across the membrane.

At rest, a nerve cell has an excess of positive charges on the outside of the membrane and an excess of negative charges on the inside. The charge separation gives rise to a difference of electrical potential across the membrane called the membrane potential that for a cell at rest is called the resting membrane potential. Its usual range in neurons is -60 mV to -70 mV. During this resting phase there are: i) more sodium (Na^+) and calcium (Ca^+) ions outside than inside the cell membrane; ii) more potassium ions (K^+) inside than outside the cell membrane; iii) more chlorine ions (Cl^-) outside than inside the cell membrane. (Figure 2.23). This equilibrium potential results from the balance of two forces: the thermodynamic and the electrical forces. K^+ ions tend to flow down their concentration gradient from inside to outside the cell through specific specialized ionic pores, called ionic channels present on the cell membrane. This movement of ions change electrical voltage inside the cell tending to become more negative. In turn, this increased negativity results in an electrical attraction between the negative potential inside the cell and the positively charged K^+ ions, thus offsetting their outward flow. At this time, there is no net flow of ions and the equilibrium is reached.

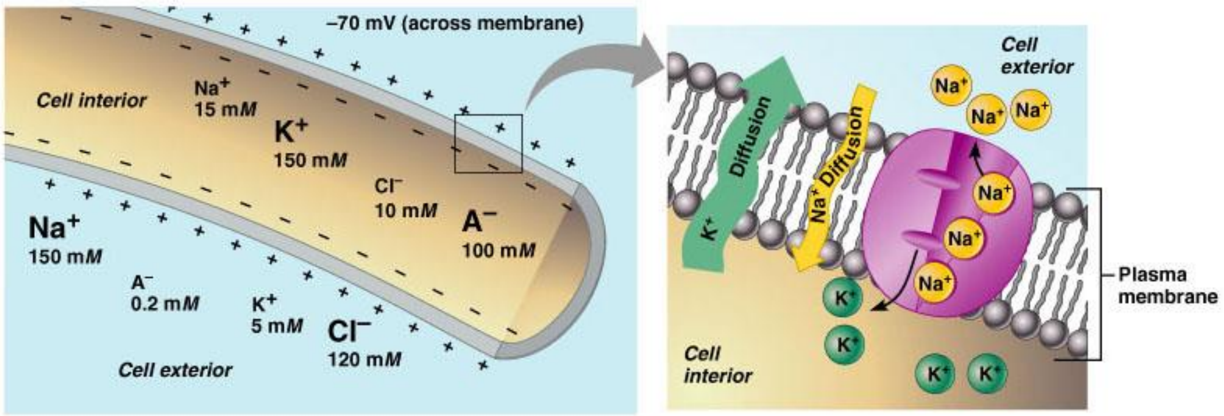

Figure 2.23. Resting membrane potential of a neuron: due to ionic disequilibria between sodium and potassium concentrations, the cell is charged positively on the outside and negatively on the inside with a typical value of -70mV. (Image taken from Pearson Education, 2004).

The resting potential undergoes continuous fluctuations due to incoming signal to the neuron. Most of these fluctuations are unable to trigger an action potential producing just simple deviations of potential either towards more positive level (*depolarization*) or towards negative level (*hyperpolarization*). If the input is strong enough to move upwardly the potential to a threshold range between -45 and -35 mV, an action potential occurs and a fastest depolarization is triggered driven by a massive sodium ion entrance into the cell. It is important to clarify that action potentials are said to be *all-or-none signals,* since either they occur fully or they do not occur at all. The massive Na^+ flux reverses the ionic balance across the membrane bringing the internal milieu to positive values (+20, +35 mV) relative to the external one. This sudden event lasts around 400μs. At the very peak of depolarization, suddenly, all the sodium channels close under the electrochemical gradient push and a new rush of potassium channel opening takes place. Due to the current internal positivity, the potassium ions tend to rush outside the cell both for chemical and electrical gradient. This potassium outflow has a greater temporal length 500-600μs and tends to restore the original negative resting potential with the outflow of positive charges. The potassium current is so powerful that the internal potential is pulled to even more negative (−80mV) values before regaining the normal negativity. During this hyperpolarizing period the neuron is insensitive to further depolarization input (*absolute refractory period*). The short time length running between the end of depolarization and the normal resting potential is called *partial refractory period*, since the neuron is again excitable by inputs stronger than the usual ones. From beginning to end, the action potential lasts about 2 ms. All the action potential phases are depicted in the Figure 2.24.

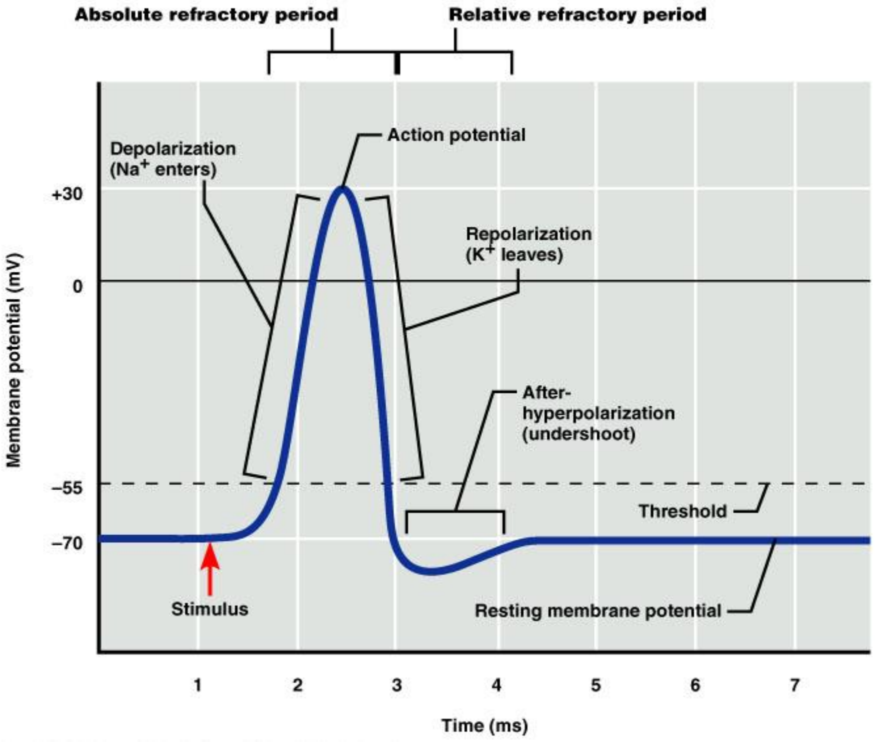

Figure 2.24. Sequence of an action potential and its ionic current sequences. (Image taken from Pearson Education, 2004)**.**

Action potentials in neurons are also known as *nerve impulses* or *spikes*, and the temporal sequence of action potentials generated by a neuron is called its *spike train*. A neuron that emits an action potential is often said to *"fire"*.

2.4.5.2 Intracellular and extracellular recordings

Two are the main methods for measuring the cell activity: intracellular and extracellular recordings. Intracellular recording requires impaling the neuron or axon with a microelectrode (Figure 2.25). Using this technique it is possible to measure the potential difference between the tip of the intracellular electrode and another electrode placed in the solution bathing the neuron (electrically continuous with the earth, and thus called ground). The intracellular electrode is filled with a concentrated salt solution (often KCl) having a high electrical conductivity. The electrode is connected to an amplifier that compares the potential difference between this electrode and ground and then to an oscilloscope. In 1963, Alan Lloyd Hodgkin and Andrew Fielding Huxley won the Nobel Prize in Physiology or Medicine for their contribution to understanding the mechanisms of action potentials generation in neurons. Their experiments involved intracellular recordings from the giant axon of Atlantic squid (Loligo pealei), and were among the first applications of the "voltage clamp" technique. Today, most microelectrodes used for intracellular recording are glass micropipettes, with a tip diameter of < 1 micrometre, and a resistance of several megaohms. The micropipettes are filled with a solution that has an ionic composition similar to the intracellular fluid of the cell. A chlorided silver wire, inserted into the pipet, electrically connects the electrolyte to the amplifier and to the signal processing circuit. The voltage measured by the electrode is compared to the voltage of a reference electrode, usually a silver chloride-coated silver wire in contact with the extracellular fluid around the cell. In general, the smaller the electrode tip, the higher its electrical resistance; therefore an electrode is a compromise between size (small enough to penetrate a single cell with minimum damage to the cell) and resistance (low enough so that small neuronal signals can be discerned from thermal noise in the electrode tip). The advantage of intracellular recording systems is the good electrical coupling with the cell and the accurate readout of the entire dynamic range of voltages generated by cells without distorting the readout over time. Yet, the use of sharp or patch microelectrodes is limited to individual neurons as steering of the electrode tips into target cells requires the use of bulky micromanipulators and the duration of intracellular recording sessions is limited by mechanical and biophysical instabilities (Spira and Hai 2013). Electrical currents across the neuronal membrane of the neuron can be detected also by simply placing an electrode near the membrane. Again, the potential difference between the tip of the recording electrode and the ground is measured and the extracellular potentials are recorded. The electrode can be a fine glass capillary filled with a salt solution, but it is often simply a thin insulated metal wire. Normally, in the absence of neural activity, the potential difference between the extracellular recording electrode and ground is zero.

The recordings of a neural ensemble can be studied at two granular levels. At the microscopic level the dynamic features exhibited are expressed by single neuron (SN) spike trains, i.e., the time series of neuronal action potentials. At the mesoscopic level, the collection of the recorded spike trains is identified in the multitrace recordings by definite time windows (from now called neuronal ensembles, NE).

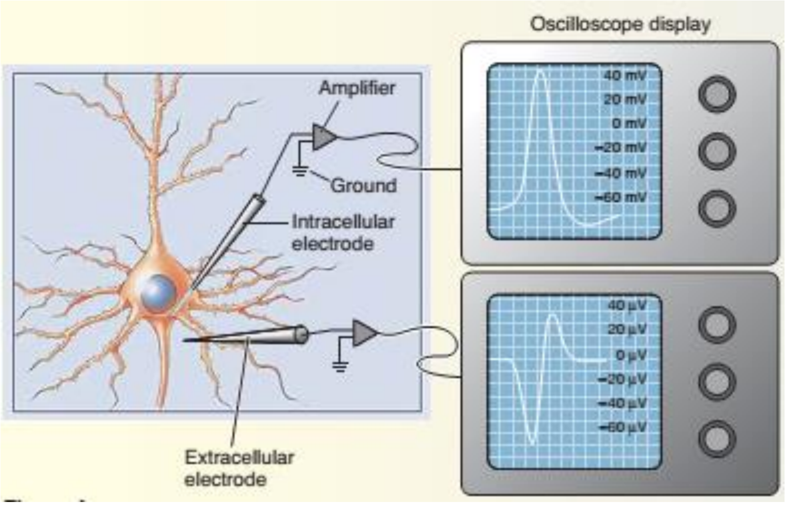

Figure 2.25. Scheme of intracellular and extracellular recordings from a neuron. (Image taken from Bear, M; Connors, B; Paradiso 2014).

The electrophysiological recordings carried out in the present study have been:

- **Acute recordings**: the extracellular activity of multiple ensemble of neurons has been detected by multiple *single-unit* microelectrodes. They are formed by a n x n electrodes framed, in our case, in 3x3 arrays of single shanks, inter-tip distance 150-200µm, tip impedance 0.5-1MΩ (FHC Inc., ME, USA) (Figure 2.26). Fast thalamic and cortical responses to light stimuli on the sciatic innervation field (the plantar aspect of the left hind limb) were the anatomo-functional acceptance criteria to start the activity acquisition. In this Thesis, Single Neuron recordings and Unit recordings are distinguished; the latter are meant as the collection of neuron micro-populations read-out by each single shank in the matrix.

Figure 2.26. Picture of the single-unit microelectrodes used for *in vivo* acute electrophysiological recordings.

- **Chronic recordings**: matrices of n x n microelectrodes are clustered together with one end sealed in an epoxy resin and to a connector. The other end is composed by arrays of electrodes with defined lengths (opportunely shaped in parallel combs) in order to reach diverse areas of the brain. In our experiments, we used 32 microelectrode matrices divided into four rows [8x4], the two front rows (550 μm long from the body of the matrix) addressing the somatosensory cortex 480 μm in depth from the brain surface) leaving thus few tenths of microns to allow a minimal space from the lower side of the matrix, the other two (long some 5700 μm) addressing the Ventral-Lateral nucleus of the Thalamus at 5500 μm in depth. The two subgroups of 16 electrodes each were opportunely paired in order to reach their right depth when the whole matrix is inserted in the brain. The microelectrodes were spaced 150 μm one from the other, with the tip diameter of 2 μm. The matrix was wireless connected with a multichannel device recording station (Triangle Biosystems Int'l.) (Figure 2.27). The matrix was inserted (by micro-motors driving its holder) into the right targets, first by delicately touching the brain surface with the two longest rows addressed to the thalamus. Then, after a descent allowing for the cortical rows to touch at their time the cortex, the motors of microstepper were stopped.

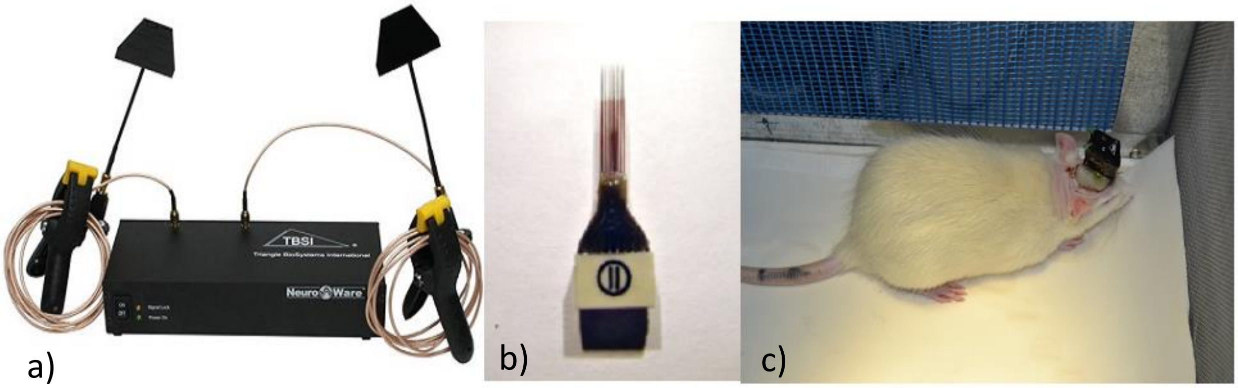

Figure 2.27. Equipment for chronic electrophysiological recordings: **a)** wireless recording station, **b)** microelectrodes matrix, **c)** implanted matrix on rat.

2.4.5.3 Neuronal electrical behaviour

Neurons are not all alike; they vary in shape, size, gene expression, and connections and in their specific electrical properties. The cerebral cortex has two major types of neurons as defined by their connections: cortical excitatory and inhibitory neurons with different characteristic modes of firing, by the synaptic density of each single neuron afferences and efferences and by the geometrical properties of these synaptic connections. Ultimately, each neuron's physiology is also determined by the properties and numbers of ion channels in its membrane. Cortical excitatory neurons can express the following behavioural electrical patterns (Izhikevich and Hodgkin-Huxley 2003) (Figure 2.28):

1. *Regular Spiking* (RS). The most diffuse in cortex. They emit few spikes with short interspike period and then the period increases.

2. *Intrinsically Bursting* (IB). They emit first a short burst of spikes then a series of regular spikes.

3. *Chattering* (Ch). They generate a sequence of spike bursts (at 40Hz) spaced out (at 0.1 to 0.8Hz) by resting periods.

Cortical inhibitory neurons can express the following electrical patterns:

1. *Fast Spiking* (FS). They emit a series of spikes like RS but with higher frequency.

2. *Low Threshold Spiking* (LTS). They show high frequency regular spikes followed by a fast adapting phase.

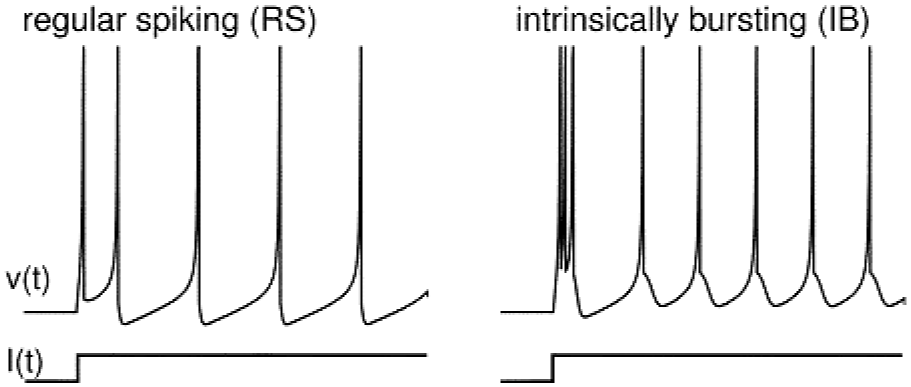

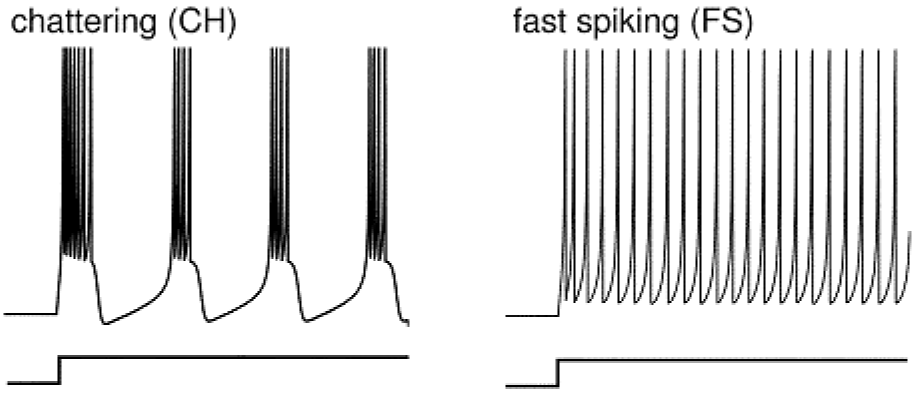

Figure 2.28. Different firing patterns of cortical neurons in the mammalian brain. (Picture adopted from Izhikevich and Hodgkin-Huxley 2003).

It is the complex interaction among multiple ion channels that create the eclectic electric signature of each class of neurons; all these different ways of communications enhance the complexity of the system and ensure a variability of information.

2.4.6 Basic principles of Near Infrared Spectroscopy (NIRS)

Near Infrared Spectroscopy (NIRS) is an optical imaging technique used for monitoring *in vivo* changes of the oxygen saturation of haemoglobin molecules in the investigated tissue, based on the absorbance of near-infrared light by haemoglobin. The importance of such a measure, especially in cerebral physiology, is related to the fact that in an average adult human being, the brain represents about 2% of the body weight. Remarkably, despite its relatively small size, the brain accounts for about 20% of the oxygen and, hence, calories consumed by the body (Raichle and Gusnard 2002). This high rate of metabolism is remarkably constant despite widely varying mental and motoric activity (Sokoloff 1973). These features indicate clearly the importance of the metabolic front in brain functional studies.

The basis of NIRS relies upon two principles: (1) tissue is relatively transparent to near infrared light and (2) there are compounds in tissue in which absorption of light is dependent on the oxygenation status of the tissue (Koh et al. 2007). The propagation of light in tissue depends on the combination of absorption, scattering, and reflection properties of photons. Absorption and scattering in tissue are wavelength dependent. Scattering decreases with the increasing of radiation wavelength, thereby favouring the transmission of near-infrared light compared to visible light. Reflection, in contrast, is generally a function of the angle between the light beam and the tissue surface (Jobsis 1977). Absorption occurs at specific wavelengths, determined by the molecular properties of the materials in the light path (Delpy et al. 1988).

The primary light-absorbing compounds in tissue within the near-infrared range are called *chromophores* (Jobsis 1977). Most chromophores can be considered to have stable concentrations during a measurement period (~10 min); however, their presence adds to the total light attenuation (i.e. melanin, bilirubin, water). The primary chromophores of interest are oxyhemoglobin (HbO_2), deoxyhemoglobin (Hb) and cytochrome c oxidase (Cyt), because the concentration of these chromophores varies with time and oxygenation status (Delpy et al. 1988). Each chromophore has a unique absorption spectrum, where the specific extinction coefficient (ε) is expressed as a function of the wavelength (Horecker 1943; Pellicer et al. 2011). It describes how strongly a chromophore absorbs light at a particular wavelength. In Figure 2.29 the absorption spectra for Hb, HbO_2, cytochrome c oxidase and water (H_2O) are reported.

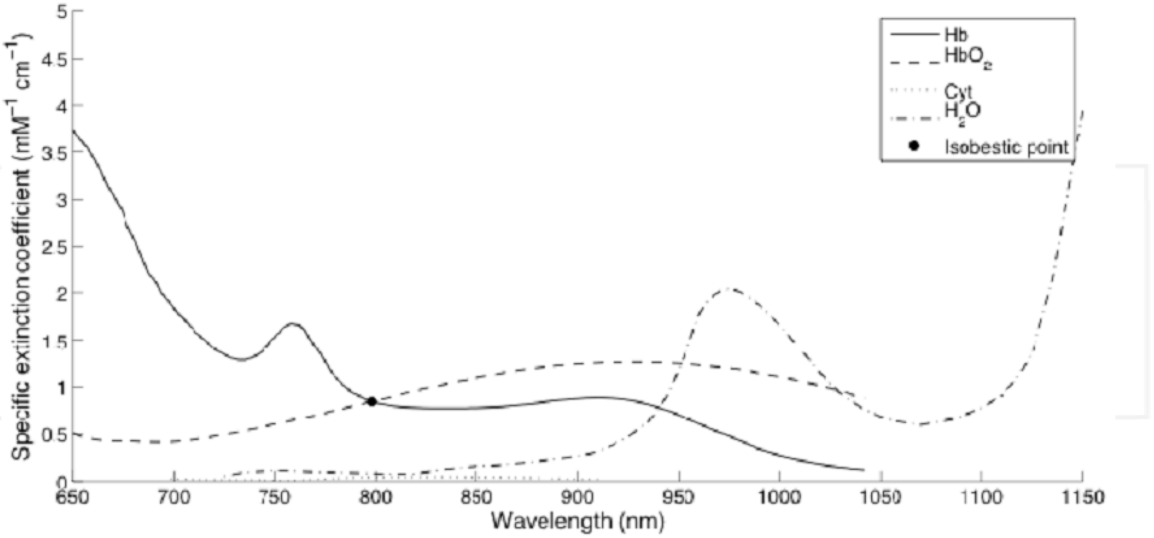

Figure 2.29. Absorption spectra for deoxyhemoglobin (Hb), oxyhemoglobin (HbO_2), cytochrome c-oxidase (Cyt), and water (H_2O) in the near-infrared range. The isobestic point (when the total absorbance of a sample does not change during a chemical reaction) near 800 nm is the point where the absorptivity of Hb and HbO_2 are equal (Image taken from Palmer and Williams 1974; Wray et al. 1988).

Hb and HbO_2 are responsible for the transport, delivery and removal of oxygen (O_2) and carbon dioxide (CO_2) throughout human body. NIRS instruments utilize light in the 700-1000 nm wavelength range to transilluminate cerebral and muscular tissues. This range follows from the increased absorption bands of H_2O above 1000 nm and increased scattering and more intense absorption bands of Hb below 700 nm. In the 700-1000 nm range Hb and HbO_2 have unique absorption spectra, which allows emitted light to propagate through tissue for several centimetres. The attenuation of the emitted light can be related to the change in chromophore concentration using the Beer-Lambert law:

$$A = \log\frac{I}{I_0} = \varepsilon \, C \, d \tag{2.38}$$

Attenuation (A) is the logarithmic ratio of two intensities, the intensity of the incident light (I_0) and the transmitted light (I). ε is the molar extinction coefficient, as shown in Figure 2.29, expressed in $mM^{-1}cm^{-1}$ C is the concentration of a chromophore and d is the direct pathlength of the photon from the emitting to the receiving optode, i.e. the inter-optode or geometrical distance.

2.4.6.1 The NIRS probe

To estimate the near-infrared spectroscopy signalling we first designed a Printed Circuit Board (PCB), which accommodated the following major components:

- programmable microcontroller (Arduino Due);

- a couple of lock-in amplifier;

- a couple of 24 bit Analog-Digital Converters with a sampling frequency of 8 Hz;

- two Light-Emitting Diode (LED), with a wavelength respectively of 780 nm (Thorlabs M780F2) and 850 nm (Thorlabs M850F2).

The PCB was powered by a 5V DC source with a consumption of about 8 W per hour. The PCB was mainly responsible for: i) the fine-tuned generation of the LED sources and ii) the acquisition of the signal from the avalanche diode (Thorlabs APD430A) connected to probing fibre optics used to prevent the current concentration (and the subsequent voltage derivation).

The NIRS signal was acquired through a serial USB interface between the microcontroller (Arduino Due) and a laptop opportunely programmed in Matlab® to store the signals in a resident data structure. The logical sequence of the acquisition was the following:

-Switch on the 780 nm LED.

-Acquisition of the voltage variation at the probe related to oxygenated haemoglobin.

-Switch off the 780 nm LED.

-Switch on the 850 nm LED.

-Acquisition of the voltage variation at the probe related to deoxygenated haemoglobin.

-Switch off the 850 nm LED.

2.5 Experimental procedures

After giving an extensive description of all the materials and methods adopted for the present study, a direct insight into the experimental part is given. The major experimental procedures carried out were:

- X-ray microCT imaging experiments by which the whole microvasculature has been revealed in 3D in order to highlight potential microstructural changes in cortical microvessel network induced by CP.
- X-ray nanoCT imaging experiments aiming at visualizing in 3D, at very high resolution, the tripartite synapse components.
- Immunofluorescence analysis of somatosensory cortical samples analysed through X-ray microCT Imaging.
- Electrophysiological recording coupled to NIRS measurements aiming at detecting both the neurodynamic and hemodynamic activities in control and CP rats in vivo, in order to functionally characterize the CP condition respect to the control one.
- Chronic electrophysiological recordings for the continuous observation of the neuronal network dynamics during the genesis of CP and its evolution up to six months.
- Animal behavioural test to follow the animal response in time after the onset of the induced neuropathy.

2.5.1 X-ray microCT imaging tests at ID17

For the first imaging tests the fixed micro-tomographic set-up has been used. The system is composed by solid platform that can host large samples (Ø plate: 400 mm, 30 kg maximum load), with a long vertical stroke (600 mm) adapted to large samples. The rotation, placed upon a Y movement that is used to acquire white fields, is a Leuven air bearing system (RT500) highly performing in terms of stiffness; the speed can reach 1 turn/s and has a very smooth rotation movement also at low speed (~1 turn/hour). An X-Y system is installed on top of the rotation to align the sample with respect the rotation centre (Figure 2.30).

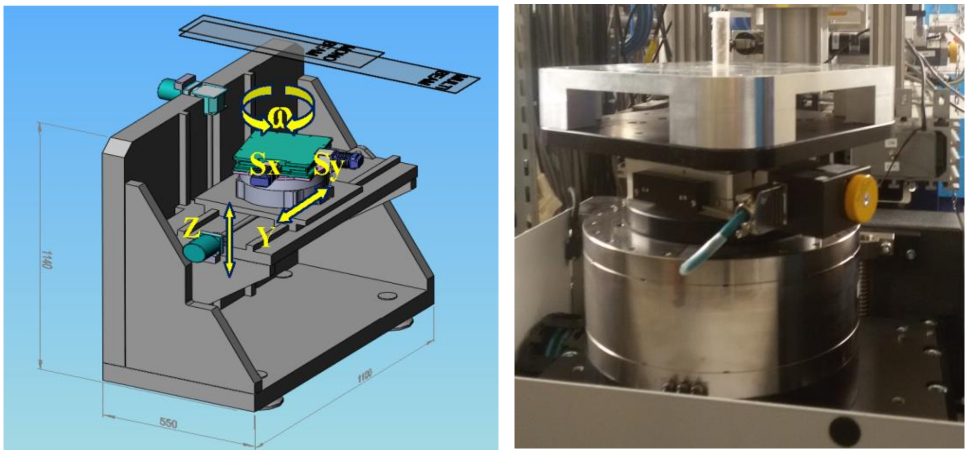

Figure 2.30. (left) Scheme of the microtomography sample stage showing all movements and the beam position when the sample stage is out of the beam. (right) Picture of the actual stage.

The Propagation Based Phase Contrast Imaging (PBPCI) technique was applied by using the CCD FReLoN camera (2048x2048 pixel) as detector combined with two different optics giving a final pixel size of respectively 8 µm and 3.1 µm. The X-ray beam was converted into visible light by a LuAG scintillator. The double Si Laue crystal was used to select a quasi-monochromatic ($\Delta E/E \approx 10^{-4}$) and quasi-parallel X-ray wave (divergence <1 mrad, horizontally, and <0.1 mrad, vertically) from the beam produced by the 21-pole wiggler (Paragraph 2.1.1.2); the energy selected was 33 keV and the sample-detector distance around 11 meters. For this first imaging test, samples of somatosensory cortex have been prepared according to the procedure previously described (Paragraphs 2.4.4.1 and 2.4.4.2). A tomographic scan follows a two-step process: 1) the acquisition of projections at different angles of the sample along the ray trajectory; during the scan the sample rotates around an axis parallel to the vertical axis of the detection plane; 2) the reconstruction, which calculates a 3D representation of the object, based on the projection images. A CT scan consists in the acquisition on three types of projection images (De Witte 2010):

- **Dark fields**: images acquired when the X-ray source is turned off. Such images contain the contributions of dark current and possible pixel offsets.
- **Flat fields**: the images are acquired when the X-ray source is turned on but the sample is outside the field of view. This acquisition allow for the correction for spatial-temporal inhomogeneity in the X-ray beam profile.
- **Projections**: a set of projections is taken while rotating the sample at equiangular steps in a range of rotation of 180°.

3000 projections, 10 flat fields and 10 dark field images have been acquired with an exposure time of 0.2s. Each acquired projection was first corrected, using the flat-field and the dark-field signals. The flat field correction aims at normalizing the beam inhomogeneity and the beam current variations. The dark-field aims at correcting the detector read-out dark-current background-noise. Several dark-current images (10) are recorded once per tomographic scan, and the average signal is called the dark-field.

The applied correction is:

$$\mathrm{I}_{\mathrm{corrected}} = \frac{\mathrm{I}_{\mathrm{acq}}\text{-}\mathrm{I}_{\mathrm{dark}}}{\mathrm{I}_{\mathrm{flat}}\text{-}\mathrm{I}_{\mathrm{dark}}} \tag{2.39}$$

where $\mathrm{I}_{\mathrm{acq}}$ is the acquired signal, $\mathrm{I}_{\mathrm{corrected}}$ is the corrected signal, $\mathrm{I}_{\mathrm{dark}}$ is the averaged dark-current signal, and the $\mathrm{I}_{\mathrm{flat}}$ flat-field signal.

Another X-ray microCT imaging test has been performed at BM05 of the ESRF, a beamline dedicated to test and develop X-ray optical elements, to beam characterization (coherence, polarisation…), and to the commissioning of instrumentation in general. The beamline is available for internal development and for proprietary research. Also in this case the PBI technique was applied by using a PCO Edge detector with a 3.1 µm of pixel size. The energy set was to 75 keV, 3000 projections have been acquired with an integration time of 0.07s.

After the data acquisition, the image reconstruction process was carried out the PyHST program, developed by Mirone et al. and adopted at the ESRF for tomographic reconstructions (Mirone et al. 2014). This program was interfaced using a (ID17) homemade Python script. It is used for the simultaneous extraction of amplitude and phase signals form a single recorded image.

2.5.2 X-ray microCT imaging at TOMCAT

The samples, extracted both form normal and CP rats at different time stages from the neuropathy onset were mounted on a metallic support through a piece of wax in order to assure their stability during the rotation of the sample stage. In Figure 2.31 the sample and the detector are shown.

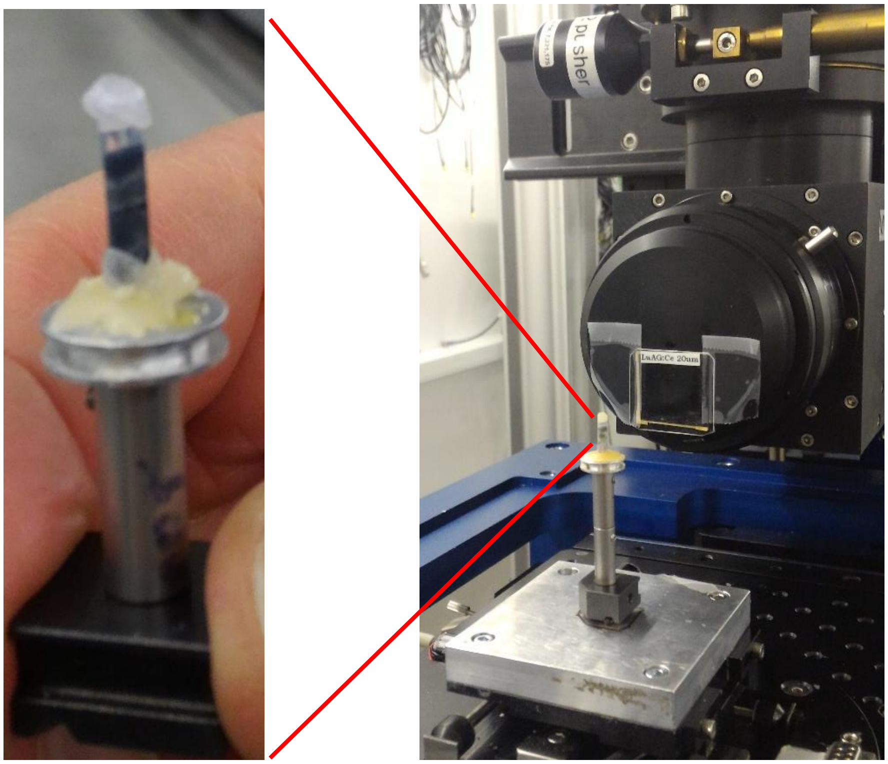

Figure 2.31. Sample stage of TOMCAT beamline with the sample zoomed: the Teflon tube containing the somatosensory cortex sample, immersed in PBS, is covered on the top with paraffin layer.

At TOMCAT beamline, the Propagation Based Phase Contrast Imaging (PBPCI) technique was applied. The photons, after interacting with the sample, are converted in visible light by a LuAG:Ce scintillator of 20 µm in thickness, which provides an absorption efficiency up to 12% at the selected energy of 20 keV and excellent resolution (below 1 µm). Then the light is collected by a diffraction limited microscope optics with a selected 20X objective (NA=0.70) and the information is projected on a PCO.Edge sCMOS camera with a 16 bit dynamic range. The configuration used leads to a field-of-view of 832×702 µm^2 respectively on the horizontal and vertical directions and a pixel size resulting in 0.325 µm. The detector, located at a distance of 20 mm from the sample, acquired 1401 (plus 30 dark fields and 100 flat fields) radiographic projections at equiangular positions over a total rotation angle range of 180° with an exposure time of 300 ms. Four stacked scans were acquired along the vertical direction of the sample in order to image at least 2 mm over 8 mm of the cortical sample, resulting in a total of scanning time of 30 minutes per sample. The sample to detector distance was experimentally optimized on a test sample, thus adopting a propagation-based method. Under certain approximations, X-ray phase propagation images can be processed to obtain the sample phase information using the non-iterative phase retrieval algorithm (Paganin et al. 2002) thus translating the edge information into a more convenient area contrast. The reconstruction process was run through a home-made software algorithm *“Gridrec”*, implemented on Fiji, based on the Paganin phase retrieval method. During this process the δ and β values have been optimized to reach the best image contrast. Each reconstructed volumes consisted in 2048 16-bit images of 2560x2160 pixels.

2.5.3 X-ray nanoCT Imaging experiments

The samples, prepared according to the procedure described in Paragraph 2.4.3 were mounted on metallic pins using a small drop of glue, in order to assure their perfect adhesion to the metal. Then, they were placed in the sample transfer load-loack that can host a total of 12 samples. Then the samples can be inserted into the vacuum chamber, (7 e^{-7}bar) and mounted on the sample stage via a robotized system. An automatic control system using piezo-legs maintains the sample stable during scanning.

The selected beam energy was 17 keV to allow for both sufficient transmission and high contrast. Each sample was first pre-scanned at a pixel size of 200 nm to obtain an overview image of the sample, using only 1400 projections of 0.2 seconds each to keep the imaging dose low. From this preliminary scan we selected regions of interest in each sample, which were then scanned at higher resolution. The field of view corresponding to the chosen settings was approximately 200 µm in diameter and height. Radiographs were collected at four different focus-to-sample distances with the focus-to-detector distance kept constant, yielding a pixel size of 100 nm (focus-to-detector distance: 1.208 m; distances between focus and sample: 36.1, 37.1, 41.1, and 51.1 mm). Holograms at 2000 projection angles were recorded at each distance with an exposure time of 0.2 seconds. The total scan time for each data set was around 4 hours. 21 empty beam and 20 dark field images have been taken. Based on these tomographic scans, phase maps were retrieved for each angle. From the phase maps, the spatial distribution of the refractive index decrement, δ, was reconstructed using the filtered back projection algorithm.

Each reconstructed dataset consisted of a stack of 32-bit 2048 vertical slices of 2048x2048 pixels, occupying 32 GB of memory. In order to reduce the computation time for the further analysis, the volume was converted to 8-bit format.

2.5.4 Immunofluorescence protocol

Immunofluorescence has been applied for qualitatively assess the presence of vascular neo-genesis in somatosensory cortical samples previously analysed through microCT imaging. It consisted in several consecutive steps here illustrated.

Tissue inclusion in Paraffin. Brain tissue was dehydrated through a series of graded ethanol baths to displace the water inside the tissue. Indeed, the tissue, after being washed in PBS, was maintained 18 hours in ethanol (EtOH) 70% in a gentle agitation. Then, changing the bath each hour, it was passed through

EtOH 80%, 95% and two times in EtOH 100%. After the dehydratation procedure, the tissue was put in a clearing agent (Xylene) for 1 hour to displace the ethanol, and then 1 hour in Xylene-paraffin (1:1) at 56°C. The paraffin is solid at room temperature, but at its melting point (56-58°C) it tends to be slightly viscous, needing a gentle melting before use. Then, the tissue was embedded in a Bio Mold, covered with paraffin in a liquid state and let it cold down. When the wax was completely cooled and hardened (30 minutes at 4°C), the paraffin block could be easily popped out of the Bio Mold. The tissue and the paraffin attached to the cassette had formed a block, which was ready to be sectioned. Tissue blocks could be stored at room temperature also for years.

Tissue slicing. The obtained block can be sectioned by a microtome in order to obtain thin slices. A brand-new blade for soft tissue was placed on the microtome; the block was inserted into the microtome so that the wax block faces the blade, aligning the block in the vertical plane. The microtome bath, filled with distilled water, was heated up to 37ºC. The chosen slice thickness was 6 µm. After cutting, the obtained sections have been placed on the surface of the 37ºC water bath and then floated onto the surface of clean glass slides. The operation was repeated until all the tissue slices were gathered. The slides were dried overnight at 37°C and stored at room temperature until the immunohistochemical labelling.

Deparaffinization. The paraffin was removed from the slides by rinsing them for 5 minutes in Xylene, 10 minutes in EtOH 100%, 5 minutes in EtOH 95%, 5 minutes in EtOH 75%. Then, they were rehydrated by immersion in deionized water at first, and then in PBS, five minutes each.

Antigen retrieval. Most of formalin-fixed tissue requires an antigen retrieval step before the immunohistochemical staining. During this step the disulphide bridges of the proteins are broken and so the protein antigenic sites are easily exposed to antibodies binding. The antigen retrieval was performed using heat-mediated method (also known as heat-induced epitope retrieval, or HIER). A solution of sodium citrate (10mM, pH 6.0) was prepared and heat up to 98°C. The slides were immersed here for 3 minutes. Then, they were left cooling down for 40 minutes at room temperature; finally three washes in PBS of 2 minutes each with gentle agitation have been performed.

Permeabilization. The antibody entrance in the cell is promoted in this process by producing microlesions on the cell surfaces. A solution of 0.2% Tween20-PBS was used. The slides were maintained for 30 minutes within this solution with gentle agitation.

Saturation. This procedure is needed to block unspecific binding of the antibodies. A solution of 10% bovine serum albumine (BSA) in 0.1% Triton-PBS was used. The slides were maintained with gentle agitation for overnight at 4ºC.

Immunofluorescence staining. Immunohistochemical staining is accomplished with specific antibodies that recognize each of the target proteins. Since primary antibody is highly specific, it will bind only to the protein of interest in the tissue section. The antibody-antigen interaction is then visualized using fluorescent detection, in which a fluorophore is conjugated to the secondary antibody and can be visualized using fluorescence microscopy (Paragraph 2.4.4). The slides have been incubated with a solution containing the primary antibody. As previously explained four antibodies have been used. The different procedure applied for each antibody are here described:

-CD31 1:200 in BSA 10%, for 1 hour at room temperature. Thereafter, the solution was decanted and the slides were washed in PBS three times, 2 minutes each, in gentle agitation. The incubation with a solution containing goat anti-mouse secondary antibody (GAM cy3) (1:2000) for 1 hour at room temperature in the dark was then performed.

-VEGFR1/VEGFR2/VWF 1:250/1:200/1:500 in BSA 10% for 1 hour at room temperature for both VEGFR1 and VEGFR2 and at 4°C for the VWF. Thereafter, the solution was decanted and the slides were washed in PBS three times, 2 minutes each, in gentle agitation. The samples were then incubated at room temperature, in a dark ambient, for 1 hour, in a solution containing goat anti-rabbit secondary antibody (GAR 488) (1:2000).

Then, as final step, slices were incubated with Hoechst33342 in PBS (1:500) for 5 minutes, in a dark ambient, and rinsed with PBS for 5 minutes. Hoechst stains are part of a family of blue fluorescent dye used to stain DNA, thereby it will be possible to recognize the nuclei and, accordingly, all the cells.

Mounting on the fluorescent microscopy and observation. Coverslips were mounted on the slides with a drop of mounting medium (30% glycerol in PBS) and sealed with nail polish to prevent drying and movement under microscope. A Nikon Eclipse80i microscope equipped with mercury vapour lamp has been used. The used filters were DAPI/Hoechst filter (340-380nm excitation, 435-485nm emission); FluoresceinIsothiocyanate (FITC) filter (465-495nm excitation, 515-555nm emission); and Tetramethylrhodamine-Isothyocyanate (TRITC) filter (540-25nm excitation, 605-655nm emission). The pictures were taken with automatic exposure by the Nikon software called 'NIS elements' (Nikon OS.02/L2 USB; F package).

2.5.5 Acute Electrophysiological and NIRS recordings

For this experimental session, a set of n. 4 animals have been used (2 control and 2 CP rats).The animals were anesthetized through intraperitoneal (IP) injection of barbiturate (Pentobarbital [Nembutal®], 50 mg/kg). After 10 minutes, the level of anaesthesia was checked by testing the rat response to opportune sensory stimuli usually provoking limb retraction. If no evident reactions were observable, the surgical manoeuvres were started. The trachea was cannulated to gain a connection to the anesthesia-ventilation device. A 16-gauge butterfly was then positioned in the root of the lateral tail vein to grant intra-surgical or intra-experimental access to drug intravenous delivery. A surgical opening was then performed from the nasal bones to the occipital bone. The surgical incision was then enlarged over the skull vault. The periostium was accurately removed from the bone vault to clear the access to the bone (the frontal and parietal left bones). At this point, the rat were was placed on a warmed surgical bed within a stereotaxic frame and the animal was paralyzed by intravenous Gallamine thriethiodide (20 mg/kg/h) injection and connected to the respiratory device delivering (1stroke/s) an Isoflurane® (2.5% 0.4 to 0.8 l/min in Oxygen 0.15–0.2 l/min) gaseous mixture. Curarization was maintained stable throughout the whole experiment by Gallamine fractioned injections. Then, a small square was drawn on the skull surface by a blue fine tip pen in the coordinate point corresponding to the underlying sensory cortex. This small square defined the borders of the hole to be drilled on the skull. For the simultaneous electrophysiological neuronal and near infrared spectroscopy recordings, a unique hole of 3 mm^2 for the cortical matrix access and for the NIRS probe positioning was made. With respect to the reference point (the bregma), for the cortical access it was centered − 1.5 mm AP and +2.5 mm ML and − 6 mm AP and − 2.5 mm ML for the thalamic access. The bone window was then trephined exposing the meningeal dura mater surface under surgical microscope control. During the drilling operation, the bone powders springing off the drilled surface were conveniently drawn by a pipette connected to a void-pump. The exposed surface was covered with a small piece of surgical foam soaked with warm (37°C) sterile physiological solution. Then, the dura mater covering the surface of the sensory cortex was delicately excised assuring that the cortical surface and the superficial blood vessels were not damaged. After the meningeal removal, the cortical surface was maintained well hydrated by warmed artificial cerebrospinal fluid (aCSF) and by a covering tile of aCSF moistened Gelfoam®. At this point it was possible to place the NIRS probe on the wet cortical surface. It was moved down manually as far as the space between them reached a very small distance, some 200-400 µm, laterally respect to the electrode position. In this way, the contact probe-cortex was avoided, which could produce a noise to the measurement, arising from the mechanical noise transmission from the animal breathing. A picture of the NIRS recording session is shown in Figure 2.32.

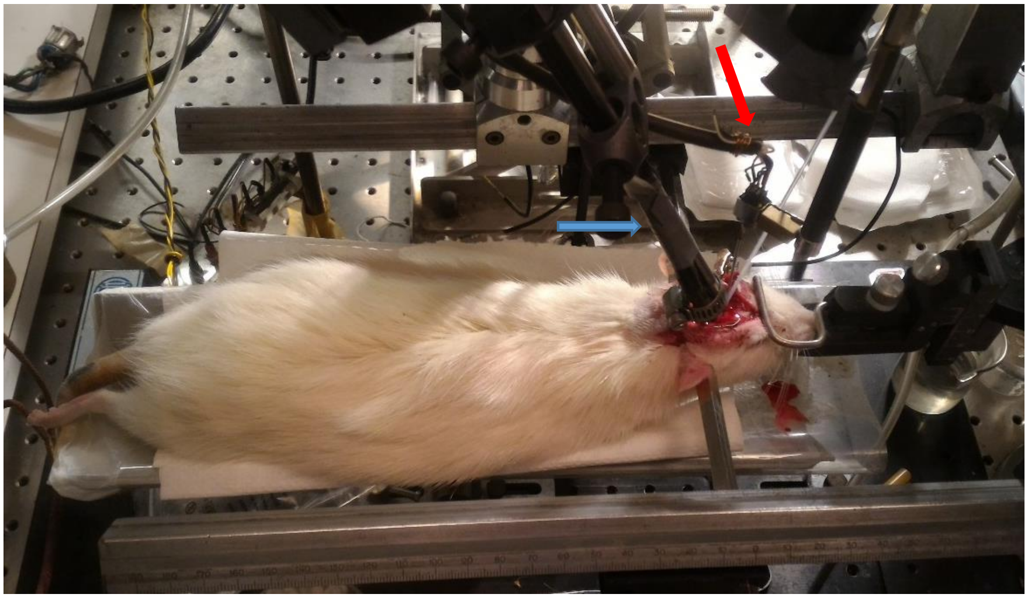

Figure 2.32. Experimental set-up of NIRS and electrophysiological recording session. The animal is placed on a warmed bed within the stereotactical apparatus. The NIRS probe (blue arrow) and the microelectrodes (red arrow) are placed over the exposed somatosensory cortical region.

We simultaneously recorded spiking and local field potential activities by microelectrode matrix from the primary somatosensory (SS1) cortex. The neuronal electrophysiological recordings have been obtained from the cortex contralateral to the stimulated paw; the microelectrode matrix consisted of extracellular Pt-Ir electrodes framed in 3 × 3 arrays of single shanks, inter-tip distance 150–200 µm, tip impedance 0.5–1 MΩ (FHC Inc., ME, USA) (Paragraph 2.4.5.2). The coordinates have been estimated from a Stereotaxic Atlas. In detail, the matrix was placed at − 1.2 mm AP, 2.6 mm ML from a reference point (bregma). It was inserted 400 µm deep at the superior border of the granular layer and then slowly advanced, by an electronically controlled microstepper (PI Instruments, Germany), at 10 µm steps, quickly driven to avoid excessive tissue damage. Fast and cortical responses to light tactile stimuli with a brush-test on the sciatic innervation field (the plantar aspect of the left hind limb) were considered the anatomo-functional acceptance criteria for the beginning of the signal acquisition. All the experimental blocks were organized with periods of ongoing activity recordings lasting no more than 20 min, to preserve at most the data homoscedasticity in the additional stable conditions of gaseous anaesthesia.

After a cycle of spontaneous and stimulated activities was completed, we repeated twice the original recording series in order to improve the statistical significance of data. Then, in order to register the neuronal activity in adjacent activated regions, we advanced in depth the electrodes (20 µm and 50 to100 µm respectively for the cortical and the thalamic matrix ensembles). Before acquiring the signal, the area activation is checked again with the tactile stimulus response. If the activation is sufficiently stimulated, we repeated the recording cycle as above. For signal amplification and data recordings a 40 channel Cheetah Data Acquisition Hardware was used (Neuralynx, MT, USA, sampling frequency 32 kHz). Electrophysiological signals were digitized and recorded with bandpass at 6 kHz and 0.1 Hz for spikes and Local Field Potentials and at 475 Hz–1 Hz for the EEG. The data stored were analysed off-line both by Matlab and by locally developed software.

Two experimental conditions were considered: the resting state in spontaneous unstimulated activity and the stimulated state. The stimulated state was characterized by the neuronal response periods to be matched to isochronic unstimulated time-lags. Briefly, controlled stimulation was delivered through a blunted cactus thorn on each of five sites of the rat right hind limb (Figure 2.33). The tip was mounted on the dust cap of a speaker and driven through an Arduino microcontroller board (available at http://www.arduino.cc) (Rinaldi et al. 2015). At the beginning of each stimulation phase, the tip was lightly placed over the skin. Fast (5 ms long) pressure pulses were applied following a semi-random sequence. Pulses were applied in couplets. The delay between the first pulses of each couplet was set at 500 ms. Every second pulse of each couplet followed the first by a random delay extracted uniformly in the range 150-200 ms. The stimuli semi-randomness was adopted to avoid habituation phenomena (Zippo et al. 2013).

Figure 2.33. Typical sites for the rat paw for tactile stimulation.

2.5.6 Chronic Electrophysiological recordings

In vivo long-term electrophysiological recordings have been performed by means of wireless microelectrode arrays chronically implanted in two areas of neuropathic rat brains, i.e. the somatosensory cortex (SS1) and the ventral postero-lateral (VPL) thalamic nuclei, the core regions of the somatosensory thalamocortical (TC) circuit. The main aim was to follow the rat neuronal activities both before the model of pain induction and during the entire period of neuropathy development. Five Sprague Dawley rats were used for the chronic implant, after 3 days of acclimatization at our animal facility. We administered tetracycline orally (50mg/500ml) two days before the operation as preventive therapy to avoid post-surgical infections after the chronic multielectrode matrices implant. All the working surgical instruments were preventively sterilized. The working desk where the stereotactical apparatus was mounted, was conveniently disinfected and placed under UV light overnight. The planar measurements of the stereotactical position of the region of interest (that is the SS1 cortex underlying the bone and VPL thalamic nucleus) had been defined along the indications of a specific stereotactical atlas of the rat brain (Paxinos and Watson 1986). Using the bregma as reference, we used the stereotactic coordinates of -1.2 mm AP and 2.6 mm midlateral that identifies an area on the parietal bone overlying the SS1 cortex. The animal was anesthetized intraperitoneal injection of barbiturate, (Pentobarbital [Nembutal®], 50 mg/kg). After a 10 minute delay, the level of anaesthesia was checked by testing the rat response to opportune sensory stimuli usually provoking limb retraction. If no evident reactions were observable, we started the surgical manoeuvres. The head was shaved down to the level of the descending trapezium and the skin was disinfected. The rat was placed on a sterilized surgical desk in prone position. The rat skin was incised from the nasal bones to the occipital bone. The surgical incision was then enlarged over the skull vault. The periostium was then accurately removed from the bone vault to clear the access to the bone (the frontal and parietal left bones). A sterile dressing soaked with physiological solution was placed on the surgical field and fixed with surgical clips. The rat, but the head, was then inserted within a plastic multiperforated sack to avoid contaminations from fur and placed on a warmed surgical bed with temperature regulation at 37.5 °C within the frame of the stereotactical apparatus. After fixing the rat head to the apparatus, the bone surface was again cleaned and dried. If serous or bleeding sources were evident, they were dried out by pressing cotton blobs or burned by cauterization. In some cases a 2% silver chloride solution was used to dry the bone surface. By drawing the borders of the tile to be drilled off the bone on the skull surface, a 3.5x3.5mm^2 bone window was then trephined exposing the meningeal dura mater surface under surgical microscope control. During the drilling operation, the bone powders springing off the drilled surface were conveniently removed by a pipette connected to a void-pump. The exposed surface was covered with a small piece of surgical foam soaked with warm (37 °C) sterile physiological solution. The skull surface around the square was kept dried and cleaned by dabbing cotton with silver nitrate solution. Five small pilot holes were made to aid for the insertion of 5 micro-screws around the bone hole. The five micro-screws were then placed as support points for the microelectrode matrix implant. Then, the dura mater covering the surface of the sensory cortex was delicately excised making sure of not damaging the cortical surface and the superficial blood vessels. After the meningeal removal, the cortical surface was maintained well hydrated and in correct osmotic environment by warmed artificial cerebrospinal fluid (aCSF) and by a covering tile of aCSF moistened Gelfoam®. The matrix electrodes, previously cleaned with fast Ethanol solution (70%) rinsing and then by immersion in sterile distilled water, were fixed to a sterile clamp, mounted on a stepping motor previously fixed on the stereotactic frame. The electronic motor was initially placed over the insertion area by manual control in orthogonal position respect to the cortical surface and slowly lowered toward the cortical surface. The further phase was carried out under a remotely controlled programmable microstepper motor (M228 Stepper-Mike Linear Actuators) driving the two microelectrode combs to touch the cortical surface at first. A final, electronically controlled descent step was then made to reach the respective thalamic and cortical final targets (between 450 and 650 μm for the cortical electrodes and 4800 to 5300 μm for the thalamic endpoints). Then, the electrode reference wires were fixed to two of the previously implanted micro-screws. The exposed cortical surface was then gently covered with PolyEthyleneGlycol 4000, removing the excesses from the bone around. The whole operation area was then covered by dental cement, moulded around the plastic basis of the electrodes. After the drying of the cement, the electrode matrix was freed from blocks. The rat was extracted from the protecting sack, removed from the stereotactic frame and placed in its cage in a warm environment. Gentamycin was spread around the surgical region and eyewash drops were then administered and repeatedly placed in the next days. Systemic antibiotic was administered to the rats for the entire week after the surgery and their conditions were constantly monitored.

The recording sessions, one for each day, started four days after the operation. All the collected data were stored in external memories and completed in two weeks gathering the “normal” or control condition dataset. Thereafter, we induced the neuropathy in the rats through a sciatic nerve ligature (Paragraph 2.4.2) and we proceeded with the daily recording session for the following six months. The recording sessions lasted half to 1 hour each. Thanks to the wireless recording technique, the rats were able to freely move in their cage during the recording without the anaesthesia effects. The recording set-up consisted of a special wireless head stage with 32 microelectrodes connected to a 32 recording channel device (Triangle Biosystems Int’l.). Data were analysed off-line both by Matlab® and by locally developed software.

2.5.7 Behavioural tests

Tests were done both before the CP surgery and for six weeks after the induction of pain. They were performed in order to evaluate whether all the signs of chronic pain were clearly detectable. We performed Von Frey and Hot Plate tests to measure allodynia and hyperalgesia, respectively. Moreover, the motor patterns were checked by a walking motor scheme test, showing the postural rhythms and patterns of paw placing during walking.

2.5.7.1 The Von Frey behavioural test

Von Frey filaments are the “gold standard” method for measurement of mechanical nociceptive threshold (MNT) in rodents (De Sousa et al. 2014). For this test, a set of nylon filaments, each able to exert a different force, is applied to the plantar aspect of the animal paw (well accessible after placing the rat over a metal grid), from the weakest to the strongest, until the paw is retracted. These devices are based on Euler's buckling law, which states that an elastic column (in this case the filament) will buckle elastically at a specific force, dependent on the length, diameter and modulus of the material. Before the filaments starts to bend, the force can be increased, but once buckled, the force imparted is fairly constant. The set of filaments have all the same length, but various diameters in order to provide a range of forces (from 0.008 to 300 g). The filaments are calibrated according to the formula (Dellon, Mackinnon, and Brandt 2017; Weinstein 1993):

$$\text{Quoted stimulus} = \text{Log}\,(\text{force in grams} \times 10\,000) \tag{2.40}$$

We normally used filaments ranging between 4.31 and 5.46 which correspond to a "light-touch" application force, suitable to test allodynia. The method we utilized was the up-down method: filaments of different force ratings were used in succession; if a response was elicited, then the next lower rated filament was used; if there was no response, the next higher rated filaments was used. We considered 5.46 as ceiling, so we did not use stronger filaments even if the rat had not retracted the paw. In this case we considered 5.46 as final value.

The tests have been carried out both on the implanted rats before the Seltzer operation (T_0), 3 days after the operation and once a week for the following six weeks. We tested both paws, the ipsilateral and the contralateral to the sciatic nerve ligature side.

2.5.7.2 The Hot plate test

The hot-plate test is commonly used for evaluating thermal pain sensitivity (heat hyperalgesia). For this test, the rat was placed on the testing apparatus (a plate heated at 51°C) and the timer started. The latency to respond to a thermal stimulus applied to the hind paws was determined by the time the rat took to lick the hind paw, vocalize, or to lift the paw (nociceptive responses). The rat was immediately removed once one of these response were observed. If there were no responses within 30 seconds, the test terminated and the rat was removed from the hot plate.

We performed this test both before the PSL operation (T_0) and 3 days, 1 week, 2, 4 and 6 weeks after the operation. We collected data from both paws.

2.6 Data analysis

From the experimental sessions described, four kinds of data have been collected:

- 3D images of somatosensory cortical microvasculature from control and CP rat samples acquired through microCT imaging;

- 3D images of the vascular, neuronal and glial compartments, forming the tripartite synapse, obtained through nanoCT imaging;

- Extracellular electrical traces of neuronal activity both form acute and chronic *in vivo* electrophysiological recordings;

- Haemodynamic electrical signal from *in vivo* NIRS measurements.

All the techniques employed for image and signal treatment are illustrated in this section.

2.6.1 Image post-processing for microCT datasets

Once reconstructed, the sample volume was assembled, by removing the overlap between each acquired dataset, and then cropped at the borders, where the presence of some artefacts affected the image visualization. During the preparation phase, some samples were damaged, more often when performing the the manoeuvre for the final extraction with the Teflon tube; the investigated region was then confined within to 3200 transversal slices that correspond to ~1.020 mm from the top of the sample. The image equalization was then applied to obtain a uniform range of pixel intensity values throughout the volume (processing performed by means of *Image J*). A list of all the reconstructed samples is reported in the Results chapter 3.2.

After this short pre-processing step, the analysis was addressed to the 3D morphological analysis of the vascular network in the cortical regions. The main consecutive steps were the following:

- Image segmentation for the extraction of the region occupied by microvasculature and analysis of the geometrical features of the morphology;
- Image skeletonization and consecutive 3D graph transformation: for the characterization of the topological features of the vascular network morphology;
- Comparative study between control and chronic pain model groups through statistical analyses to assess morphometric changes even in a longitudinal perspective.

2.6.1.1 Image segmentation

In computer vision, image segmentation is the process of partitioning a digital image into multiple segments (sets of pixels, also known as super-pixels). The goal of segmentation is to simplify and/or change the representation of an image into something that is more meaningful and easier to analyse (Stockman and Shapiro 2001).

In this case, the region occupied by blood microvasculature, already highlighted by the injection of the contrast agent, needs to be isolated from the rest of the volume. This process has been performed using the VG Studio Max software, recently acquired at ID17, thanks to its large variety of tools available, its easy graphical user interface and its fast 3D rendering visualization. Two are the morphological operators used:

- *Image thresholding*: in order to select only the pixel belonging to the vasculature, appearing brighter than the background, because of the high contrast achieved through the contrast agent injection. The thresholding value was not the same for all the volume and, for this reason, was every time recalculated by visual inspection.

- *Region growing*: to select all the remaining pixels belonging to the vasculature. Region growing needs a set of starting pixels, called seeds. The region growing process consists of picking a seed from the set, investigating all 4-or 8-connected neighbours of this seed, and merging suitable neighbours to the seed. The seed is then removed from the seed set, and all merged neighbours are added to the seed set. The region growing process continues until the seed set is empty (Gonzalez and Woods 2008). The algorithm used enables the selection of the seed and the range of values within all the 8-connected pixels will be automatically picked up and added to the seed.

- Other morphological operators, like the "*opening-closing"* tool, are used to remove all the small pixel from the area of interest and, in the end, the *"fill holes"* tool has been used in order to fill all the holes inside the region occupied by blood vessels.

Once obtained the final binarized volume, it was displayed allowing for the detailed 3D visualization of the microvessel architecture.

2.6.1.2 Image skeletonization and graph transformation

Skeletons provide a simple and compact representation of 2D or 3D shapes that preserves many of the topological and size characteristics of the original image. Skeletons can be defined in several ways. One of the first definitions was given by Blum (Blum 1967) as the locus of the centres of maximal disks contained in the original object. If the skeleton points are attributed with their distances to the original object's boundary, the skeleton can be used to exactly reconstruct the shape it originates from (Ogniewicz 1995). Skeletons can be obtained in different ways. In the present analysis, the *"skeletonize_3d"* function available on *Python scikit image* library performed the skeleton computation. The method developed by Lee (Lee, Kashyap, and Chu 1994) uses an octree data structure to examine a 3x3x3 neighbourhood of a pixel.

The algorithm proceeds by iteratively sweeping over the image, and removing pixels at each iteration until the image stops changing. Each iteration consisted of two steps: first, a list of candidates for removal is assembled; then pixels from this list are rechecked sequentially, to better preserve connectivity of the image. Once the vessels, considered as cylinders, as illustrated in the Figure 2.34 are skeletonized and reduced to their centreline, the function "*skel2graph3D*", available on Matlab® Image Processing toolbox, allows for the final transformation of the 3D skeleton into the network graph G = (V, E) where V represents the set of arrow starting points (node) and E represents the set of connections between nodes (edges). A more detailed explanation of graph theory will be given in the section 2.6.4.3.

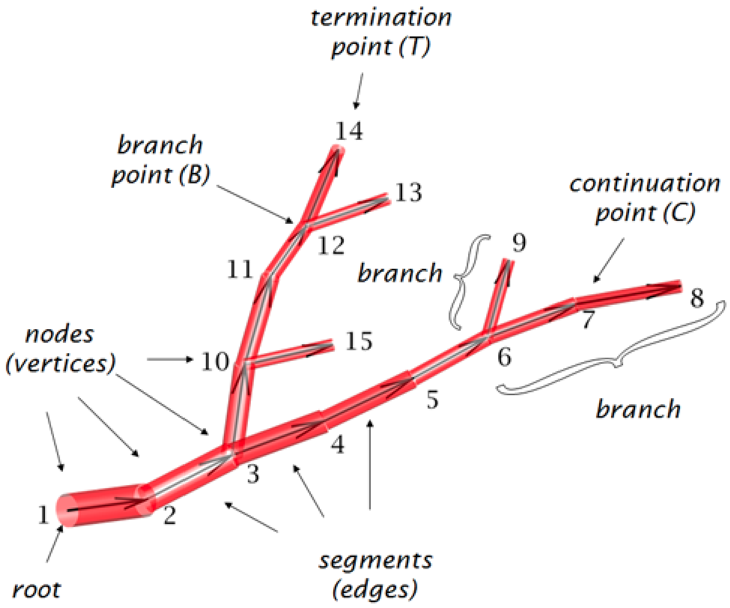

Figure 2.34. Illustration of vascular network: each blood vessel can considered as cylinders (in red), while the skeleton segments are the arrows contained in the cylinders.
The skeleton has been conveniently converted into a graph G=<V, E> where V represents the set of arrow starting points (node) and E represents the set of connections between nodes (edges).

The characterization of this intricate network is based on the computation of the number of segments (egdes), number of nodes, number of branch points, number of vessels and their diameters. The diameters were estimated by modelling the microvessel transections with circle equations. According to this method, the circle area was approximated by the number of pixels containing the vessel representation and the diameter computed by the inverse formula: $d = 2\sqrt{\#\text{pixel}/\pi}$.

2.6.1.3 Maximum flow estimation

The transformation in graphs was necessary for the evaluation of the mechanical properties exhibited by the vascular network. According to a general vessel modelling, graph nodes represent the bifurcation points and graph edges the vessel connection among the bifurcation points. Since, in our case, vessels are supposed to host fluid dynamics of blood, a set of graph theory algorithms have been applied to investigate the putative fluid dynamics that a network can support according to its topology (the specific edge displacements). The most representative of this class of algorithm estimates the maximum flow given a graph and a couple of nodes as source and sink. For an overall estimation of the maximum flow, these pivotal nodes are randomly chosen and each of them averages the final estimation. The function *"maxflow"* has been used for this kind of computation. It is based on "*Ford-Fulkerson algorithm"*, a heuristic algorithm, which iteratively maximises the flow sustainable among all nodes which connect a source (S) and a termination point (T) (Ford, Jr. and Fulkerson 1956). In practice, as long as there is a path from the source (start node) to the sink (end node), with available capacity on all edges in the path, the algorithm exhausts the capacity of that path currently setting the maximum flow to that capacity value. Subsequently, the algorithm seeks for another path with non-zero capacity and update the maximum flow estimation by adding the novel found capacity of the current path (*augmenting path*) , and so forth until no further augmenting path are available. Specifically, in our analysis, we randomly chose a couple of nodes (one as sink, and one as source) for 10000 times and we computed at each time, the maximum flow between the chosen nodes. At the end, the estimated average maximum flow for the graph will be the average among the 10000 random estimations.

2.6.1.4 Statistical analysis

After the morphological analysis of vascular network, all the results have been collected in order to perform a comparative study "Control vs neuropathic" in relation to each time stage (14, 60 and 180 days from the neuropathy onset). Non parametric statistical tests were adopted to reject the null hypothesis (Ranksum test, Welch test and Paired-t test, *Matlab Statistical Toolbox*).

2.6.2 Image post-processing for nanoCT datasets

The large variety of cells and structures detected within the sample, and their very tiny contrast, prevented the implementation of an automatic method for their virtual extraction. For this reason, the segmentation process has been conducted using the VG studio Max Software by proceeding in this way:

- Visual inspection of all the structures in order to recognize and subsequently classify them into groups according to their shape, morphology and contrast intensity.
- Manual selection slice-by-slice of all the structures identified through the *region growing* operator.

This kind of segmentation was performed only for one sample, due to the extensive time required for its completion. At this point, the segmented volume can be easily rendered, providing a detailed visualization of the cortical tripartite synapse.

2.6.3 Electrophysiological data analysis

The collected raw data have been analysed by applying complex mathematical tools and algorithms based on theory of signals, graph theory and complex network theory. The general workflow for the signal off-line processing is here briefly described:

-Spike sorting: consisting in the extraction and grouping of spikes into clusters based on a similarity criterium of their sampled waveforms. As a matter of fact, in extracellular recording assets, the position of the recording probe (the electrode tip) and the active recordable neurons (within a radius of 150 µm or so from the tip) arranged in a kind of lattice, are supposed to be stable during each recording stage (Figure 2.35). This assumption, thus, admits that the field of a depolarizing neuron can be steadily acquired throughout a recording session providing self-similar signals. Each neuron may be thus functionally labeled by a specific spike shape and each resulting cluster corresponds to the collection of similar-shaped spikes emitted by one putative single neuron. From now to the rest of work, the name "unit" is referred to the activity of a single neuron.

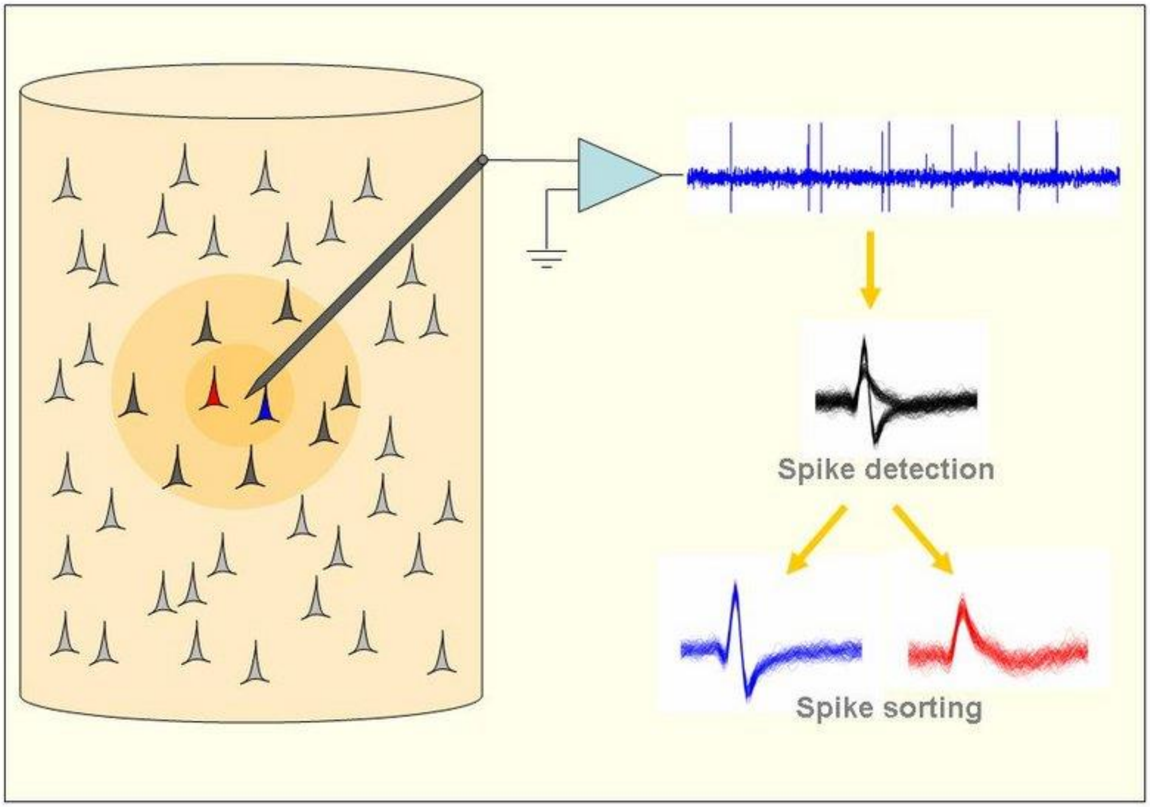

Figure 2.35. An electrode that records the electrical activity within a microcolumn. The dark yellow circle represents the detectable region that vary with the electrode impedance. (Image taken from Quiroga, Nadasdy, and Ben-Shaul 2004).

-Functional interaction among spike signals detection: in order to find functional couplings between pairs of neurons.

-Extraction of a coherent complex network features: for network community structure identification.

All the steps will be described in the next sections providing a detailed analysis of all the algorithms used and/or developed here. I will introduce also some useful concepts to achieve a basic understanding of the principles applied to our analysis.

2.6.3.1 Spike sorting

In general, spike sorting algorithms consist in four major steps. The basic procedure is illustrated in the Figure 2.36, starting with the continuous data and finishing with the classified spike shapes. The

"*Wave_clus"* unsupervised algorithm (Quiroga, Nadasdy, and Ben-Shaul 2004), running on Matlab$^{®}$, was used for spike detection and sorting.

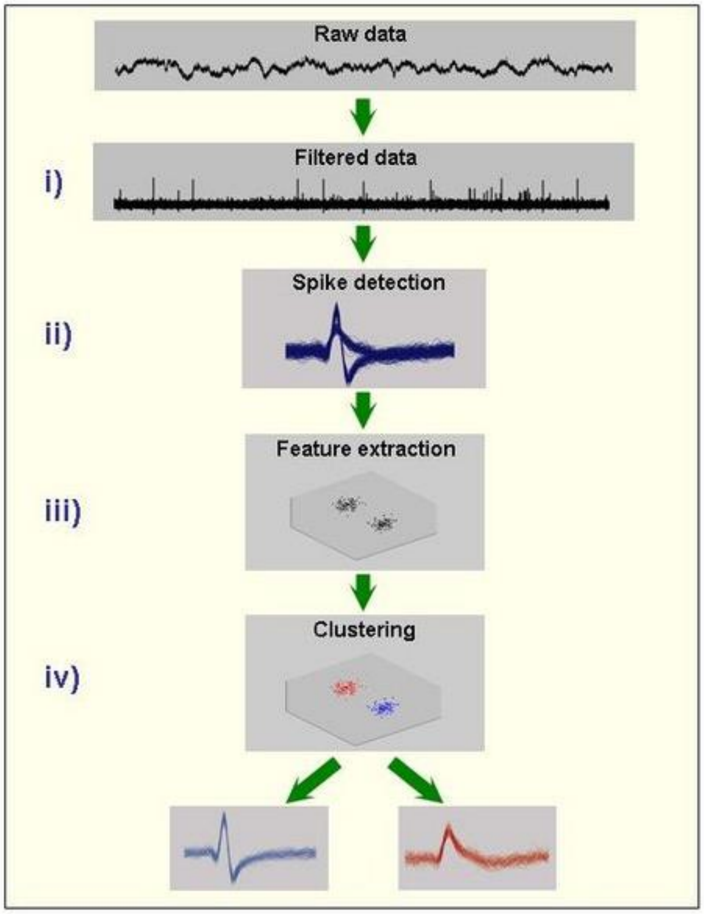

Figure 2.36. Spike sorting phases: **i)** the raw signal data is band-pass filtered; **ii)** spikes are detected imposing an amplitude threshold; **iii)** relevant features of the spike shapes are extracted; **iv)** a clustering algorithm is applied for spike classification and grouping. (Image adapted from Quiroga, Nadasdy, and Ben-Shaul 2004).

Filtering. A band pass filter was applied to the raw signal in order to remove the low frequency noise and to better visualize the spikes. The band pass filter was set between 300 and 3000 Hz. Frequencies below 300 Hz were cut to delete the slow components of the raw data and frequencies over 3000 Hz were cut to diminish the noisy appearance of the spike shapes.

Spike detection. After the signal filtration step, an amplitude threshold was applied to detect the spikes from filtered signal. False positive and negative spikes are unavoidable. Under the assumption of stable experimental conditions, the threshold was automatically set in this case. Finally, the spike waveforms are extracted with a fixed sample size (i.e. 64 samples, 24 points before the spike peak and 40 after, corresponding to a sampling frequency of 30 KHz) and aligned in order to keep the spike peak in the same sample point (Figure 2.37). The latter stage is called *peak alignment*.

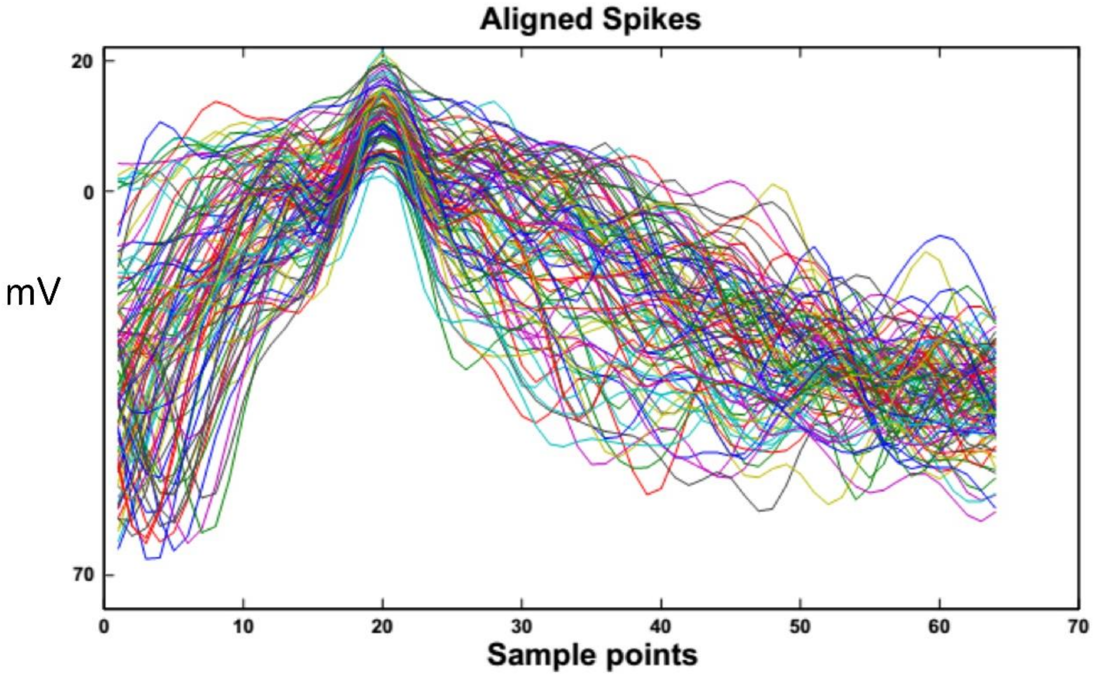

Figure 2.37. Example of aligned spikes: 100 spike waveforms each of them with 64 samples

Feature Extraction. The collected spikes belong to one or more neurons. To define two different spike waveforms it is useful to reduce the dimensionality of the spike dataset in order to consider only the feature that strongly characterizes a spike waveform. This stage is called feature extraction procedure. The dimensionality reduction consists in passing from a space of dimension m (with m the number of samples per spike) to a lower dimensional space features for extracting those features that best separate the different clusters of spikes and getting rid of all the dimensions dominated by noise. The search for the best discriminating features improves the performance of clustering algorithms and in many cases makes feasible the cluster algorithm computations. The approach used in our analysis is based on wavelet analysis, widely employed to analyse non-stationary and non-periodic signals. The wavelets transform reconstructs the signal using simple mathematical functions (as base of a vector space) that can be translated and scaled in order to recombine the original signal. The wavelet transform can detect time-frequency features that the Fourier transform cannot discriminate (Letelier and Weber 2000). The advantage of using wavelets for feature extraction is that much localized shape differences can be discerned because wavelet coefficients are localized in time.

Clustering. The fourth and final step of spike sorting is to group spikes with similar features into clusters, corresponding to the different neurons. The spike membership to a particular group means that the spike has been generated by the neuron associated with this group. The searching for the best clustering algorithm usually involves theoretical and heuristic assumptions like *a priori* feature distributions (often Gaussian). A more recent clustering method, the Super-Paramagnetic Clustering (SPC) (Quiroga, Nadasdy, and Ben-Shaul 2004), does not assume any particular distribution of the features, and it was used in this case. Such clustering method tries to replicate the natural grouping of atoms in magnetic islands (i.e. atoms with identical magnetic moment) in paramagnetic materials according to a well-known state transition mediated by temperature modulation. It groups the spikes into clusters as a function of a single parameter, i.e. the temperature. In analogy with statistical mechanics, for low temperatures all data were grouped into a single cluster and, for high temperatures, data were split into many clusters with few members each. There was, however, a middle range of temperatures corresponding to the super-paramagnetic regime where they were split into relatively large size clusters corresponding to the optimal sorting.

Validation. The sorting procedure is, however, a semi-supervised technique. Each step required the human supervision in order to prevent no biologically plausible results, e.g. an unsuitable detection threshold, too many extracted cells with similar wave shapes or otherwise few cells with different wave shapes. When this happened, the procedure was repeated changing opportunely the parameters of the previous stages (for instance, the range of temperature and the magnetic susceptibility).

2.6.3.2 Functional connections by spike-train similarities

The functional connections in neuronal spiking activity have been estimated by using the Normalized Compression Similarity (NCS) function to detect functional couplings between pair of neurons. NCS is formally defined as follows; given x and y two spike trains, the NCS is equal to:

$$\mathrm{NCS}(x,y)=\frac{\mathrm{C}(x\cdot y)\text{-}\min\big(\mathrm{C}(x),\mathrm{C}(y)\big)}{\min\big(\mathrm{C}(x),\mathrm{C}(y)\big)} \tag{2.41}$$

Where the C function represents the compressed sequence length and · is the sequence concatenation operator (e.g. 0101·101=0101101). NCS is defined in the range [0,1], where 0 indicates no interaction and 1 indicates an exact correspondence between the firing patterns of the two neurons considered. This measure was chosen in place of more conventional ones (e.g. cross-correlation) because of its ability to capture both short-range (synchronous) and long-range (delayed) interactions between neurons (Zippo et al. 2013). After the NCS estimation on all possible pairs of simultaneously recorded neurons, the resulting adjacency matrices were binarized by applying a suitable threshold in order to discard weak functional connection likely compatible with the noise in the recorded tracks.

2.6.3.3 Hints of complex brain networks and graph theoretical analysis

For understanding the organization of a complex network like the brain it is a necessary, as a first step, to understand its function as an integrated system (Bullmore et al. 2009). Over the past decade, the study of networks has rapidly expanded across a number of scientific disciplines, from social sciences to economics, systems biology, and, most recently, neuroscience (Girvan and Newman 2002). The principal reason for this expansion is the realization that a wide range of complex interconnected and dynamic systems can be described and analysed using a set of mathematical and statistical techniques originally developed in graph theory (Wilson et al. 2014; Hart et al. 2015).

Fundamentals of the Graph theory

Graphs are mathematical representations of a system that is composed of interconnected elements, comprising a set of nodes and edges. The nodes are the fundamental functional units of the system and the term *network* very often refers to a set of point-like components, nodes or vertices, V, and the relationships between them, links or edges, E. In the brain, nodes may correspond to individual neurons, neuronal populations, or brain regions (Stam and Reijneveld 2007). The edges are connections or links that relate the nodes to each other; in the brain, edges can be synapses, fibre pathways, statistical or causal relationships that describe functional association or similarity. A graph may be either undirected or directed. Intuitively, an undirected graph has “two way” connections between its nodes, while a directed edge is a “one-way” connection, and is typically drawn with arrows. The complete graph is typically represented through a connection matrix, also called “adjacency matrix”, where its elements indicate which pairs of nodes are “adjacent” i.e., directly connected by an edge (representing the structural connections) or indirectly by a path (representing the functional connections).

Given a graph $G = (V, E)$, the adjacency matrix is an $n \times n$ matrix $D = (d_{ij})$, where n is the number of vertices in $G, V = \{v_1, \dots, v_n\}$ and d_{ij} = number of edges between v_i and v_j . In particular, $d_{ij} = 0$ if (v_i, v_j) is not an edge in G. The matrix D is symmetric, i.e. $D^T = D$. In the Figure 2.38 is reported an example of graph and its adjacency matrix is illustrated.

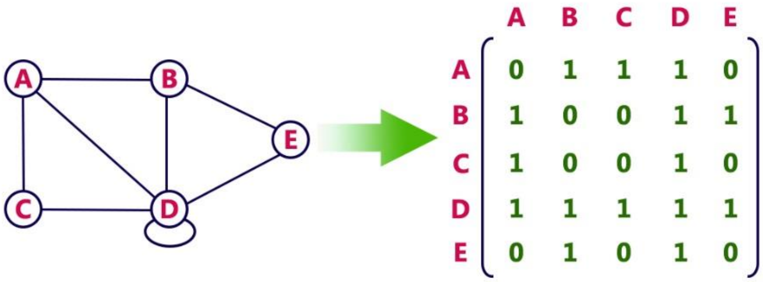

Figure 2.38. Example of graph and its adjacency matrix (Image taken from http://btechsmartclass.com).

Network measures. Once the graph is formed, its properties (and therefore those of the real-life network it represents) can be analysed mathematically (Sporns 2010). Thence, graph topology can be quantitatively described by a wide variety of measures, some of which are discussed below. All formulas are referred to a (undirected) graph$\langle V, E\rangle$, with $|V| = N$, opportunely described by the adjacency $N \times N$-matrix $A = a_{ij}$ where $a_{ij} = 1$ if and only if there exist the element (i, j) in the set E and 0 otherwise. They are:

Node degree, degree distribution. The degree of the vertex v, written as d (v), is the number of edges with v as an end vertex. By convention, a loop is counted twice and parallel edges contribute separately. The degree of a node is the number of connections that link it to the rest of the network. It is a measure of how well the node is connected.

The degrees of all the network nodes form a degree distribution P (k) defined as the fraction of nodes in the network with degree k. Thus, if there are n nodes in total in a network and n_K of them have degree k, we have $P(k) = n_k/n$.

The clustering coefficient. If the nearest neighbours of a node are also directly connected each other they form a cluster. The clustering coefficient (C) quantifies the number of connections existing between the nearest neighbours of a node as a proportion of the maximum number of possible connections. Random networks have low average clustering whereas complex networks have high clustering.

For our analysis, the clustering coefficient has been computed as follows:

$$C = \frac{1}{n}\sum_{i\in N} C_i = \frac{1}{n}\sum_{i\in N} \frac{2t_i}{k_i(k_i\text{-}1)} \tag{2.42}$$

With $t_i = \frac{1}{2}\sum_{j,h\in N} a_{ij}a_{ih}a_{jh}$.

In practice, it counts the average number of triangles t (3-node fully connected graphs) present in the network. It is a measure of fine-grain network segregation (for its definition, see Network Modularity).

Network characteristic path length and efficiency. The characteristic path length (L) of a network is the shortest path length (the minimum number of edges that must be traversed to go from one node to another) between two nodes averaged over all pairs of nodes. It is mathematically expressed as:

$$L = \frac{1}{n}\sum_{i\in N} L_i = \frac{1}{n}\sum_{i\in N}\frac{\sum_{j\in N, j\neq i} d_{ij}}{n\text{-}1} \tag{2.43}$$

It is a measure of network integration. Small values identify strongly integrated networks.

The shortest characteristic pathlength can be also defined as follows:

$$d_{ij} = \sum_{a_{fg}\in r_{i\leftrightarrow j}} a_{fg} \tag{2.44}$$

where $r_{i\leftrightarrow j}$ is the shortest path between i and j.

Efficiency is inversely related to path length but is numerically easier to use to estimate topological distances between elements of disconnected graphs.

Random and complex networks have short mean path lengths (high global efficiency of information transfer) whereas regular lattices have long mean path lengths.

Network hubs, centrality and robustness. Hubs are nodes with high degree, or high centrality. The centrality of a node measures how many of the shortest paths among all other node pairs in the network pass through it. A node with high centrality is thus crucial to efficient communication. The importance of an individual node to network efficiency can be assessed by deleting it and estimating the efficiency of the ‘lesioned’ network. Robustness refers either to the structural integrity of the network following deletion of nodes or edges or to the effects of perturbations on local or global network states.

Network modularity. Many complex networks consist of a number of modules. The modularity of a network can be computed through a large variety of algorithms, many of them based on hierarchical clustering. In the present study modularity has been computed as follows:

$$Q = \sum_{u\in M}\left[e_{uu}\text{-}\left(\sum_{v\in M} e_{uv}\right)^2\right] \tag{2.45}$$

where M is a partition of V (whose elements are called *modules*) and e_{uv} is the proportion of links that connect nodes in module u with nodes in module v. Each module contains several densely interconnected nodes, and there are relatively few connections between nodes in different modules. Hubs can therefore be described in terms of their roles in this community structure. Provincial hubs are connected mainly to nodes in their own modules, whereas connector hubs are connected to nodes in other modules.

From the computation of all these features it is possible to extract information on the network ability to integrate and segregate the signals (Sporns 2013). More in detail, network **segregation** relates to how well the network can be separated into constituent communities of nodes. Measures of segregation focus on community structure either in the form of small triangles (clustering coefficient) or larger groups of related components (modules). **Integration** is the ability of the network to integrate distributed information. One way to characterize it is the characteristic path length. It is often found to be maximized in networks with random topology, i.e. networks that do not have pronounced community structure and hence allow for very little segregated information in favour to integration. Many complex networks show a “Modules and Hubs” topology, characterized by dense local clustering of neighbouring nodes and a short path length between any (distant) pair of nodes due to the existence of relatively few long-range connections. This is an attractive model for the organization of brain anatomical and functional networks because a “Modules and Hubs” topology can support both segregated (specialised) and integrated (distributed) information processing. Moreover, “Modules and Hubs” networks are economical, tending to minimize wiring costs while supporting high dynamical complexity (van den Heuvel and Sporns 2013).

Complex networks. Different models of graph structures have been proposed during the years. Among them, lattice (or regular) and random graphs have represented the traditional classes of all network models (M. Newman 2010). (Figure 2.39). Lattice graph is a regular array of nodes with connections established exclusively between adjacent nodes. They are all local connections, ensuring a high clustering coefficient but also a high path length (since a large number of nodes characterize the path to get from one edge to the other). Random graphs, also called Erdős-Rényi graphs, are conversely characterized by nodes connected by randomly placed links. Few local connections are generated leading to a low clustering coefficient but short path lengths. Small-world organization, or better “Modules and hubs” organization, is an intermediate configuration between that of random networks and that of lattice networks. For this reason its characteristics ensure an optimal compromise between integration and segregation of the signal.

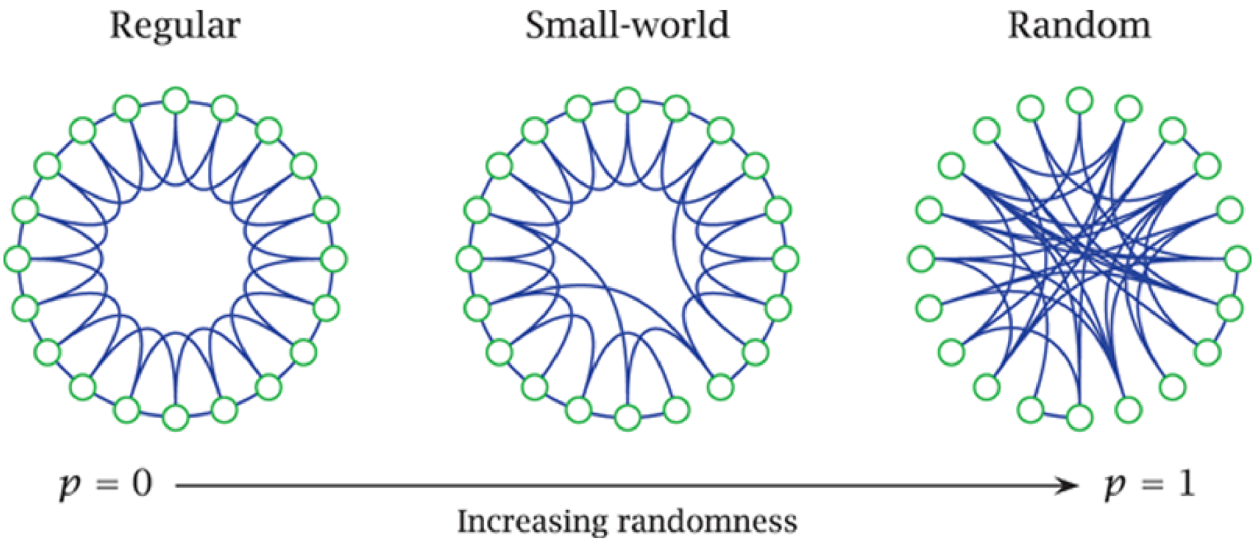

Figure 2.39. Representation of the three kinds of network models. From the left Regular (or Lattice), Small-world and Random networks. By rewiring a few of the short range connections in the lattice to any other node with a fixed probability, the small-world graphs maintains high clustering (a key feature of the lattice) but dramatically reduces its path length (in keeping a random graph), thereby parsimoniously balancing the features of segregation and integration. (Image taken from Olofsen and Dahan, 2015).

The strength of graph theory is the fact that, once a graph has been constructed, the specific meanings of nodes and edges becomes irrelevant, and the same analyses can therefore be applied to graphs originating from a wide spectrum of real-world networks. Most real-life networks are complex by definition, and their analysis has allowed to develop methodological tools which have led to a fundamental insight: profoundly different complex systems often share certain key organizational principles, and these can be quantitatively characterized by the same parameters. Thence, we could define complex networks as an informal description of a network with certain topological features that are not typical of random graphs or regular lattices. In other words, many complex systems show remarkably similar macroscopic behaviour despite profound differences in the microscopic details of the elements of each system or their mechanisms of interaction. One example of an apparently ubiquitous macroscopic behaviour in complex systems is the "Small-World-Network" architecture. However, it has been recently recognized that the correlation between complex network and "Small World Network" were not always true. Thence, the "Modules and Hub" network architecture has emerged, to better identify the complex network (van den Heuvel and Sporns 2013).

2.6.3.4 Complex brain network features

By using the NCS function (Paragraph 2.6.3.2), we estimated the functional connections of the recorded neuronal networks. We first split each recorded sequence into 250 ms time windows and then we computed the adjacency matrix for all neurons. The resulting matrices exhibited values in the unitary interval. The functional connections extracted from extracellular recordings represented the counterpart of non-oriented graphs (Figure 2.40). For the extracted graphs, we introduced a set of common statistics from the Complex Network Theory able to detect possible matches between the extracted graphs and prominent topological properties (Paragraph 2.4.3.3)

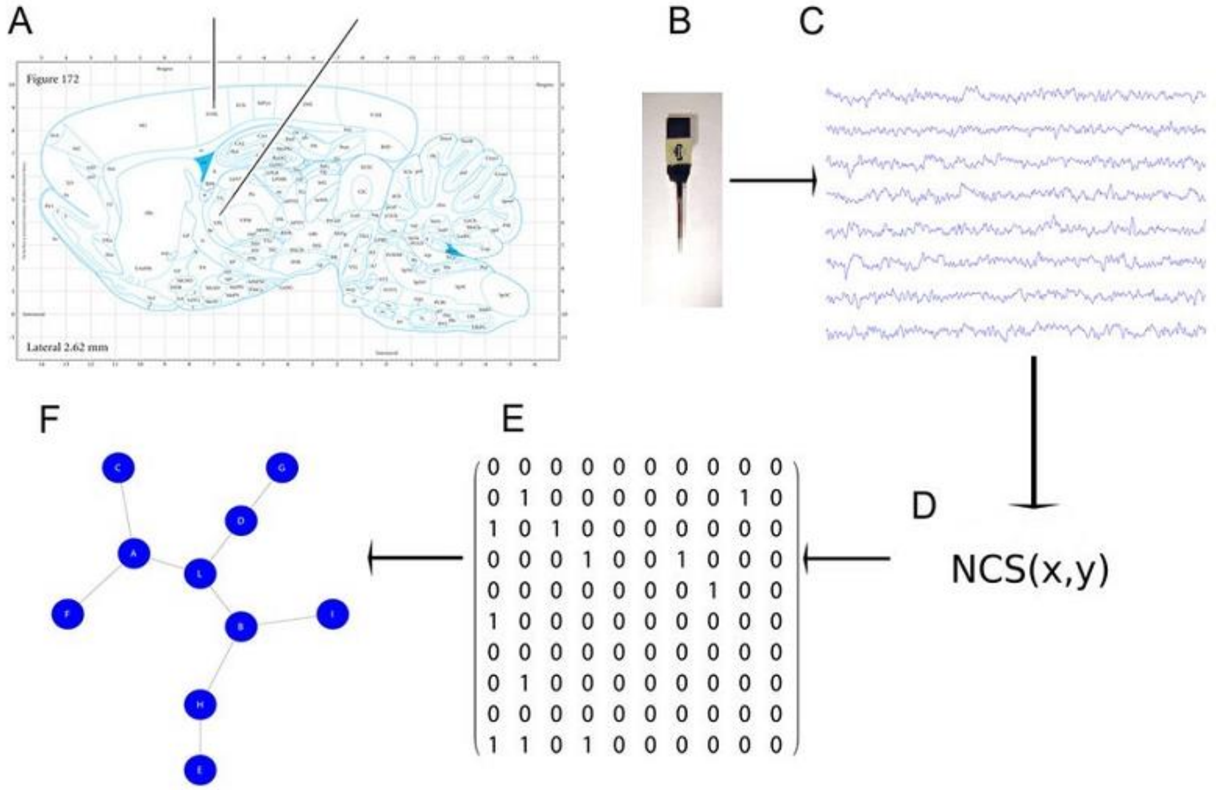

Figure 2.40. Illustration of the electrophysiological experimental work-flow. **(A)** Stereotactile coordinates are taken from Paxinos's atlas (Paxinos and Watson, 2006). The two black lines represent our regions of interest, where microelectrode matrices **(B)** were placed. **(C)** A typical time series of the raw extracellular recordings where the functional connections were extracted by means of the function in **(D)**. **(E)** A sample of a binary matrix extracted by recordings that corresponds to the graph in **(F)**.

"Modules and Hubs"network identification. From a functional perspective, "Modules and Hubs" networks can express two important information-processing features: information integration and segregation. Functional segregation recruits specialized processing within densely interconnected nodes. Functional integration combines information processed in distributed nodes. These network properties can be measured by two statistics: the clustering coefficient (C) and the characteristic path length (L). The former measures how close the neighbours of a node are to being a cluster. The latter estimates the average shortest path length in the graph, i.e. how much the nodes are accessible. Both measures, implemented in a Matlab toolbox, were used for our network analyses (Rubinov and Sporns 2010).

Community structure identification. Community structure identification methods normally assume that the network of interest divides naturally into subgroups and the experimenter's job is to find those groups (M. E. J. Newman 2006; Blondel et al. 2008). The number and size of the groups are thus determined by the network itself and not by the experimenter. We wanted to determine whether there exists any natural division of its vertices into non overlapping groups or communities, where these communities may be of any size. We focused initially on the problem of whether any network division exists into just two communities looking for divisions of the vertices into two groups so as to minimize the number of edges running between the groups. A good division of a network into communities was not merely one in which there were few edges between communities; it was one in which there were fewer than expected edges between communities. If the number of edges between two groups was only what one would expect on the basis of random chance, then few thoughtful observers would claim this constitutes evidence of meaningful community structure. On the other hand, if the number of edges between groups was significantly less than we expected by chance, or equivalent if the number within groups is significantly higher, then it is reasonable to conclude that we are dealing with community groups. An example of the spiking activity functional graph is reported in Figure 2.41.

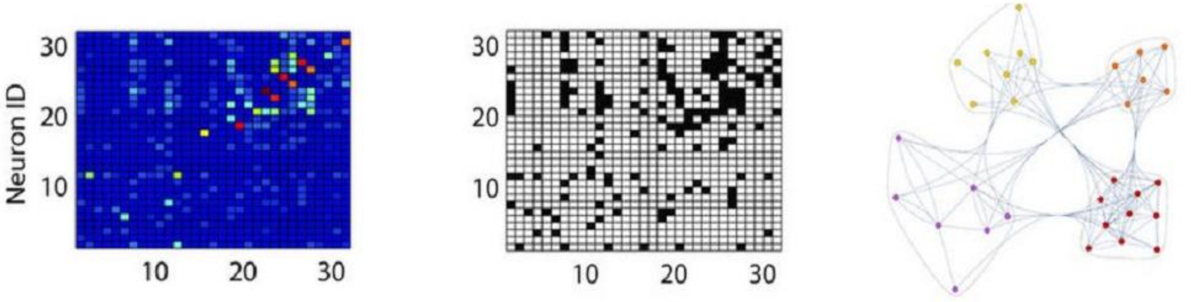

Figure 2.41. Example of the spiking activity functional graphs. Left: the raw weighted adjacency matrices. Centre: the respective binarized versions. Right: the graphs as plotted by the "CommunityGraphPlot" function (Mathematica, www.wolfram.com).

This idea, that true community structure in a network corresponds to a statistically surprising arrangement of edges, can be quantified by using the measure known as modularity (Paragraph 2.6.3.3). The modularity is the number of edges falling within groups minus the expected number in an equivalent network with edges placed at random. The modularity can be either positive or negative, with positive values indicating the possible presence of community structure. Thus, one can search for community structure precisely by looking for the divisions of a network that have positive, and preferably large, values of the modularity. In order to find more than two communities, so we have extended the method to find good divisions of networks into larger numbers of parts. The standard approach to this problem, and the one adopted here, is repeated division into two: we use the algorithm previous mentioned to divide the network into two parts, then divide those parts, and so forth.

References

Assad J.A., Berdondini L., Cancedda L., De Angelis F.,… and Leonardo Sileo. 2014. “Brain Function: Novel Technologies Driving Novel Understanding.” *Bioinspired Approaches for Human-Centric Technologies*, 299–334. doi:10.1007/978-3-319-04924-3_10.

Azároff L.V. 1968. “*Elements of X-Ray Crystallography*.”

Baruchel J., Buffiere J.Y., Cloetens P., Di Michiel M., … and Salvo L. 2006. “Advances in Synchrotron Radiation Microtomography.” *Scripta Materialia*. doi:10.1016/j.scriptamat.2006.02.012.

Bear M., Connor B. and Paradiso M. 2014. *“NEUROSCIENCE Exploring the Brain.” Lippincott Williams & Wilkins*. doi:10.1007/s13398-014-0173-7.2.

Beer. 1852. “Determination of the Absorption of Red Light in Colored Liquids.” *Annalen Der Physik Und Chemie. 86: 78–88. Oxford University*.

Blondel V. D., Guillaume J.L., Lambiotte R. and Lefebvre E. 2008. “Fast Unfolding of Communities in Large Networks.” *Journal of Statistical Mechanics*. doi:10.1088/1742-5468/2008/10/P10008.

Blum H. 1967. “A Transformation for Extracting New Descriptors of Shape.” *Models for the Perception of Speech and Visual Form*. papers2://publication/uuid/33A7D570-B63C-4E43-996A-4DE15D8EE75F.

Bonse U., Johnson Q., Nichols M., Nusshardt R. and Kinney J. 1986. “High Resolution Tomography with Chemical Specificity.” *Nuclear Inst. and Methods in Physics Research, A*. doi:10.1016/0168-9002(86)90167-1.

Born M. and Emil W. 1994. “*Principles of Optics: Electromagnetic Theory of Propagation, Interference and Diffraction of Light*.” *Pergamon Press*. doi:10.1016/S0030-3992(00)00061-X.

Bräuer-Krisch E., Requardt H., Brochard T., Berruyer G., Renier M., Laissue J.A. and Bravin A. 2009. “New Technology Enables High Precision Multislit Collimators for Microbeam Radiation Therapy.” *Review of Scientific Instruments*. doi:10.1063/1.3170035.

Bravin A., Fiedler S., Coan P., Labiche J.C., Ponchut C., Peterzol A. and Thomlinson W. 2003. “Comparison between a Position Sensitive Germanium Detector and a Taper Optics CCD ‘FRELON’ camera for Diffraction Enhanced Imaging.” *Nuclear Instruments and Methods in Physics Research, Section A: Accelerators, Spectrometers, Detectors and Associated Equipment*. doi:10.1016/S0168-9002(03)01675-9.

Bravin A., Coan P. and Pekka Suortti. 2013. “X-Ray Phase-Contrast Imaging: From Pre-Clinical Applications towards Clinics.” *Physics in Medicine and Biology* 58 (1): R1–35. doi:10.1088/0031-9155/58/1/R1.

Bullmore E.T., Sporns O. and Solla S.A. 2009. “Complex Brain Networks: Graph Theoretical Analysis of Structural and Functional Systems.” *Nature Review Neuroscience*. doi:10.1038/nrn2575.

Cittert Van P. 1934. “Die Wahrscheinliche Schwingungsverteilung in Einer von Einer Lichtquelle Direkt Oder Mittels Einer Linse Beleuchteten Ebene.” *Physica* 1 (1–6): 201–10. doi:10.1016/S0031-8914(34)90026-4.

Cloetens P., Ludwig W., Baruchel J., Van Dyck D., Van Landuyt J., Guigay J.P. and M. Schlenker. 1999. “Holotomography: Quantitative Phase Tomography with Micrometer Resolution Using Hard Synchrotron Radiation X Rays.” *Applied Physics Letters*. doi:10.1063/1.125225.

Cloetens P., Barrett R., Baruchel J., Guigay J.P. and Schlenker M. 1996. “Phase Objects in Synchrotron Radiation Hard X-Ray Imaging.” *J. of Physics. D:Applied Physics.* doi.org/10.1088/0022-3727/29/1/023.

Cnudde V. and Boone M.N. 2013. “High-Resolution X-Ray Computed Tomography in Geosciences: A Review of the Current Technology and Applications.” *Earth-Science Reviews*. doi:10.1016/j.earscirev.2013.04.003.

Contreras D. 2004. “Electrophysiological Classes of Neocortical Neurons.” *Neural Networks* 17 (5–6): 633–46. doi:10.1016/j.neunet.2004.04.003.

Davidoiu V., Sixou B., Langer M. and Peyrin F. 2013. “In-Line Phase Tomography Using Nonlinear Phase Retrieval.” *Annals of the University of Bucharest. Mathematical Series* 4 (LXII): 115–22. https://hal.archives-ouvertes.fr/hal-01123786#.WapwMfs50M0.mendeley.

Dellon A.L., Mackinnon S.E. and Brandt K.E. 2017. “The Markings of the Semmes-Weinstein Nylon Monofilaments.” *Journal of Hand Surgery* 18 (4). Elsevier: 756–57. doi:10.1016/0363-5023(93)90333-X.

Delpy D.T., Cope M., Van der Zee P., Arridge S., Wray S. and Wyatt J. 1988. “Estimation of Optical Pathlength through Tissue from Direct Time of Flight Measurement.” *Physics in Medicine and Biology* 33 (12): 1433–42. doi:10.1088/0031-9155/33/12/008.

Elliott J. C. and Dover S.D. 1982. “X-Ray Microtomography.” *Journal of Microscopy* 126 (2). Blackwell Publishing Ltd: 211–13. doi:10.1111/j.1365-2818.1982.tb00376.x.

Elliott J.C. and Dover S.D. 1985. “X-Ray Microscopy Using Computerized Axial Tomography.” *Journal of Microscopy* 138 (3). Blackwell Publishing Ltd: 329–31. doi:10.1111/j.1365-2818.1985.tb02627.x.

Ford L. R. and D. R. Fulkerson. 1956. “Maximal Flow through a Network.” *Canadian Journal of Mathematics*. doi:10.4153/CJM-1956-045-5.

Gilboy W.B. 1984. “X- and γ-Ray Tomography in NDE Applications.” *Nuclear Instruments and Methods in Physics Research* 221 (1): 193–200. doi:10.1016/0167-5087(84)90199-6.

Girvan M. and Newman M.E.J. 2002. “Community Structure in Social and Biological Networks.” *Proceedings Of The National Academy Of Sciences Of The United States Of America-Biological Sciences*.

Gonzalez R. C. and Woods R.E. 2008. *“Digital Image Processing.”*

Grodzins L. 1983. “Optimum Energies for X-Ray Transmission Tomography of Small Samples. Applications of Synchrotron Radiation to Computerized Tomography I.” *Nuclear Instruments and Methods In Physics Research*. doi:10.1016/0167-5087(83)90393-9.

Guigay J P. 1977. “Fourier Transform Analysis of Fresnel Diffraction Patterns and in-Line Holograms.” *Optik* 49 (1).

Hart M. G, Ypma R., Romero-Garcia R., Price S.J. and Suckling J. 2015. “Graph Theory Analysis of Complex Brain Networks: New Concepts in Brain Mapping Applied to Neurosurgery.” *Journal of Neurosurgery*. doi:10.3171/2015.4.JNS142683.

Herman G. and Gabor H. 2009. *“Fundamentals of Computerized Tomography: Image Reconstruction from Projections. ” Science (New York, N.Y.)*. doi:10.1007/978-3-642-15992-3.

Heuvel van den M. and Olaf Sporns. 2013. “Network Hubs in the Human Brain.” *Trends in Cognitive Sciences*. doi:10.1016/j.tics.2013.09.012.

Holmes K., Roberts O.L., Thomas A.M. and Cross M.J. 2007. “Vascular Endothelial Growth Factor Receptor-2: Structure, Function, Intracellular Signalling and Therapeutic Inhibition.” *Cellular Signalling*. doi:10.1016/j.cellsig.2007.05.013.

Horecker B. L. 1943. “The absorption spectra of hemoglobin and its derivatives in the visible and near infra-red regions.” *J. Biol. Chem* 148-173.

Izhikevich E.M. 2003. “Simple Model of Spiking Neurons.” *IEEE Trans. Neural Networks*. doi:10.1109/TNN.2003.820440.

Jackson J.D. 1975. *"Classical Electrodynamics." Wiley, New York.*

Jaggi A.S., Jain V. and Singh N. 2011. "Animal Models of Neuropathic Pain." *Fundamental and Clinical Pharmacology* 25 (1): 1–28. doi:10.1111/j.1472-8206.2009.00801.x.

Jobsis F.F. 1977. "Noninvasive, Infrared Monitoring of Cerebral and Myocardial Oxygen Sufficiency and Circulatory Parameters." *Science* 198 (4323): 1264 LP-1267. http://science.sciencemag.org/content/198/4323/1264.

Kak A.C. and Slaney M. 1988. "*Principles of Computerized Tomographic Imaging*." doi:10.1118/1.1455742.

Keyriläinen J., Fernández M. and Suortti P. 2002. "Refraction Contrast in X-Ray Imaging." *Nuclear Instruments and Methods in Physics Research, Section A: Accelerators, Spectrometers, Detectors and Associated Equipment*. doi:10.1016/S0168-9002(02)00442-4.

Koh P.H., Glaser D.E., Flandin G., Kiebel S., Butterworth B., Maki A., Delpy D.T. and Elwell C.E. 2007. "Functional Optical Signal Analysis: A Software Tool for near-Infrared Spectroscopy Data Processing Incorporating Statistical Parametric Mapping." *Journal of Biomedical Optics* 12 (6): 64010. doi:10.1117/1.2804092.

Labiche J.C., Mathon O., Pascarelli S., Newton M.A., …, and David Fernandez Carreiras. 2007. "The Fast Readout Low Noise Camera as a Versatile X-Ray Detector for Time Resolved Dispersive Extended X-Ray Absorption Fine Structure and Diffraction Studies of Dynamic Problems in Materials Science, Chemistry, and Catalysis." *Review of Scientific Instruments* 78 (9): 91301. doi:10.1063/1.2783112.

Langer M., Cloetens P., Pacureanu A. and Peyrin F. 2012. "X-Ray in-Line Phase Tomography of Multimaterial Objects." *Optics Letters*. doi:10.1364/OL.37.002151.

Langer M., Cloetens P. and Peyrin F. 2010. "Regularization of Phase Retrieval with Phase-Attenuation Duality Prior for 3-D Holotomography." *IEEE Transactions on Image Processing*. doi:10.1109/TIP.2010.2048608.

Lee T.C., Kashyap R.L. and Chu C.N. 1994. "Building Skeleton Models via 3-D Medial Surface Axis Thinning Algorithms." *CVGIP: Graphical Models and Image Processing* 56 (6): 462–78. doi:10.1006/cgip.1994.1042.

Letelier J.C. and Weber P.P. 2000. "Spike Sorting Based on Discrete Wavelet Transform Coefficients." *Journal of Neuroscience Methods* 101 (2): 93–106. doi:10.1016/S0165-0270(00)00250-8.

Llinas R.R. 1988. “Intrinsic Electrophysiological Properties Central Nervous System Function.” *Science* 242(4886):1654-64.

Mandrell R.E., Griffiss J.M. and Macher B.A. 1988. “Lipooligosaccharides (LOS) of Neisseria Gonorrhoeae and Neisseria Meningitidis Have Components That Are Immunochemically Similar to Precursors of Human Blood Group Antigens. Carbohydrate Sequence Specificity of the Mouse Monoclonal Antibodies That Recognize Crossreacting Antigens on LOS and human erythrocytes” *Journal of Experimental Medicine* 168 (1). http://jem.rupress.org/content/168/1/107.

Marone F., Hintermüller C., McDonald S., Abela R., Mikuljan G., Isenegger A. and Stampanoni M. 2008. “X-Ray Tomographic Microscopy at TOMCAT.” *Developments in X-Ray Tomography IV*. doi:10.1117/12.803147.

Marone F., Mokso R., Modregger P., Fife J., Pinzer B., Thüring T., Mader K., Mikuljan G., Isenegger A. and Stampanoni M. 2010. “Present and Future X-Ray Tomographic Microscopy at TOMCAT.” In *AIP Conference Proceedings*. doi:10.1063/1.3625318.

Mills D.M., Helliwell J.R., Kvick Å., Ohta T., Robinson I.A. and Authier A. 2005. “Report of the Working Group on Synchrotron Radiation Nomenclature - Brightness, Spectral Brightness or Brilliance?” *Journal of Synchrotron Radiation* 12 (3). International Union of Crystallography: 385. doi:10.1107/S090904950500796X.

Mirone A., Brun E., Gouillart E., Tafforeau P. and Kieffer J. 2014. “The PyHST2 Hybrid Distributed Code for High Speed Tomographic Reconstruction with Iterative Reconstruction and a Priori Knowledge Capabilities.” *Nuclear Instruments and Methods in Physics Research, Section B: Beam Interactions with Materials and Atoms* 324: 41–48. doi:10.1016/j.nimb.2013.09.030.

Mobilio S. and Balerna A.. 2003. “Introduction to the Main Properties of Synchrotron Radiation.” *Italian Physical Society* 82:1–24. http://server2.phys.uniroma1.it/gr/lotus/Mariani_carlo/didattica/cap_01_Mobilio.pdf.

Mobilio S., Boscherini F. and Meneghini C. 2015. “Synchrotron Radiation: Basics, Methods and Applications.” *Synchrotron Radiation: Basics, Methods and Applications*, 1–799. doi:10.1007/978-3-642-55315-8.

Momose A., Takeda T., Itai Y. and Hirano K. 1996. “Phase-Contrast X-Ray Computed Tomography for Observing Biological Soft Tissues.” *Nature Medicine*. doi:10.1038/nm0496-473.

Newman M.E.J. 2010. “*Networks: An Introduction*.” *Oxford Press.*

doi:10.1093/acprof:oso/9780199206650.001.0001.

Newman, M. E. J. 2006. “Modularity and Community Structure in Networks.” *Proceedings of the National Academy of Sciences*. doi:10.1073/pnas.0601602103.

Ogniewicz, R L. 1995. “Automatic Medial Axis Pruning by Mapping Characteristics of Boundaries Evolving under the Euclidean Geometric Heat Flow onto Voronoi Skeletons.” *IEEE Transactions on Pattern Analysis and Machine Intelligence.*

Paganin D., Mayo S.C., Gureyev T.E., Miller P.R. and Wilkins S.W. 2002. “Simultaneous Phase and Amplitude Extraction from a Single Defocused Image of a Homogeneous Object.” *Journal of Microscopy*. doi:10.1046/j.1365-2818.2002.01010.x.

Palmer K.F. and Williams D. 1974. “Optical Properties of Water in the near Infrared.” *J. Optical Society of Ameruca* 64 (8). OSA: 1107–10. doi:10.1364/JOSA.64.001107.

Paxinos G. and C Watson. 1986. *“The Rat Brain in Stereotaxic Coordinates.” New York: Academic Press.*

Pellicer A., Bravo M.D.C., Bauersfeld U., … and Bucher H.U. 2011. “Near-Infrared Spectroscopy: A Methodology-Focused Review.” *Seminars in Fetal & Neonatal Medicine* 16 (1). Elsevier: 42–49. doi:10.1016/j.siny.2010.05.003.

Peyrin F., Cloetens P., Salome-Pateyron M., Baruchel J. and Spanne P. 1997. “Reconstruction 3D En Tomographie Par Rayonnement Synchrotron Coherent.” *16° Colloque Sur Le Traitement Du Signal et Des Images, 1997 ; P. 423-426*. GRETSI, Groupe d’Etudes du Traitement du Signal et des Images. http://documents.irevues.inist.fr/handle/2042/12639#.WapxOyJYxsM.mendeley.

Quiroga R.Q., Nadasdy Z. and Ben-Shaul Y. 2004. “Unsupervised Spike Detection and Sorting with Wavelets and Superparamagnetic Clustering.” *Neural Computation*. doi:10.1162/089976604774201631.

Raichle M.E. and Gusnard D.A. 2002. “Appraising the Brain’s Energy Budget.” *Proceedings of the National Academy of Sciences* 99 (16): 10237–39. doi:10.1073/pnas.172399499.

Randi A. M. and M.A. Laffan. 2017. “Von Willebrand Factor and Angiogenesis: Basic and Applied Issues.” *Journal of Thrombosis and Haemostasis* 15 (1): 13–20. doi:10.1111/jth.13551.

Raven C., Snigirev A. and Snigireva I. 1996. “Phase-Contrast Microtomography with Coherent High-Energy Synchrotron X Rays.” *Applied Physics Letter.* 69 (13): 1826–28.

Renier M., Brochard T., Nemoz C. and Thomlinson W. 2002. “A White-Beam Fast-Shutter for Microbeam

Radiation Therapy at the ESRF.” *Nuclear Instruments and Methods in Physics Research, Section A: Accelerators, Spectrometers, Detectors and Associated Equipment*. doi:10.1016/S0168-9002(01)00905-6.

Rinaldi S., Calzà L., Giardino L., Biella G.E.M., Zippo A.G. and Fontani V. 2015. “Radio Electric Asymmetric Conveyer: A Novel Neuromodulation Technology in Alzheimer and Other Neurodegenerative Diseases.” *Frontiers in Psychiatry* 6. doi:10.3389/fpsyt.2015.00022.

Río Del M.S. and Dejus R.J. 2004. “XOP 2.1 -A New Version of the X-Ray Optics Software Toolkit.” In *AIP Conference Proceedings*. doi:10.1063/1.1757913.

Rositi H., Frindel C., Wiart M., Langer M., Olivier C., Peyrin F. and Rousseau D. 2014. “Computer Vision Tools to Optimize Reconstruction Parameters in X-Ray in-Line Phase Tomography.” *Physics in Medicine and Biology*. doi:10.1088/0031-9155/59/24/7767.

Rubinov M. and Sporns O. 2010. “Rubinov and Sporns - 2010 - Complex Network Measures of Brain Connectivity.” *NeuroImage*. doi:http://dx.doi.org/10.1016/j.neuroimage.2009.10.003.

Salomé M., Peyrin F., Cloetens P., Odet C., Laval-Jeantet A.M., Baruchel J. and Spanne P. 1999. “A Synchrotron Radiation Microtomography System for the Analysis of Trabecular Bone Samples.” *Medical Physics*. doi:10.1118/1.598736.

Sato T., Ikeda O., Yamakoshi Y. and Tsubouchi M. 1981. “X-Ray Tomography for Microstructural Objects.” *Applied Optics*. doi:10.1364/AO.20.003880.

Seltzer Z., Dubner R. and Shir Y. 1990. “A Novel Behavioral Model of Neuropathic Pain Disorders Produced in Rats by Partial Sciatic Nerve Injury.” *Pain* 43 (2): 205–18. doi:10.1016/0304-3959(90)91074-S.

Serduc R., Van De Looij Y., Francony G., Verdonck O., … and Lahrech H. 2008. “Characterization and Quantification of Cerebral Edema Induced by Synchrotron X-Ray Microbeam Radiation Therapy.” *Physics in Medicine and Biology*. doi:10.1088/0031-9155/53/5/001.

Snigirev A., Snigireva I., Kohn V., Kuznetsov S. and Schelokov I. 1995. “On the Possibilities of X-Ray Phase Contrast Microimaging by Coherent High-Energy Synchrotron Radiation.” *Review of Scientific Instruments*. doi:10.1063/1.1146073.

Sokoloff L. 1973. “Metabolism of Ketone Bodies by the Brain.” *Annual Review of Medicine* 24 (1): 271–80. doi:10.1146/annurev.me.24.020173.001415.

Sousa De M.V.P., Ferraresi C., De Magalhes A.C., Yoshimura E.M. and Hamblin M.R. 2014. "Building, Testing and Validating a Set of Home-Made von Frey Filaments: A Precise, Accurate and Cost Effective Alternative for Nociception Assessment." *Journal of Neuroscience Methods*. doi:10.1016/j.jneumeth.2014.04.017.

Spira M.E. and Hai A. 2013. "Multi-Electrode Array Technologies for Neuroscience and Cardiology." *Nature Nanoscience* 8 (2). 83–94. http://dx.doi.org/10.1038/nnano.2012.265.

Sporns O. 2010. "Networks of the Brain : Quantitative Analysis and Modeling." *Analysis and Function of Large-Scale Brain Networks*.

Sporns O. 2013. "Network Attributes for Segregation and Integration in the Human Brain." *Current Opinion in Neurobiology*. doi:10.1016/j.conb.2012.11.015.

Stam C.J. and Reijneveld J.C. 2007. "Graph Theoretical Analysis of Complex Networks in the Brain." *Nonlinear Biomed Phys*. doi:1753-4631-1-3 [pii] 10.1186/1753-4631-1-3 ET - 2007/10/03.

Stockman G. and Shapiro L.G. 2001. *Computer and Robot Vision. 1st ed. Upper Saddle River*, NJ, USA: Prentice Hall PTR.

Stuttfeld E. and Ballmer-Hofer K. 2009. "Structure and Function of VEGF Receptors." *IUBMB Life* 61 (9). Wiley Subscription Services: 915–22. doi:10.1002/iub.234.

Teague M.R. 1982. "Irradiance Moments: Their Propagation and Use for Unique Retrieval of Phase." *Journal of the Optical Society of America*. doi:10.1364/JOSA.72.001199.

Weinstein S. 1993. "Fifty Years of Somatosensory Research." *Journal of Hand Therapy*. doi:10.1016/S0894-1130(12)80176-1.

Wilson R.J. 2014. *"Introduction to Graph Theory." Pearson Education India*. doi:10.1007/s13398-014-0173-7.2.

Witte De Y. 2010. "Improved and Practically Feasible Reconstruction Methods for High Resolution X-Ray Tomography," 270. https://biblio.ugent.be/publication/1002586/file/4335339.pdf.

Wray S., Cope M., Delpy D.T., Wyatt J.S. and Reynolds E.O.R. 1988. "Characterization of the near Infrared Absorption Spectra of Cytochrome aa3 and Haemoglobin for the Non-Invasive Monitoring of Cerebral Oxygenation." *Biochimica et Biophysica Acta (BBA) - Bioenergetics* 933 (1): 184–92. doi:10.1016/0005-2728(88)90069-2.

Wu X., Liu H. and Yan A. 2005. "X-Ray Phase-Attenuation Duality and Phase Retrieval." *Optics Letters*.

doi:10.1364/OL.30.000379.

Zachariasen W H. 1945. *“Theory of X-Ray Diffraction in Crystals.” J.Wiley & Sons Inc. New York.*

Zippo A.G., Gelsomino G., Duin P.V., Nencini S., Caramenti G.C.,Valente M. and Biella G.E.M. 2013. “Small-World Networks in Neuronal Populations: A Computational Perspective.” *Neural Networks* 44. doi:10.1016/j.neunet.2013.04.003.

Chapter 3: Results

Abstract

The results coming from the composite experimental activity is here illustrated. The first part of the chapter is dedicated to the microstructural analysis: the cortical microvasculature, revealed by X-ray microCT Imaging has been rendered in 3D. From a comparative study, "Neuropathic vs Control" rats, evidences of vascular neo-genesis have been found in all CP rats. In a second moment, results coming from immunofluorescence microscopy are shown, aiming at confirming previous findings in rat microvasculature. Finally, in vivo chronic electrophysiological recordings, planned for investigating the neuronal dynamic are presented by means of Graph Theory.

Résumé

Les résultats provenant de l'activité expérimentale composite sont ici illustrés. La première partie du chapitre est dédiée à l'analyse microstructurale: la microvasculation corticale, révélée par micro-tomographie par rayons X, a été rendue en 3D. À partir d'une étude comparant des rats "Neuropathic" vs des rats "Control", une néo-genèse vasculaire a été trouvée dans tous les rats CP. Dans un second temps, les résultats provenant de la microscopie d'immunofluorescence sont montrés, visant à confirmer les résultats précédents dans la microvasculation de rat. Enfin, les enregistrements électrophysiologiques chroniques in vivo, prévus pour l'étude de la dynamique neuronale, sont présentés au moyen de la théorie des graphes.

Contents

3 Results

The extensive and multidisciplinary experimental activity, underlying the morpho-functional study of CP-induced effects on somatosensory cortical region, produced a large amount of data, opportunely processed in order to extract both quantitative and qualitative information. Data can be grouped into four categories:

1) 3D images of the somatosensory cortical samples analyzed by three different X-ray CT Imaging modalities (at the ID17, TOMCAT and ID16A beamlines).
2) Morphometric characterization of the cortical microvascular network to establish a structural comparative study "Control vs Neuropathic" rats.
3) Immunofluorescence microscopy images to validate the results coming from the X-ray Imaging study.
4) Neurodynamic analysis for the identification of differences in the functional connectivity network of Thalamo Cortical (TC) circuit.

All the results obtained contributed to characterize both functionally and structurally the CP in experimental rats, providing interesting new findings at the level of the tripartite synapse and the blood microvessel environment. They will be presented in this chapter according to each experimental session performed.

In the last paragraph also the very preliminary results relatives to the NIRS recordings experiment will be illustrated.

3.1 MicroCT Imaging tests: preliminary investigation of cortical vasculature

The first X-ray imaging analysis of rat somatosensory cortex led to the identification of blood vasculature at macro-scale level. The reconstructed volumes of samples coming from control rats at two different pixel sizes (8 µm and 3.5 µm) proved that the large diameter vessels were detectable by applying the PBPCI technique (Materials and Methods, 2.2.3 and 2.2.4) without the injection of any contrast agent within the rat vascular system. In the Figure 3.1 the CT transversal slices of the cortical sample of control rat clearly show the presence of big blood vessels (from 70 µm down to 30 µm in diameter). In order to detect the whole vascular thread, extending from the big arteries to the small capillaries, higher resolution imaging was needed.

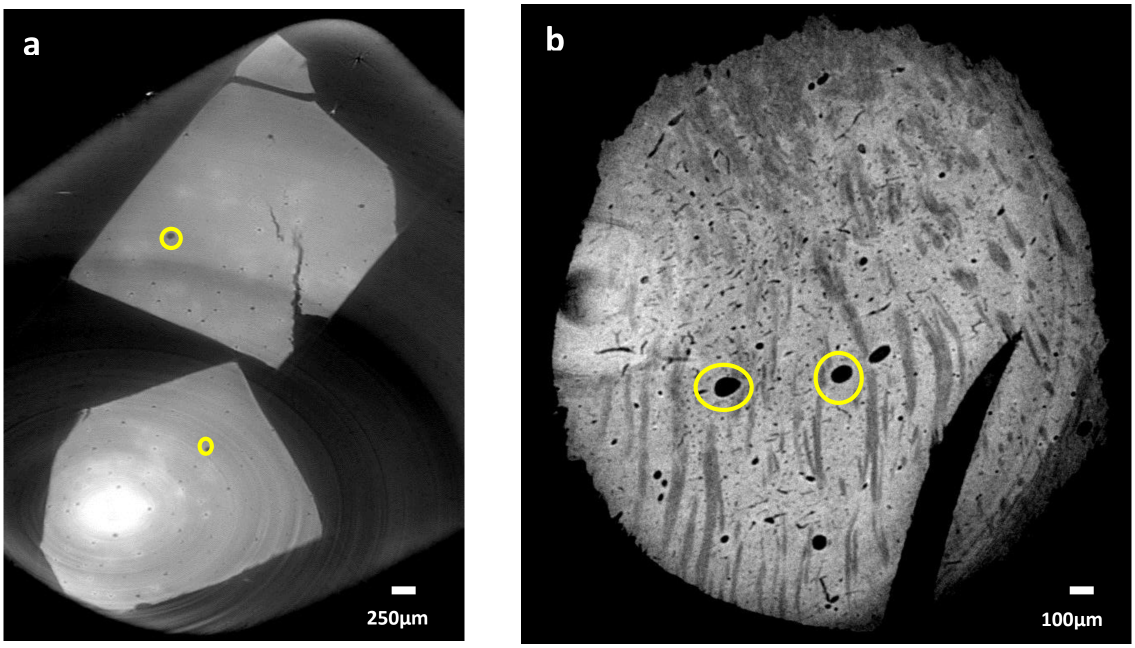

Figure 3.1. CT transversal slices of control rat somatosensory cortical regions showing the large diameter cortical vessels (cycled) at two different resolutions 8 µm **(a)** and 3.5 µm **(b)** through PBPCI technique.

3.2 MicroCT Imaging at TOMCAT: revealing microvascular changes in CP rats

During these experimental sessions, the very high resolution achieved together with the ad-hoc developed sample preparation protocol allowed for the 3D visualization of the cortical vascular network at micro-scale. Volumes of the somatosensory cortical microvasculature have been collected and post processed according to the procedure described before (Materials and Methods, 2.4.3-2.4.4 and 2.5.2). The first sample analysed, belonging to a control rat, was used to test the experimental technical parameters and the volume reconstruction modality. The optimization of the parameters involved both in image acquisition and in image reconstruction yielded to the detection of the whole cortical microvasculature: from the arteries up to the capillary elements (inner diameter < 8 µm). The image reconstruction and post-processing phases have been performed according to a step-by-step procedure. In order to understand all the operations applied for the first sample scanned, "*s_9*", the results relative to each single step are presented. Only for this sample the total height investigated was larger than the following ones (1769 µm from the top of the cortical surface) to attempt, in this way, the 3D visualization of the whole microvasculature. Two pixel sizes have been used: 0.325 µm for the entire sample and 0.162 µm just on a reduced portion of it, in order to allow for the detection of neuronal and glial elements within the tissue. All the results achieved step by step are reported following the procedure fully described in Materials and Methods 2.6.1).

Image reconstruction. The Paganin phase retrieval algorithm has been applied and the optimal values for δ and β has been set equal to $1.70*10^{-8}$ and $1.70*10^{-10}$ respectively. After the image cropping and intensity normalization, the total volume can be opened and visualized through *ImageJ* as *.tiff* image sequence (8-bit).In the transversal slices of the same sample, scanned at the two different pixel sizes, the blood microvessels are clearly highlighted by the contrast agent used (Figure 3.2).

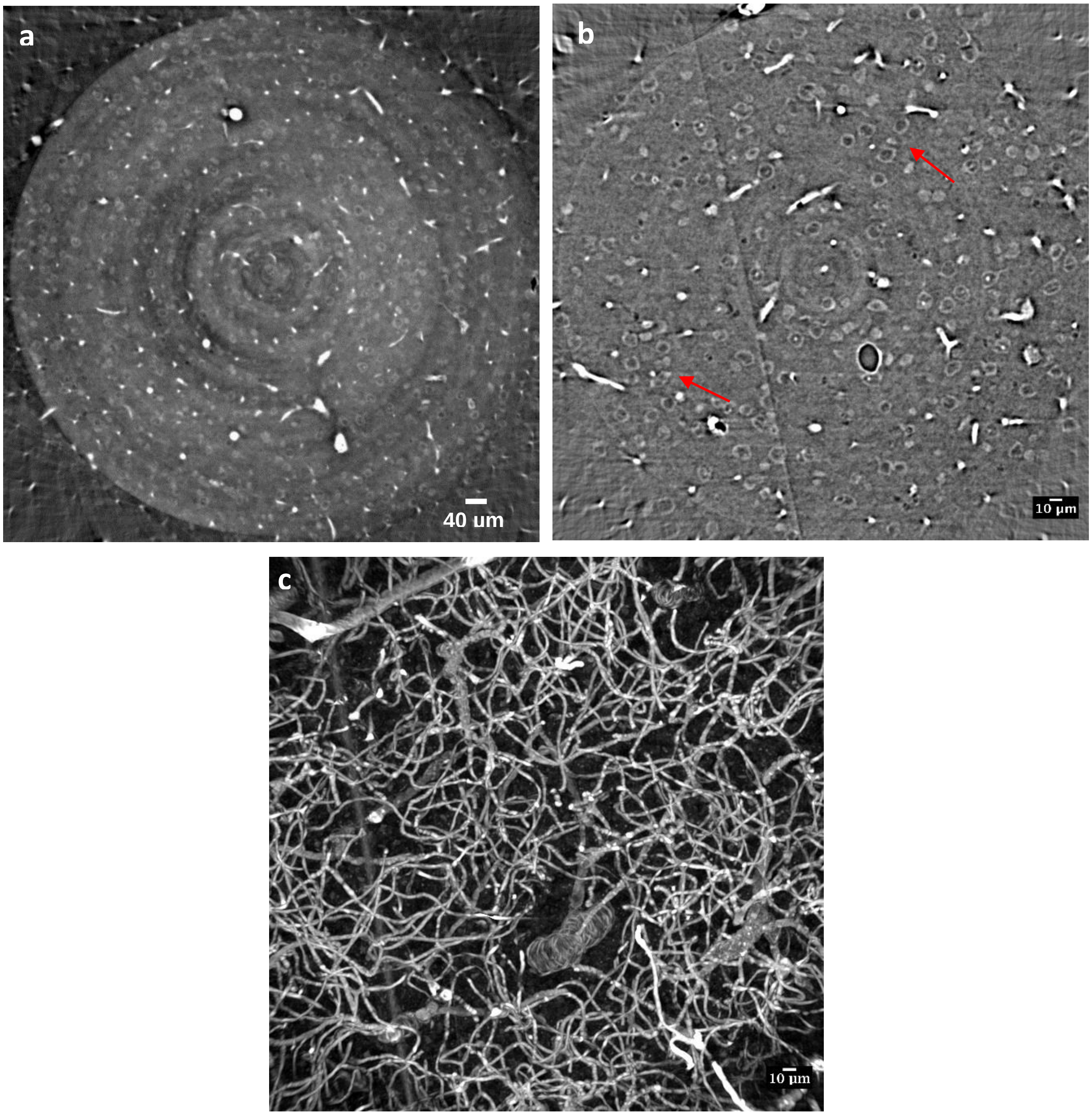

Figure 3.2. CT transversal slices of the "*s_9"* sample (control rat) of somatosensory cortex at two different pixel sizes. **a)** Blood microvessels in white are clearly visible, at 0.325 µm of pixel size, by the injection of a specific contrast agent (Indian Ink); **b)** groups of neuronal cells (red arrows) have been detected together with the blood microvasculature also without the contrast agent treatment (0.162 µm of pixel size); **c)** maximum intensity projection of the volume analysed at 0.162 µm.

It is remarkable to notice the widespread distribution of neuronal bodies throughout the tissue, detected without the use of any contrast agent. The maximum intensity projection view, a method for 3D data visualization that projects in one plane the voxels with the maximum intensity, shows the intricate architecture of cortical microvasculature

Image segmentation. The semi-automatic procedure, performed by morphological tools on *VG Studio Max*® Software, was implemented to extract only the portion occupied by the microvasculature. Therefore, the resulting volume was binarized, as shown in the Figure 3.3.

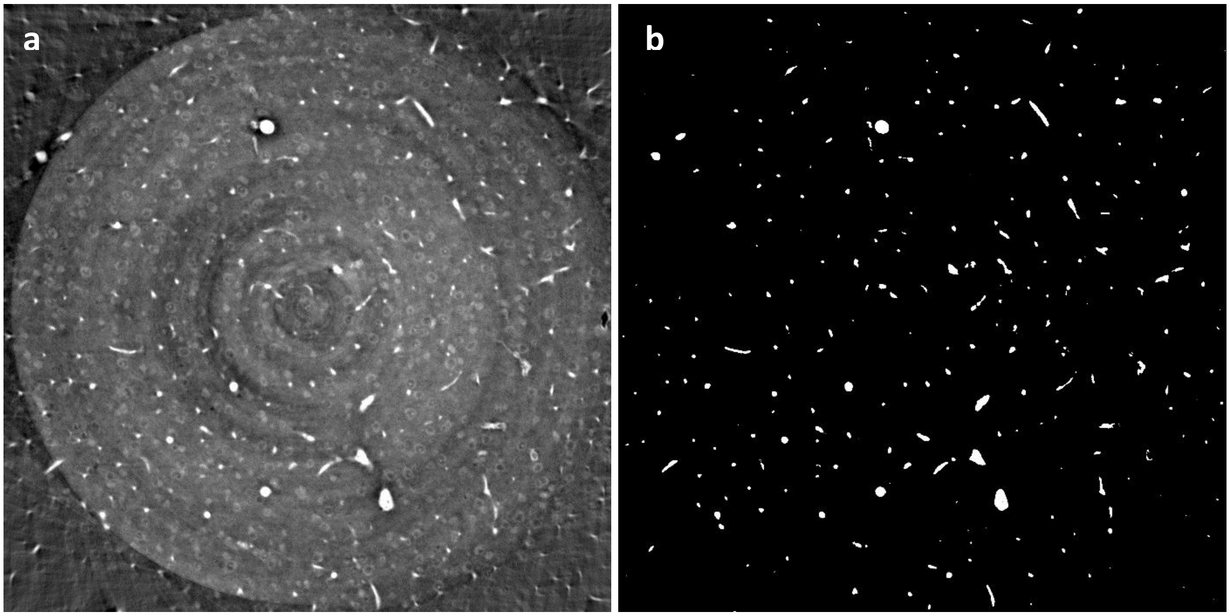

Figure 3.3. CT transversal slices of the "*s_9"* sample (control rat) of somatosensory cortex: **a)** starting image; **b)** binarized image after image segmentation procedure.

Volume rendering. The whole microvasculature can be rendered in 3D space thanks to the applied segmentation (*VG StudioMax*®). A detailed visualization of the cortical microvessel arborisation is reported in (Figure 3.4).

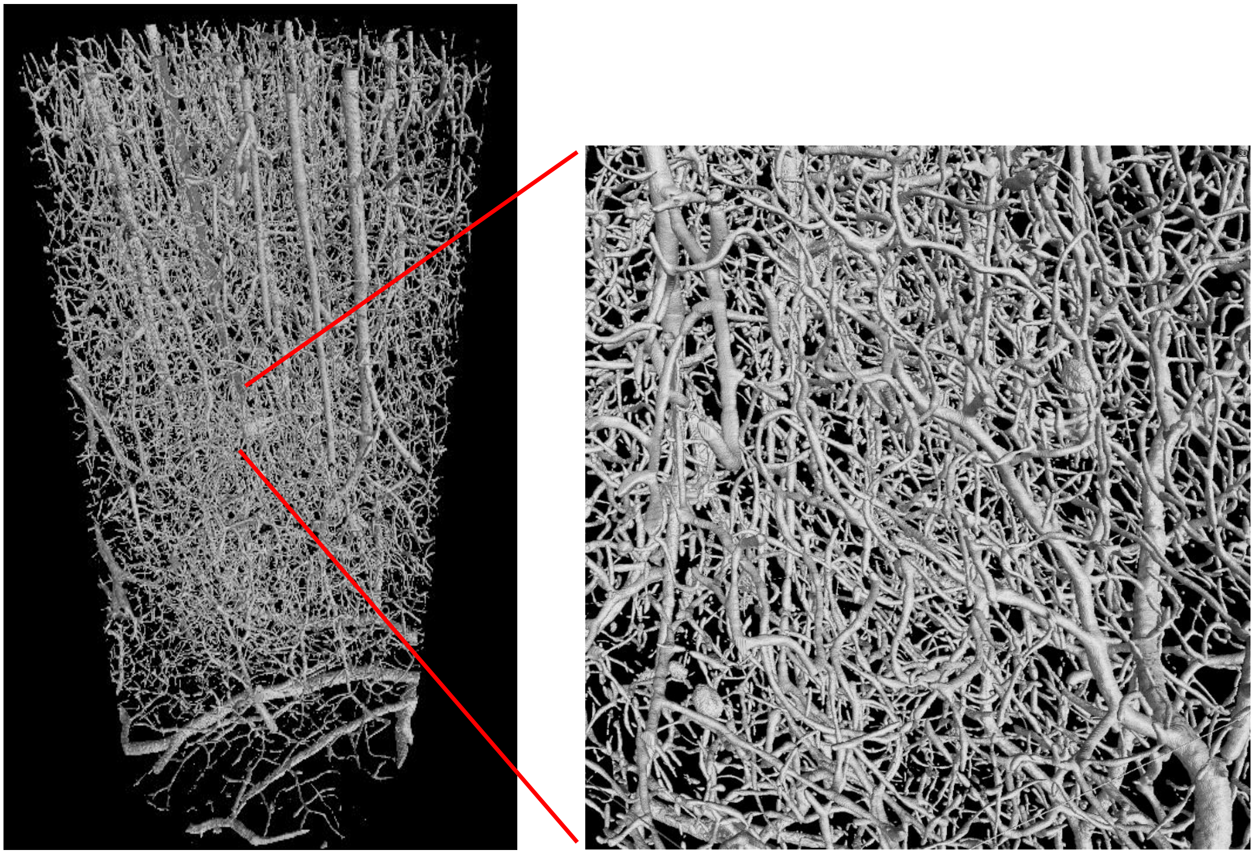

Figure 3.4. Volume rendering of the cortical microvasculature (785x760x1769 μm^3). A zoomed view along the vertical axis show the intricate vascular network.

Image skeletonization and graph transformation. The binarized cortical volume was firstly reduced to a skeleton, allowing for the extraction of the vessel centerline and then to a graph network, in order to characterize the vascular morphology and topology in 3D space. In Figure 3.5 the resulting skeletonized and graph volumes are depicted.

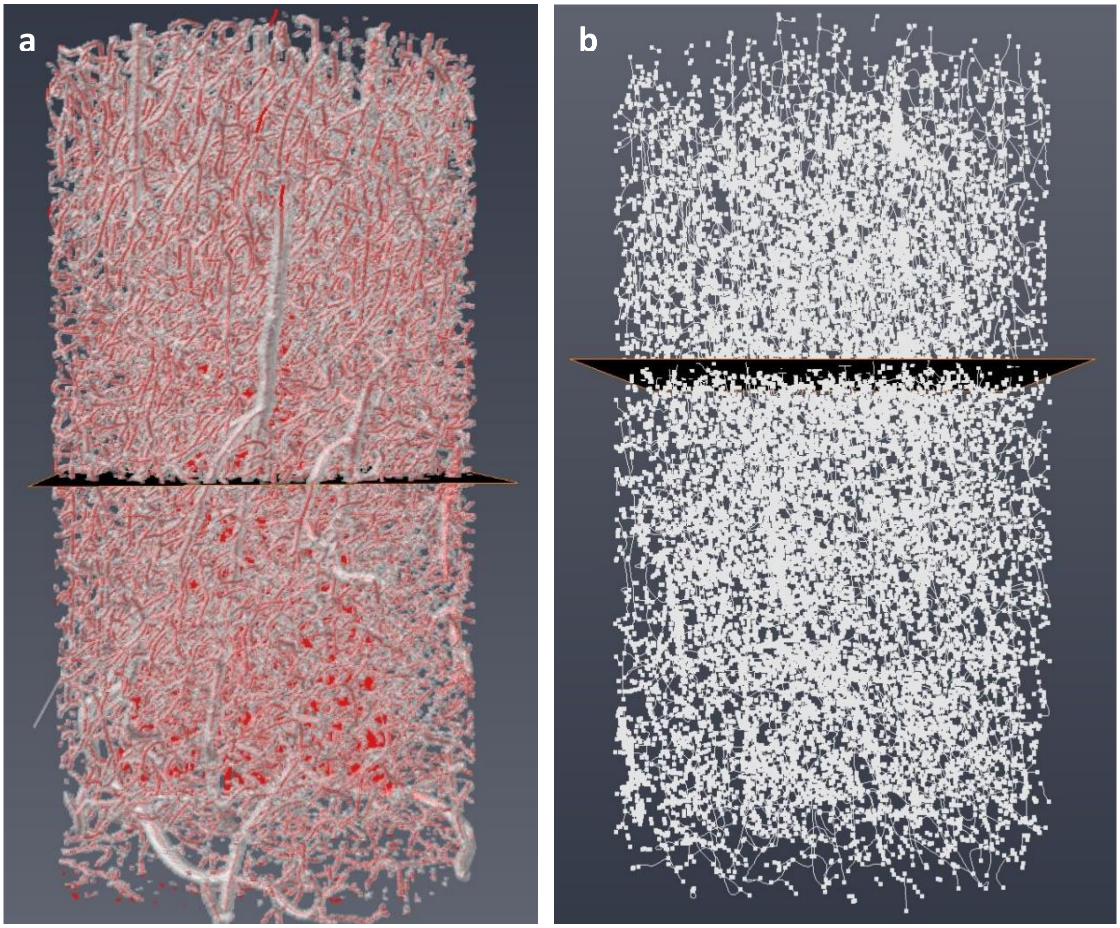

Figure 3.5. **a)** Volume rendering of the skeletonized vessels. **b)** Volume rendering of the spatial graph network where links and nodes are represented.

The presented analysis has been applied on all the samples prepared for the microCT imaging experiments. As reported before, they have been extracted from both CP and control rats belonging to three different temporal groups: i) neuropathic rats sacrificed 14 days after the PSL surgery and the respective control ones; ii) neuropathic rats sacrificed 30 days after the PSL surgery and the respective control ones and iii) neuropathic rats sacrificed 180 days after the PSL surgery and the respective control ones. These consecutive stages have been set in order to follow the temporal evolution of the neuropathy. Due to sample damaging problems and some image artifacts that affected the quality of the images, some of the scanned samples have been discarded from the following analyses. A final list containing all the good ones accompanied by the respective quantitative data is reported in Table 3.1. Due to the tissue damaging during its extraction, the total investigated height was set to 1 mm from the top surface for all the samples. In this way the five layers, from the I up to layer Va according to the literature (Meyer et al. 2011) have been reconstructed (Figure 3.6).

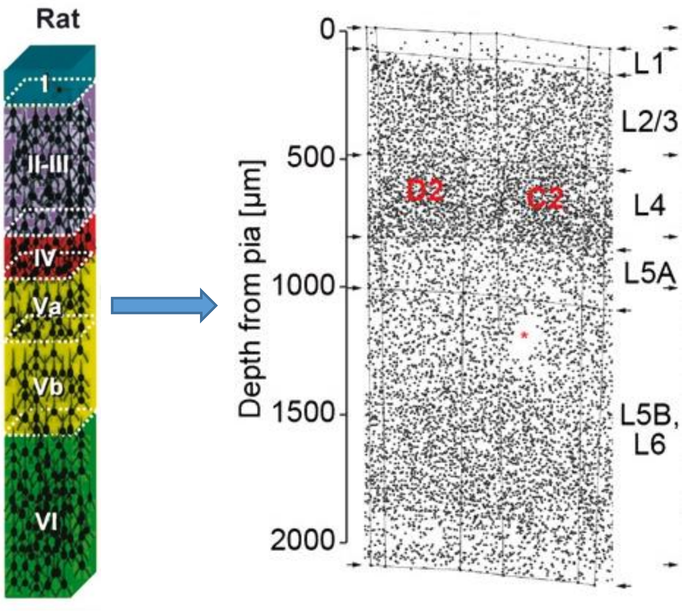

Figure 3.6. Representation of rat cortical layers. The portion analysed in our case corresponds to 1 mm (from layer I to layer VA). (Image redrawn from Meyer et al. 2011; DeFelipe 2011).

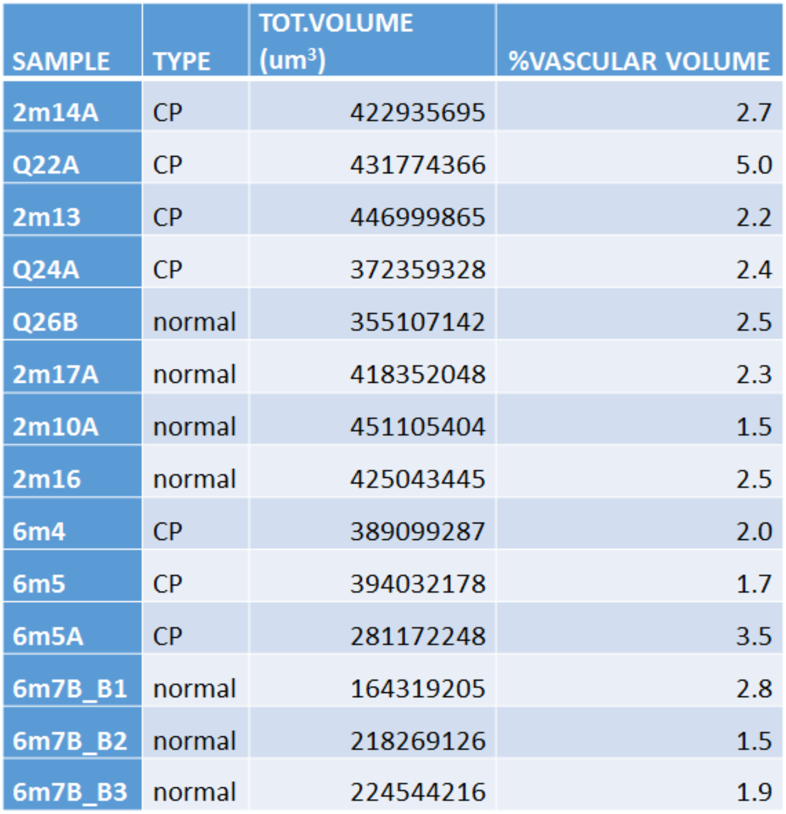

SAMPLE	TYPE	TOT.VOLUME (um^3)	%VASCULAR VOLUME
2m14A	CP	422935695	2.7
Q22A	CP	431774366	5.0
2m13	CP	446999865	2.2
Q24A	CP	372359328	2.4
Q26B	normal	355107142	2.5
2m17A	normal	418352048	2.3
2m10A	normal	451105404	1.5
2m16	normal	425043445	2.5
6m4	CP	389099287	2.0
6m5	CP	394032178	1.7
6m5A	CP	281172248	3.5
6m7B_B1	normal	164319205	2.8
6m7B_B2	normal	218269126	1.5
6m7B_B3	normal	224544216	1.9

Table 3.1. List of all the samples successfully analysed by microCT imaging. They belong to the three different time stages: Q = 2 weeks, 2m = 2 months, 6m = 6 months after the PSL surgery.

The following characterization of vascular system has been achieved through a morphometric and topological analysis implemented on *Matlab*®. Number of skeleton segments, number of branch points, number of vessels and their diameter have been computed in order to detect if changes in these morphological features could possible emerge in CP condition.

3.3 Comparative study "Neuropathic versus Control" rats

All the processed volumes, shown in Table 1, have been included in the comparative *"Neuropathic vs Control"* study, which is based on the morphometric characterization of the cortical microvasculature. It is remarkable the fact that, through the only inspection of the volume renderings, differences in cortical microarchitecture among control and CP rats (Figure 3.7) could be clearly evidenced. In particular, the CP rats show a denser distribution of blood microvessels, strongly pronounced in CP 2 weeks rats. This first finding has opened the way towards a deeper investigation of these changes carried out through a morphological analysis of the vascular network starting from the computed skeletons to the graph organization in 3D space.

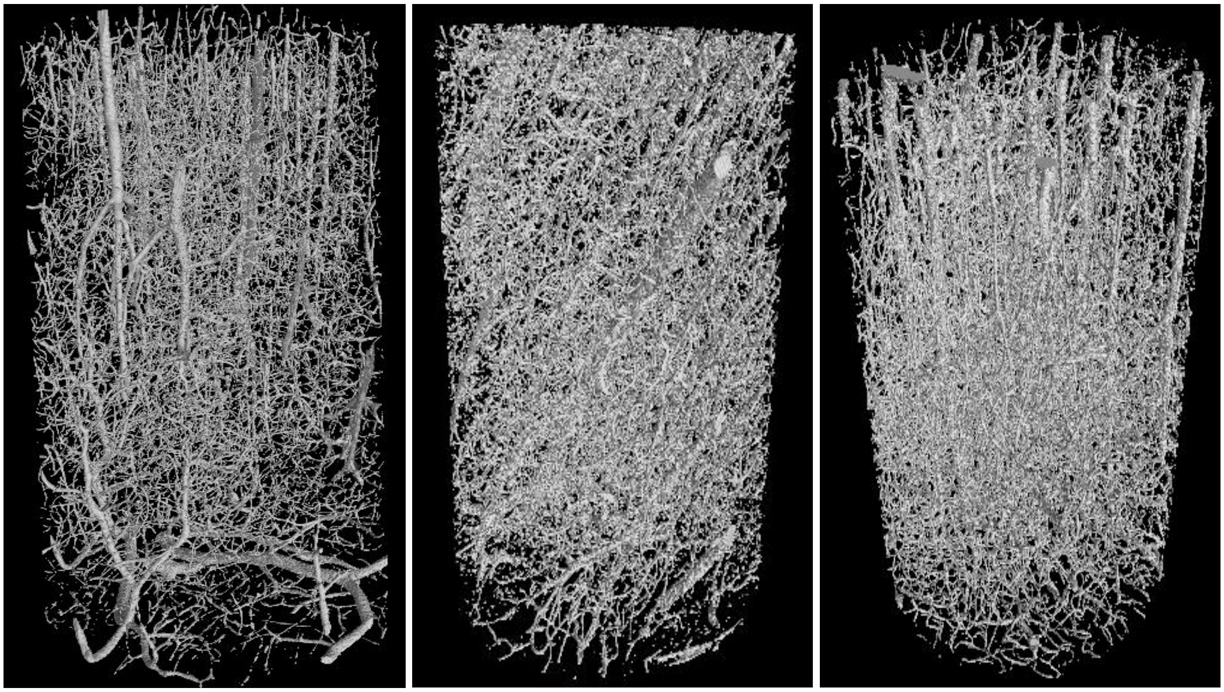

Figure 3.7. Volume rendering of the analysed samples in the order from the left: control (s_9), CP 2 weeks (Q_24A) and CP 2 months (2m13). It is possible to appreciate even visually the increased vascular density in the two CP models.

Whisker box-plots and the corresponding violin plots have been adopted for graphically depicting the statistical quantitative differences among the groups in skeleton segments, branch points and vessels number. All the statistics have been derived by applying common statistical tests as Ranksum Test, Welch test, Paired t-test and Kruskal-Wallis test (*Matlab Statistical Toolbox*®), adopting as threshold value for significance level α=0.05 . It has emerged that a big amount of vessels and branch points characterized the CP pathology respect to the control condition as illustrated by the mean values of number of segments, number of branch points and number of vessels computed for normal and CP rats (Table 3.2).

	Normal	CP
#segments	15997 (3096)	22176 (3951)
#branch points	23989 (4518)	44039 (5570)
#vessels	10085 (922)	14371 (1082)
vessel diameter	9.3 µm (1.3)	8.2 µm (1.1)

Table 3.2. Mean values and standard deviations in brackets of number of segments, branch points, vessels and vessel diameter for normal and CP rats.

These results clearly envisaged a possible neo-genesis onset in somatosensory cortical spaces in CP conditions, so justifying the first finding from the rendered volumes. The vessel diameter has also been compared in the two conditions: a reduced value of vessel mean diameter has been found in all CP samples.) (Table 3.2). The results are graphically represented in two blocks: block 1 shows the global effects **(GE)** throughout the six months of the experimental period (Figure from 3.8 to 3.13) and block 2 shows the dynamic of the angiogenetic events specifically observed at the three stages of 2 weeks, 2 months and 6 months (Staged Effects, **SE**) (Figure from 3.14 to 3.19).

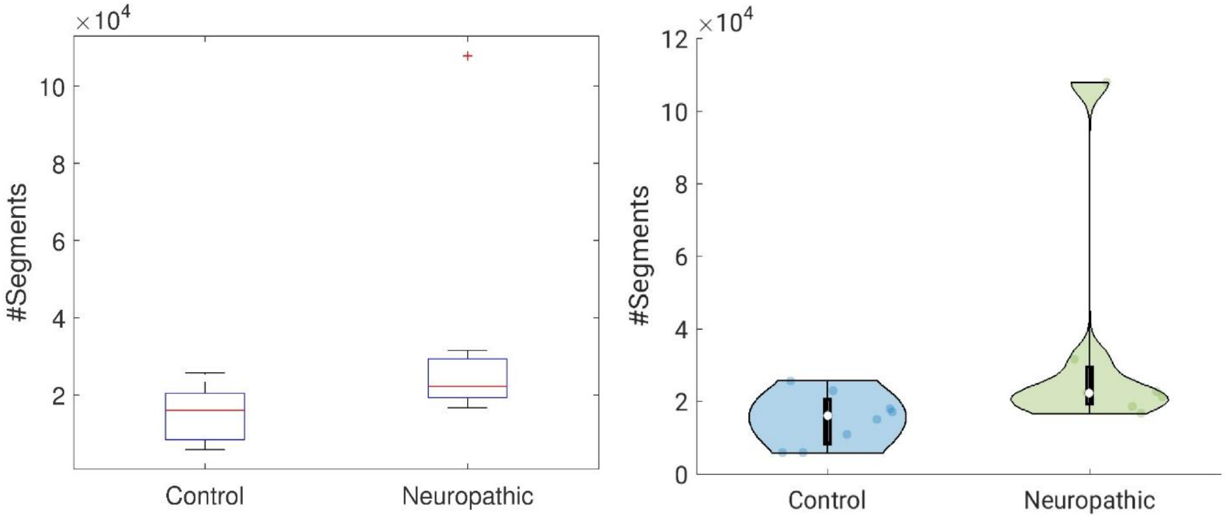

Figure 3.8. Distribution of the number of segments in control vs neuropathic rats (whisker box plots on left and violin plot on right, p = 0.059, α=0.05, Ranksum test) **(GE).**

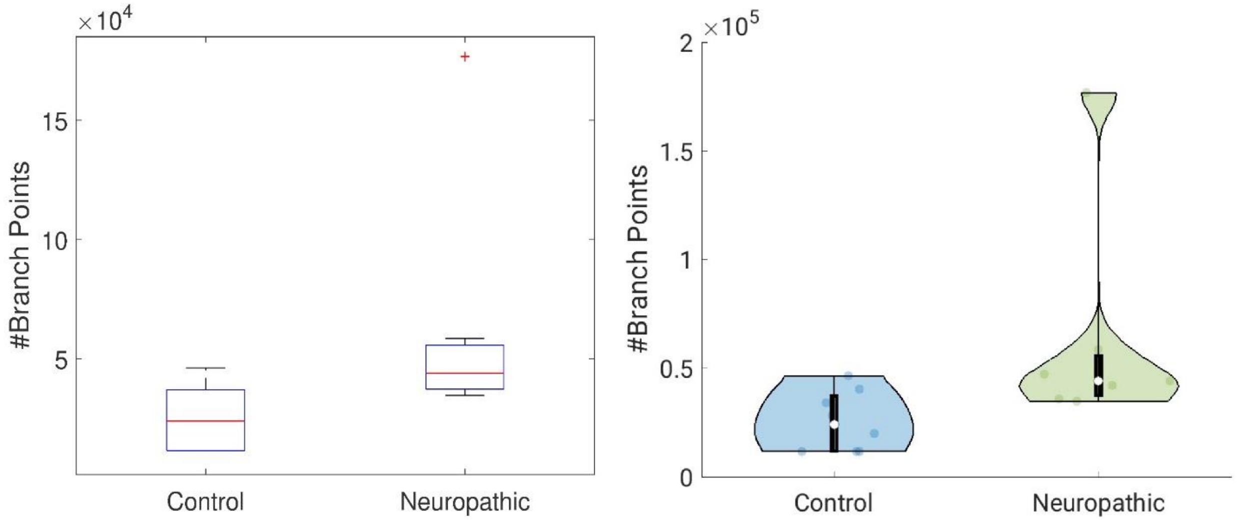

Figure 3.9. Distribution of number of the branch points in control vs neuropathic rats (whisker box plots on left and violin plot on right). A statistical significant difference has been found between the two classes (p= 0.008, α=0.05, Ranksum test) **(GE)**.

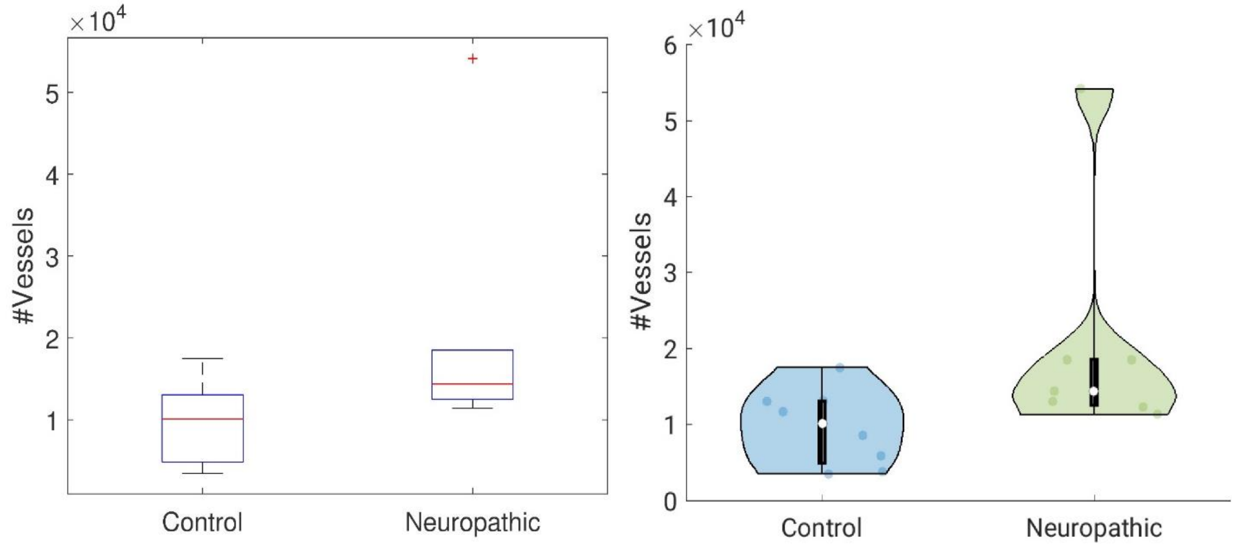

Figure 3.10. Distribution of the number of vessels in control vs neuropathic rats (whisker box plots on left and violin plot on right). A statistical significant difference has been found between the two classes (p = 0.045, α=0.05, Ranksum test) **(GE)**.

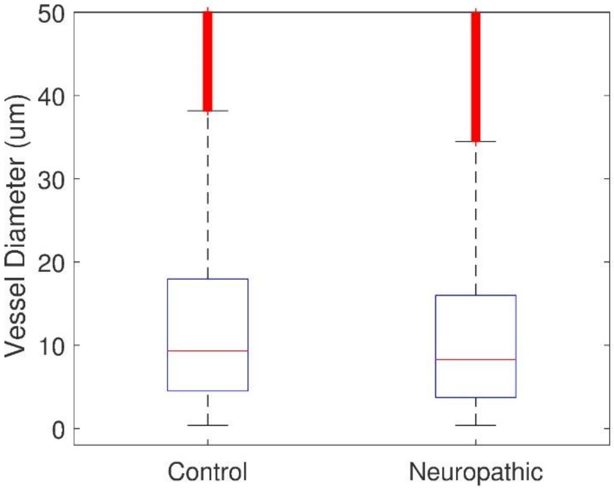

Figure 3.11. Distribution of the vessel diameter in control vs neuropathic rats (whisker box plots on left and violin plot on right). A statistical significant difference has been found between the two classes ($p<<0.001$, $\alpha=0.05$, Ranksum test; $p<<0.001$, Welch test) **(GE)**.

All these data together highlighted the increased number of capillary segments, branch points and the reduction of the mean vessel diameters. These features may be accountable for the emergence of neogenetic microvessel episodes.

A further analysis has been addressed on vessel diameter in order to assess the incidence level of vascular neo-genesis. A diameter threshold has been imposed for the identification of small vessels and then all the morphometric features of vessel trees have been re-computed: the differences among control and neuropathic classes were again significant, confirming that the vascular neo-genesis occurs at the micro-scale level (Table 3.3 and Figure 3.12, 3.13).

	normal	CP
#vessels<15 µm	7322 (825)	9699 (1149)
vessel diameter<15 µm	5.9 µm (0.6)	4.9 µm (0.8)

Table 3.3. Mean values and standard deviations in brackets of number of vessels with diameter < 15 µm and their diameter for normal and CP rats.

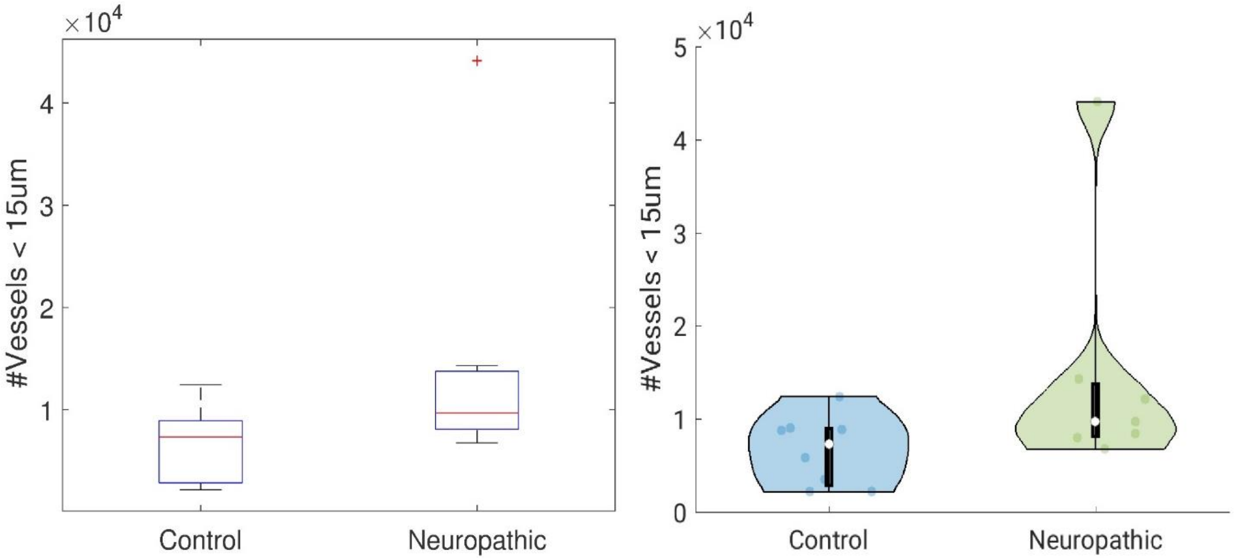

Figure 3.12. Distribution of number of vessels (diameter threshold = 15 μm) "control vs neuropathic rats" (whisker box plots on left and violin plot on right). (p = 0.011, α=0.05, Ranksum test) **(GE)**.

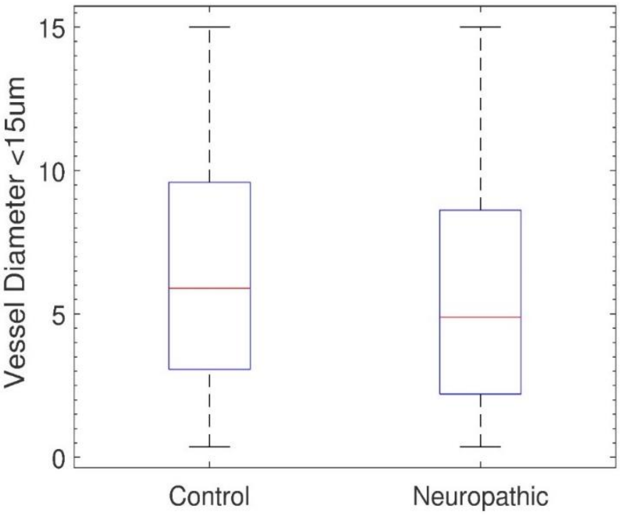

Figure 3.13. Distribution of vessel diameter (diameter threshold= 15 μm) "control vs neuropathic rats" (whisker box plots on left and violin plot on right). A statistical significant difference has been found between the two classes (p<<0.001, Ranksum test; p<<0.001, Welch test; p<<0.001, α=0.05, Paired t-test) **(GE)**.

In order to evaluate this vessel rearrangement during the entire evolution of the neuropathic condition, further analyses have been focused on the comparisons between control and neuropathic rats at three different time stages and namely at 2 weeks, 2 months and 6 months from the neuropathy onset. The results are show in Figures 3.14, 3.15, 3.16, 3.17, 3.18 and 3.19. Differences among the two distributions are clearly visible at each time stage in number of segments, number of branch points, number of vessels and vessel diameters. Due to the obvious paucity of samples for each condition we did not collect any true statistics but the visual inspection evidence.

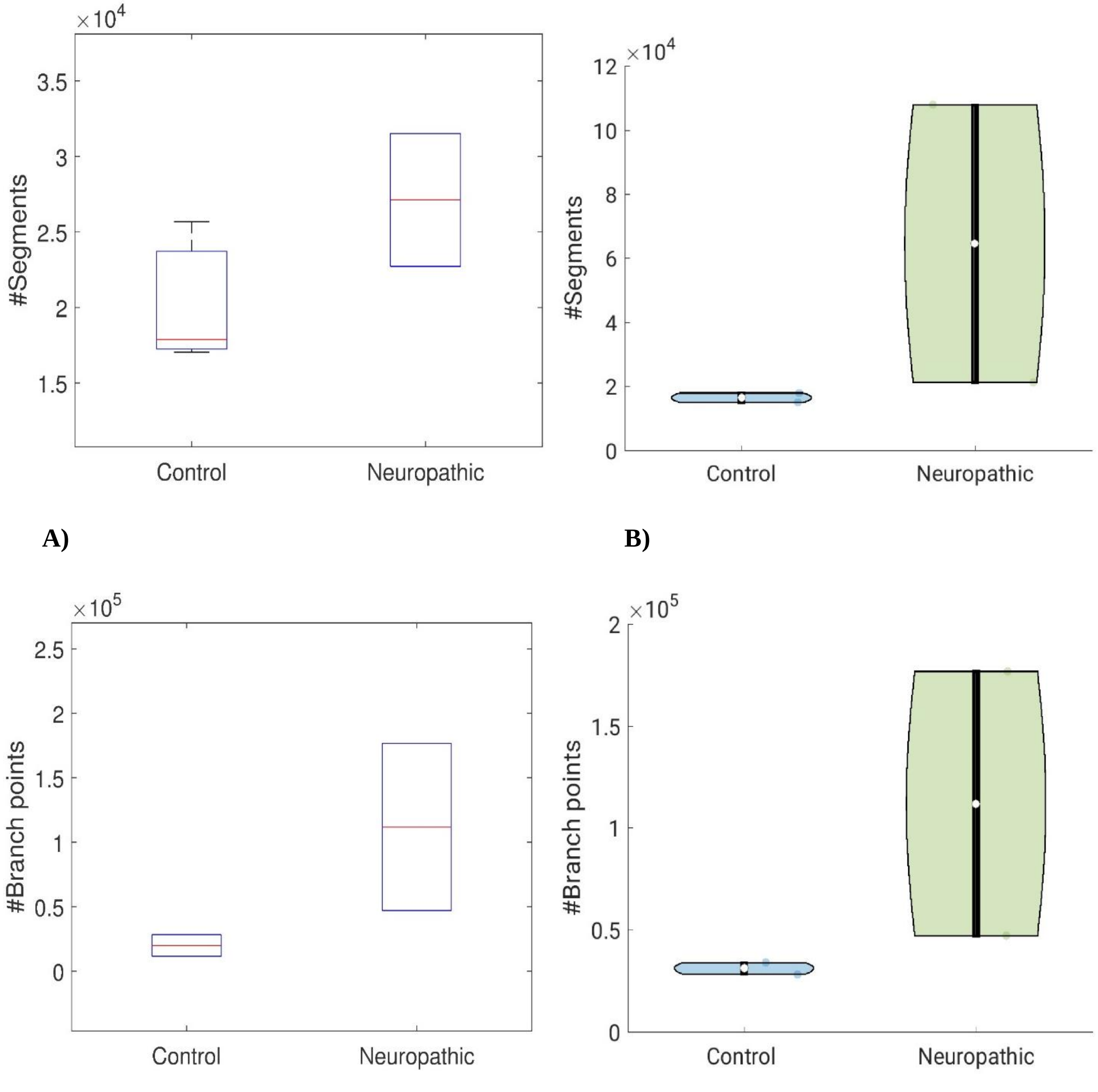

A) **B)**

C) **D)**

Figure 3.14. Comparison between control and neuropathic rats at two weeks from the neuropathy onset: distribution of number of segments, (whisker box plots A and violin plot B) and number of branch points (whisker box plots C and violin plot D, $p<<0.001$, $\alpha=0.0$, Kruskal-Wallis test). **(SE)**.

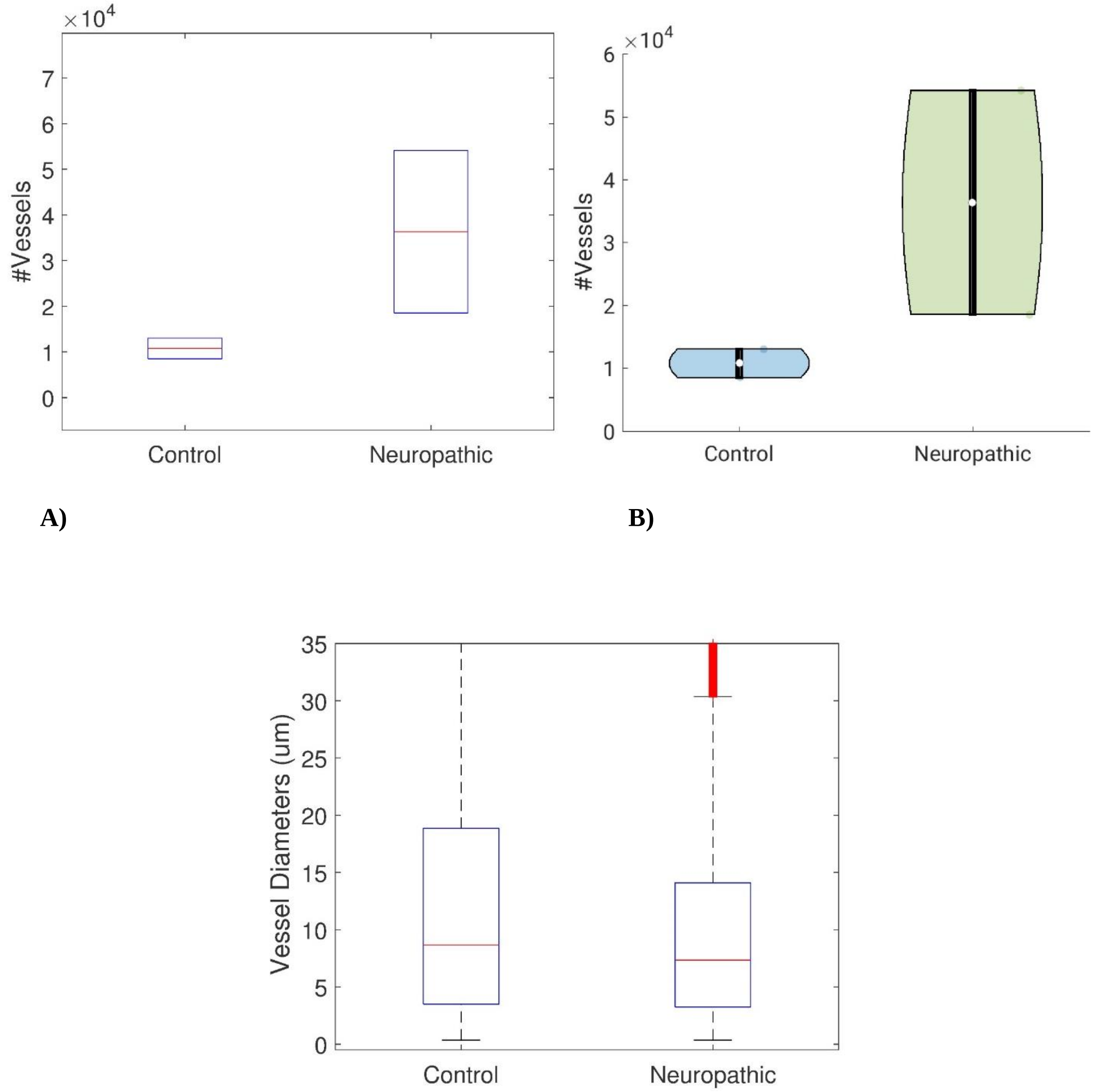

A) **B)**

C)

Figure 3.15. Comparison between control and neuropathic rats at two weeks from the neuropathy onset: distribution of number of segments, (whisker box plots A and violin plot B) and vessel diameter (whisker box plot C, $p<<0.001$, $\alpha=0.05$, Kruskal-Wallis test). **(SE)**.

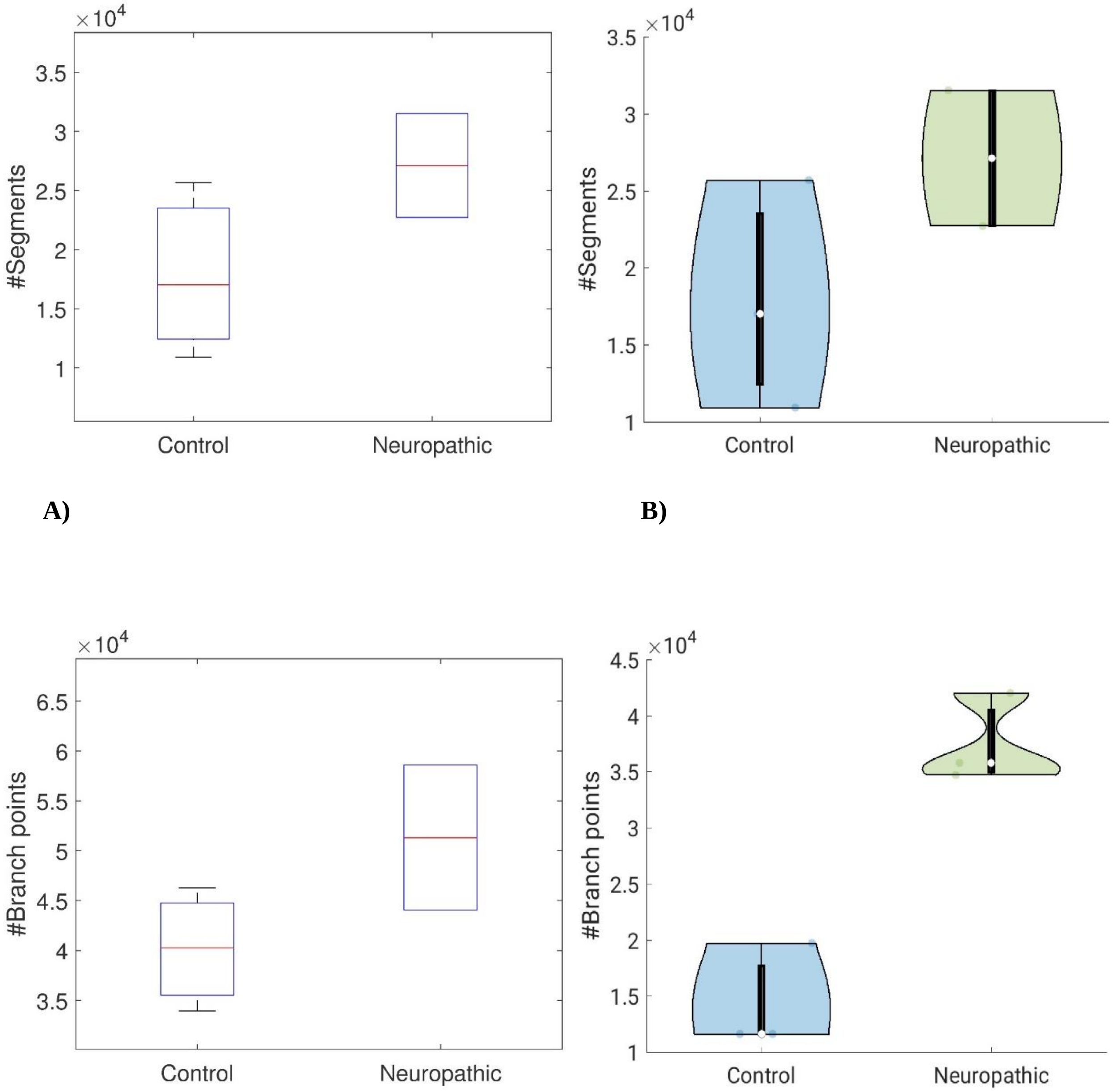

A) **B)**

C) **D)**

Figure 3.16. Comparison between control and neuropathic rats at two months from the neuropathy onset: distribution of number of segments, (whisker box plots A and violin plot B) and number of branch points (whisker box plots C and violin plot D, $p \ll 0.001$, $\alpha = 0.05$, Kruskal-Wallis test). **(SE)**

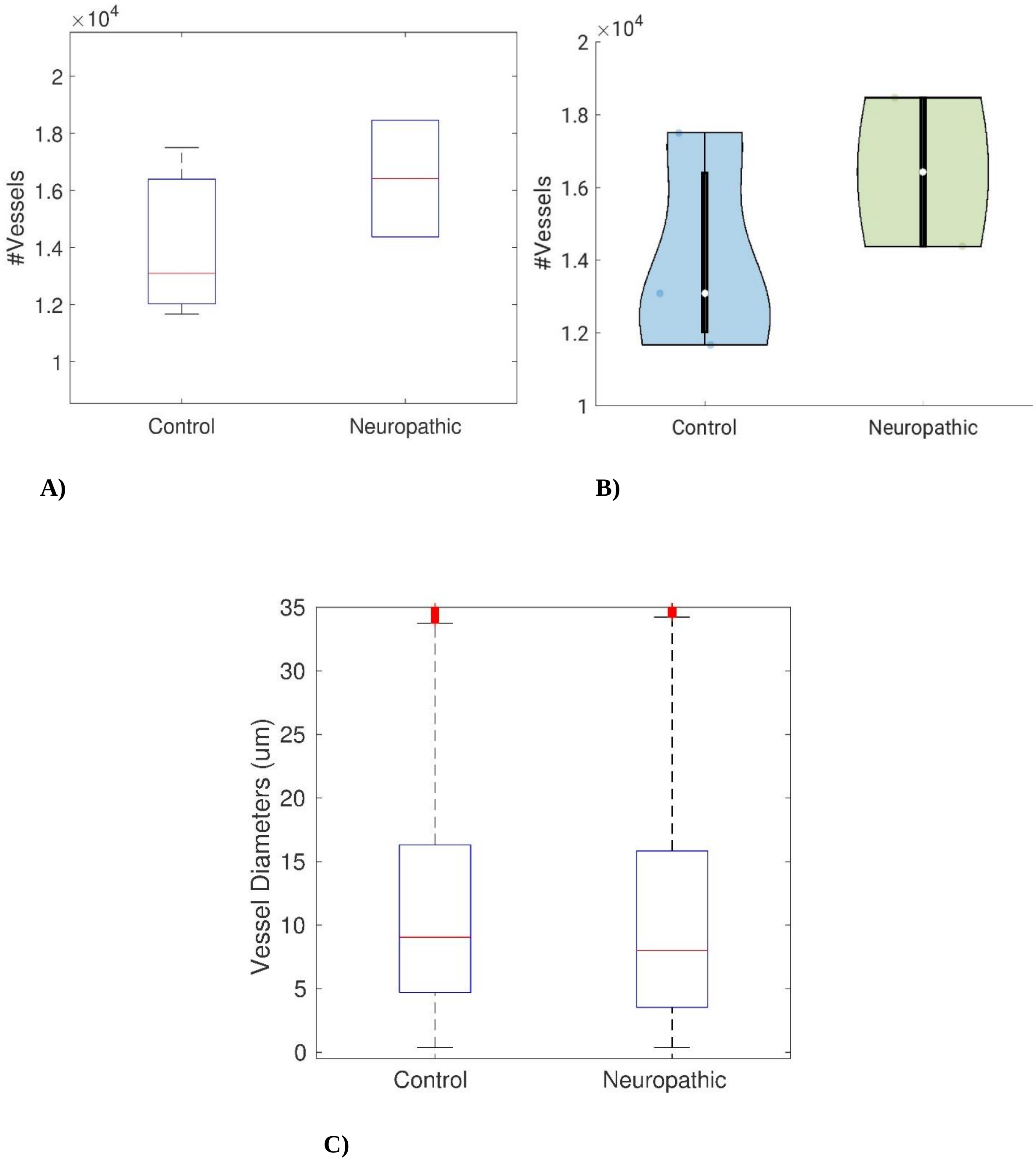

Figure 3.17. Comparison between control and neuropathic rats at two months from the neuropathy onset: distribution of number of vessels (whisker box plots A and violin plot B) and vessel diameter (whisker box plot C, p<<0.001, α=0.05, Kruskal-Wallis test). **(SE)**

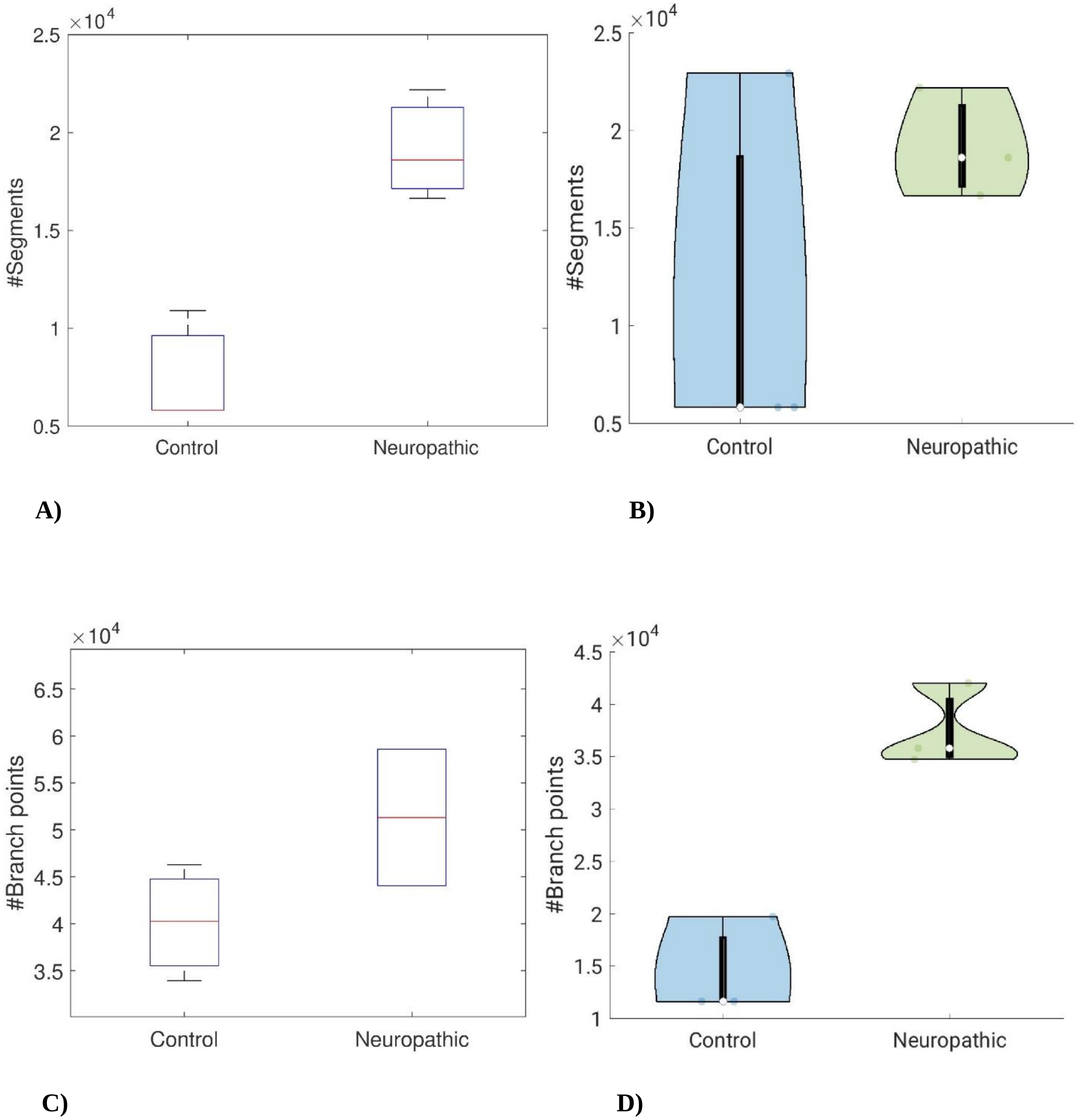

Figure 3.18. Comparison between control and neuropathic rats at six months from the neuropathy onset: distribution of number of segments, (whisker box plots A and violin plot B) and number of branch points (whisker box plots C and violin plot D, $p<<0.001$, $\alpha=0.05$, Kruskal-Wallis test). **(SE)**

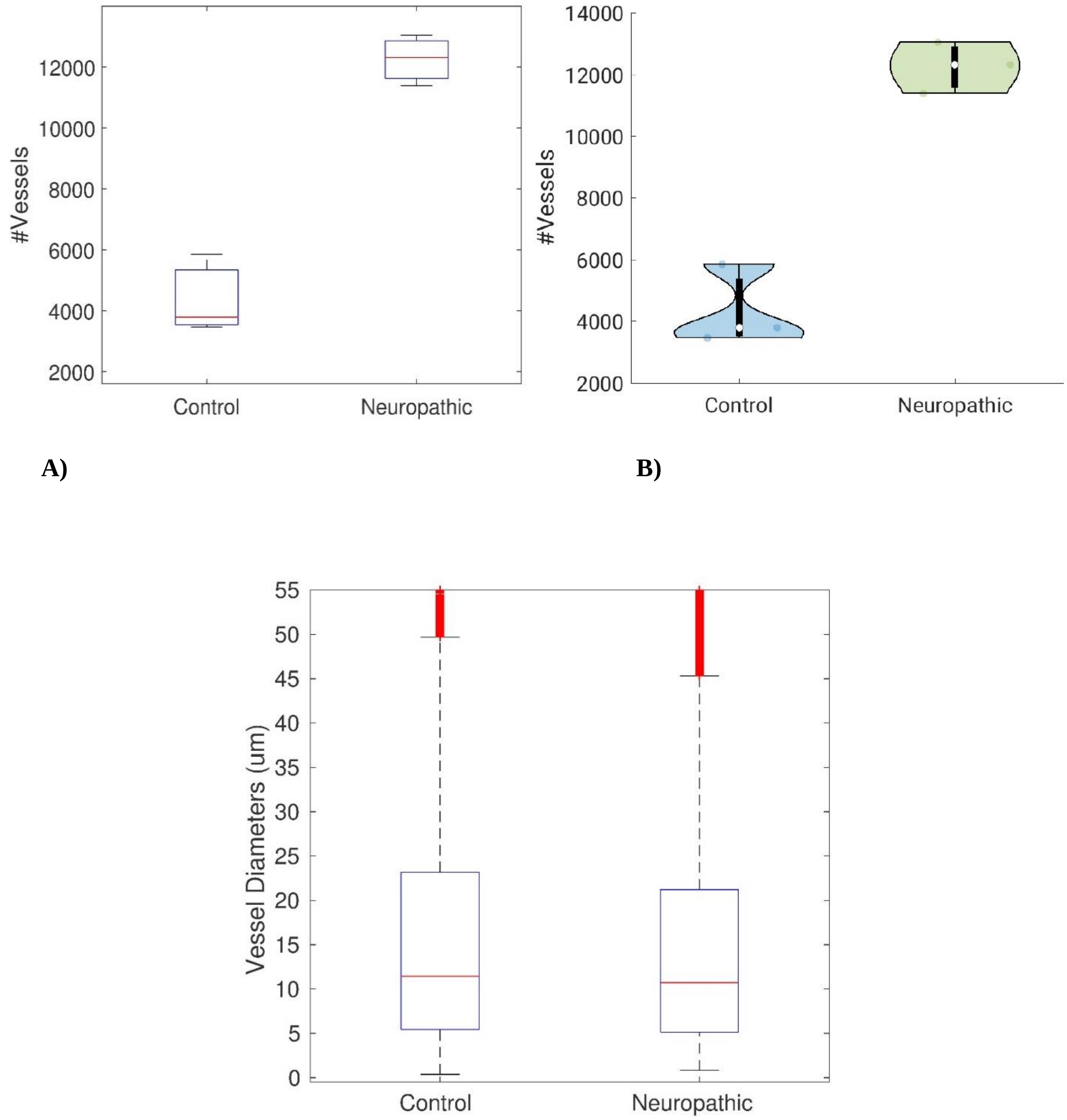

A) **B)**

C)

Figure 3.19. Comparison between control and neuropathic rats at six months from the neuropathy onset: distribution number of vessels (whisker box plots A and violin plot B), vessel diameter (whisker box plot C, $p<<0.001$, $\alpha=0.05$, Kruskal-Wallis test). **(SE)**

The evolution in time of the angiogenetic events has been traced at two weeks, two months and six months by plotting the skeleton segments, branch points and vessels numbers (Figure 3.20). All these distributions conserve a symmetric trend: a very remarkable increase of microvessel structures affects the two weeks stage, while the neo-genesis becomes less pronounced at two months to fade almost to null at six months. In the last curve, showing the vessel diameter trend, is possible to notice that, to an increase of vessel components corresponds, at two weeks and two months stages, a decrease in the vascular diameter mean value. The vessel diameters show a dramatic drop at two weeks, a finding strongly consistent with our hypothesis of angiogenetic events induced by neuropathies. In the following months this measure tends to assume less significant values and at six months the diameter size shows a trend exceeding the control values in the presence of strongly reduced branching and vessel number counts. At six months the data are more complex and deserve a specific evaluation; namely, the skeleton segments, the branch points and the number of vessels tend to values comparable to the respective control conditions.

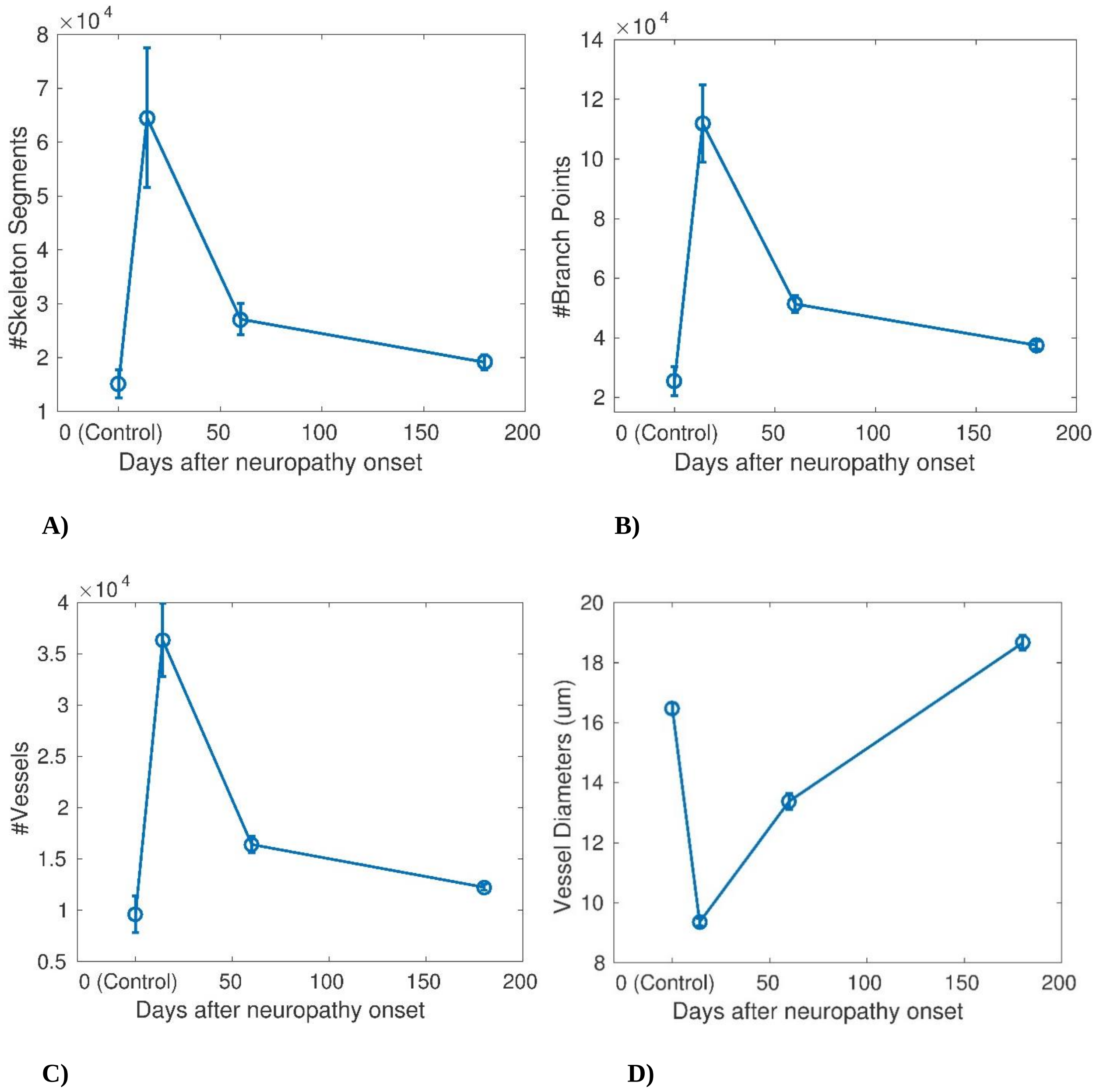

Figure 3.20. Time evolution of CP disease at three different stages: two weeks, two months and six months after the neuropathy onset. The mean values and the standard deviation of number of segments **(A)**, number of branch points **(B)**, number of vessels **(C)** and vessel diameter **(D)** is plotted. (p= 0.154, (A); p= 0.033, (B); p=0.0482 (C); p<<0.001, α=0.05 (D)).

Further, in order to investigate the spatial distribution of the induced angiogenesis throughout the cortical layers analysed, (in particular I, II/III, IV and Va), the vessel density has been computed for all the cortical layers in all the CP conditions (Figure 3.21). An inhomogeneous distribution of the vessel density among layers (p<<0.001, Kruskal-Wallis test) has been found. In particular, after 2 weeks of CP onset, all layers appear tightly affected by a significant increase of the vessel density (p <<0.001, Kruskal-Wallis test); after

2 months, layers I and IV are primarily involved in the increased vessel density followed by layers II/III and Va (p<<0.001, Kruskal-Wallis test). At last, after six months of CP progression, only layer I is copiously interested by vessel density inflation followed by the other layers (p<<0.001, Kruskal-Wallis test).

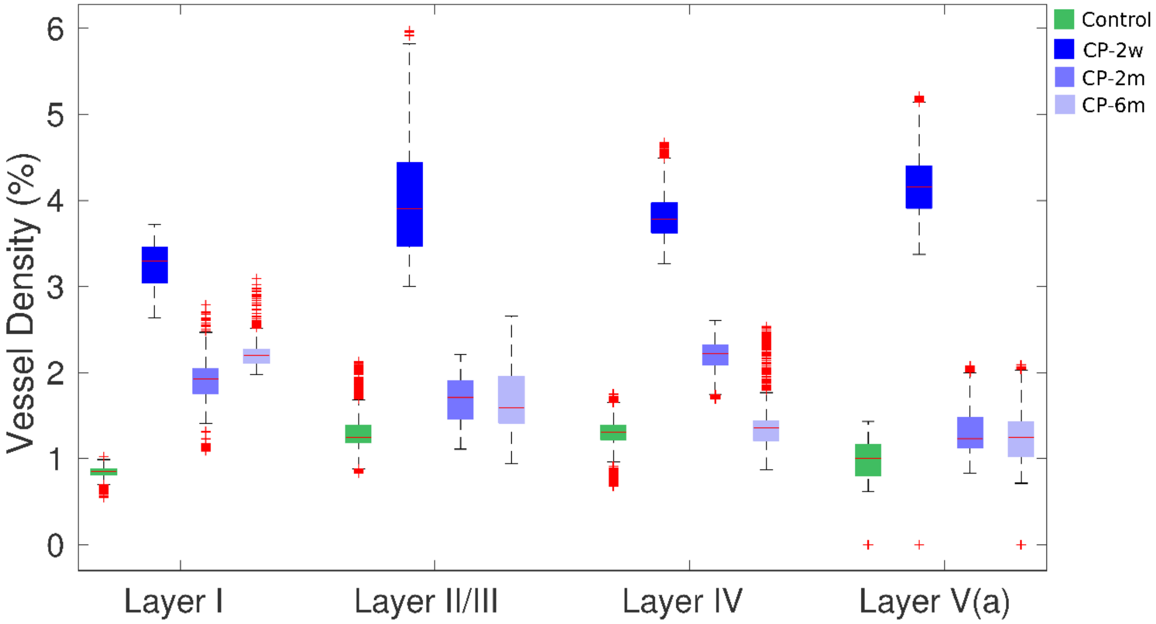

Figure 3.21. Distribution of vessel density (% vessel over the total volume) among all the analysed layers (from I to Va) at each time stage (2 weeks, 2 months and 6 months).

Additionally, three further complex network statistics have been computed according to the analysis described in Materials and Methods, 2.6.2.c and 2.6.4.c and d. The *maximum flow* (Ford, Jr. and Fulkerson 1956) evaluated the theoretical capacity of a network (modelled as a *pipeline*) to load low viscosity fluids (e.g. water or blood). We have found that the maximum flow sustainable in CP vascular networks is much greater than control networks (p<<0.001, Kruskal-Wallis test) (Figure 3.22). Specifically, after 2 weeks the network reached a boost of 12.5x that slowed down to 5.7x after 2 months and 4.3x after 6 months on average. These results indicate that CP vascular networks are compatible with an enriched blood flow sustained by the promoted novel angiogenesis.

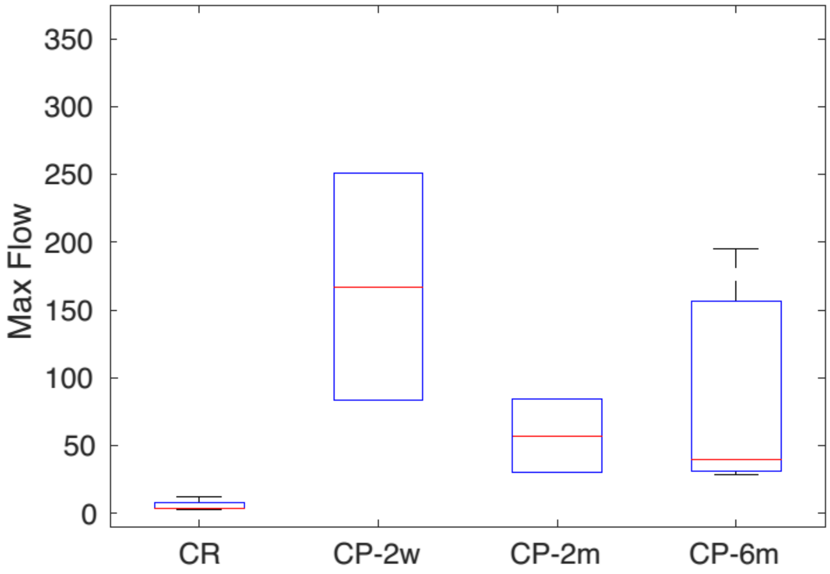

Figure 3.22. Distribution of the maximum flow hosted by the vascular network in control rats (CR) and all the CP rats (2weeks, 2 months and 6 months).

Further, complex networks as vascular trees are regularly featured by two common statistics, i.e. the clustering coefficient (C, C^w for the weighted form) and the characteristic path length (L, L^w for the weighted form). The former indicates the tendency of network nodes to form highly dense clusters, the latter represents the network efficiency in communications among nodes (Material and Methods, 2.6.4.c and d). As shown in Figure 3.23 these complex network statistics of the vascular networks are not significantly affected by CP. Indeed, C^w does not significantly changes in all groups ($p = 0.542$, Kruskal-Wallis test) as well as L^w ($p = 0.370$, Kruskal-Wallis test).

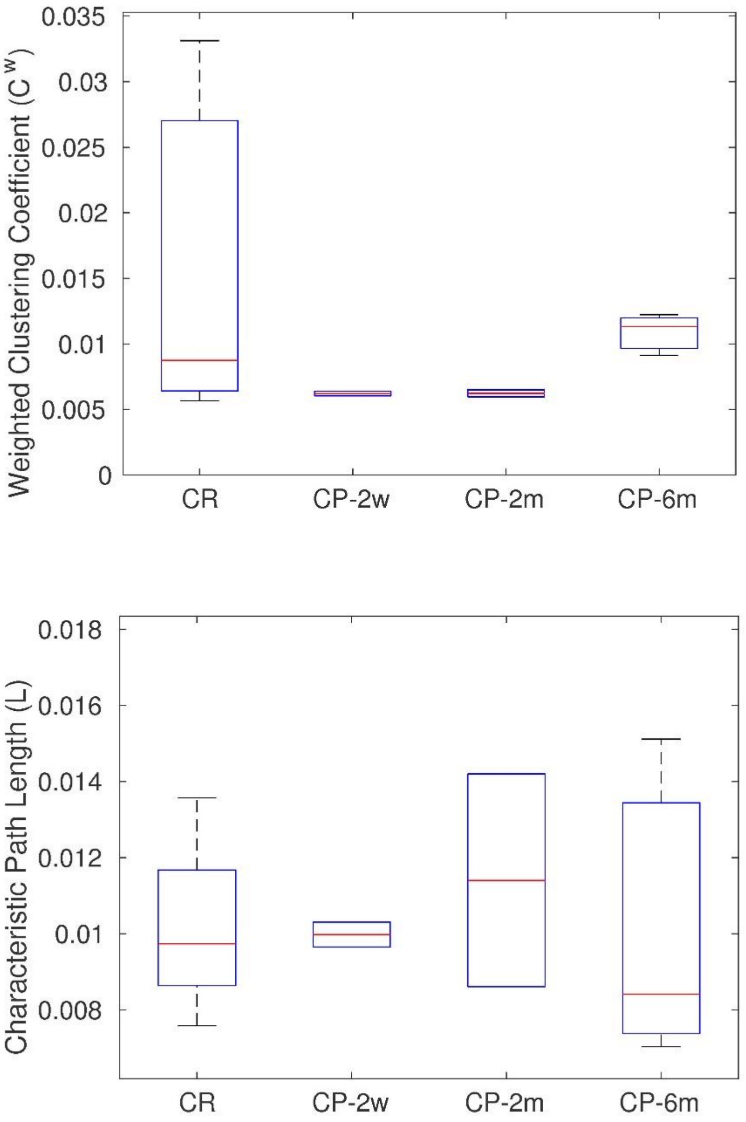

Figure 3.23. Distribution of the weighted clustering coefficient (C^w) (top) and the characteristic path length (down) in control rats (CR) and all the CP rats (2 weeks, 2 months and 6 months).

This last result show that, from a common topological network perspective, vascular networks do not alter their architecture suggesting that CP modification maintained the same topology of the control networks.

3.4 Immunofluorescence analysis: confirmation of vascular neo-genesis

The results achieved with the X-ray imaging analysis needed to be validated through histological techniques. In particular, the involvement of vascular neo-genesis in CP condition revealed through the 3D X-ray morphological analysis of the cortical vascular network has been verified by mean of immunofluorescence microscopy. The samples underwent the immunofluorescence treatment as described in Materials and Methods, 2.5.4. The significant positivity to vessel neogenesis antibodies (namely, VEGFR1, VEGFR2 and VWF) is clearly shown in Figure 3.24 and 3.25. The DAPI fluorescent stain (blue) has been used to reveal also neuronal cell population.

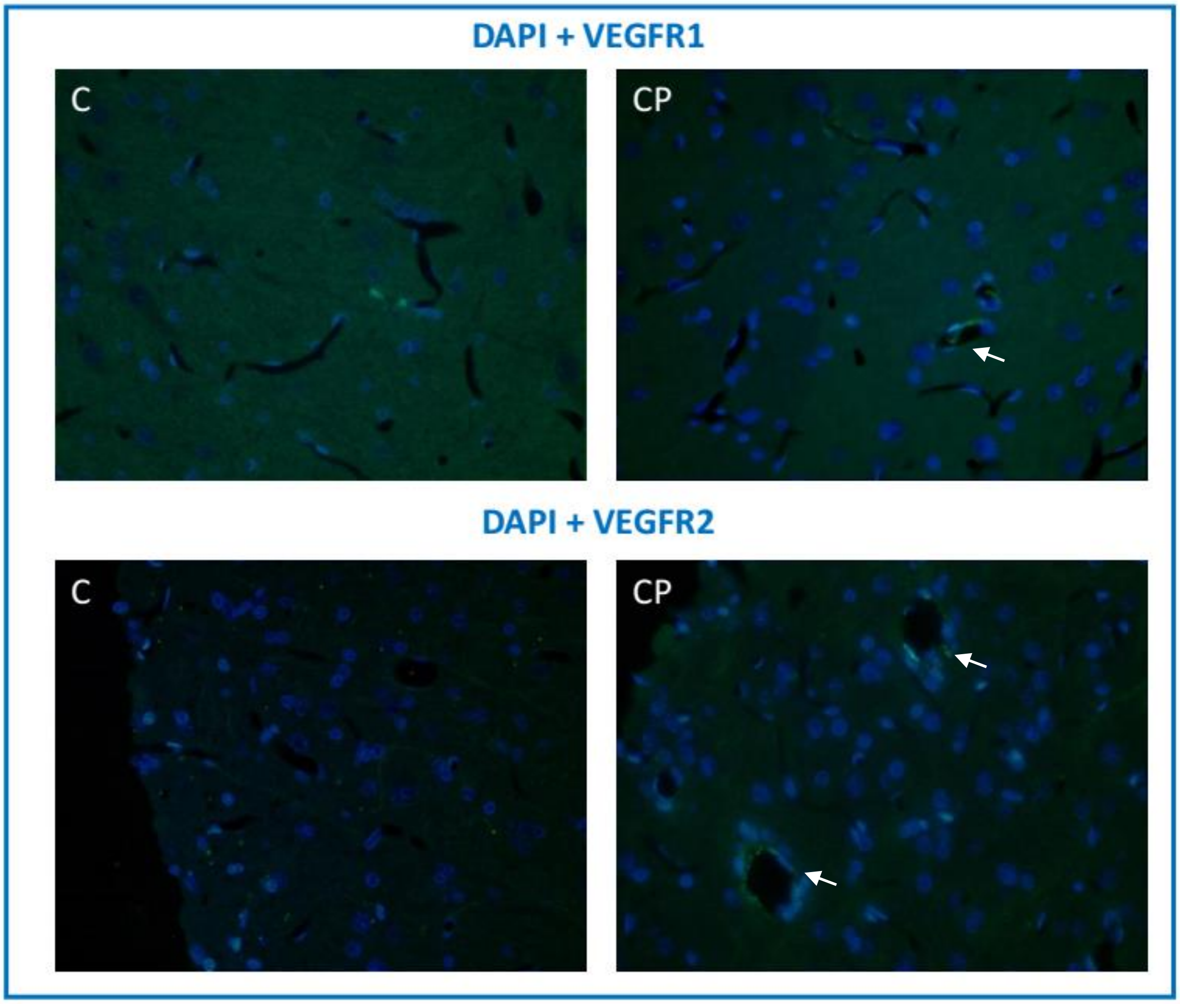

Figure 3.24. Immunofluorescence microscopy images of rat somatosensory cortical tissue (40X): comparisons between control (C) and CP 2 months (CP) rats. The positivity to the VEGFR1 and VEGFR2 is clearly visible (in green) around vessels in CP conditions confirming the episodes of vascular neo-genesis (arrows).

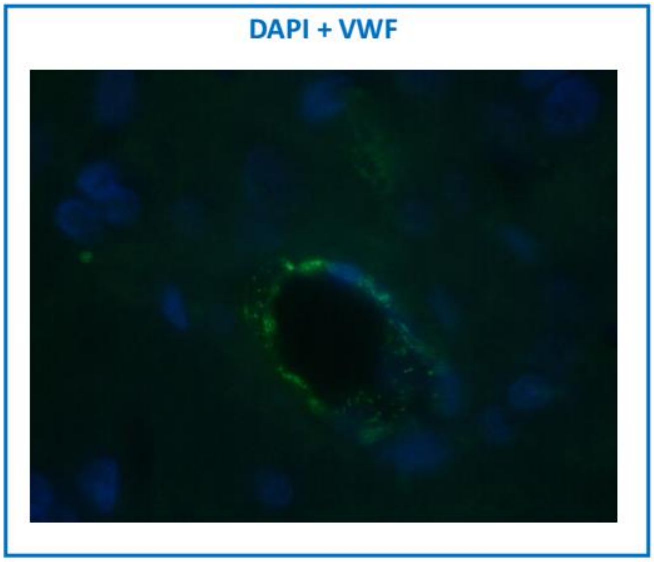

Figure 3.25. Immunofluorescence microscopy image of CP rat cortical blood vessel (100X): the positivity to VWF antibody is evidenced by the fluoscerence detection around the vessel.

3.5 NanoCT Imaging analysis: a deeper insight into the tripartite synapse

The nanoCT Imaging experiments have been addressed to the investigation of the anatomical network existing in the somatosensory cortical spaces among the neuronal cells, the glial surroundings and the blood microvessels. As previously explained (Materials and Methods, 2.5.3), the nano-tomo imaging set-up adopted and the new environment conditions forced us to the development of a totally new sample preparation protocol. Several samples have been prepared with the aim of revealing the microscopic misalignments potentially nested in the tripartite synaptic unit in CP condition. Unfortunately, due to technical difficulties encountered both during the sample preparation and the sample mounting on the sample-holder, only few samples have been successfully imaged with a very high-resolution (100 nm of pixel size). Each sample has been analysed through 200 µm steps from the surface of the somatosensory cortex reaching a total height of 600-800 µm. The results relative to the best analysed sample, *"control_12a"*, are illustrated for each step of the procedure described in Materials and Methods, 2.6.2.

Image reconstruction. By applying the PC holotomography technique described in Materials and Methods, 2.2.9, the whole investigated volume has been reconstructed. Each final data set consisted in 2048 32-bit images (2048x2048pixel). The CT transversal slice showed in Figure 3.26 reveals the great variety of cells detected without any contrast agent to mark them.

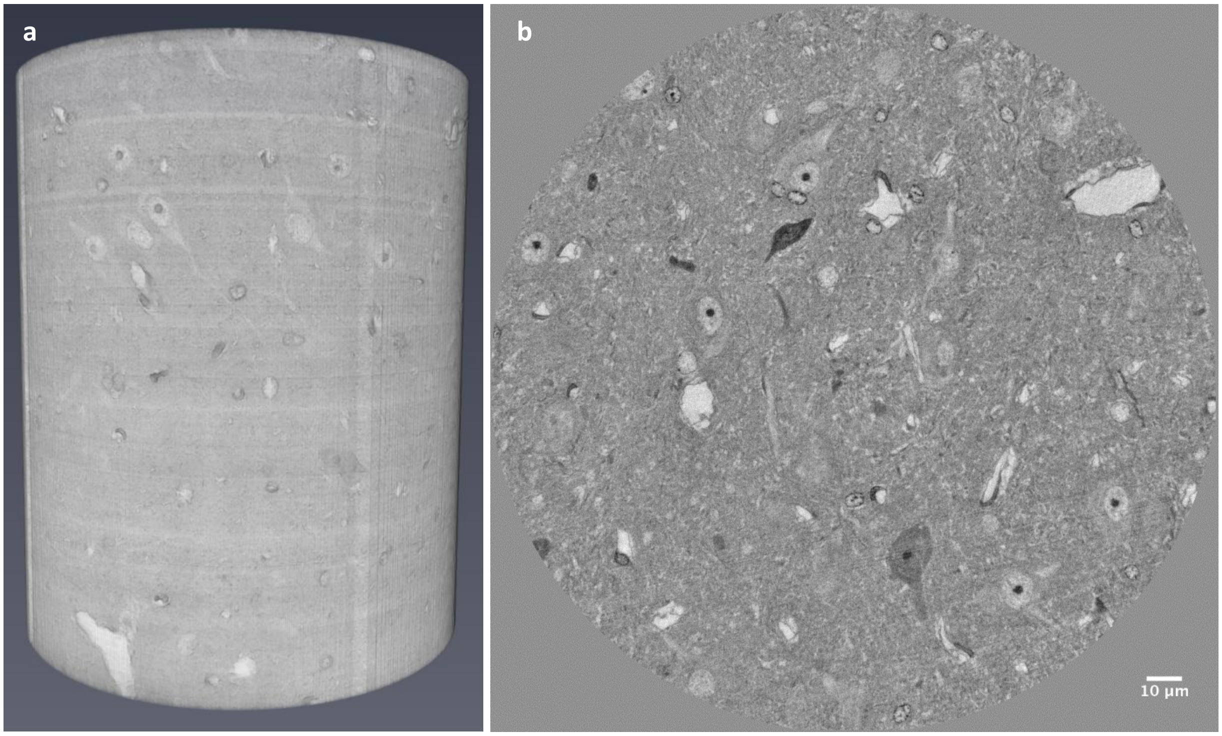

Figure 3.26. **a)** Reconstructed volume (200x200x200 µm^3) of somatosensory cortical rat sample (*control_12a*). **b)** The holotomographic reconstruction (100 nm of pixel size) led to the visualization of different kinds of cells within the cortical tissue with a very good contrast.

A first 3D visualization has been achieved, before performing the real segmentation process, in order to observe the entire shape and distribution of all the structures revealed. The 3D view (Figure 3.27) related to a small portion of the sample (200 slices) and performed through an open 3D software, *ParaView*, clearly show the different structures in a colored density scale (from red, less dense to blue more dense). In red are evidenced blood vessels and other structures not well identified and in azure neurons and glial cells are depicted.

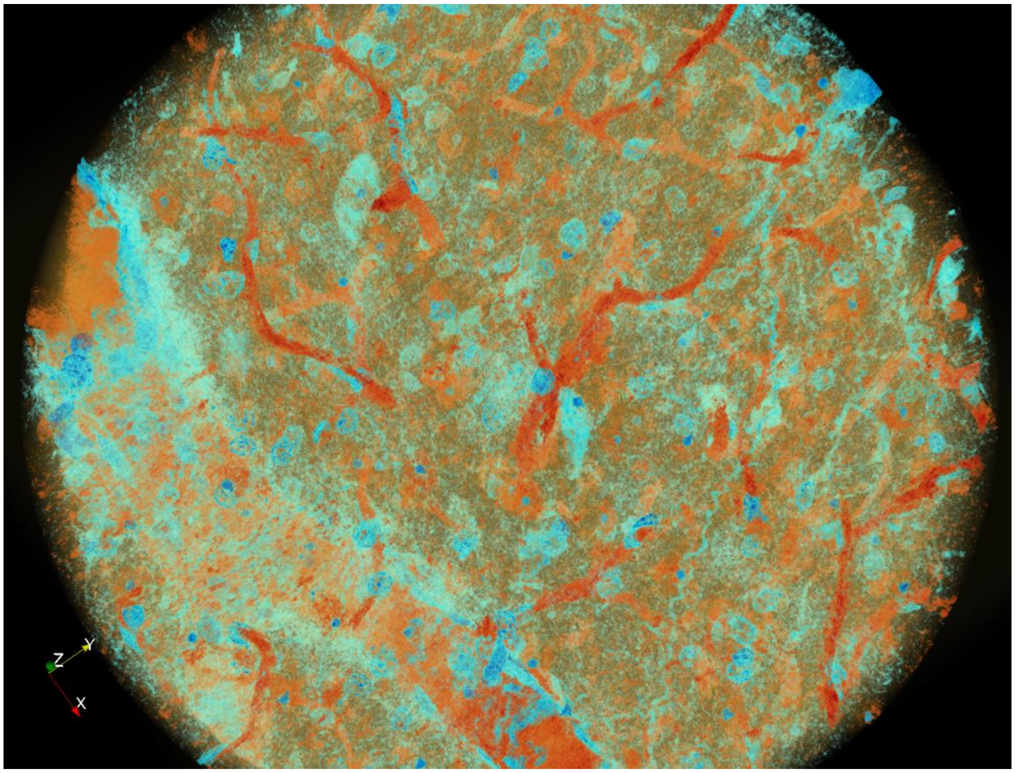

Figure 3.27. Preliminary 3D rendering of a small portion of the same sample: the colour scale is based on material density: from red (less dense structures, like blood vessels) to azure/blue (more dense structures, like cells) (*ParaView*®)

Image segmentation. Due to the failure of all the tools and free software to build a relatively quick and automatic image segmentation method, this procedure has been performed manually by visual inspection of each slice along the sample height. (*VG Studio Max*®). Through the visual comparison with brain histological slices available in literature, five categories of components have been identified in the reconstructed volumes. They are: 1) vessels; 2) light neuronal cell; 3) dark neuronal cells; 4) light glial cells and 5) dark glial cells. In Figure 3.28 an example of cell identification and segmentation is showed.

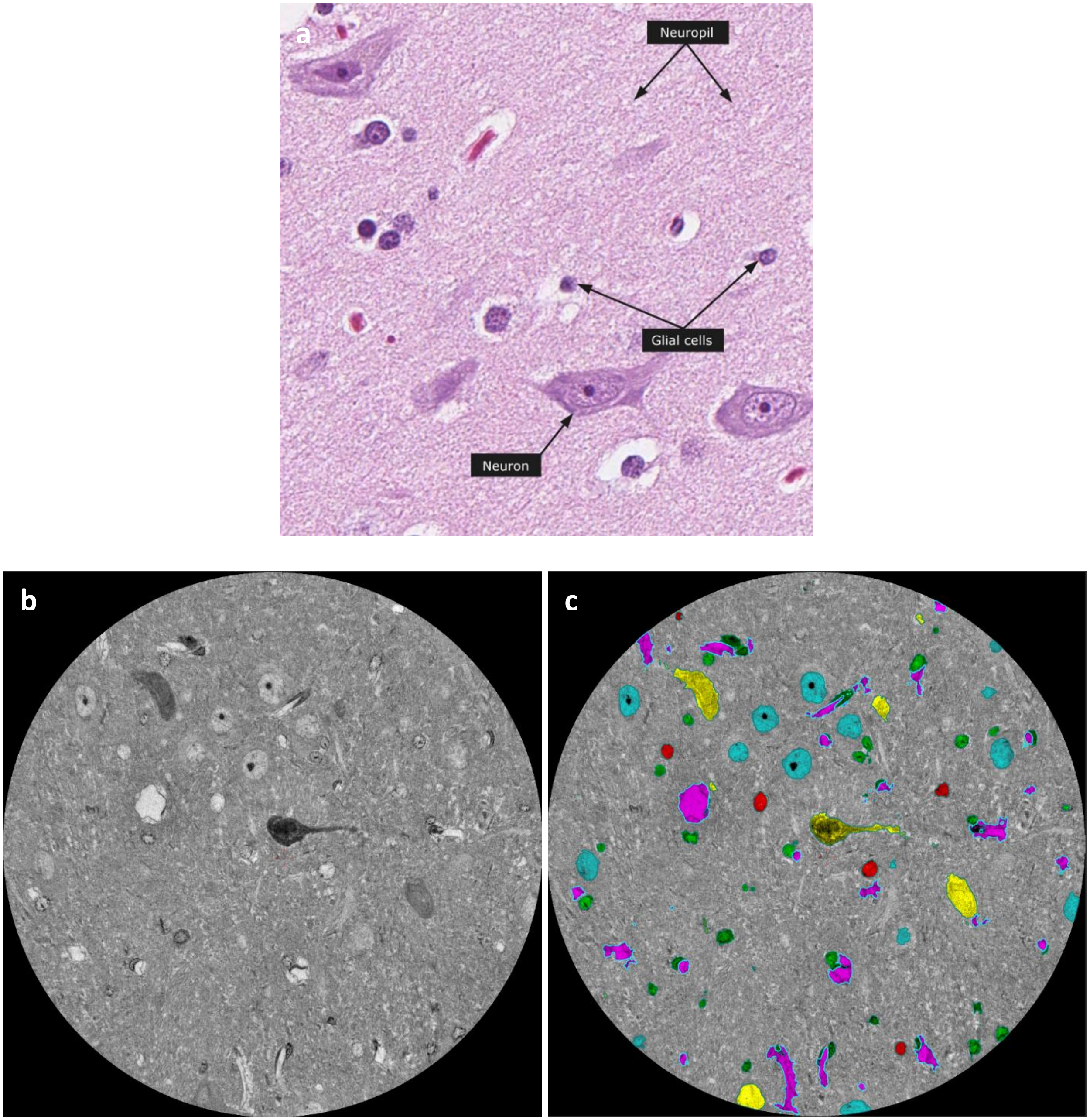

Figure 3.28. Example of cells identification and manual segmentation on a single slice. In the histological slice **(a)** the neuronal and glial cells are highlighted. These structures have been identified in the reconstructed volume **(b)** and then manually selected with different colours (vessels = magenta, glial cells = red and green, neuronal cells = azure and yellow) **(c)**.

Volume rendering. After the segmentation process, the volume rendering can be displayed (*VG Studio Max*®). The more accurate representation of the vascular-glial and neuronal thread is reproduced in 3D space (Figure 3.29).

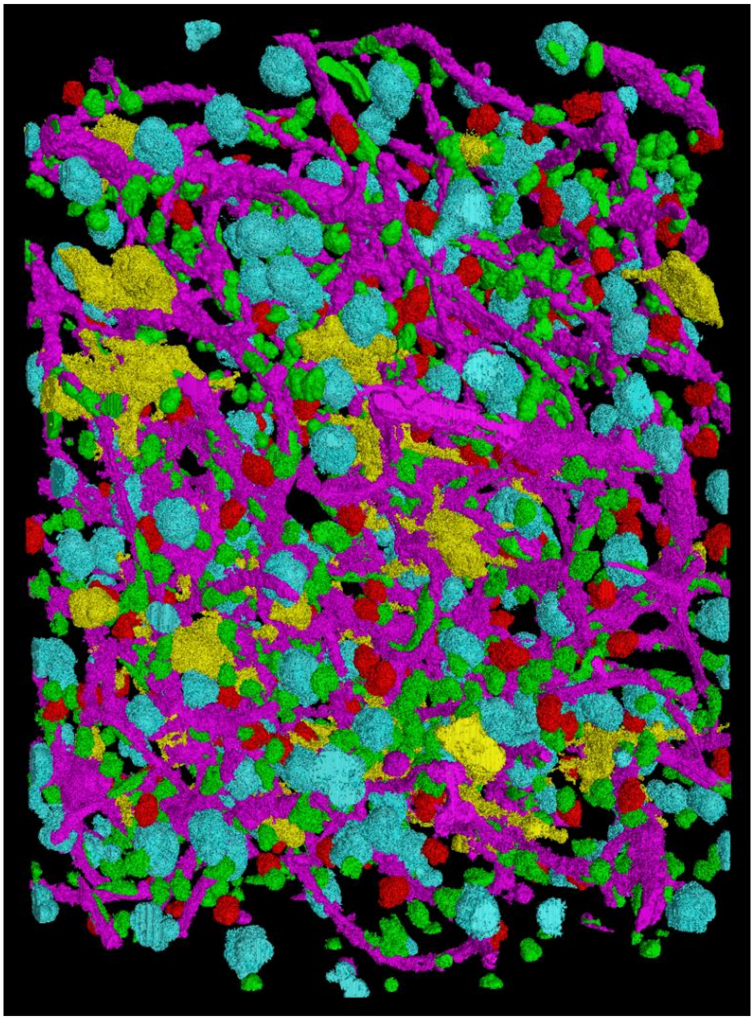

Figure 3.29. Volume rendering of the intricate neuronal-glial-vascular network (200x200x200 μm^3).

Spatial configuration. As preliminary analysis of the spatial configuration of the elements identified within the cortical tissue, the Euclidean distance between centroids of neurons and vessels and between centroids of glial and vessels has been computed on the skeletonized volumes through the *"dist.m"* Matlab® function. All the distances have been plotted in function of the vessel diameter (Figure 3.30). An inverse proportional law between the vessel diameter length and the minimum distance between vessels and glia (as well as for neurons) has been found.

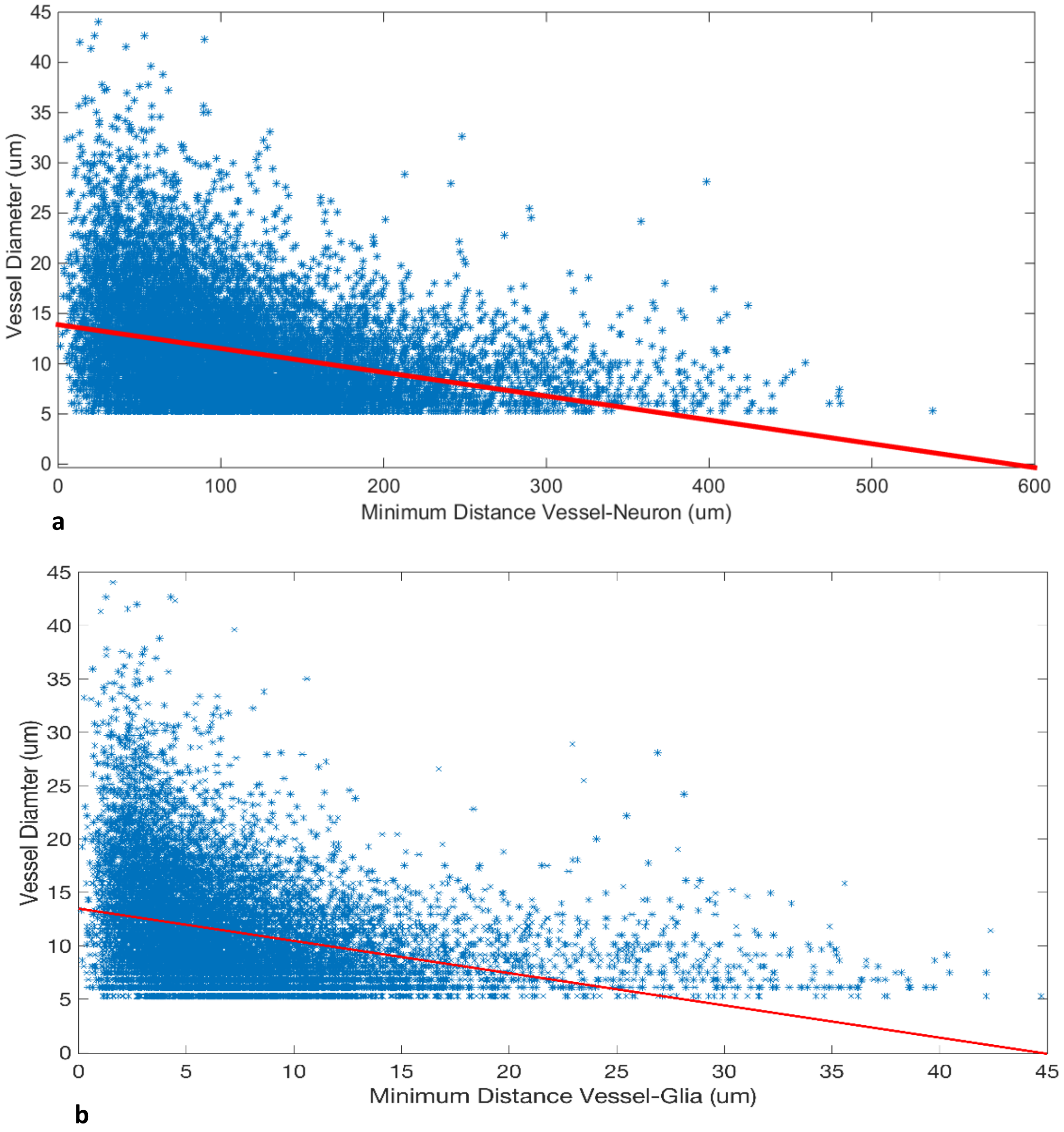

Figure 3.30. Diagrams of the minimum Euclidean distance between vessels and neurons **(a)** and vessels and glia **(b)** in function of the minimum vessel diameter (5 µm). In red the linear regression line is represented (R= -0.3265 (a) and R= -0.3178 (b)). The minimum detectable vessel diameter has been set to 5 µm; accordingly a threshold has been introduced.

In other words, larger vessels require closer neurons or glia displacements. From a metabolic perspective, this result suggests that larger vessels are less prone to supply metabolites so that energy demanding brain cells (glia and neurons) are subject to fewer spatial restrictions.

3.6 Neurodynamic analysis: functional characterization of CP

To analyse the genesis and the evolution of the TC circuits in CP conditions, the neural activity has been recorded by means of 32-microelectrode matrices implanted into the rat brains, simultaneously receiving signals from the VPL thalamic nucleus and the SS1 cortex. The recording sessions, lasting half an hour each, were performed each working day for six months. Along this period, the signal amplitude progressively decreased; in fact we assisted to an increasing impedance arising from the glial envelopes that made the signal-to-noise ratio unacceptably low during the recordings. The spike timings of each putative neuron were extracted by means of a spike sorting procedures and a set of coherent complex network features have been subsequently obtained (Materials and Methods, 2.6.3).

3.6.1 Qualitative functional connections: communities identification

The topology of the functional connections among neuronal populations in VPL thalamic nucleus and SS1 cortex is visualized by means of "graph layout" pointing out the community structures within the TC network. As explained before, in network science, a community is a group of nodes that have a higher likelihood of connecting to each other than to nodes from other communities. Figures 3.31 and 3.32 show the functional connections in the normal condition, namely before the CP induction. The situation at 11, 5 and 2 days (in the Figure: -11; -5; -2) before the PSL have been represented (for -2 days representation, Figure 3.31).

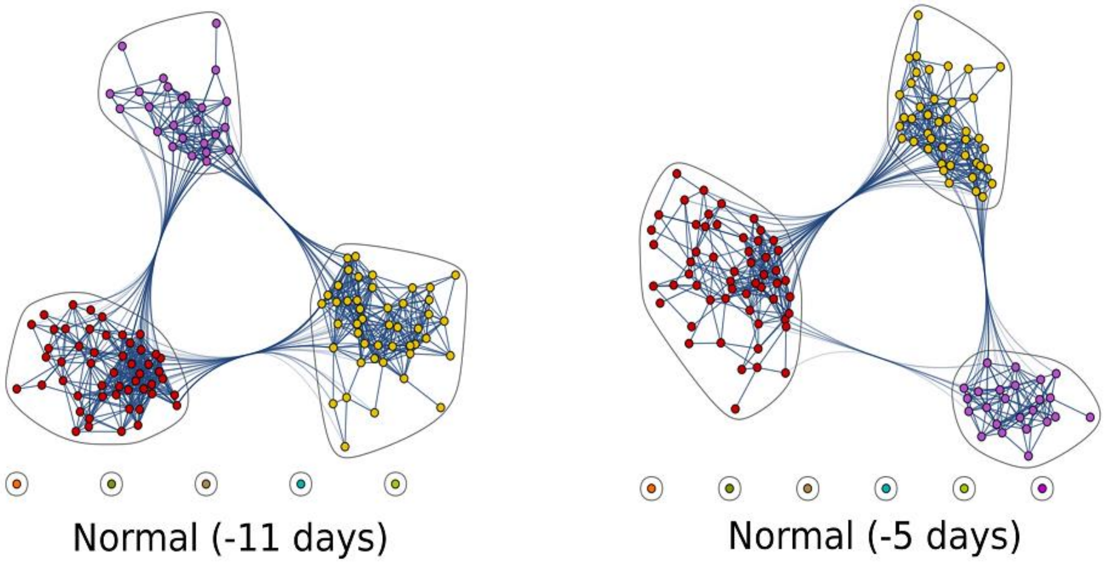

Normal (-11 days)

Normal (-5 days)

Figure 3.31. Graphs representing the qualitative functional connections within the TC loop at different times (11 and 5 days before the CP induction). Data obtained using the function "CommunityGraphPlot" (Wolfram Research, Inc. Mathematica, Version 8.0, Champaign IL).

The illustration of all the communities during the surgical day and after the induction of CP condition are showed in Figure 3.32 and 3.33. The spiking activities of each recording day has been opportunely processed. Obviously, we chose only a finite number of recordings at sufficiently spaced recording times

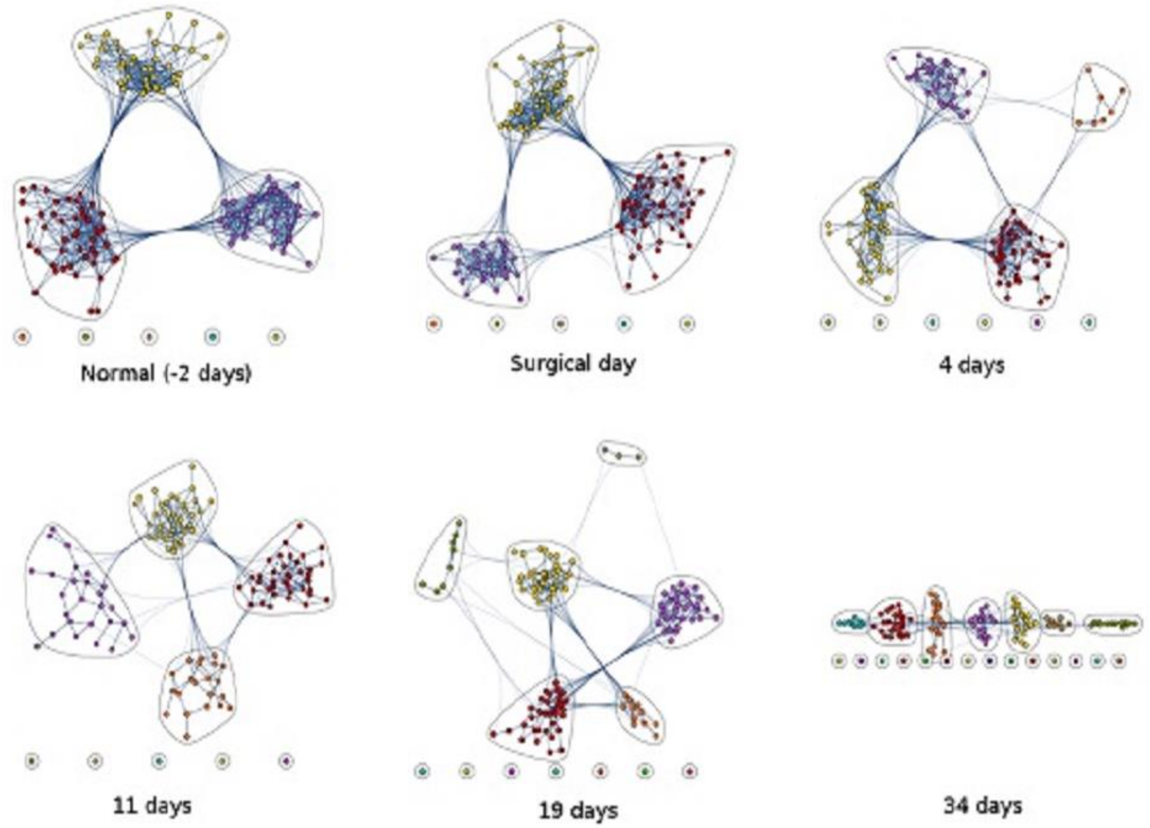

Normal (-2 days)

Surgical day

4 days

11 days

19 days

34 days

Figure 3.32. Graphs representing the qualitative functional connections within the TC loop at different times before (normal), during (surgical day) and after the CP induction (at 4, 11, 19 and 34 days). Data obtained using the function “CommunityGraphPlot” (Wolfram Research, Inc. Mathematica, Version 8.0, Champaign IL).

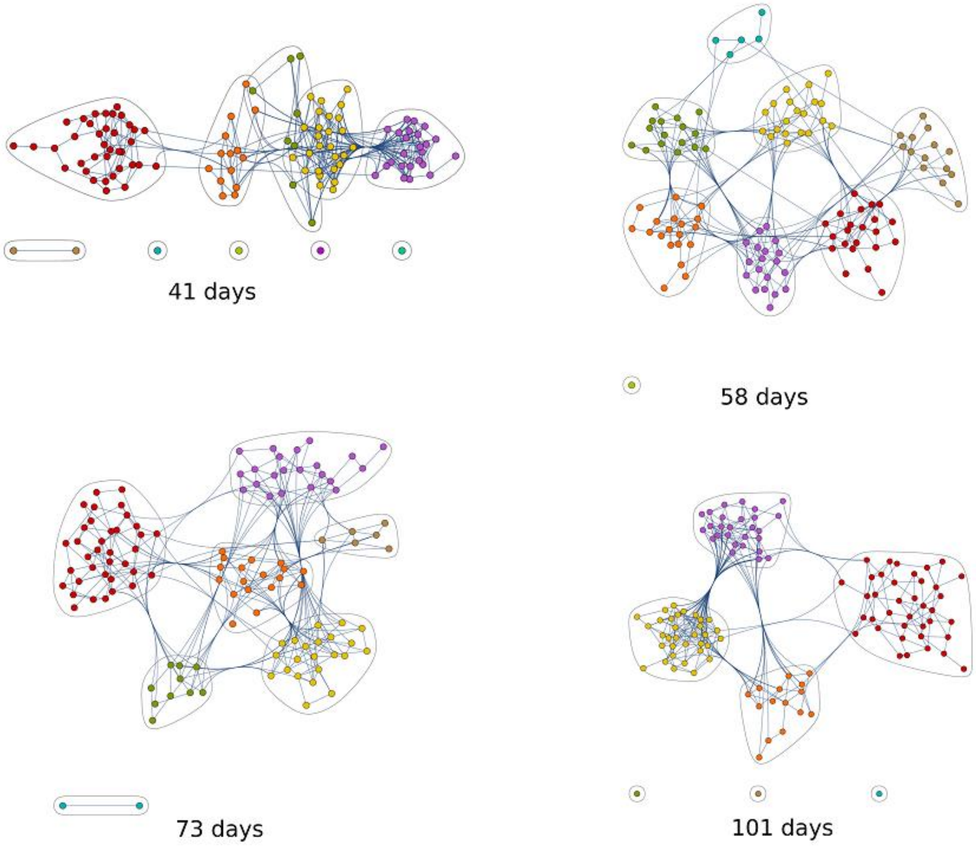

Figure 3.33. Graphs representing the qualitative functional connections within the TC loop at different times after the CP induction (at 41, 58, 73 and 101 days). Data obtained using the function “CommunityGraphPlot” (Wolfram Research, Inc. Mathematica, Version 8.0, Champaign IL).

3.6.2 Segregation and Integration: “Modules and Hubs” network indices

The clustering coefficient (C, the node tendency to form highly dense clusters) and the efficiency (E, inversely related to the characteristic path length, that is, the average shortest path length among nodes) were estimated on the extracted graphs (Materials and methods, 2.6.3.3). The results obtained are shown in the box whisker plots (Figure 3.34), where the C and E values were estimated on a weekly average. C and E values appeared significantly different between the control condition and the periods after CP induction. In particular, the C values were higher before the PSL operation than after CP induction, as well as the E values. As said before, the “Modules and Hubs” topology is characterized by dense local clustering of neighbouring nodes and a short path length between any (distant) pair of nodes, supporting both segregated (specialized) and integrated (distributed) information processing. Therefore, these results indicated that TC circuits of the CP rat segregate and integrate information significantly worse in comparison to the normal condition.

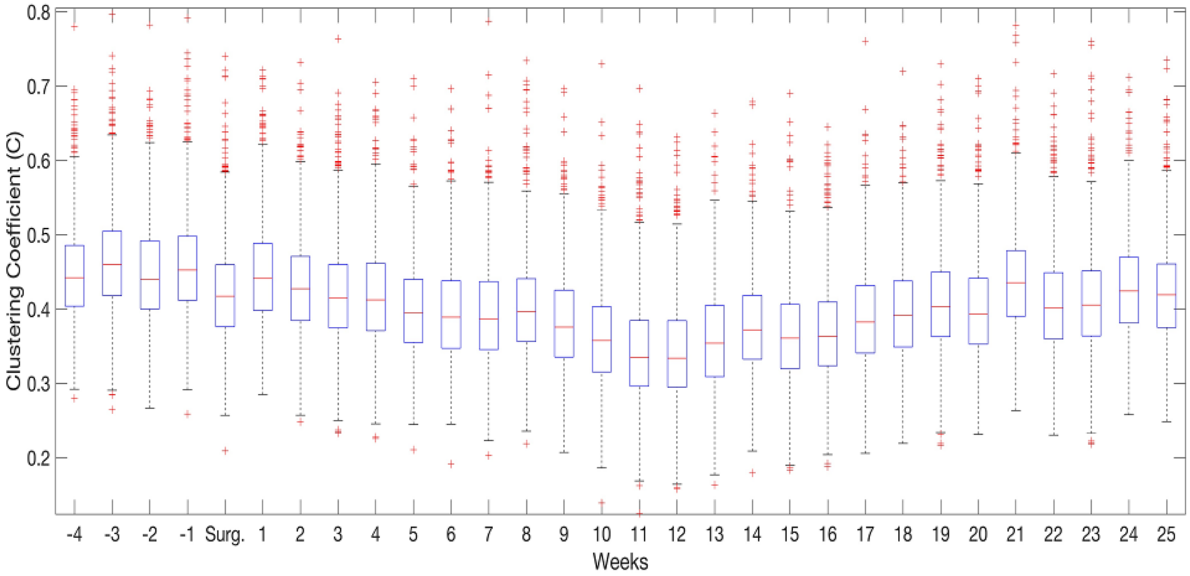

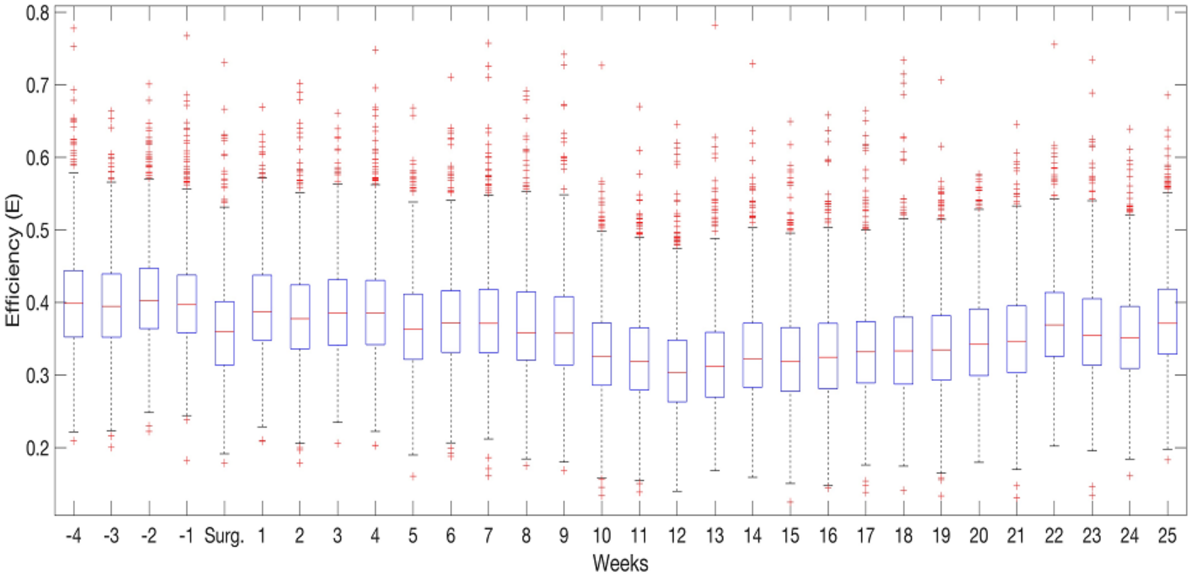

Figure 3.34. Distribution of the Clustering coefficient, C (top) and Efficiency, E (bottom) of the extracted graphs during all the time stages considered before, during and after the CP induction.

3.7 Behavioural data

The rats after the CP induction showed the complete CP behavioural phenotype marker of a "painful state" within few days with a variable persistence of signs up to more than 1 month after surgery, in comparison with the same rats before the PSL operation. Specific signs and symptoms such as spontaneous postural guarding and paw withdraw during gait, combined with allodynia and hyperalgesia, in sensory tests were all observed.

3.7.1 Von Frey test data

The results obtained from Von Frey test are synthesized in the histogram of Figure 3.35. On the y-axis are represented the values of force exerted in a logarithmic scale (Materials and Methods, 2.5.7.1). On the x-axis the time-course of the measurements is represented. Indeed, T_0 refers to the time before the induction of chronic pain, or rather, the control values. Then, we tested the rats 3 days after the PSL and once a week until 6 weeks after the operation. All the columns were obtained from the averaged values of all five rats used for the chronic implants. The blue columns show the values of the left hind paw, whereas the red columns show the values for the right hind paw, the operated ones. In this way at each time it's possible to discriminate between the two paws, the healthy one (ipsilateral to the brain implant) and the operated one (contralateral to the brain implant). It's remarkable that already after 3 days from the induction of chronic pain, there were increased sensitivity signs in the contralateral hind paw; vice versa there wasn't any type of alteration in the sensitivity of the ipsilateral hind paw for all the 6 weeks. For the first 4 weeks after the PSL operation, the contralateral hind paw showed a pronounced sensitivity for lower values of application force in respect to the "control" hind paw, i.e. the ipsilateral one. After the sixth week the responsiveness of the operated hind paw showed reduced signs of allodynia.

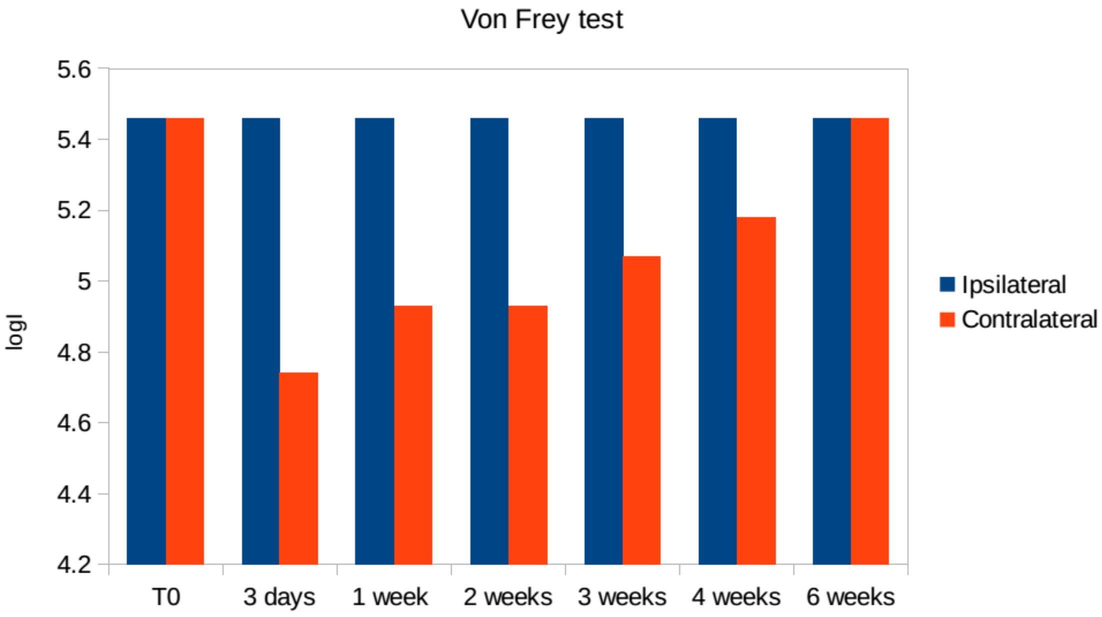

Figure 3.35. Histogram of the Von Frey test data: the response to the force exerted (in logarithmic scale) is evaluated during time (from T_0, day of the operation until the 6 weeks after the CP induction) for both the hind paws: ipsilateral (blue) and contralateral (orange) to the brain implant.

3.7.2 Hot plate test data

The results obtained from the hot plate test are synthesized in the histogram below (Figure 3.36). On y-axis is represented the latency time (in seconds) that the rats took to show a nociceptive response, such as licking the hind paw, vocalizing, or lifting the paw. On x-axis is represented the time-course of the measurements. Indeed, T_0 refers to the time before the induction of chronic pain, or rather, the control values. Then, we tested the rats 3 days after the PSL operation, and at one week, 2, 4 and 6 weeks after CP induction. All the columns are obtained from the averaged values of all five rats we used for the implants. The blue columns show the values of the left hind paw, whereas the red columns show the values for the right hind paw, the operated one. In this way it is possible to discriminate at each time between the two paws, the healthy one (ipsilateral to the brain implant) and the operated one (contralateral to the brain implant). The results obtained show that the latency to respond to a thermal stimulus decreases already from 3 days after the operation in the case of the contralateral hind paw, whereas, regarding ipsilateral hind paw, the latency decreases from the first week. Both the responses come back to their initial values from the fourth week.

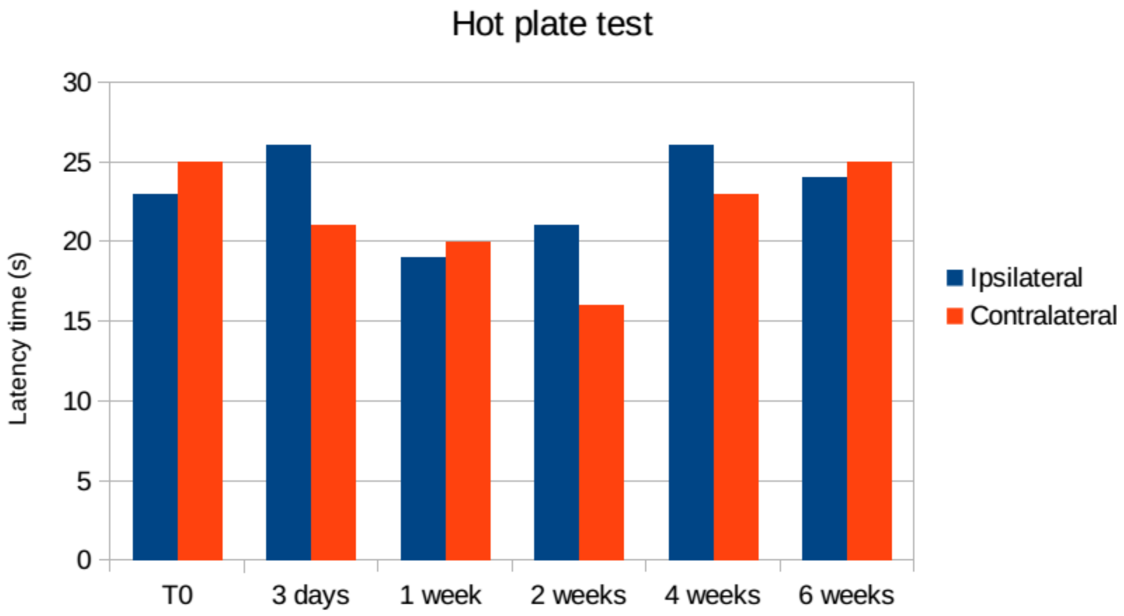

Figure 3.36. Histogram of the Hot plate test data: the latency time (in seconds) that the rats took to show a nociceptive response is evaluated during time (from T_0, day of the operation until the 6 weeks after the CP induction) for both the hind paws: ipsilateral (blue) and contralateral (orange) to the brain implant.

Besides the walking scheme irregularities and the sensory threshold anomalies, no other evident anomalous behavioural signs have been observed either in feeding or sleeping rhythms.

3.8 Near Infrared Spectroscopy analysis: preliminary results

Electrical traces of cortical blood microvasculature have been collected from NIRS recordings (Materials and Methods, 2.5.5). From a preliminary analysis, we related the estimated values of deoxygenated and oxygenated haemoglobin in order to see if any changes in the signal correlations were evident in control and CP rats. A crucial difference has been observed, since neuropathic signals appeared less correlated (R = 0.367, p = 0.001, permutation test) in comparison to control ones (R = 0.232, p<<0.01 permutation test) as reported in Figure 3.37.

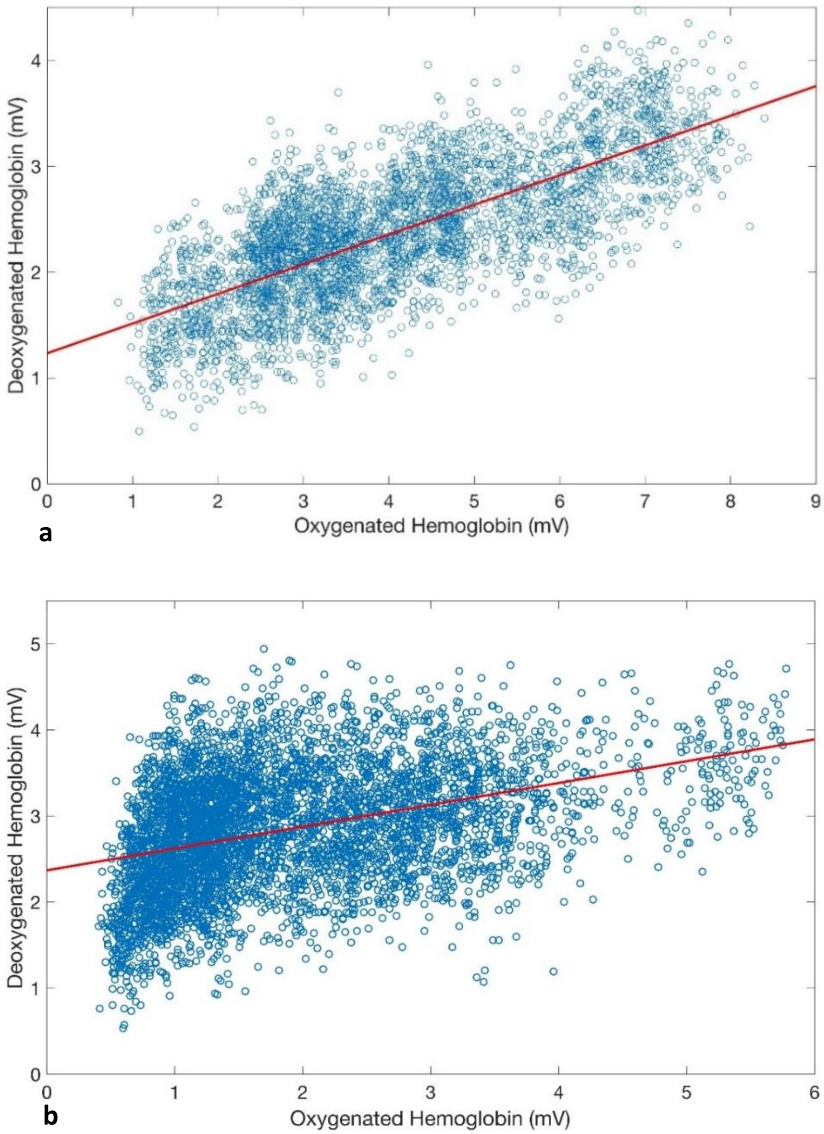

Figure 3.37. Correlation between the oxygenated and deoxygenated haemoglobin signals in control **(a)** (R=0.232) and CP **(b)** (R= 0.367) rats.

Whether confirmed by further experiments and conclusive analyses, such a result could suggest that a copious alteration of the regular balancing between the oxygen intake and carbon dioxide outtake occur in the central somatosensory neuronal populations. In such a scenario, CP could severely induce a hypoxic/ hypercapnic state activating a cascade of injuring consequences for the nervous tissue. However, such analysis still remain preliminary and further experiments could confirm or revoke such claims.

References

DeFelipe J. 2011. “The Evolution of the Brain, the Human Nature of Cortical Circuits, and Intellectual Creativity.” *Frontiers in Neuroanatomy* 5. Frontiers Media SA.

Ford L. R. and Fulkerson D.R. 1956. “Maximal Flow through a Network.” *Canadian Journal of Mathematics*. doi:10.4153/CJM-1956-045-5.

Meyer H. S., Schwarz D., Wimmer V.C., Schmitt A.C., Kerr J.N.D., Sakmann B. and Helmstaedter M. 2011. “Inhibitory Interneurons in a Cortical Column Form Hot Zones of Inhibition in Layers 2 and 5A.” *Proceedings of the National Academy of Sciences* 108 (40): 16807–12. doi:10.1073/pnas.1113648108.

Chapter 4: Discussion

Summary

This last chapter is dedicated to the discussion risen around the important findings emerged through this morpho-functional study in the complex scenario of CP disease. The involvement of microvascular changes in somatosensory cortical anatomy is strongly correlated to the detected disruption of neuronal functional connectivity. The present findings suggest a novel interpretation of CP, where not only the neuronal substrate, but also the glial-vascular unit play a central role during the development of the disease.

Résumé

Ce dernier chapitre est dédié à la discussion sur les résultats importants découlant de cette étude morpho-fonctionnelle dans le scénario complexe de la maladie de la DC. L'implication des changements microvasculaires dans l'anatomie corticale somatosensorielle est fortement corrélée à la perturbation détectée de la connectivité fonctionnelle neuronale. Les résultats actuels suggèrent une nouvelle interprétation de la DC, où non seulement le substrat neuronal, mais aussi l'unité gliale-vasculaire jouent un rôle central lors du développement de la maladie.

Contents

4 Discussion

Through the present study we have revealed both structural and functional changes in tripartite synapse and blood microvessel compartments in the somatosensory cortex of CP rats. Two novel methodologies have been developed for the investigation of CP pathology in collaboration with the neuroscientists of the Institute of Molecular Bioimaging and Physiology (IBFM) of the Consiglio Nazionale delle Ricerche (CNR) in Milano (Italy). The first one aimed at characterizing the functional changes induced by CP in the somatosensory thalamo-cortical circuitry through electrophysiological recordings from experimental rats with three different models of CP (Bennett and Xie or CCI model; Partial Sciatic Nerve Constriction, Seltzer model; Peripheral Inflammation). The functional substrate was investigated from a graph-theoretical perspective and a common set of complex network statistics estimated the measures of interest. All the CP groups showed connectivity disorders in the VPL thalamic nucleus and in the afferent somatosensory cortex which severely drain the repertoire of functional state expressed by the circuit (Antonio G Zippo et al. 2016). Specifically, the observed network showed a reduction in information transmission among the two brain regions and the increased redundancy in firing patterns in CP models (compared to controls) have been interpreted as precise markers of CP. The abnormal recursive and stereotyped network configurations, those expressed by the thalamocortical loop in CP animals, seemingly appear as anatomo-functional counterparts of the continuous percept of pain, a picture recoverable from all the examined CP models. Eventually, a distinctive feature emerged by network analysis of the thalamocortical circuit: while brain networks are regularly organized in groups (moduli) of nodes with dense intra-connectivity and sparse interconnectivity among groups (literature commonly refers to such an architecture as “Module-and-Hubs”), the observed CP networks showed a strong agglomerative tendency to form fewer moduli (Antonio G Zippo et al. 2016). On the basis of these findings, an innovative strategy has been proposed by the IBFM group, aiming at manipulating the thalamic-cortical circuitry in order to increase the number of functional moduli in the affected thalamo-cortical loop. Thus, an experiment has been performed at ID 17 beamline of the ESRF (Grenoble, France) featured by 7 collimated X-ray microbeams (360 Gray, Gy) delivered over the somatosensory cortex of both normal and CP rats *in vivo*. These microbeams, arranged to induce thin cuts (100 µm wide) mostly to the cortical intercolumnar horizontal connections, boost the reorganization of the involved brain regions able to communicate through new paths along the vertical direction. As a matter of fact, the electrophysiological and behavioural analysis show a recovery of all the measured parameters in CP animals with values comparable to the control ones. In this scenario, a deeper investigation of the microarchitectural anatomical compartments appeared necessary even taking into account of the large collection of CP studies focused on the functional counterpart (e.g. with fMRI techniques) (Apkarian et al. 2007). Since adult neuronal modifications mostly keep unaltered the tissue’s cytoarchitecture, we proposed, as working hypothesis, that relevant changes should affect the thinnest elongations of the vascular system, i.e. capillaries and arterioles commonly called *microvessels*. Therefore, a subsequent analysis for revealing the structural changes of microvessels has been carried out on experimental rats.

4.1 Microstructural analysis

A series of microCT Imaging experiments have been performed at the TOMCAT beamline of the Swiss Light Source (SLS, Villigen Switzerland) to acquire the whole cortical microvasculature of a core region of the relative somatosensory cortex at the resolution of 0.325 µm (Materials and Methods, 2.5.2). Microvessels were highlighted by the high contrast of a carbon-rich solution (Indian Ink) which selectively pervaded experimental animal's vessels by perfusion. The phase contrast imaging technique has been applied to resolve the brain vasculature at micro scale. Five of the six layers (from I to Va) of the somatosensory cortex have been reconstructed for 15 samples (7 CP and 8 CR) for total length of about 1.2 mm. Technical limitations prevent the acquisition of deeper regions and related data analyses are still on going. The volume renderings allowed for a detailed visualization of the vascular thread, subsequently characterized through a morphological and topological analysis which underlined a set of tight CP induced vascular changes that will be presented in the following sections:

- Comparative study *"Neuropathic vs Control"* rats.
- Evaluation of CP dynamics.
- Estimation of vascular network properties.

4.1.1 Comparative study "Neuropathic vs Control" rats

From a comparative study *"Neuropathic vs Control"* a widespread increase of blood microvessels and capillaries in the somatosensory cortical investigated region has been found in all CP rats. The microvascular system is characterized by an increased number of vessels, skeleton segments and branch points in all CP rats respect to the control ones. This angiogenetic event appeared to affect the small vessels and capillary structures, as proved by the increased number of microvessels with a diameter lesser than 15 µm found in CP rats. The results obtained have been confirmed also by parallel immunofluorescence microscopy analysis: CP samples have shown the positivity to three markers of vascular neo-genesis (VEGFR1, VEGFR2 and VWF). Correlations between neoangiogenesis and pathological conditions are not new. While tumour, obesity and inflammation and other factors are known to locally promote neoangiogenesis in the central nervous system such phenomenon is generally induced by endogenous factors (e.g. Alzheimer's disease) (Qin et al. 2015) and Parkinson disease (Janelidze et al. 2015). So far, an abundant reconfiguration of the microvascular network as a consequence of a peripheral actor (induced peripheral neuropathy) has never been observed.

4.1.2 Evaluation of CP dynamics

The global angiogenetic event has been followed in three times: 2 weeks, 2 months and 6 months after the CP model induction. The initial 2 weeks stage appeared the most affected from the vascular increase: indeed, the vessel proliferation soon manifested goes to a progressive reduction in 2 months, slowing down at 6 months. This phenomenon could be assumed as a consequence of the neuronal metabolic needs from anomalous activities in CP where changes in microvessel may indeed not only respond to but also sustain the alterations of the served neurons. The microvascular components have to be considered in the whole tripartite synapse environment, comprehending pre- and postsynaptic neuronal terminals and the astrocytic synaptic envelopes. Altogether these elements build up a hardly dividable *functional entity* or neuro-glial-vascular (NGV)-*unit* where each one act simultaneously contributing to the functionality of the unit itself. As a matter of facts, all the disorders involving even one element of the *NGV unit* appears to implicate all the unit elements. For instance, the cortical gross laminar misalignments, evidenced in fMRI from CP patients, should be carefully evaluated in view of the local meso- and microscopic environment. However, the mechanisms underlying these structural and functional disorders need a deeper investigation in order to clarify their metabolic effects. The results relative to CP-related microvessel neogenesis could help to examine, in a new perspective, the haemodynamic conditions expressed in CP and conjecture, along with the pathogenesis, the ensuing metabolic costs and the subsequent complex adaptive responses of the NGV unit in CP genesis and maintenance.

4.1.3 Estimation of vascular network properties

Graph theoretical analyses have been used to analyse the microvascular network. Regarding the computed vascular network properties, a remarkable difference between CP and control conditions have been found in the network *maximum flow*, representing the theoretical capacity of the network (modelled as a *pipeline*) to load low viscosity fluids. We have found that the maximum flow sustainable in CP vascular networks is much greater than control networks. Although our computational estimation of the *maximum flow*, it remains to be clarified if an efficient blood flux in the anomalously packed microstructures may take place, yet globally preserving stable biophysical processes such as blood shear thinning or thixotropy, i.e. the blood fluidity changes with shape changes, or the gaseous and solute exchanges. Murray's law has also to be taken into account since it provides an interpretation of the fluid transport in vascular systems where functional relation between vessel radius and volume flow, velocity of flow, and vessel wall shear assures an optimum operation of the system. Indeed, the arrangement of vessels in the organism is influenced by general physical laws as well as by specific physiological requirements (Sherman 1981). In particular, by analysing the vascular branching system, it has been found that the daughter vessel diameters are related to parental vessels in a regime where the radii of the vessels must be in relation to flow (the larger the radius, the smaller *power* required for *flow*, P_f), and to metabolic upkeep costs or *power* of the vessel *wall tissue* (P_{wt}). Namely, vessels have to be neither too large nor too small if the *total power*, $Pt = P_f + P_{wt}$, is to be minimized, a configuration probably acquired under selective pressure. However, the novel microvessels, due their crowding, anomalous topology and mutual relations, rise critical conditions that changing the large-to small vessel ratio, contravene this law of parsimonious minimal biological workload and flux continuity. On the other side, the surge of microvessels appears a reasonable response to the increased energetic requests and it would be a nonsensical event, further energetic request from vessel generation, in a linear cause-effect biologic chain

Then, considering the slow but significant, even if not complete, decay of the microvessel surge in the following months, we can consider it the result of an adapting phenomenon or recovery process of exceeding upkeep costs of the newly generated vessels and the sustenance of pathological CP related energetic costs. In topological terms, the unchanged values of clustering coefficient and characteristic path length suggest that the surge of novel microvessels as well as the progressive decay of the majority of them in the next months presents a steady topological organization. As a side note, these vascular event cascades recoverable also in CP patients, by fMRI scanning, may become more complex to be understood, being assignable also to microvessel volume changes with debatable signs of activations of already extant vessel compartment.

From a functional point of view, a large array of molecular and cellular mechanisms take place for assuring cerebral blood flow (CBF) regulation allowing for the trans cellular transport of gases and various substances and nutrients to neurons through a continuous interaction among glial end feet and microvessels (Kisler et al. 2017). The neo angiogenetic microvessels to supply the neuronal metabolic demand have to be efficient in terms of metabolites transport and, therefore, to establish mutual efficient contacts with the glial interface. It is conceivable that at least a significant fraction of these vessels may represent active energy sites for different reasons. In first place, the surge of the phenomenon could be hardly justified in a period when high neuronal energy consumption, with additional energetic costs of vessel neogenesis, would have no energy trade-off counterbalance. Secondarily, the novel vessels could play protective roles to avoid that severe energy shortage conditions might trigger hypoxic and apoptotic processes. The slightly persistence of neo-genetic vessels remaining at six months could be considered a long-term remnant response of metabolic compensation, integrated within the brain tissue on a hyperactive or anomalous neuronal network.

4.2 Neurodynamic analysis

In vivo chronic recordings with implantable wireless multi-electrode array technology have been carried out on CP rat to investigate the functional connectivity changes in TC neuronal ensemble induced by CP. From these electrophysiological observations, we have obtained an analytic representation of the functional connectivity of TC loop during three time stages: before the PSL operation, during and immediately after the PSL operation and after the CP induction. It has been shown that, during in-vivo recordings, active neurons form functional assemblies that may not necessarily depend on the underlying anatomical connectivity. Therefore, while the anatomical connectivity is stable for relatively long times, the functional connections are highly dynamic and depend on the particular tasks triggered by internal and/or external events.

4.2.1 The neuronal network architecture in normal condition: a “Modules and Hubs” network configuration

Within the period of control recording, that is, before the induction of CP, the sensory TC network architecture exhibited typical features of “Modules and Hubs” configuration as named in graph theory science. In fact, in the days before the PSL operation, we can observe high values of clustering coefficient, a measure that indicates good segregation properties, accompanied by high efficiency values, due to the presence of few long-range connections, ensuring a good global integration. Thence, this typical network configuration, shared by many complex systems, can be considered the result of an evolution process developed for reaching an efficient signal integration and segregation ensuring an effective information processing. Moreover, the “Modules and Hubs” architecture is structured to achieve lower level the energy consumption, in order to minimize wiring costs while supporting high dynamical complexity. For these reasons, it appears to be the most diffuse configurations adopted by complex systems.

4.2.2 The network reconfiguration during the PSL operation and the immediate events in the first days after the ligature

The functional connection graphs underwent significant topological reconfigurations after the system perturbation. Indeed, not statistically significant changes have been detected during the surgical procedure of CP instantiation on the implanted rats. However, just after four days from the PSL operation, we can observe rearrangements of the functional connections, as it has been shown in the community graph layout. In parallel, behavioural tests evidenced profound changes after the CP surgery: in comparison to the control periods, in fact, signs of persistent hyperalgesia and allodynia are observable already from the third day after the CP induction, up to the fourth week (as evidenced in the von Frey allodynia test). We could thus hypothesize that after an initial massive sensory input (namely the PSL) significant anomalous events with permanent effects are able to perturb the system with functional connectivity changes already after few days, dramatically decaying in the following period. The conditions enabled by these events are seemingly the start-point which promote the onset and the maintenance of CP related states.

4.2.3 The evolution of the network dynamics in the weeks and months after CP induction

From the fourth day, up to the nineteenth-twentieth day after CP induction, the network dynamics evolved towards a progressive collapse of the system which completely loses the characteristics of “Modules and Hubs” network structure, as confirmed by the clustering coefficient and efficiency values reduction. These changes are accompanied also by a gradual disintegration of the community architecture: both the intra-community and inter-community functional connections decrease, whereas the number of communities increases. Altogether this cascade of events concurs to damage the system operations. Again, after one month the signal integration and segregation get worst until the limit of network disintegration is reached. Thence, this new functional architecture is responsible for the final information dropping off to its lowest levels. The functional modules in CP fade away, generating new connectivity conditions that could contribute to the maintenance of that pathology.

On large-scale brain networks in other neuropathological contexts, it has been observed that the eventual disruptions of the robust balance between integration and segregation are tightly related to pathological conditions (Schizophrenia, Epilepsy, Autism, etc.). Indeed, a “Modules and Hubs” organization appears a fundamental requirement for the proper physiology of information processing in the brain (Bullmore and Sporns 2012; Deco et al. 2015; A.G. Zippo et al. 2013) as well as in spontaneous activations of neuronal cultures (Bettencourt et al. 2007) that are lost in neuronal samples exposed to damage and maladaptive processes, leading to pathologic conditions (Fornito, Zalesky, and Breakspear 2015).

4.2.4 The correlation between microvascular and neuronal network dynamics in CP

The involvement of microvascular changes during CP has been observed from the extensive morphological analysis of cortical vascular network in a comparative study “control vs neuropathic” rats. In parallel, rat *in vivo* chronic electrophysiological studies clearly identified the alteration of TC neuronal network connectivity a constant functional feature of CP. The correlation between these important findings appear now more understandable if we think about the previously mentioned brain functional entity formed by the NGV unit. Its unique functional importance for brain energy consumption and metabolic activity is assured by the intense communication between the glial cells and the blood microvessels, whose walls are wrapped by astrocytes’ end feet. Proper function of precisely wired neural circuits depends on a close physical and functional relationship with a complex and overlapping network of blood vessels (Lecrux and Hamel 2011). In addition, recent studies showed how sensory-related neural activity regulates the structure of vascular network in mouse cerebral cortex (Lacoste et al. 2014). In this scenario, it’s conceivable that the well evidenced cortical microvessel neo-genetic events in CP, strongly present since the first-time stage of the neuropathy, should be followed by a mutual change in neuronal network dynamic.

The present findings suggest that a novel approach to study CP should be developed, where, not only the neuronal substrate, but also the glial-vascular unit has to be considered in terms of metabolic energy efficiency during the development of the disease.

Conclusions and future perspectives

The microstructural study focused on the cortical architecture of the neuronal-glial-vascular complex in CP have revealed strong episodes of vascular neo-genesis in cortical rat samples analysed through Synchrotron X-ray microCT Imaging. In parallel, electrophysiological studies have identified the disruption of functional connectivity of the TC network a peculiar feature shared by all CP rats.

The present findings are in consistent with the recent studies evidencing the importance of the functional role played by the NGV unit for assuring brain functional metabolic efficiency. The complex anatomo-functional thread formed by neurons, vessels and glial cells cooperates to allow reliable dynamics of the system. Large-scale imaging studies have already demonstrated a relationship between neurons and vessels dynamics, but a precise appraisal of the microvascular architecture, by sure influencing the gaseous and metabolic exchanges among neurons, glial cells and vessels at the subcellular levels, is still missing.

Namely, the correlated findings open a new way of interpretation of CP disease, not only recognized as sensory pathology, but also as a neurological disease where neuronal and vascular connectivity networks are extensively involved in the whole system. Indeed, disrupted functional connectivity and neurovascular uncoupling that result from a mismatch between CBF, O_2 delivery and neuronal activity have been found in the early stages of many neurological disorders including Alzheimer’s disease (AD), amyotrophic lateral sclerosis (ALS) and stroke (Zlokovic 2011; Iadecola 2004; Iadecola 2013). Therefore, future experiments will be addressed to a deeper investigation of the functional relationships among neurons and glia during the onset and the development of CP through new *in vivo* NIRS recordings on CP rats.

From these experiments, we could advance in the knowledge of CP related conditions, where not only the structural microvascular rearrangements, but also the correct operation of the vascular micro-circuitry may be affected with potential detrimental effects on the whole brain metabolism.

The study here proposed could possibly contribute to understand the CP core anomalies and to find new therapeutic solutions, different from the existing ones, which could act to the origin of the disease.

References

Baliki M.N., Geha P.Y. and Apkarian A.V. 2007. "Spontaneous Pain and Brain Activity in Neuropathic Pain: Functional MRI and Pharmacologic Functional MRI Studies." *Current Pain and Headache Reports*.

Bettencourt L.M.A., Stephens G.J., Ham M.I. and Gross G.W. 2007. "Functional Structure of Cortical Neuronal Networks Grown in Vitro." *Physical Review E*. doi:Artn 021915\nDoi 10.1103/Physreve.75.021915.

Bullmore E.T. and Sporns O. 2012. "The Economy of Brain Network Organization." *Nature Reviews Neuroscience*. doi:doi:10.1038/nrn3214.

Deco G., Tononi G., Boly M. and Kringelbach M.L. 2015. "Rethinking Segregation and Integration: Contributions of Whole-Brain Modelling." *Nature Reviews Neuroscience*. doi:10.1038/nrn3963.

Fornito A., Zalesky A. and Breakspear M.. 2015. "The Connectomics of Brain Disorders." *Nature Reviews Neuroscience*. doi:10.1038/nrn3901.

Iadecola C. 2004. "Neurovascular Regulation in the Normal Brain and in Alzheimer's Disease." *Nature Reviews Neuroscience* 5 (5): 347–60. http://dx.doi.org/10.1038/nrn1387.

Iadecola C. 2013. "The Pathobiology of Vascular Dementia." *Neuron*. doi:10.1016/j.neuron.2013.10.008.

Janelidze S., Lindqvist D., Francardo V., Hall S., Zetterberg H., and O. Hansson. 2015. "Increased CSF Biomarkers of Angiogenesis in Parkinson Disease." *Neurology*. doi:10.1212/WNL.0000000000002151.

Kisler K., Nelson A.R., Montagne A. and Zlokovic B.V. 2017. "Cerebral Blood Flow Regulation and Neurovascular Dysfunction in Alzheimer Disease." *Nature Reviews Neuroscience* 18 (7). 419–34. http://dx.doi.org/10.1038/nrn.2017.48.

Lacoste B., Comin C.H., Ben-Zvi A., Kaeser P.S., Xu X., Costa L.F. and Gu C. 2014. "Sensory-Related Neural Activity Regulates the Structure of Vascular Networks in the Cerebral Cortex." *Neuron* 83 (5). Elsevier Inc.: 1117–30. doi:10.1016/j.neuron.2014.07.034.

Lecrux C. and Hamel E. 2011. "The Neurovascular Unit in Brain Function and Disease." *Acta Physiologica* 203 (1). Blackwell Publishing Ltd: 47–59. doi:10.1111/j.1748-1716.2011.02256.x.

Qin W., Jia X., Wang F., Zuo X. and Jianping J. 2015. "Elevated Plasma Angiogenesis Factors in Alzheimer's Disease." *J Alzheimers Dis*. doi:10.3233/JAD-142409.

Sherman T. F. 1981. “On Connecting Large Vessels to Small. The Meaning of Murray’s Law.” *The Journal of General Physiology*. doi:10.1085/jgp.78.4.431.

Zippo A.G., Gelsomino G., Duin P.V., Nencini S., Caramenti G.C., Valente M. and Biella G.E.M. 2013. “Small-World Networks in Neuronal Populations: A Computational Perspective.” *Neural Networks* 44. doi:10.1016/j.neunet.2013.04.003.

Zippo A.G., Valente M., Caramenti G.C. and Biella G.E.M. 2016. “The Thalamo-Cortical Complex Network Correlates of Chronic Pain.” *Scientific Reports*. http://dx.doi.org/10.1038/srep34763.

Zlokovic B.V. 2011. “Neurovascular Pathways to Neurodegeneration in Alzheimer’s Disease and Other Disorders.” *Nature Reviews Neuroscience*. doi:10.1038/nrn3114.